

Novel Metal Oxide Semiconductor-Based Multifunctional Nanomaterials for Gas Sensing and Optical Applications

Thesis submitted for the degree of
Doctor of Philosophy in Science

To



**Department of Physics
Jadavpur University**

By

Tanushri Das

Registration Number: SOPHY1104721

Date-23.03.2021


Jadavpur, Kolkata-700 032, India

September, 2024


Dedicated to my beloved parents

CERTIFICATE FROM THE SUPERVISORS

This is to certify that the thesis entitled “*Novel Metal Oxide Semiconductor-Based Multifunctional Nanomaterials for Gas Sensing and Optical Applications*” submitted by **Smt. Tanushri Das** (Registration number: **SOPHY1104721**) who got her name registered on 23rd March, 2021 for the award of Ph.D. (Science) Degree of Jadavpur University, is absolutely based upon her own work under the supervision of **Dr. Chandan Kumar Ghosh**, Assistant Professor, School of Materials Science & Nanotechnology, Jadavpur University, Kolkata-700032, India and **Dr. Mrinal Pal**, Chief Scientist, Head of the Department, Functional Materials and Devices Division, CSIR- Central Glass and Ceramic Research Institute (CGCRI), Kolkata-700032, West Bengal, India and that neither this thesis nor any part of it has been submitted for either any degree / diploma or any other academic award anywhere before.


19/09/2024
Dr. Chandan Kumar Ghosh
Assistant Professor,
School of Materials Science &
Nanotechnology,
Jadavpur University,
Kolkata-700032,
West Bengal, India.

Dr. Chandan Kumar Ghosh
Assistant Professor
School of Materials Science
& Nanotechnology,
Jadavpur University
Kolkata - 700 032


19/9/24
Dr. Mrinal Pal
Chief Scientist & Head,
Functional Materials and Devices Division,
CSIR-Central Glass & Ceramic Research
Institute,
Kolkata-700032,
West Bengal, India.

Dr. Mrinal Pal
Chief Scientist & Head
Functional Materials and Devices Division
CSIR-Central Glass & Ceramic Research Institute
Kolkata- 700 032

DECLARATION

I hereby declare that the work presented in this thesis entitled, “*Novel Metal Oxide Semiconductor-Based Multifunctional Nanomaterials for Gas Sensing and Optical Applications*” has been carried out by me at the School of Materials Science & Nanotechnology, Jadavpur University, Kolkata-700032, and Functional Materials and Devices Division (FMDD), CSIR-Central Glass and Ceramic Research Institute, Kolkata-700032, under the supervision of Dr. Chandan Kumar Ghosh, Assistant Professor, School of Materials Science & Nanotechnology, Jadavpur University, Kolkata-700032, India and Dr. Mrinal Pal, Chief Scientist & Head, CSIR-Central Glass and Ceramic Research Institute, Kolkata-700032, India. Neither this thesis nor any part of it has been submitted for any degree / diploma or any other academic award anywhere before.

Tanushri Das

Jadavpur University
Jadavpur, Kolkata-700032
India

Acknowledgements

I would like to express my heartfelt gratitude to my superiors Dr. Chandan Kumar Ghosh and Dr. Mrinal Pal for guiding and supervising me throughout my research journey. I am profoundly appreciative of their exceptional mentorship. Their guidance has been a beacon of clarity and inspiration. I am truly grateful for their unwavering dedication and for fostering an environment where curiosity and excellence thrive.

I want to convey my gratitude to my supervisor, Dr. Mrinal Pal, Chief Scientist, HoD, FMDD, CSIR-CGCRI, for his kind effort, consideration and appreciation towards me in every circumstances. I am grateful to him for giving me freedom in pursuing my research work and always being supportive of me. The wisdom and support he has generously shared have not only propelled my academic growth but have also deeply influenced my personal development. I am truly thankful to my supervisor, Dr. Chandan Kumar Ghosh, Asst. Prof., School of Materials Science & Nanotechnology, for his insightful advice, patience, and expert knowledge that have been invaluable in shaping my academic endeavour. His unwavering support, guidance, and encouragement have motivated me to achieve higher-quality work. I am truly thankful for having such knowledgeable persons as my supervisors.

I am grateful to the Director, School of Materials Science & Nanotechnology, Jadavpur University, and the Director, CSIR-CGCRI, for giving me permission to carry out my work in their institutes. I want to thank central characterisation facility of CGCRI for helping me carry out research work. I am grateful to the entire School of Nano Science and Technology, and Department of Physics, Jadavpur University for letting me use their instrument facility.

I would like to extend my heartfelt gratitude to Dr. Debdulal Saha, Principal Scientist, FMDD, CSIR-CGCRI, for his kind support and encouragement throughout my PhD journey. My immense gratitude goes to Dr. Srabanti Ghosh, Senior Scientist, EMDD, CSIR-CGCRI, for her constant encouragement in my work. She has helped me to gain knowledge beyond my core research area. I can not be more thankful to her for the support and guidance.

I want to thank my lab-mate and research partner, Subhajit Mojumder, for being an integral part of the research experience. His scientific discussions and suggestions have been invaluable. His presence has made the challenges more manageable and the achievements even more meaningful. It has been a privilege to work with him, and I truly appreciate his helpful gesture in the time of need. I want to thank my junior lab-mate Riddhiman for his tireless efforts and valuable contribution in helping me carry out my research work. I also want to thank my

junior lab-mates Krishnendu, Sanjib for their selfless assistance. My heartfelt gratitude goes to my lab-seniors, Sagnik Das and Sonam Chakraborty, for being there to support and help me in my initial days in the lab. Their willingness to share knowledge and provide constructive feedback has been instrumental in shaping my work.

I want to express my deepest gratitude to my Maa and Baba for their unwavering belief in me that have been the cornerstone of my journey. They have been my steadfast support system through the highs and lows of my life and provided me with the strength to overcome obstacles and pursue my dreams. Their belief in my abilities and constant motivation have been a source of inspiration. The values they have instilled in me have been my guiding light through every challenge. Their unwavering support and boundless encouragement have been integral part of my journey, and I am profoundly appreciative of everything they have done for me. This accomplishment is as much theirs as it is mine, and I am eternally grateful for the foundation they have provided and the faith they have shown.

My special thanks go to my sister, Suvashree, whom I call as Putu, for her enthusiasm, patience, and belief in me. I thank her for being my cheer-person and for bringing a lightness and joy that I will always cherish. Her late-night pep-talks during my lowest moments have always brought happiness that will forever hold a special place in my heart. Her enthusiasm has made this accomplishment even more special.

Finally, I would like to extend my heartfelt gratitude to everyone who has supported me throughout my academic journey. Thank you for being there in every step of the way.

Tanushri Das
September, 2024

Abstract

Metal oxide semiconductor nanomaterials-based chemiresistive gas sensors hold merits for its cost-effectiveness, simplicity of operation and stability. High surface area-to-volume ratio provides myriads of surface-active sites making MOS nanomaterials superior for interaction with ambient gas molecules. The monitoring and selective detection of volatile organic compounds (VOCs) and gases is crucial for environmental protection and minimizing the risk of toxic gas exposure. Another important aspect of gas sensors is their utility in diagnosing diseases by detecting exhaled breath biomarker VOCs/gases associated with specific health conditions. Thus, the analysis of exhaled breath has opened the door to the development of portable devices for medical diagnostics. However, major drawback faced by binary metal oxide semiconductor-based sensors is their difficulty in detecting specific gases in complex environments, along with slow response and recovery times, which hinder their ability to perform real-time monitoring. Another challenge these sensors encounter is that their inability to detect target gases at ppb-level concentrations, restricting their widespread application. Therefore, new materials as alternatives of binary oxides are needed to expand the area of gas sensing materials.

This research thesis delineates the exploration of novel metal oxide semiconductor nanomaterials to overcome the drawbacks of the binary metal oxide gas sensors. Barium hexaferrite ($\text{BaFe}_{12}\text{O}_{19}$), a widely known magnetic material, has diverse application in microwave devices and recording systems due to its excellent electromagnetic property, but has never been used as a gas sensor material before. This thesis demonstrates the development of novel gas sensor based on $\text{BaFe}_{12}\text{O}_{19}$ nanoparticles, capable of detecting sub ppm level concentration of ammonia gas rapidly with high resolution while effect of interfering gases on the detection of target gas is minimum. The mechanism of ammonia sensing of prepared $\text{BaFe}_{12}\text{O}_{19}$ nanoparticles has been explained with the gas adsorption model. The excellent ammonia sensing characteristics of $\text{BaFe}_{12}\text{O}_{19}$ nanoparticles has proved its potential for practical application.

With another exploration, the effect of Zn doping on ammonia sensing property of barium hexaferrite ($\text{BaFe}_{12}\text{O}_{19}$) has been delineated. Substantial enhancement in response towards ammonia by virtue of Zn-doping in $\text{BaFe}_{12}\text{O}_{19}$ has been observed. The Zn-doped $\text{BaFe}_{12}\text{O}_{19}$ nanoparticles with hexagonal platelet-like morphology exhibited improved ppb level concentration detection and decrease in operating temperature compared to pristine

BaFe₁₂O₁₉. Extensive study has revealed that, the enhanced sensing characteristics is attributed to the tuning of Fe²⁺/Fe³⁺ ratio, oxygen vacancies and improved electron-hole separation due to Zn doping. Furthermore, simulated breath test validated the Zn-doped BaFe₁₂O₁₉ nanoparticles-based ammonia sensor's suitability for exhaled breath analysis.

Perovskite type bismuth ferrite (BiFeO₃), which is a multiferroic material, has been studied for its gas sensing activity. Pure and Sn-doped BiFeO₃ nanoparticles exhibited ppb-level concentration detection of formaldehyde (HCHO) in indoor air environment. The study delineates, charge compensation mechanism during the incorporation of Sn in BiFeO₃ matrix. The enhancement of formaldehyde sensing property due to Sn-doping is a combined effect of variation of charge carriers due to valency mismatch, improved charge-separation efficiency and enhanced oxygen defects generated in the system. Excellent formaldehyde sensing activity of Sn-doped BiFeO₃ nanoparticles indicates its potential towards the monitoring of indoor air quality.

In the next exploration, the formation of n-n-type heterostructure between MoO₃/BiFeO₃ with unique morphological structure and its hydrogen sulfide (H₂S) gas sensing capability has been demonstrated in this thesis. Utilizing photoelectrochemical measurement of the heterostructure, the electron transfer mechanism from conduction band (CB) of BiFeO₃ to the CB of MoO₃ has been revealed. Modification of band edges by formation of heterojunction with wide bandgap, α -MoO₃ and narrow bandgap, BiFeO₃ and tuned oxygen defects have synergetic effect on its enhanced sensing performance. Moreover, presence of oxygen defects has created myriads of active sites for H₂S adsorption which significantly enhanced the response value. This study provides a route for designing bandgap-engineered α -MoO₃/BiFeO₃-heterostructure with enriched oxygen defects to address the need for environmental air-quality monitoring.

Finally, for optical study, NaTb(MoO₄)₂ nanoparticles has been explored. In addition, NaTb(MoO₄)₂ exhibited formaldehyde sensing activity with outstanding response characteristics. The multifunctional property of the NaTb(MoO₄)₂ nanoparticles has been investigated by inducing structural disorder in the system via controlled synthesis procedure. The formation of band structure has been studied by employing ab initio calculations based on density functional theory (DFT). Excellent green photoluminescence property of disordered NaTb(MO₄)₂ structure revealed its potential for commercial use in light emitting devices. Moreover, the gas response characteristics has established NaTb(MO₄)₂ nanoparticles as a

novel formaldehyde sensing material suitable for real-time air quality monitoring. This study provides new insights into the fabrication and engineering of nanomaterials that exhibit multifunctionality driven by structural disorder.

In totality, a combined study of different types of metal oxide semiconductor nanomaterials and their heterostructures for gas sensing and optical properties have been delineated. Improved gas sensing property has been achieved for these materials in terms of sensitivity, response time and low concentration gas detection which overcomes the demerits of binary metal oxide semiconductor-based gas sensors. Some of the materials have exhibited both photoluminescence and gas sensing property. Both of these properties are controlled by surface electronic states, charge transfer mechanism and structural disorder in the system. All of these investigated materials can positively contribute to efficient gas sensing and optical applications.

Table of Contents

	<u>Contents</u>	Page No.
I	Acknowledgements	9
II	Abstract	11
III	Table of Contents	15
Chapter 1	Introduction and literature review.....	19-68
1.1.	Introduction	21
1.2.	Application areas of metal oxide semiconductor nanomaterials	21
1.3.	Types of gas sensing techniques	22
1.4.	Applications of chemiresistive gas sensors	23
1.5.	Working principle of chemiresistive gas sensing	25
1.6.	Influencing parameters of MOS based gas sensors	29
1.7.	Photoluminescence properties of MOS nanomaterials	31
1.7.1.	Mechanism of photoluminescence	31
1.7.2.	Applications of photoluminescence	32
1.8.	Material synthesis and characterization techniques	33
1.9.	Review of literature	42
1.9.1.	Binary MOS-based chemiresistive gas sensors	42
1.9.2.	Different doping on MOS-based chemiresistive gas sensors	47
1.9.3.	Heterostructure based chemiresistive gas sensors	48
1.9.4.	Ferrite-based chemiresistive gas sensors	49
1.9.5.	Scheelite nanomaterials for solid state lighting	51
1.10.	Objective of the work	53
1.11.	Thesis outline	55
1.12.	References	59
Chapter 2	Novel barium hexaferrite-based highly selective and stable trace ammonia sensor for detection of renal disease by exhaled breath analysis	69-94
2.1.	Introduction	71
2.2.	Experimental Section	73
2.2.1.	Materials	73
2.2.2.	Synthesis of Barium Hexaferrite nanopowder	73
2.2.3.	Fabrication on Barium Hexaferrite nanopowder based sensor	74
2.2.4.	Preparation of trace ammonia vapor and sensor measurement setup	75
2.2.5.	Characterization	76
2.3.	Results and Discussion	77
2.3.1.	Structural Characterization	77
2.3.2.	Electrical Characterization	82
2.3.3.	Sensitivity Study	83

2.3.4.	Sensing Mechanism	89
2.4.	Conclusion	91
2.5.	References	92
Chapter 3	Enhanced ammonia sensing performance of barium hexaferrite enabled through Zn doping: Mechanistic study considering modulation of $\text{Fe}^{2+}/\text{Fe}^{3+}$ ratio and oxygen vacancy	95-127
3.1.	Introduction	97
3.2.	Experimental section	99
3.2.1.	Materials and reagents	99
3.2.2.	Synthesis of Zn doped $\text{BaFe}_{12}\text{O}_{19}$ samples	99
3.2.3.	Characterization of materials	99
3.2.4.	Fabrication of prototype chemiresistive sensor	100
3.2.5.	Gas preparation procedure	100
3.2.6.	Study of effect of relative humidity on gas sensing property	101
3.3.	Results and discussion	102
3.3.1.	Crystallographic structure and morphological analysis	102
3.3.2.	Chemical state and surface area analyses	107
3.3.3.	Optical properties	111
3.3.4.	Gas sensing properties for ammonia	112
3.3.5.	Simulation of breath analysis	118
3.3.6.	Mechanism of NH_3 sensing	119
3.4.	Conclusion	122
3.5.	References	123
Chapter 4	Beneficial effect of Sn doping on bismuth ferrite nanoparticle-based sensor for enhanced and highly selective detection of trace formaldehyde	129-161
4.1.	Introduction	131
4.2.	Experimental section	134
4.2.1.	Materials and reagents	134
4.2.2.	Synthesis of Sn doped bismuth ferrite nanoparticles	134
4.2.3.	Characterization of materials	135
4.2.4.	Fabrication of chemiresistive sensor module and gas measurement setup	135
4.3.	Results and discussion	136
4.3.1.	Crystallographic structure and morphological analysis	136
4.3.2.	Chemical state and surface area analyses	140
4.3.3.	FTIR spectra analysis and band gap measurement	143
4.3.4.	Electrical properties	145
4.3.5.	Gas sensing properties	146
4.3.6.	Performance comparison to other chemiresistive formaldehyde gas sensors	151
4.3.7.	Mechanism of gas sensing	152

4.4.	Conclusion	156
4.5.	References	158
Chapter 5	n-n type α-MoO₃/BiFeO₃ heterostructure for enhanced charge transfer induced H₂S gas sensing	163-200
5.1.	Introduction	165
5.2.	Experimental Section	167
5.2.1.	Chemicals	167
5.2.2.	Synthesis of BiFeO ₃ nanoparticles	167
5.2.3.	Synthesis of α -MoO ₃ and α -MoO ₃ /BiFeO ₃ heterostructure	167
5.2.4.	Growth mechanism of α -MoO ₃ nanorods α -MoO ₃ /BiFeO ₃ heterostructures	168
5.2.5.	Characterization of heterostructures	169
5.2.6.	Photoelectrochemical measurements	170
5.2.7.	Gas sensors fabrication	171
5.3.	Results and discussion	171
5.3.1.	Structure and morphology	171
5.3.2.	Optical and surface electronic properties	177
5.3.3.	Photoelectrochemical properties	182
5.3.4.	H ₂ S sensing properties	186
5.3.5.	Mechanism of H ₂ S sensing	192
5.4.	Conclusion	196
5.5.	References	197
Chapter 6	Structural disorder driven multifunctionality of NaTb(MoO₄)₂ nanoparticles toward green photoluminescence and detection of formaldehyde.....	201-239
6.1.	Introduction	203
6.2.	Experimental Section	205
6.2.1.	Chemicals and materials	205
6.2.2.	Synthesis of NaTb(MoO ₄) ₂	206
6.2.3.	Characterization of NaTb(MoO ₄) ₂	206
6.2.4.	Fabrication of gas sensors using NaTb(MO ₄) ₂ nanomaterials	207
6.2.5.	Calculation using ab initio density functional theory (DFT)	208
6.3.	Results and discussion	209
6.3.1.	Crystallographic structure and morphological analysis	209
6.3.2.	Spectroscopic analysis of defects and electronic property	213
6.3.3.	Analysis of optical property	219
6.3.4.	Gas sensing properties of NaTb(MoO ₄) ₂ nanoparticles	225
6.3.5.	Band structure and adsorption energy calculations using density functional theory (DFT)	229
6.4.	Conclusion	234
6.5.	References	235
Chapter 7	Overall conclusion and future prospects	241
Appendix I	List of publications	249

Appendix II	Awards	251
Appendix III	Conference presentations	252

CHAPTER 1

Introduction and literature review

1.1. Introduction

Nanotechnology plays a pivotal role in advancement of modern civilization by providing state-of-the-art materials across wide range of application areas. Nanomaterials are classified by their particle size ranging from 1 nm to 100 nm. Materials designed in nanoscale exhibit enhanced surface area to volume ratio which enhances its surface reactivity by providing abundance of active sites for surface activity. Due to their high surface area greater number of atoms are located on the surface of nanoparticles compared to bulk materials. The improved chemical reactivity of nanomaterials enables efficient surface reaction kinetics. [1,2]

Over the past few decades, metal oxide semiconductors (MOSs) nanomaterials have emerged as a class of material with excellent thermal and chemical stability, the tunable energy band gaps enabling them to exhibit interesting properties suitable for wide range of applications. MOS nanomaterials have been explored for their unique characteristics originating from strong ionic bonds between positively charged metal cations and negatively charged oxygen anions. Nanostructured materials based on MOSs demonstrate unique electrical, optical, mechanical, magnetic and surface catalytic activity that differ greatly from their bulk counterparts. The morphology and structure of the MOS nanomaterials can be tailored to achieve desirable electronic properties.[3]

1.2. Application areas of metal oxide semiconductor nanomaterials

Metal oxide semiconductor (MOS) based nanomaterials are advantageous in scaling and incorporating in miniaturized micro-electronic systems that have diverse applications ranging from healthcare devices, energy storage and conversion, catalysis, green energy generation, environmental remediation, and optoelectronic devices etc.[3] The modification in their structural, morphological and chemical properties open up new application areas. Due to their large surface area and efficiency in visible light, MOS nanomaterials are excellent alternatives for conventional catalyst which offers efficient contact between reactants and catalysts. MOS with excellent catalytic activity is widely used in green energy generation technologies such as solar cell, photocatalytic hydrogen generation, fuel cell etc. In recent years, MOS nanomaterials for targeted therapeutics and diagnostics have played significant advancement of healthcare technologies. Anti-bacterial applications of MOS make them highly

effective in antibacterial defence across wide range of applications, starting from medical equipment to environmental purification. [3,4]

However, among the various application areas, gas sensing and optical application of nanomaterials has been chosen as area of study for this thesis.

Gas sensors play crucial role as an instrument for detection and discrimination of gas molecules in environment, industrial, agricultural and medical facilities since its discovery sixty years ago. Due to their versatile shape, surface functionalization capabilities MOSs are highly suitable for sensor applications. The intrinsic property of MOSs is their ability to chemically or physically adsorb gases due to their high surface-to-volume ratio which make them ideal candidates for gas sensing technology. Nanomaterial-based gas sensors provide superior sensitivity, reproducibility and cost-effectiveness. Integration of nanotechnology has resulted in major advancements in sensor design, enabling miniaturization, portability and real-time data producibility.

Since last century, the luminescence properties have been studied extensively in bulk materials. But in recent years, the study of the optical and luminescence properties on nanostructured materials has attract wide research interest. Due to their advantageous optical properties such as wide bandgap, efficiency in absorbing and emitting light, MOS nanomaterials hold significant potential in optical applications. The tunable optical properties of MOS nanomaterials make them ideal for the fabrication of photonic and optoelectronic devices such as light-emitting diodes, solid-state lightening systems, and colour display devices. The nanophosphors with efficient solid-state lighting property have been of increasing demand in bioimaging, imaging-guided therapy drug delivery and chemotherapy.

1.3. Types of gas sensing techniques

Various technologies have been developed by researchers for the soul purpose of detection of gases in various environment. Depending on operating principle these techniques can be categorized as follows [2]:

- 1) Gass chromatography mass spectroscopy:** Gas chromatography mass spectroscopy (GCMS) is a powerful analytical technique that is used for analysis and detection of volatile organic compounds (VOCs) and gas molecules. Precise identification of gas molecules can be done utilizing their molecular structure. However, the GCMS instrument is expensive and analysis process is time-consuming.

- 2) **Electrochemical sensing technique:** Electrochemical sensor technique operates by measurement of electrical changes of sensor material that takes place when it is exposed to gaseous substances, ions or biomolecules. It operates based on chemical reaction between the electrode and target molecules. However, the accuracy of the electrochemical sensors can be affected by interference from substances present alongside the target gas molecules.
- 3) **Optical sensing technique:** Optical sensing technique is based on the principle of interaction between light and the substance and provides information about the composition and characteristics of the target substance. Even though this technique is generally used in healthcare and industrial needs, the optical components and light source required for this technique is expensive and its is ineffective in detection of complex systems.
- 4) **Calorimetric gas sensing technique:** Calorimetric gas sensing is a technique utilise the heat generated or absorbed between sensor material and target gas molecule upon exposure to the target gas. By detecting the change in temperature for exothermic or endothermic reaction process, this technique is capable of providing direct information about the presence of gas. But temperature fluctuation often obstacles its performance.

In summary, these techniques are expensive, cumbersome, require train manpower and lab facility for operation which hinders their practical applicability. Therefore, significant efforts have been made by researchers for development of chemiresistive gas sensors owing to their cost-effectiveness, miniaturized size, ease of operation. Metal oxide semiconductor based chemiresistive gas sensors possess numerous advantages that include stability, quick operation, facile fabrication technique.

1.4. Applications of chemiresistive gas sensors

Compared to conventional gas sensing techniques, metal oxide semiconductor (MOS)-based chemiresistive gas sensors have wide range of application areas due to their cost-effective, stable, steadfast detection method of gas molecules. The key application areas of MOS based chemiresistive gas sensors are (schematically illustrated in [Fig. 1.1](#)):

1) Sensors for environmental monitoring:

With evolution of human civilization there has been a surge of industries and modern technologies. With hand in hand, there has also been a steep rise in toxic air pollutants emerging from the industrial facilities, factories, chemical laboratories, plants. Rapid increase of population, emission from industrial process, excessive usage of fossil fuel has given rise to

alarming increase of pollutants and toxic gases in environment. Few of the common toxic air pollutants found in outdoor environment that can cause direct effect on human health are H_2S , CO , NO_x , SO_x , NH_3 etc. Therefore, continuous monitoring of these pollutants is vital to avert environmental air quality degradation. Effective and real-time monitoring of gas sensors for environmental monitoring can help in enforcing precautionary measurements to mitigate adverse effects of air pollution on human health.[5]

2) Sensors for detection of disease

Detection of disease through invasive procedures are costly and require trained medical supervision. Breath analysis offer a non-invasive and cost-effective alternative. Human exhaled breath contains several VOCs (viz. acetone, ammonia, formaldehyde, ethanol, isoprene etc.) and gases (viz. H_2 , CO_2 , N_2 , H_2S etc.). Some of these gases/VOCs in breath have been identified as biomarker for diseases. Ammonia and acetone are biomarker of renal disease and diabetes, respectively. Elevated concentration of these biomarkers in exhaled breath is an indication of disease development. Therefore, MOS based chemiresistive gas sensors are utilised for the real time detection of and monitoring of exhaled-biomarker for diagnosis of disease.[6,7]

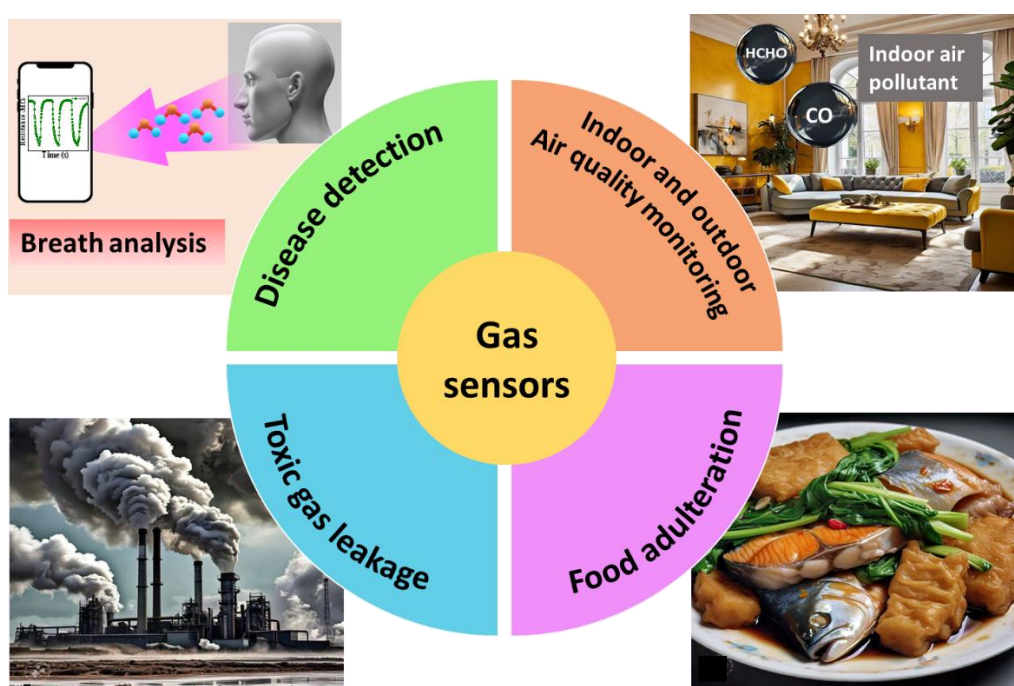


Fig. 1.1. Schematic illustration of various applications of chemiresistive gas sensors.

3) Indoor air quality monitoring

Chemiresistive gas sensors are extremely useful for detection of harmful/toxic gases and pollutants present in indoor environment. Several toxic gases (formaldehyde, benzene, toluene) are emitted from paints, newly furnished furniture, coatings, adhesives, floor cleaners which can lead to health issues if safe exposure limit is exceeded. Therefore, real-time exposure monitoring is essential for health safety.[8,9]

4) Detection of toxic gas leakage

People working in industrial facilities, coal mines, chemical laboratories often face the risk of toxic gas leakage. Therefore, chemiresistive gas sensors are extremely useful in these work environments to address the need for hazardous gas leakage monitoring.[10]

5) Detection of food adulteration

Chemiresistive gas sensors can be utilised in detection of food adulteration, contamination, spoilage. These sensors can be used in monitoring indicative VOCs such as trimethyl amine (TMA), triethyl amine (TEA), formaldehyde (HCHO) for contamination and spoilage of food. [11–13]

1.5. Working principle of chemiresistive gas sensing

Chemiresistive gas sensors based on MOS is a resistive-type device. The conductivity of the MOS materials changes when it is exposed to target analyte gases. Chemiresistive gas sensors detect the presence of gas and its concentration based on the change of its electrical resistance due to chemical reaction kinetics between the sensing surface and the target gas molecules. The gas sensing MOSs are classified into two categories: n-type and p-type, depending on whether they exhibit an increase or decrease in resistance when exposed to reducing or oxidizing target gases (ref. [Table 1.1](#)). Upon exposure to reducing (electron-donating) gases such as NH_3 , CO , CH_4 , the resistance of the MOS sensing layer with n-type characteristics decreases (schematically shown in [Fig. 1.2a](#)). While on the other hand, upon exposure to oxidizing (electron drawing) gases such as NO_2 , the resistance increases. This behaviour is reversed in case of MOS with p-type sensing characteristics (schematically shown in [Fig. 1.2b](#)).

Table 1.1 Type of gas sensing response based on change in resistance/conductivity of the materials.

Material	Exposure to reducing gas	Exposure to oxidizing gas
n-type	Resistance decreases	Resistance increases
p-type	Resistance increases	Resistance decreases

Predominantly metal oxide semiconductors act as insulators in room temperature due to their relatively wide band gap. However, donor type or acceptor type defect states exist between the band gap of n-type and p-type MOSs, respectively. Therefore, external temperature is needed to be applied for the activation of MOS sensors. When temperature is elevated to 100-500 °C, the free electrons of n-type MOSs are elevated from the donor band to the conduction band, while in p-type SMOs they move from the valence band to the acceptor band, resulting in a decrease of resistance of the material. The gas sensing mechanism of MOS sensors comprises of following steps:

- 1) Surface chemisorption of ambient oxygen molecules
- 2) Change of majority charge carrier concentration
- 3) Interaction between the target gas molecule and the ionised oxygen species on the active sensing layer surface
- 4) Change of resistance due to oxidation/reduction in the MOS active sensing layer

Due to high electronegativity, the oxygen molecules in atmosphere undergo ionisation by taking electrons available on the sensing layer and form electron depletion layer (EDL) in n-type MOS and for p-type MOS it forms hole accumulation layer (HAL), which leads to band bending. Ionisation of these chemisorbed oxygen molecules depends on the temperature of the sensor. At temperature below 100 °C, the chemisorbed oxygen species is O_2^- . At relatively higher temperature, (100 °C-300 °C) the oxygen species is ionised as O^- , and when the temperature is higher than 300 °C, the O^- ions transform into O^{2-} . When the n-type sensor surface is exposed to a reducing target gas, the target gas molecules react with these pre-adsorbed ionised oxygens the electrons are re-released back to the conduction band of sensing material, which results in decrease of resistance of the sensor. Whereas, for oxidizing gas, the resistance of the n-type MOS increases. When the target gas is removed, the EDL reformed back and the sensor recovers. The adsorption of the target gas molecule is physisorption,

making it a reversible process. The opposite situation happens in case of p-type MOS sensor. The performance of the sensors is measured by detecting the change in conductance.[14–16]

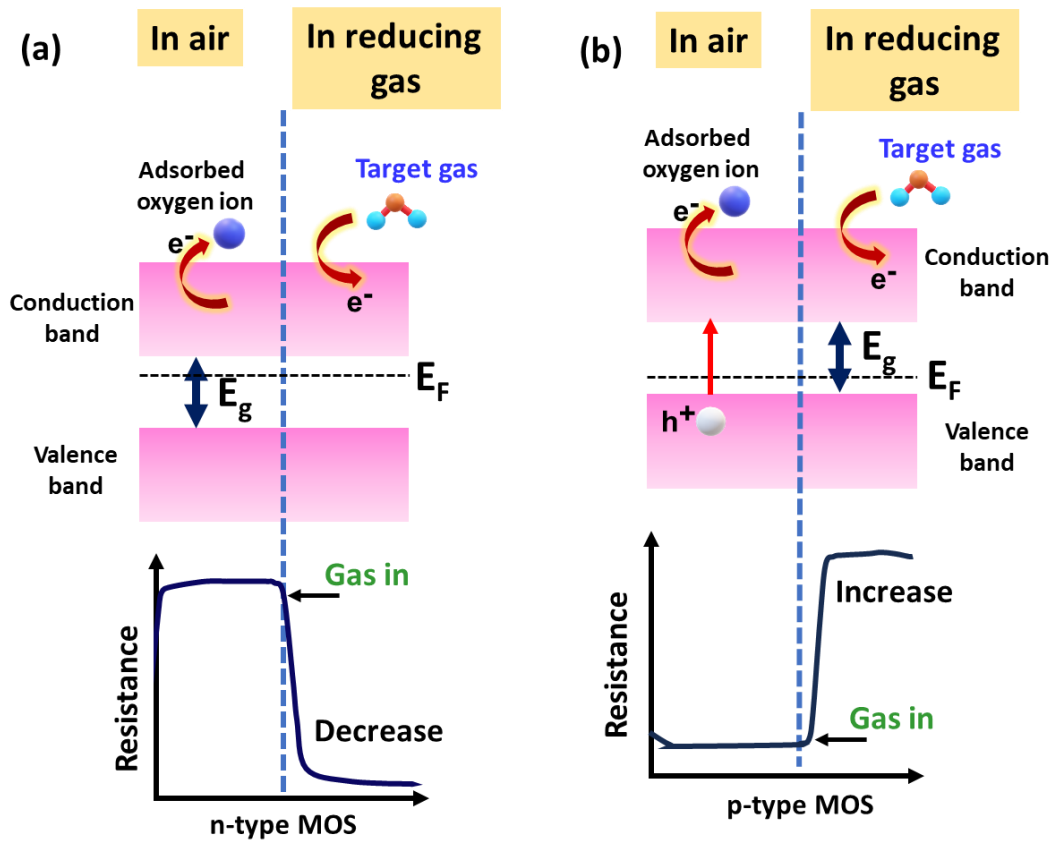


Fig. 1.2. Schematic illustration of change of resistance of (a) n-type MOS, (b) p-type MOS in presence of oxygen (in air) and in presence of reducing target gas.

The important parameters for chemiresistive gas sensing characteristics are explained as follows:

Response (S): The response of a sensor is defined as the change of resistance value (or current value) resulting from exposure to certain concentration of the target gas. Depending on the type of resistance change, the response value of a sensor in terms of change in resistance value can be expressed in two different ways as given below [16,17],

- (a) When the resistance of the sensor increases hugely upon exposure to a target gas, the response is calculated as the ratio of the sensor resistance in presence of target gas (R_{gas}) and sensor resistance in presence of air (R_{air}),

$$\text{Response (S) (times)} = \frac{R_{gas}}{R_{air}} \quad (1)$$

- (b) When the resistance of the sensor decreases upon exposure to target gas the response is defined by,

$$\text{Response (S)}(\%) = \frac{\Delta R}{R_{\text{air}}} \times 100 = \frac{(R_{\text{air}} - R_{\text{gas}})}{R_{\text{air}}} \times 100 \quad (2)$$

Sensitivity: Sensitivity of a sensor is defined by the change in response of a sensor per unit concentration of target gas as given below, $\text{Sensitivity} = \frac{\text{Response}}{\text{Concentration}}$. Therefore, the sensor with high sensitivity is desired for efficient sensing.

Response/recovery time: Response time (R_{res}) of a sensor is defined as the time required for a sensor to reach 90% of its total resistance change when exposed to a particular concentration of a target gas. Recovery time (R_{rec}) of a sensor is defined as the time needed for the sensor to reach 10% of its initial state resistance value (base resistance) after the target gas concentration is removed. A sensor having short response time is considered to be efficient as the rapid detection and recovery to normal state is needed.

Lower limit of detection (LOD): LOD is defined by the lowest concentration of target gas that can be detected by the sensor. A sensor is fabricated to have lowest possible detection limit in mind.

Dynamic response range: Dynamic response range of a sensor is defined by the range of concentration between the lowest and highest detection limit in which the resistance change is highly correlated with the concentration of the target gas. High dynamic response range gives a sensor better efficiency.

Selectivity: Selectivity of a sensor is defined as the sensor's ability to detect a particular target gas with high sensitivity. It is very important for a sensor to be selectively able to detect target gas among various gases. If a sensor can not distinguish between different target gas it is said to have poor selectivity. Therefore, selectivity of a sensor needs to be high.

Reproducibility: Reproducibility of a sensor is defined as the sensor's ability to produce data in the similar range even after change in experimental condition.

Stability: Stability of a sensor is defined as the sensor's ability to produce data in a similar range after repeated and same experimental condition.

1.6. Influencing parameters of MOS based gas sensors

In order to enhance the performance of the MOS sensors certain parameters are pivotal for controlling the response characteristics [16,18,19],

i) Crystallographic phase:

Gas sensing mechanism of MOS is largely influenced by crystallographic phase of the MOS. Particular phase of a MOS can be more energetically favorable for gas adsorption. Different crystallographic phases exhibit different surface energy, that influences the reactivity of the surface to target gas molecules.

ii) Microstructure and morphology:

Surface morphology has significant effect on gas sensing property of MOSs. Nanostructured morphologies such as (1D, 2D structure, hierarchical structure) help in gas diffusion and penetration through the sensor surface leading to enhanced sensitivity. Microstructural parameters and grain size can be tailored by controlling the synthesis conditions.

iii) Surface area and porosity:

Gas sensing is a surface related phenomenon. Therefore, specific surface area of sensor surface influences the sensitivity of MOS. A higher surface area offers larger number of active sites for the target gas molecule adsorption. Nanostructured materials of lower dimension such as nanowires, nanoparticles provide large surface-to-volume ratio resulting in significantly enhanced surface interaction. Porous structure helps the gas molecules to diffuse into the sensing layer more easily. Highly porous (mesoporous, microporous) surface structured MOS sensor provides the channel for the gas molecules to penetrate into depth of the sensing layer, making the sensor more sensitive.

iv) Defect structure:

Defect in the crystal systems (such as vacancies, substitutional defect) play crucial role in gas sensing activity of MOS. Defect states arise within the bandgap of the material due to lattice mismatch, ionic substitution or during synthesis of the material. Oxygen defects can trap electrons, that can act as active sites for the gas molecule adsorption. Therefore, high concentration of defects in the system leads to higher sensitivity of MOS.

v) Doping:

Pristine MOS sensor materials suffer from the disadvantage of low selectivity. To overcome this drawback addition of dopants or impurities result in better sensing mechanism of MOS. Doping changes the band gap, and modifies the structural arrangement to improve sensing properties. Dopants are selected based on the difference in ionic radius, valency between the dopant and host ion. Preferential site doping can alter the electronic band structure that can be beneficial to the sensing characteristics.

vi) Formation of heterostructure:

The electronic property of the MOS can be altered by formation of heterostructure between two MOS. Formation of n-n type, n-p type, p-p type heterostructure configuration hugely enhances sensitivity, selectivity and response time of the sensors. This is because, the heterostructure formation leads to enhanced charge transfer between the constituent MOS that favours the conductivity of the material.

vii) Sensor design and geometry:

The thickness, shape of the sensor film, distance between the electrodes and shape of the sensor surface effects the sensing property of the MOS. By changing the layer thickness the exposed active sensing layer can be altered, that in turn have positive influence on sensing mechanism.

viii) Humidity and temperature:

Relative humidity of sensor environment influences the sensing performance of the gas sensors. In most cases, the surface adsorbed oxygen reacts with the water molecules causes decrease in baseline resistance of the sensor material that can result in decreased sensitivity. The water molecules hinder the chemisorption of the oxygen species, which leads to a smaller number of active sites for target gas adsorption. On the other hand, the reaction kinetics between the target gas molecule and the sensing layer is greatly controlled by the temperature. At lower temperature, the target molecules are less likely to react with the sensor surface due to lack of activation energy. When temperature rises to optimum value, the gas adsorption kinetics becomes dominant because the activation energy is reached. With further increase in temperature the desorption kinetics become faster than the adsorption kinetics, resulting in decrease of response.

Therefore, by tuning of these parameters a better sensor characteristic can be achieved.

1.7. Photoluminescence properties of MOS nanomaterials

According to the International Union of Pure and Applied Chemistry (IUPAC) luminescence is defined as the spontaneous emission of radiation from a species in an electronically or vibrationally excited state. Photoluminescence (PL) in metal oxide semiconductors is the process by which the materials absorb photons and subsequently emit them as light. [20] When a substance absorbs energy in any form, a portion of that energy may be re-emitted in the form of electromagnetic radiation. This process involves two steps: first is the excitation of the electronic system of the substance and the second step is the subsequent emission of a photon. This whole process is known as luminescence and it is named based on the type of excitation involved in the process. This phenomenon offers valuable insights into the electronic and optical properties of semiconductors, offers insight into the pathways of excited-state deactivation and it also provides a straightforward way to gather valuable information about bulk and surface defects in the system which are vital for applications in optoelectronics, sensors, photocatalysis, and various other fields.[21]

1.7.1. Mechanism and parameters of photoluminescence

Excitation mechanism: When a metal oxide semiconductor absorbs photons with energy equal to or greater than its bandgap, electrons are excited from the valence band to the conduction band, generating electron-hole pairs in the process.

Recombination mechanism: After excitation, the electrons and holes recombine and emitting photons in the process. This is called radiative recombination in photoluminescence from which the information about the band structure, defect and impurity states can be obtained.

Impurity levels and defect detection: Metal oxide semiconductors frequently exhibit defect-related photoluminescence (PL). Defects such as oxygen vacancies, interstitials, anti-site defects introduce additional localized energy levels within the bandgap. Due to presence of defects in the system, trap states are created which effects the PL spectrum. Trap states in nanomaterials arise from defects or surface states within the bandgap of MOS nanomaterials. PL is a useful technique for detecting the presence of these trapped states. It reveals insights into the distribution and density of trapped states within the bandgap.

Relationship between bandgap and PL: The intensity and wavelength of the emitted light can be greatly influenced by the nature of band gap (direct or indirect) and the defects (intrinsic or extrinsic) present in the nanomaterials. MOS with a direct band gap is observed to have

stronger PL intensity than a semiconductor with indirect band gap. The indirect band gap semiconductors need phonon interaction for radiative recombination.

Quantum efficiency: Photoluminescence efficiency of a material is determined by photons emitted per photon absorbed (or per populated excited state). By balancing between radiative recombination and non-radiative processes like phonon interactions, defect states, or surface recombination the quantum efficiency can improve. PL efficiency of a semiconductor can be improved using techniques such as surface passivation or controlled doping by minimizing non-radiative pathways.

Temperature dependent photoluminescence:

PL intensity of semiconductors vary depending on the temperature of the material due to the thermal excitation of states, variation in non-radiative recombination rates, change in the efficiency of radiative recombination or variations in rate of non-radiative recombination. The analysis of temperature dependent PL spectra is utilised to obtain information about the activation energy of the semiconductor. By analysing the variation of PL spectra at different temperature, material's electronic structure,

1.7.2. Applications of photoluminescence

Luminescent materials with high colour purity in their emitted light have garnered significant attention across various scientific fields as promising candidates.[22]

- 1) **Optoelectronic devices:** Multi-colour emission achieved by luminescence materials open up plethora of applications in many fields such as white light emitting diode, solid state lighting, and display devices.
- 2) **Fluorescent probe:** Fluorescent materials are generally used as indicator for the generation of excited fluorescence at a predetermined wavelength and are widely used in a variety of detection and labelling fields such as metal ions and pesticide residue detection, bio molecular tracing etc. By measuring changes in fluorescence intensity caused by environmental effects on the fluorescent probe, visual monitoring of the detected substance is done which offers insights into the characteristics or specific information about the environment.
- 3) **Drug delivery activity:** In recent decades, research in medicine utilizing the luminescence opened the door for biomedical application of the nanomaterials in drug delivery, diagnostics, and therapeutic monitoring. Luminescent materials can be tailored

to target specific cells or tissues, such as cancerous cells, ensuring precise drug delivery to the intended site. By monitoring of the luminescence particles several information can be obtained on how the particles interact with the target cells or whether it reached the intended target cells.

- 4) **Bio imaging:** Luminescent materials are essential in bioimaging because of their light-emitting properties, allowing for non-invasive visualization of biological processes at both the cellular and molecular levels. PL active materials provide numerous benefits in bioimaging, such as high sensitivity, real-time tracking, and compatibility with a range of imaging techniques.

1.8. Material synthesis and characterization techniques

Nanomaterials of specific chemical and physical properties are synthesised via to synthetic approaches: Top-Down approach and Bottom-Up approach (the schematic representation of the techniques is shown in [Fig. 1.3](#)). [3]

In top-down approach is a destructive approach in which bulk materials are broken down into nanosized particles via mechanical or physical method. This approach initially starts with bulk material and its size is reduced to desired nanostructures by applying external forces. Top-down approach encompasses techniques such as mechanical milling, lithography, sputtering, electro explosion, arc discharge method, laser ablation. However, these techniques lead to high power consumption and limited size control.

Bottom-up is a constructive approach in which nanomaterials are synthesised at atomic level. Through self-assembly or integration of atomic level particles, the larger and more complex nanostructures are formed. Bottom-up approach encompasses techniques like, vapor Deposition (chemical vapour deposition (CVD), liquid phase deposition, electrodeposition), solvothermal method, sol-gel method, soft and hard templating method.[3,4]

Among the various synthesis techniques, sol-gel, solvothermal and solid-state synthesis routs have been used in this thesis work for their speed, simplicity and cost-effectiveness. The primary goal of these synthesis techniques is to produce MOS nanomaterials with a high surface-area to volume ratio and crystallinity.

Sol gel:

Sol-gel synthesis is a bottom-up approach for synthesising MOS nanomaterials. This method is distinguished for its cost-effectiveness, simplicity, which makes it one of the most used synthesis techniques among other physical and chemical synthesis techniques. Controlling the stoichiometry of precursor solution, modification of compositions, maintaining a molecular level homogeneity and size tailoring of the nanoparticles are easier via sol-gel synthesis method. Sol-gel synthesis required a relatively lower annealing temperature that is advantageous for controlling and maintaining the growth of the nanoparticles. “Sol” is the precursors used (mainly inorganic metal salts such as water-soluble nitrates, chlorides or metal organic compounds such as metal alkoxides) in synthesis. During the mixing of the precursors a colloidal solution is formed in water (mainly used as solvent) and pH of the solution is controlled to avoid precipitation. After reacting with water and going through hydrolysis, the polycondensation of the precursors happens and colloidal dispersion of particles of small size (in nm) is obtained which finally transforms into complex intermediate “gel” of corresponding metal oxide. The unreacted components and solvent are removed by heat treatment and crystalline nanoparticles of desired phase and morphology is achieved by optimizing the calcination temperature and duration.[3,4]

Solvothermal:

To achieve nanocrystals and nanoparticles of uniform size and unique morphology, the solution based colloidal synthesis methods are useful. Highly crystalline nanomorphology such as nanospheres, nanorods, nanotubes are produced. Solvothermal technique via reaction between the metal precursors and directing agents in the solution medium. Surfactants (surface-active agent) or capping agents are used for stabilization, shape or size and porosity control. For controlling the pH level of the solution inorganic or organic minerals are added to the solution. This method highly depends on the concentration of precursor solution, pH level and temperature of synthesis. The synthesis technique needs relatively low temperature ranging from 120 °C to 250 °C which is above the boiling point of the solution medium in a small and closed volume of Teflon-lined environment. The solution evaporates in the closed environment and creates high pressure to yield highly crystalline nanocrystals with required phase. This technique does not require the calcination step and causes minimum loss of materials during synthesis technique.[3,4]

Solid-state route:

Solid-state is a widely known synthesis technique for metal oxides. Nanomaterials with high purity can be achieved via solid state technique by utilizing the chemical reaction between the solid precursors without the requirement of any solvent. Solid precursors such as metal oxides and salts are mixed using grinding or ball-milling technique to achieve homogeneous solid mixture. The powders are subjected to heat treatment (calcination or annealing) at high temperature (500 °C – 1200 °C). During this heat treatment, by controlling the temperature of the calcination, power nanomaterials of high purity, desired morphology and particle size is obtained via solid-state reaction between the precursors.

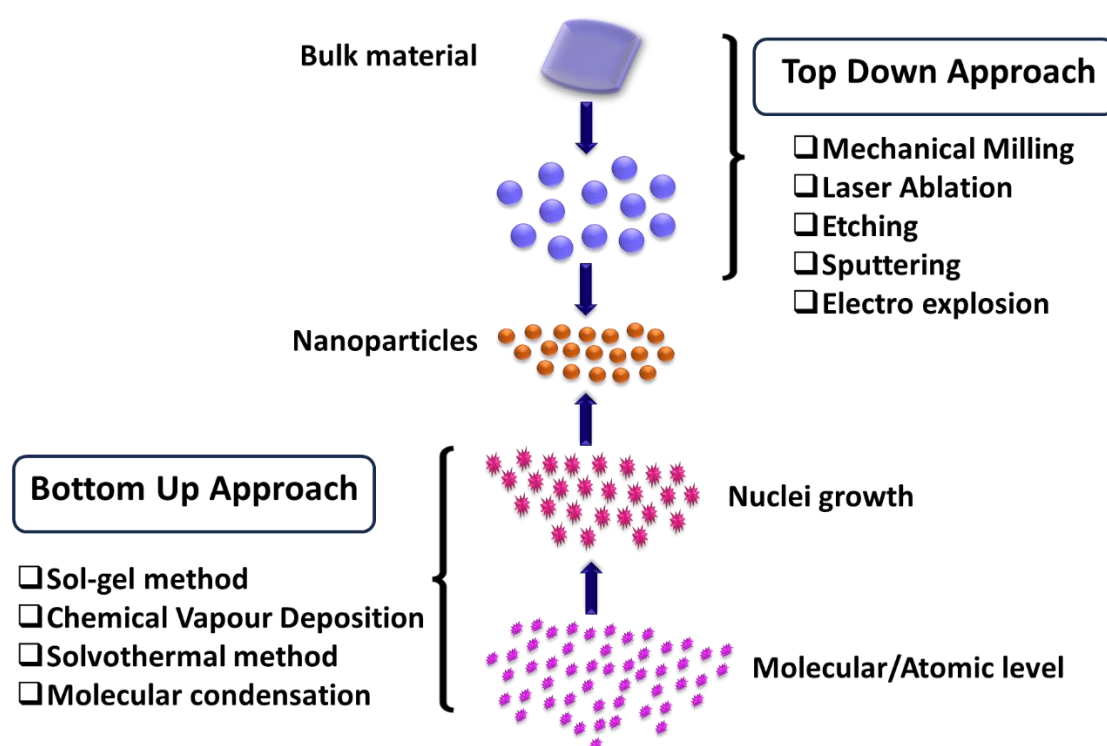


Fig. 1.3. Synthesis of nanomaterials via Top-Down and Bottom-Up approach.

Characterization techniques of nanomaterials

The sensing property is greatly influenced by structural and elemental properties of the sensing materials. The successful chemical synthesis of MOS nanoparticles is evaluated based on the crystal phase, particle size, morphological structure, that ensures the performance of the sensor material. The characterization techniques that are employed to evaluate different properties of the synthesised materials in this thesis work are given as follows,

➤ **X-ray Diffraction (XRD)**

X-ray diffraction (XRD) provides an analytical technique which is non-destructive and it offers detailed information on the crystallinity, crystallographic phase and structure of the nanomaterials. The information that are obtained from XRD give us the idea about the dimension of unit cell, grain size, bond length and bond angle between atoms, orientation of crystal of the synthesized materials. Working principle of XRD is based on constructive interference of X-rays. X-ray generated by cathode ray tube is filtered to produce monochromatic radiation. Then it is collimated to concentrate so that it is directed towards the sample. Crystalline samples are appropriate for the study. Constructive interference is produced due to the interaction between the incident ray and the sample satisfying Bragg's Law. Then the relation between the wavelength (λ) of the incident radiation, the lattice spacing (d), and diffraction angle (θ) is used, given as follows,

$$n\lambda = 2d \sin \theta \quad (3)$$

The samples are scanned by arrangement of 2θ angles. By random orientations of the powdered samples, all possible diffraction directions of the lattice are captured. To identify the composition and phase of the material, comparison of the position and the intensity of the peaks is done with the International Centre for Diffraction Data (ICDD) pattern (which was previously known as Powder Diffraction Standards, JCPDS). Information about the particle size, defect and stain in the nanocrystals are obtained as they are closely related to the widths of the diffraction lines. The broadening of the peak-widths (full width half maxima) indicate the decrease of the size of the nanocrystals which arises as a result of the loss of long-range order compared to the bulk. Crystallite size of the nanoparticles are estimated with Debye-Scherrer formula given as follows,

$$D = \frac{0.9\lambda}{\beta \cos \theta} \quad (4)$$

where D is the crystallite size, λ is the wavelength of the source light, β indicates the full width half at maximum (FWHM) of the peak in radians, and θ indicates the Bragg angle. However, amorphous materials are not suitable for Debye Scherrer formula.

➤ **Field Emission Scanning Electron Microscopy (FESEM)**

Field Emission Scanning Electron Microscopy (FESEM) is a useful instrument used for the examination of material morphology. It utilizes a focused beam of high-energy electrons to

capture microstructural image of the sample surface with micrograph resolution down to ~1 nm depending on the conditions of operation and type of the sample to be analysed. Basic working principle of FESEM is that electron beams are produced by field emission to achieve high resolution with minimum distortion in comparison with conventional SEM imaging technique. Signals are generated containing the information about the surface of the specimen due to the interaction between the incident beam and the atoms of the sample and the secondary and backscattered electrons are utilised for imaging. To avoid the disruption of gas molecules with the electron beams and the backscattered electrons the FESEM is performed in a high vacuum space. Highly focused and coherent beam of electrons with minimal spread is produced by a field emission gun which enables the extremely fine spatial resolution in nanometre scale allowing the imaging of small and intricate features. This beam is operated at very low accelerating voltages (1-5 keV) (to reduce beam-induced damaging of samples and minimise charging effects of samples) passes through electromagnetic lens focusing sharply on the material. Different types of secondary electrons are emitted from the material surface. A detector detects the secondary electrons and by comparing the intensity of the secondary electrons to the scanning primary electron beam the image of the sample surface is constructed. Large depth of field of FESEM micrographs yields a 3D appearance of the sample surface from which we can gain the surface topology, morphology and chemical composition of the materials.

➤ **Energy Dispersive X-Ray (EDX)**

Energy Dispersive X-Ray (EDX) Spectroscopy, an analytical technique, is used for the identification and quantification of elements and their composition in a sample. Energy-Dispersive X-ray is coupled with Scanning Electron Microscopy (SEM) or Transmission Electron Microscopy (TEM) instrument and conducted on the same samples. The electron beams are focused on the sample surface and after striking the specimen surface, the electrons which were previously on the ground energy state, are excited to higher energy state causing ejection from the inner-shell. This creates a vacancy or electron hole. To fill this vacancy, electrons from outer, higher energetic shell drops down and because of the difference in the energy between the higher and lower energy-shell, X-ray is emitted in the process as a characteristic ray. This X-ray is detected by an energy dispersive detector and the energy of the X-ray is measured. Unique set of X-rays with specific energy levels are produced by each element which allows the identification of the elements in the specimen. A spectrum is generated corresponding to specific elements. The elemental composition, relative

concentration and chemical characteristics of the samples are obtained using the height and area under the peaks.

➤ **Transmission Electron Microscopy (TEM)**

Transmission Electron Microscopy (TEM) is an imaging technique with a high spatial resolution which is used for studying the structural and chemical characterisation of materials at the atomic or nanometre scale. This microscopy technique provides surface image of the sample by transmitting electrons through an ultra-thin specimen. The principle of imaging technique of TEM is, a high energy monochromatic electron beam (with energy between 100-300 eV) is generated through an electron gun. The beam is focused onto a small, very thin sample with the help of two condenser lenses. The specimen should be thin enough to allow the electrons to transmit through it. A condenser aperture removes the high-angle electrons before they reach the specimen material. The electron beams pass through the thin sample and interacts with the specimen's atoms. The electrons are elastically and inelastically scattered, absorbed or transmitted through the sample depending on the density and composition of the specimen. The transmitted electrons that carry the information about the internal structure of the material are detected. The process of detection involves series of electromagnetic lenses and the electrons focused by the lenses reach the detection fluorescent screen to form a 2D image of the specimen. The image displays the intricate details of the sample's internal structure, reaching atomic level resolution. The resolution of upgraded TEM instrument can reach down to 0.1 nm, which is smaller than interatomic distance. Additionally, TEM can conduct electron diffraction, which reveals crystallographic information about the material, such as lattice spacing and orientation. The transmitted beam is selected by an objective diaphragm inserted at focal plane at the back and an amplitude contrasted image is obtained. Bragg oriented crystalline parts appear dark and parts without Bragg orientation appear bright which is called bright field mode (BF). These bright and dark field modes are utilised for nanometre scale imaging of specimens. Selected area electron diffraction (SAED) pattern generates an image consisting of a pattern of dots, which is for single crystalline materials and it generates series of rings for polycrystalline/amorphous materials. The information about space group symmetry and crystal orientation is obtained from SAED. Utilising TEM technique, the crystallographic information viz. shape, particle size distribution, crystallinity, interplanar spacing, compositional information, defects, dislocations in crystals and single crystal properties can be obtained.

➤ **X-ray Photoelectron Spectroscopy (XPS):**

X-ray Photoelectron Spectroscopy (XPS) is an analytical technique which is surface sensitive, used for chemical analysis and study of elemental composition, core-shell electronic structure, oxidation states of the elements as well as the surface functionalisation, ligand exchange interaction taking place in the nanomaterials. It is utilised in obtaining qualitative and quantitative information of the specimen surface, thin films and coatings. The working principle is based on photoelectric effect. A beam of X-ray (Al K_{α} or Mg K_{α}), with energy sufficient enough to excite the electrons from the core-level of the atoms, is directed onto the sample surface. After interaction between the X-ray and the atoms, core-level electrons are emitted from the material as a result of the photoelectric effect. A detector is used to measure the kinetic energy of these emitted electrons ejected from the valence shell. Each element exhibits specific peaks in the photoelectron spectra measured in the form of kinetic energy. The binding energy of the ejected photoelectrons and the elemental composition on the surface of the specimen is determined by subtracting the kinetic energy from the energy of the incident X-ray (which is known). XPS is highly sensitive to surface because the electrons are emitted from the top few nanometres of the specimen surface and escape with minimal energy loss.

➤ **Brunauer-Emmett-Teller (BET) surface area analysis**

Nanomaterials with large surface area and exhibit high surface activity with gas molecules due to their exposed active surface. The nanomaterials with high surface area show higher response and optimum operating temperature for gas sensing is also reduced. The Brunauer-Emmett-Teller (BET) surface area analysis is an analytical technique utilised for the measurement of the specific surface area of porous nanomaterials. The surface area is measured by adsorption of gas (typically nitrogen gas is used as adsorbate) molecules on the surface of the nanomaterial. The adsorption can be physisorption or chemisorption. The physisorption causes due to Van der Waals force of attraction between the nanomaterial and the adsorbate gas molecule. Whereas, the chemisorption happens when there is a reaction between solid nanomaterials and the gas molecule (adsorbate). The amount of gas adsorbed at different pressure at the surface of the nanomaterial is correlated to the surface area of the material. BET specific surface area, pore volume and pore diameter are determined by plotting the data applying the BET model by analysis of the adsorption isotherm of the adsorbate gas.

➤ **Fourier transform infrared (FTIR) spectroscopy**

Fourier Transform Infrared (FTIR) Spectroscopy is a vibrational spectroscopy analytical technique utilised for the characterization of structural property such as vibrational frequency of the organic and inorganic molecules by measuring their infrared (IR) light absorbance pattern. In FTIR spectroscopic technique, a continuum source of IR radiation is used in a broad range of wavelength. Using half-silvered mirror, this light is split into two. When the light is passed through the specimen, the IR light of certain frequency is absorbed by the specimen which causes the molecules to vibrate. Each chemical bond is identified by the absorbed infrared radiation of characteristic frequency corresponding to its vibrational energy levels. The Fourier transform of the transmitted light intensity is plotted as a function of wavenumber. By comparing the positions of these peaks with known spectra (available in FTIR database) the functional groups and the bonds and chemical compositions are identified.

➤ **UV-visible spectroscopy**

UV-visible spectroscopy is an analytic technique utilised for studying the optical and electronic properties of the nanomaterials. The working principle of this technique is to measure the absorbance of the of ultraviolet (UV) and visible light of the specimen. When light in ultraviolet (200–400 nm) and visible (400–700 nm) regions passes through the sample specimen it interacts with the specimen and specific wavelengths are absorbed due to the excitation of electrons from ground state to higher energy state. The fundamental electronic property of the specimen (such as energy levels, dipole moment) is obtained from the absorption spectrum of electrons. Optical band gap of the nanomaterial can be obtained from the UV-vis spectra utilizing Tauc-plot method. For direct allowed transition, the Tauc relation is given by following equation,

$$\alpha h\nu = A(h\nu - E_g)^n \quad (5)$$

here, “ α ” represents the absorption coefficient, “ $h\nu$ ” represents photon energy, “ A ” is the proportionality constant, “ E_g ” is the optical band gap energy of the material. “ n ” is the index that depends on the type of electron transition.

➤ **Photoluminescence (PL) spectroscopy**

Photoluminescence (PL) Spectroscopy is a non-destructive optical analysis technique of the materials which gives the information about the electronic structure of nanomaterials. When the materials are excited by photons the emitted light is measured to provide information about

the band gap, energy levels and defect in the materials. This technique is based on the transition of electrons from ground state to higher energy state. It is utilised to gain information about the energy band structure of the materials. The sample is irradiated with a light with energy greater than the band gap of the sample which causes excitation of the electrons from valence band to conduction band, and creates excitons in the process. As the excited electrons come back to the lower energy states to recombine with holes, releasing energy in the form of photons. The energy of the emitted photons corresponds to the energy difference between the electronic states participating in the recombination process. The emitted light which is called photoluminescence is detected to generate a spectrum. The intensity of the emitted light (recorded as a function of wavelength at a fixed excitation wavelength) provides the information about the electronic transition. The PL spectrum consists of several peaks that correspond to energy levels of the emitted photons. From these peaks, information about the band gap energy, defects, impurity levels are gathered.

1.9. Review of literature

Chemiresistive gas sensors based on Metal oxide semiconductor (MOS) have been widely employed because of its numerous interesting characteristics such as cost-effectiveness, fast response, robust nature, easy maintenance, miniature size and stability [23]. The performance of a gas sensors is affected by various characteristics such as sensitivity of the sensor material, selectivity towards a particular gas, the sensor's response/recovery time, reproducibility. A sensor material is chosen keeping on the aforementioned criteria in mind. Gas sensing mechanism is a surface reaction which is related to the surface property of the material. Therefore, by modification of microstructure, electronic and surface properties of the sensing material have great influence on the sensitive property of the MOS based gas sensors. Gas sensors with reliable detection of different gas molecules have been made possible with the help of nanotechnology. Over the last few decades, the extensively explored binary MOS based chemiresistive-type gas sensing materials include nanostructured variants of: a) Transition-metal oxides that include MoO_3 , NiO , WO_3 , Co_3O_4 , TiO_2 , Cu_2O , Fe_2O_3 etc.[24–29], b) non-transition metal oxides including ZnO , In_2O_3 , SnO_2 etc. [10,14,30,31] Because of the small energy difference between a cation with d^n and d^{n+1} or d^{n-1} the transition metal oxides can exist as different form of oxides in nature and they exhibit more sensitivity toward target gas molecules. Binary transition metal oxides with electronic configuration d^0 and d^{10} are found to have sensing activity. Among the non-transition metal oxides, ZnO and SnO_2 exhibit d^{10} electronic configuration and are among the widely investigated binary MOS based gas sensing material. Owing to the advantage of high surface area, ability to preferential growth mechanism of a crystal plane favourable to certain gas molecules, surface chemical composition, defects on the surface and quantum effects MOS based nanomaterials exhibit exceptional gas sensing ability that can be implemented in device application for real time monitoring [32].

1.9.1. Binary MOS-based chemiresistive gas sensors

Pure ZnO: Numerous reports have been found in literature based on ZnO nanostructure-based gas sensors with a variety of morphologies such as nanospheres, nanosheets, nanorods, nanowires[14,15]. Gu et al. has reported single crystalline ZnO nanowires derived by wet-chemical reduction method for the detection of volatile organic compounds [33]. Zhao et al. has demonstrated hydrothermal preparation of one dimensional ZnO nanorods for ethanol detection [34]. Acharyya et al. have reported two step electro-deposition and electrochemical etching derived ZnO nanotubes with hexagonal structure for efficient alcohol sensing [35].

Zhou et al. have demonstrated hydrothermal synthesis process of layered flower-like ZnO nanorods with methane sensing properties [36]. A work by Chen et al. demonstrated Mesoporous ZnO sheets with unique nanoparticle assembly via facile synthesis method for toxic gas NO₂ sensing applications [37]. Patil et al. reported simple successive ion layer adsorption and reaction technique for the synthesis of ZnO thin film nanostructure for efficient NO₂ gas sensing in the concentration range of 100 ppb–200 ppm. Various reports have delineated how the thickness of the ZnO nanostructure being close to Debye length has a great positive influence on the sensitivity and overall performance of the sensor [38–41]. ZnO hierarchical structure has been accomplished by Zhang et al. with 48 times enhanced sensitivity toward acetone compared to bulk ZnO [42]. Spin coating technique grown ZnO nanoparticle thin film has been grown by Patil et al. with NO₂ gas response (R_g/R_a) of 12.3 at 200 °C [43].

Pure SnO₂: SnO₂ is another *n*-type semiconducting metal oxide gas sensing material that have been widely explored for its gas sensing mechanism. Masuda et al. have reported hydrothermally grown SnO₂ microspheres for the detection of formaldehyde (HCHO) at operating temperature 200 °C [8]. SnO₂ hollow microfiber synthesised by Zou et al. via sustainable biomass conversion procedure for TEA sensing at 270 °C [44]. Cheng et al. fabricated hollow nanofibers of SnO₂ via electrospinning method for measurement of ethanol sensing properties at 300 °C [45]. Pan et al. have reported SnO₂ nanowires modified with plasma using the enhanced oxygen vacancies concentration on the surface of the material in favour of gas sensing [46]. Leblanc et al. have reported SnO₂ based sensor with NO and NO₂ sensing property [47]. ZIF-8/SnO₂ nanosheets have been prepared by Choi et al. via aqueous solution process for C₉H₁₈O sensing with 2.15-fold response to 50 ppm at 100 °C employing molecular size-based selectivity [48]. Li et al. reported hierarchical three-dimensional SnO₂ nanostructures for morphology-dependent VOC sensing at 325 °C [49]. Chi et al. have worked on mesoporous SnO₂ by controlling the synthesis procedure using amphiphilic graft copolymer as a sacrificial agent and explained the porosity dependent H₂ gas sensing at 300 °C 10s/54s response/ recovery time with a response of 13 toward 3% H₂ concentration [50]. Coral-like structure of SnO₂ nanostructure synthesised via hydrothermal method has been prepared by Yan et al. for ethanol sensing at 240 °C operating temperature with response about 25 toward 100 ppm concentration and 17s and 7s, response and recovery time [51]. Aligned epitaxial SnO₂ grown on sapphire with nanowire morphology has been reported by Wang et al. for NO₂ detection [52].

Pure In₂O₃: Yang et al. have successfully synthesised In₂O₃ microtubes with one-dimensional configuration prepared via chemical conversion method for TEA detection utilizing density gradient strategy with response value of 72.5 at 300 °C operating temperature with 12s/650s response/recovery time [53]. Zheng et al. reported isoprene sensing of In₂O₃ nanoparticles at 350 °C working temperature with a response of response time in the range 2–5 s and recovery time in the range 35–200 s [54]. A report by Shboul et al. has reported ppb level H₂S detection of In₂O₃ based sensor with anti-humid property with response time of 60 s and response value 55 to 200 ppb H₂S [55]. Cao et al. have studied crystal phase effect on acetone sensing activity of In₂O₃ flower-like nanofibers at 180 °C with response/recovery time of 1s/126s to 50 ppm acetone [56]. Another work by Han et al. have demonstrated NO₂ sensing behaviour of In₂O₃ nano-bricks working at 50 °C with a response of 402 toward 500 ppb concentration of NO₂ and response/recovery time 114 s/49 s [57]. Ou et al. have reported In₂O₃ modified by oxygen vacancies for low temperature detection of formaldehyde in room environment with a response value of 150 and response time of 433 s [58].

Pure MoO₃: Sui et al. have successfully fabricated with hierarchical three-dimensional flower-like α -MoO₃ structure for triethylamine (TEA) detection at 250 °C [59]. α -MoO₃ was synthesised via pulsed laser deposition by Bisht et al. for the purpose of NO₂ sensing at operating temperature of 100 °C and relationship between defect concentration and sensing property has been explained [60]. Hydrothermally synthesised α -MoO₃ nanobelts were reported by Mo et al. for ethanol sensing at 300 °C with response 174 to 800 ppm ethanol and response/recovery time of 33 s/9 s [61]. 2D hexagonal MoO₃ was synthesised by Sakhuja et al. for liquid exfoliation technique assisted by ultrasonication technique for NH₃ sensing with response of 42% to 5 ppm gas concentration at room temperature with response time 1–5 min [62]. Mo atom exposed MoO₃ microporous nanoflowers were reported by Li et al. for H₂S sensing ability 7.2 times higher than the MoO₃ nanosheets [63]. MoO₃ nanorods for the TEA sensing was reported by He et al. with 4 s and 2 min response and recovery time [64].

Pure NiO: Yu et al. reported net-like NiO architectures grown via hydrothermal synthesis technique which exhibited response value of 45% to 200 ppm ethanol at 300 °C working temperature [65]. Zhang et have reported nanoneedle-assembled hierarchical nanoflowers structure of NiO for ethanol sensing with response value 55 at 300 °C operating temperature and response/recovery time 1.7s/2.2s [66]. A work by Miao et al. demonstrated ethanol sensing activity of NiO flake-flower architectures synthesised via hydrothermal rout which exhibited response value 23.7 toward 400 ppm ethanol with response/recovery time of 10s/5s while

operating at 300 °C [67]. Yang et al. have demonstrated benzaldehyde sensing activity of engineered NiO nanostructure with response value of 160% to 100 ppm at working temperature 300 °C with response/recovery time 31.0s/30.9s [68]. Du et al. have reported H₂S sensing activity of NiO nanoparticles with sensitivity of 8.5 working at 150 °C temperature [69]. Zhang et al. have reported their work on nanosheet layers of NiO synthesised via hydrothermal technique for room temperature sensing activity toward NO₂ with 10s response time and explained the effect of grain boundaries on the gas sensing characteristics of NiO [70].

Pure WO₃: WO₃ with hollow microsphere structure grown via hydrothermal route mediated by glucose has been reported by Majhi et al. for detection of NO₂ in 0.5-2.5 ppm concentration range [25]. WO₃ has gained recognition as an efficient ammonia gas sensor at an ultra-low concentration with ~350% response to 60 ppm NH₃ activated by surface modification with MWCNT [71]. Monreal et al. reported their work on WO₃ based NO₂ sensor synthesised via direct laser interfering patterning with the sensing ability of low ppm concentration [72].

Pure Co₃O₄: Vetter et al. have reported CO gas sensing capability of nanostructured Co₃O₄ at low ppm concentration at 200 °C [29]. Yoon et al. developed p-type Co₃O₄ nanofibers via ultrasonication assisted method to demonstrate sensing activity toward C₂H₅OH at 310 °C [73]. Wen et al. have fabricated Rhombic Co₃O₄ nanorod using thermal conversion method for detection of ethanol at 160 °C [74]. Shen et al. have reported formation mechanism of urchin-like Co₃O₄ and utilized product morphology for the enhancement of volatile organic sensing property [75]. A work by Sun et al. have reported monodisperse structure of Co₃O₄ nanocubes synthesised by microwave assisted route to demonstrated responses to xylene and ethanol gas [76]. Choi et al. have reported Co₃O₄ nanostructures prepared via solvothermal reaction method and fabricated C₂H₅OH sensor at 300 °C utilizing the less agglomerated structure of the material [77]. Deng et al. reported mesoporous Co₃O₄ nanosheets structure for p-type VOC sensor synthesised via chemical co-precipitation method for VOC sensing [78].

Pure TiO₂: Chen et al. have reported nanoporous TiO₂ prepared via hydrothermal technique for acetone sensing with response of 25.97 for 500 ppm acetone and response/recovery time of 13s/8 s [79]. Pozos et al. have reported their work on spray pyrolysis derived TiO₂ thin films for CO detection with response value of 300 to 300 ppm CO at 350 °C [80]. Navale et al. have reported hydrothermally grown TiO₂ nanoparticles operating at 270 °C temperature with response/recovery time of 10s/9s and response value of 15.24 to 1000 ppm acetone [81]. Li et al. have reported room temperature sensing activity of mesoporous TiO₂ hollow microspheres

with response of 40 to 5 ppm formaldehyde with 40s/50s response/recovery time [82]. Tshabalala et al. reported TiO₂ nanorods room temperature sensing activity toward CH₄ with 45s/33s response/recovery time [83]. Zhao et al. have reported in situ growth technique derived TiO₂ nanorod arrays for room temperature detection of NH₃ with response value of 23% to 20 ppm NH₃ [84]. Zhou et al. have reported rutile phase TiO₂ with H₂ sensing performance of 2s/40s response/recovery time [85]. Zhu et al. have reported TiO₂ nanowires for NO₂ gas detection with fast response/recovery times 10s/19s to 100 ppm NO₂ at room temperature [86]. Ge et al. have reported their work on TiO₂ nanosheets of hierarchical structure for acetone detection at 400 °C temperature with response value of 134.40 and 14s/20s response/recovery times [87]. Zhang et al. have reported TiO₂ based hydrogen sensors implementing surface defect enhanced sensing mechanism with response value of 75% to 500 ppm H₂ and response/recovery time of 3s/10s [88].

Pure Fe₂O₃: Wu et al. have reported α -Fe₂O₃ nano-ellipsoids-based H₂S sensor synthesised via hydrothermal technique with response value of 80 to 5 ppm H₂S with response/recovery time of 0.8s/2.2s while operating at 260 °C [89]. Chuong et al. demonstrated synthesis of α -Fe₂O₃ nanoparticles via hydrothermal technique for CO sensing with response value 22.5 for 100 ppm concentration at 300 °C [90]. Zheng et al. reported hollow α -Fe₂O₃ microspheroids prepared via hydrothermal synthesis technique for acetone detection with response of 68.5 to 100 ppm acetone and response/recovery time 8s/5s at 260 °C operating temperature [91]. Wang et al. have reported porous α -Fe₂O₃ nanorods for ethanol sensing activity with response ~130 for 500 ppm ethanol concentration [92]. Huang et al. reported α -Fe₂O₃ nanoparticles with porous structure for room temperature detection of H₂S gas with response 38.4 to 100 ppm concentration [93].

Pure Cu₂O/CuO: Zhang et al. have reported Cu₂O and CuO nanospheres prepared via kinetically controlled synthesis technique for alcohol sensing at 210 °C operating temperature with 30s response time [94]. Umar et al. demonstrated ethanol sensing property of CuO nanoplates which exhibited 176% response towards 100 ppm ethanol concentration at 250 °C operating temperature [95]. Wang et al. have reported sol-gel derived CuO nanoparticles with ethanol, methanol and acetone sensing activity [96]. Wan et al. have reported morphology and particle size dependant alcohol gas sensing activity of Cu₂O nanospheres with response 3.8 toward 800 ppm gas concentration operating at 200 °C temperature [97].

1.9.2. Different doping on MOS-based chemiresistive gas sensors

Adding suitable dopants to the host matrix has proven to be an efficient way to achieve improved gas sensing property. Noble metals such as Ag and Au, transition metals such as Cu, Ni, Co have been used to enhance the sensing capabilities of ZnO, as reported in the literature. Incorporation of noble metal in ZnO have given rise to electric effect in favour of the contact resistance [98]. Ag was used as a dopant by Hamid et al. to enhance the by facile sol–gel Pechini route for enhanced ethanol sensing of 32.5 (R_a/R_g) to 50 ppm concentration of ethanol at 325 °C operating temperature [99]. Au doped plasmonic ZnO has been explored for its multifunctional property at RT as UV photo generator and NO sensing activity by Gorurla et al. [98]. Wang et al. have demonstrated the effect of Ag content and calcination temperature on the H₂S sensing ability of Fe₂O₃ [100]. By controlling the amount of Ni with ZnO nanorods the kinetic process of H₂S adsorption and desorption has been improved at 200 °C as reported by Modaberi et al. [101]. Zou et al. reported hydrothermally grown ZnO nanorods decorated with dopant Co to enhance the NO₂ sensing performance at 210 °C [102]. Vuong et al. developed ZnO hierarchical nanostructures decorated with CuO synthesised by wet chemical method to enhance H₂S sensing activity at 200 °C working temperature [103]. Varudkar et al. have fabricated NH₃ sensor based on Al doped ZnO nanoparticles via a facile co-precipitation technique [104]. Zhou et al. have explained improved ethanol sensing mechanism of Cr-doped ZnO nanorods due to adsorption of larger number of oxygen molecules on (001) surface enabled through doping [105]. Sub ppm CO gas sensing has been reported by Choi et al. by networked ZnO nanowires functionalised by Pd which showed room temperature sensing activity due to synergetic effect of chemical and electronic sensitization [106]. Gunter et al. reported Si-doped α -MoO₃ synthesised via flames followed by direct deposition and annealing method for the detection of NH₃ at 450 °C operating temperature [107]. CO sensing at 240 °C temperature has been demonstrated by Bhardwaj et al. with Cu doped SnO₂ nanostructures synthesised via wet chemical method [108]. Xu et al. have successfully fabricated SnO₂ thin films decorated with Pt single atoms for detection of triethylamine (TEA) detection at 200 °C utilizing Pt as a catalyst for the spillover activation of oxygen and oxygen vacancies on the surface [109]. Song et al. have reported porous α -Fe₂O₃ nanorods decorated with gold decahedrons prepared via one-pot polyol reaction method to sense trimethylamine (TMA) at 40 °C [110]. Suematsu et al. have fabricated SnO₂ nanoparticles by controlled particle aggregation method for toluene sensing at 300 °C utilizing catalytic and electrical sensitization effects generated through Pd doping [111]. Kwak et al. reported Tb doped SnO₂ yolk–shell

spheres for reliable acetone gas detection [6]. MoO₃ nanobelts modified by Au nanoparticles prepared by hydrothermal method have been reported by Fu et al. for 1-butylamine sensing activity at 240 °C operating temperature with response of 300 toward 100 ppm gas concentration with response time 8–31 s and recovery times of 11–749 s [112]. Cr was doped in α -MoO₃ nanorods by Li et al. for the detection of triethylamine with a response of 150.25 to 100 ppm TEA and response/recovery time of 7 s and 80 s [62]. Bai et al. have reported co-doping of In₂O nanocomposite with Ag and Tb for ppb level H₂ sensor at 160 °C which exhibited 4 times enhancement in sensing activity after doping [113]. Kim et al. have reported Sn-Doped NiO microspheres with multiroom structure for xylene detection with response ~60 toward 1 ppm xylene and 179 s response time while operating at 300 °C [114].

1.9.3. Heterostructure based chemiresistive gas sensors:

Heterostructure and composites formation has been proven to be efficient approach for the improvement of binary metal oxides based chemiresistive gas sensors [115]. MOS based heterostructures can be helpful in modulating carrier transport mechanism at the interface of two semiconductors which leads to change in resistance utilizing the difference in their working functions [116]. Katoch et al. fabricated SnO₂-ZnO composite nanofibers via electrospinning technique to achieve H₂ gas sensing at 300 °C operating temperature utilizing the metallization effect between the nanograins of SnO₂ and ZnO [117]. Ju et al. reported wet chemical method derived ZnO-rGO-Au core-shell nanohybrids for trimethylamine (TMA) sensing at 40 °C utilizing Schottky contact between Au-SnO₂ and n-n heterojunction between ZnO/SnO₂ fabricated via pulsed laser deposition (PLD) and DC-sputtering method [118]. p-CuO/n-ZnO hollow nanofibers were designed by Han et al via combination of electrospinning and atomic layer deposition method to detect H₂S at 250 °C [119]. ZnO/polyaniline nanocomposite has been fabricated by Li et al. utilizing morphology effect and p/n junction effect for NH₃ sensing at RT [120]. 3D ZnO/In₂O₃ n-n heterostructures fabricated by Zhang et al. thermal conversion method for sensitive ethanol detection at 240 °C [71]. Kim et al. reported protein templated RuO₂ functionalised WO₃ nanofibers prepared by electrospinning method to detect acetone in human exhaled breath for diagnosis of diabetes at 350 °C [7]. Hu et al reported flower-like MoO₃@WO₃ composite microstructure grown via hydrothermal and impregnation method for H₂S sensing at temperature 250 °C with 2s/5s response recovery time [121]. Gao et al. demonstrated H₂S sensing performance of MoO₃/Fe₂(MoO₄)₃ yolk/shell nanostructure at 320 °C synthesised via facile hydrothermal method [122]. Yual et al. demonstrated the synthesis and preparation of WO₃@SnO₂ core shell nanosheets heterostructure with tunable

shell thickness of SnO₂ for NH₃ sensing at 200 °C [123]. Bi et al. have reported NiO-In₂O₃ heterojunction nanospheres grown via hydrothermal technique for the detection of toxic NO₂ gas [124]. Mesoporous WO₃-SnO₂ nanocomposite prepared via nanocasting technique for the detection of amine at 200 °C temperature has been reported by Tomer et al. [11]. Ju et al. have fabricated p-n heterojunction of NiO/SnO₂ hollow sphere which was synthesised via template assisted hydrothermal method for the detection of TEA at 220 °C [12]. Xu et al. have reported to form n-n type heterojunction interface of SnO₂/TiO₂ nanosheet structure for TEA detection at 320 °C operating temperature [125]. Gup et al. have reported electrospinning followed by calcination method-prepared Al₂O₃/α-Fe₂O₃ composite nanofibers which exhibited TEA sensing at 250 °C [126]. Shi et al. have explored a metal organic framework (MOF) derived method of synthesis of Co₃O₄/In₂O₃ hollow microtubes TEA at 250 °C temperature utilizing effects of electronic, chemical and structural property [13]. Liu et al. have proposed designing method of α-Fe₂O₃/α-MoO₃ Nanostructure utilizing seed-layer-assisted growth technology followed by hydrothermal method to demonstrate TEA sensing activity [126]. Arafat et al. have reported the construction of core-shell TiO₂-Al₂O₃ nanostructures fabricated by thermal oxidation method for H₂S, CH₃OH and C₂H₅OH sensing [127]. Ling et al. reported SnO₂/WO₃ heterojunction for the measurement of its NO₂ sensitivity [128]. NiO@SnO₂ Hierarchical Nanostructures have been grown via in situ growth assisted chemical deposition technique on ceramic microchips for detection of H₂S with 23-fold and 17-fold increment in response compared to NiO and SnO₂, respectively [129]. Yuan et al. have successfully grown CeO₂ Nanodot-Decorated WO₃ nanowires heterostructure for ppm level acetone gas sensing with response of 1.31 toward 0.5 ppm and response/ recovery time of 34s/ 68s implementing abundant oxygen vacancies on the surface of sensing material [130]. Hu et al. have demonstrated fabrication of In₂O₃ hollow spheres with CeO₂-loading for hydrogen detection at 160 °C with response enhancement of 3 times compared to pristine In₂O₃ with response/recovery time of 1s/9s [131]. Mei et al. have reported their work on hierarchical heterostructure of α-Fe₂O₃/TiO₂ exhibiting response value of 40.4 toward 500 ppm ethanol and response/recovery time of 37s/46s [132].

1.9.4. Ferrite based chemiresistive gas sensors

Only few of the ferrite materials have been explored for their gas sensing ability in the past. Some of the reports in ferrite-based chemiresistive gas sensors include spinel ferrites with structure MFe₂O₄ (M=Zn, Ni Co, Cu, Mg) which showed reliable gas sensing activity to various target gas molecules [133]. Ethanol, acetone, HCHO, H₂S sensing property has been

observed in ZnFe_2O_4 structure [18,19,134,135]. NiFe_2O_4 nanostructure was reported to exhibit VOC sensing property with high response value and demonstrated how the gas adsorption property can be affected by the microstructure of the sensing material [136]. A report by Zhang et al. delineated porous NiFe_2O_4 nanorods with high surface area exhibited toluene sensing activity at 200 °C operating temperature with 59.64-fold response and lower detection limit of 1 ppm [137]. Several reports have been found on enhanced acetone sensing characteristics of NiFe_2O_4 nanostructure with different morphologies down to ppm level concentration [137,138]. Solvothermal technique-grown CoFe_2O_4 with porous nanospheres morphology, which showed acetone sensing property with 3s/185s of response/recovery time as reported by Yang et al. [139]. Porous hierarchical CuFe_2O_4 was found to exhibit LPG sensing activity at room temperature [140]. Several reports were found LPG sensing activity of MgFe_2O_4 nanoparticles, prepared via wet-chemical method [141,142].

Multiferroic materials, which exhibit both ferroelectric and ferromagnetic properties, have garnered significant attention due to their broad range of applications in information storage, photovoltaics, and sensors. Perovskite ferrites have emerged as a field of novel opportunities for the flourishing of gas sensing technology. Owing to their excellent chemical stability, tunable bandgap, the perovskite ferrites such as MFeO_3 ($\text{M}=\text{Bi, La}$) are gaining acknowledgement as reliable gas sensing material. Noteworthy characteristics include Perovskite structure with general formula ABO_3 exhibit high adsorption coefficient and improved charge transport capability which is beneficial for higher gas sensing response [143]. Consequently, perovskite ferrites demonstrate excellent electronic and ionic conductivity, as well as increased stability at comparatively lower operating temperatures and rapid response/recovery kinetics. There are some works on gas sensing ability of LaFeO_3 . 50 ppb detection limit has been achieved with honeycomblake LaFeO_3 film for ethanol sensing. [144] Ag doped LaFeO_3 has been reported for formalin and methanol sensing with high response.[145,146]

Bismuth ferrite (BiFeO_3), with a rhombohedral crystal structure, is a multiferroic lead-free material, which exhibit long-range antiferromagnetism (with $T_N = 643 \text{ K}$) and strong ferroelectricity (with $T_C = 1103 \text{ K}$). It is widely known as the only single-phase perovskite which exhibits room temperature multiferroicity. Due to the migration of electron pairs along the [111] direction of the $[\text{FeO}_6]$ octahedron, BiFeO_3 (BFO) exhibits spontaneous polarization and distinct electronic properties, making it valuable for use in sensor and electronic devices. Although BiFeO_3 is well-known for its multiferroic properties, its ability to sense low ppm

concentrations of volatile organic compounds, as well as a detailed understanding of the sensing mechanism on its surface, remains underexplored. [147–149]

Barium hexaferrite ($\text{BaFe}_{12}\text{O}_{19}$) with hexagonal crystal structure is a well-known magnetic material with high performance permanent magnetism. Due to its high Curie temperature and large magneto-crystalline anisotropy, $\text{BaFe}_{12}\text{O}_{19}$ exhibits large magnetisation along with excellent chemical stability.[150] Even though $\text{BaFe}_{12}\text{O}_{19}$ has been studied in the past for applications related to its magnetic property such as magnetic disk and video recording, microwave devices, but there are no such reports on exploration of its gas sensing property.

There are only few reports on the multiferroic and magnetic ferrite materials for their gas sensing activity. Therefore, the unexplored ferrite materials are chosen for the exploration of MOS based novel gas sensing materials.

1.9.5. Scheelite nanomaterials for solid state lighting

Light sources of new generation has expanded its area of application toward efficient solid-state lighting, 3D display systems, backlights, fluorescent sensors etc. [151] Scheelite type lanthanide double molybdates with general formula $\text{ALn}(\text{MoO}_4)_2$ (A = alkali metal ions, Ln = rare earth ions) with C_{4h} symmetry and space group $I4_1/a$ have gained significant research interest due to their chemical stability, long life and emission in long wavelength range. Diverse application fields of these Scheelite-type molybdates include solid state lighting, display devices, fluorescent probes, thermographic phosphors, photocatalytic activity, gas sensor, anode for lithium-ion batteries and nano-electronic devices.[152] Owing to the scheelite type structure's ability to accommodate different types of rare earth (RE) activator ions for achieving efficient photoluminescence property, this class of materials has been widely studied and applied in various areas such as white light emitting diodes, fingerprint detection, bio imaging, environmental lighting and medical treatment.[153]

In the past years, rare earth doped sodium double molybdates $\text{NaLn}(\text{MoO}_4)_2$ have gained recognition as exceptional luminescent material owing to their favourable optical properties. The key characteristics of the scheelite structure is its tetrahedral coordination and inherent symmetry which furnishes a stable host lattice for doping with lanthanide ions. Charge transfer from oxygen metal to molybdate phosphors leads to broad adsorption band in the rear-UV region [154]. Various reports can be found in literature where the luminescence properties have been studied for the scheelite type tetragonal double molybdate structures by varying synthesis technique, surfactant, morphology and dopant. Interesting optical properties have

been observed due to compositional variability, rare earth doping of $\text{NaLn}(\text{MoO}_4)_2$ based nanophosphors. Tb^{3+} doped double molybdate structure $\text{NaLa}_{1-x}\text{Tb}_x(\text{MoO}_4)_2$ has been studied by Wang et al. for its photoluminescence property.[155] Eu^{3+} activated $\text{NaTb}(\text{MoO}_4)_2$ microcrystals have been synthesized by Zhou et al. and various morphologies have been achieved by controlling the crystal growth environment. Efficient electron transfer mechanism indicated that the phosphors are potential candidate for multicolour lighting. [156] Morozov et al. have studied the effect of various synthesis routs on the structural formation and photoluminescence property of $\text{KTb}(\text{MoO}_4)_2$ and explained the effect of K^+ ion conductivity on its green phosphor property. [151] Another study by Morozov et al. have explained the influence of A-cations ordering on luminescence property of different polymorphs of $\text{KEu}(\text{MoO}_4)_2$ and the relationship between its structure and optical property has been delineated.[157] Hua et al. have demonstrated citric acid assisted preparation of trivalent samarium (Sm^{3+}) and terbium (Tb^{3+}) ion co-doped $\text{NaLa}(\text{MoO}_4)_2$ phosphors which emitted warm light and the emission colour could be tuned by changing the dopant concentration.[158] Moura et al. have studied the phonon properties of $\text{NaCe}(\text{MoO}_4)_2$ structure and the temperature depended Raman spectroscopy study revealed the mechanism of phase change upon change in temperature.[159] A study by Xu et al. demonstrated synthesis and $\text{NaEu}(\text{MoO}_4)_2$ with unique micro-rugby like morphology with photoluminescence property which exhibited great potential to be applied in light emitting diode.[160] Li et al. have demonstrated the controlled synthesis mechanism and the effect of rare earth ion radius on formation of $\text{NaLn}(\text{MoO}_4)_2$ micro-crystals. The down-conversion photoluminescence property of $\text{NaLn}(\text{MoO}_4)_2$ has been delineated.[161] Perera et al. have reported synthesis mechanism of different rare earth ion doped $\text{NaRE}(\text{MoO}_4)_2$ for its photoluminescence property depending on its compositional complexity.[162] Another study has shown the property of $\text{KLn}(\text{MoO}_4)_2$ phosphor for optical thermometry.[163] Jiang et al. demonstrated the effect on photoluminescence property of $\text{NaY}(\text{MoO}_4)_2$ due to Mn^{4+} doping. [164]

There are only few works in the literature to study the detailed structural property of $\text{NaTb}(\text{MoO}_4)_2$ and the effect of the structural disorder on its optical property. Moreover, there is hardly any report on its multifunctional application. Therefore, $\text{NaTb}(\text{MoO}_4)_2$ has been chosen for photoluminescence application along with the support of density functional theory calculation, the band structure formation of the nanomaterial is demonstrated in this thesis.

1.10. Objective of the work

As the literature review indicates, binary metal oxide semiconductors-based sensors face various drawbacks like selectivity issue, as they often detect all similar types of interfering gases. Binary metal oxides-based sensors generally suffer from lack of selectivity because of their reaction mechanism. A selective sensor should be capable of distinguishing a specific gas within a mixture and should respond exclusively to that particular gas for the sensor's practical use. Major bottleneck of binary metal oxide semiconductors-based sensors is slow response and long recovery time which makes it hard for these sensors to have real time monitoring capability. Another challenge these sensors encounter is their inability to detect target gases at ppb-level concentrations. As a result, in recent times, new materials as alternatives of basic binary metal oxides are needed to expand the area of gas sensing materials. The current literature lacks the extensive study on non-invasive disease detection by means of exhaled breath analysis. Sensors solely focused on detection of biomarker gases in exhaled breath can open up new direction in health monitoring and pre-diagnosis of disease.

From literature review, it is evident that ferrite-based sensors are among the most unexplored areas in the field of sensing applications. No report has been found to demonstrate hexaferrite structure for gas sensing ability. Therefore, for expanding the regime of ferrite-based gas sensors $\text{BaFe}_{12}\text{O}_{19}$, which is a widely known magnetic material which exhibits magnetism in room temperature, could be novel ferrite based stable sensing material. The microstructure, surface defect of the $\text{BaFe}_{12}\text{O}_{19}$ can be tuned in favour of larger gas adsorption rate. Another ferrite material, BiFeO_3 with perovskite structure is well known for its multiferroic activity and has diverse application in data storage media, and its visible light absorption ability has proven its efficiency in photovoltaic and catalytic application areas. Even though they are proved to have great surface activity, yet these materials are unexplored in the field of gas sensing. Therefore, this study has taken these unconventional MOSs sensors as area of study. For the study of optical properties, there are adequate number of reports in literature on the study of photoluminescence property of MOS, but few have paid attention to in depth study of structural property and electronic band structure. There is still lack in the in-depth study of relationship between the electronic property and the photoluminescence activity with the support of theoretical study. This thesis aims to achieve a clear understanding between the crystal structure of the nanomaterial with the photoluminescence property with experimental study supported by theoretical (DFT) calculations.

The major objective of this work is to conduct an in-depth investigation into the metal oxide semiconductor nanomaterials-based gas sensors and also, study of optical properties of semiconductor metal oxide nanomaterials. The goal of the thesis is to understand the underlying mechanisms and the relationship between the structural and elemental properties of MOS nanomaterials and gas sensing behaviour. In line with this focus, the specific objectives of this work are:

- To explore novel materials such as hexaferrite, perovskite ferrite nanomaterials for their gas sensing ability.
- To explore effect of doping, surface electronic states of ferrites nanomaterials to enhance the response value towards gases.
- To enhance the adsorption ability, selectivity and response time of the sensor materials.
- To fabricate prototype sensors suitable for exhaled breath analysis.
- To enhance charge transfer mechanism of sensor materials and gas detection ability of the sensors by forming heterostructures with other oxides.
- To improvise the sensor for real-time application in environmental monitoring.
- To investigate optical property of semiconductor metal oxide nanomaterials.
- To develop advanced nanomaterials that can efficiently integrate multiple functions and adapt to different field of applications viz. gas sensing and photoluminescence.
- The understanding of role of surface electronic states, defects, structural disorder in the system that affects the gas/material reaction as well as photoluminescence property.
- To establish a more generalised method of achieving desired properties by modulation of key parameters of material.

1.11. Thesis outline

This thesis comprises of seven distinct chapters demonstrating the background of research, the research findings and the overall conclusion of this thesis.

Chapter 1 is the introductory chapter containing the background and motivation of the thesis work. Metal oxide semiconductor nanomaterials-based gas sensors are holding significant role in modern world due to their utility in environmental protection, pollution detection, healthcare and workplace safety by detection of toxic gases/VOCs in ambient. Among the various gas sensing techniques available, MOS based chemiresistive gas sensors offer cost-effective, stable and easy to operate detection systems. In this chapter, the mechanism and parameters of chemoreceptive gas sensing technique is described. This chapter contains state of the art of existing MOS based gas sensors and their drawbacks. The literature review highlights the importance of choosing the appropriate material with active sensing layer, as it greatly impacts the sensitivity and selectivity of gas or VOC detection. For optical study, the mechanism of photoluminescence and extensive literature study on photoluminescent materials have been conducted. Synthesis and characterisation techniques used for the prepared materials have been described. Lastly, in this chapter, the objective of the thesis has been delineated and a brief description of thesis outline is given.

In **Chapter 2**, fabrication of a highly sensitive, selective and stable ammonia sensor has been delineated based on novel sensing material, barium hexaferrite ($\text{BaFe}_{12}\text{O}_{19}$), for the detection of trace ammonia vapor, the breath biomarker for renal diseases. Barium hexaferrite ($\text{BaFe}_{12}\text{O}_{19}$) nanoparticles has been synthesized through a simple solid-state reaction method. The prepared nanopowder and sensor film has been systematically characterized using techniques such as X-ray diffraction (XRD), field effect scanning electron microscopy (FESEM), transmission electron microscopy (TEM), energy dispersive X-ray spectra (EDX), X-ray photoelectron spectroscopy (XPS), Brunauer-Emmett-Teller (BET), and I-V measurements. The fabricated sensor exhibited p-type sensing behaviour and demonstrated the ability to detect ammonia at concentrations as low as 0.2 ppm with sensitivity of ~1.46 folds. Further, the sensor has shown remarkable response of ~2.34 folds towards 1 ppm ammonia. The sensor was unresponsive to similar concentrations of other major interfering breath volatiles, such as acetone, ethanol, and saturated moisture. Also, the sensor exhibited fast response (~2.88s) and recovery (~39.4s) times ensuring real time breath analysis. Finally, long

term stability of the sensor for more than three months rendered it suitable for commercial applications.

In **Chapter 3**, the effect of doping on ammonia sensing property of barium hexaferrite ($\text{BaFe}_{12}\text{O}_{19}$) has been delineated. Barium hexaferrite ($\text{BaFe}_{12}\text{O}_{19}$) is an unexplored metal-oxide semiconductor with regard to ammonia (NH_3) gas sensing. Herein, we have achieved substantial enhancement in response towards NH_3 by virtue of Zn doping in $\text{BaFe}_{12}\text{O}_{19}$, synthesized via facile solid-state route. The improved p-type response ($R_{\text{gas}}/R_{\text{air}}$) of Zn-doped $\text{BaFe}_{12}\text{O}_{19}$ towards 1 ppm NH_3 was 7.36 at 250 °C which was ~300% higher than pure $\text{BaFe}_{12}\text{O}_{19}$. Moreover, fast response/recovery time (2.66s/35.25s), good selectivity and long-term stability (100 days) towards NH_3 has been achieved when Zn was incorporated. The lower limit of detection of Zn doped $\text{BaFe}_{12}\text{O}_{19}$ was estimated ~150 ppb, that exceedingly favours lower concentration range of NH_3 detection. Extensive study on enhanced sensing behaviour of Zn-doped $\text{BaFe}_{12}\text{O}_{19}$ samples has resulted in the findings that, the modulation of $\text{Fe}^{2+}/\text{Fe}^{3+}$ ratio, oxygen vacancies (as confirmed from X-ray photoelectron spectroscopy (XPS) study) and improved oxygen adsorbing ability have substantial effect on sensing mechanism. Also, the improvement in sensing activity has been validated through quenching of photoluminescence (PL) spectra in favour of electron-hole separation. The usefulness of developed Zn-doped $\text{BaFe}_{12}\text{O}_{19}$ -based sensor for environmental air-quality surveillance and individualized health monitoring can be concluded through the sensor's notable resolution in detection of wide range (150 ppb - 100 ppm) of ammonia concentration. Additionally, simulated breath test validated the practical application potential of the sensor as breath analyser.

In **Chapter 4**, another unconventional gas sensing material bismuth ferrite (BiFeO_3) has been studied. Pure and Sn-doped bismuth ferrite (BFO) nanoparticles has been synthesized via facile sol-gel technique. Structural and morphological analysis of the nanoparticles have been systematically carried out by using X-ray powder diffraction, field emission scanning electron microscopy, transmission electron microscopy, energy-dispersive X-ray spectroscopy, Fourier transform infrared spectroscopy, photoluminescence spectroscopy and Brunauer–Emmett–Teller techniques. The gas sensing properties of the sensors based on prepared nanoparticles towards formaldehyde in the temperature range from 200°C to 400°C revealed that the doping of Sn enhances the formaldehyde sensing performance of BFO nanoparticles by ~4 folds. Prepared sensors demonstrate p-type sensing behaviour and high selectivity towards formaldehyde. It has been observed that the sensor based on 1.5% wt Sn doped BFO

nanoparticles exhibited maximum sensing response of 3.05 (R_g/R_a) to 1ppm formaldehyde. Prepared sensors were ultra-fast (response/recovery time of 2.71s/25.22s) and very stable having low detection limit of 100ppb. The enhancement of formaldehyde sensing property due to Sn-doping is a combined effect of variation of charge carriers due to valency mismatch and enhanced oxygen defects as confirmed from X-ray photoelectron spectroscopy study. The excellent sensing characteristics suggest that Sn-doped BFO nanoparticles could be a potential candidate for the detection of trace formaldehyde gas towards the monitoring of both indoor and outdoor environmental air quality.

In **Chapter 5**, modification of electronic properties of semiconductors by formation of heterostructure is key strategy to enhance surface activity of materials. In this chapter, the modification of sensing property of a well-known binary metal oxide semiconductor (MoO_3) has been carried out through formation of heterostructure with BiFeO_3 . Rapid development of industries has led to emission of toxic gases and provoked the need of monitoring of toxic gasses in environment. A Type II heterojunction has been proposed for $\alpha\text{-MoO}_3/\text{BiFeO}_3$ composites to explore its enhanced H_2S gas response. The optimized $\alpha\text{-MoO}_3/\text{BiFeO}_3$ heterojunction, exhibited remarkable H_2S sensing performance ($\sim 98\%$ to 100 ppm H_2S at 210°C , with rapid response/recovery time of 4.7s/14s). Modification of band edges by formation of heterojunction with wide bandgap, $\alpha\text{-MoO}_3$ and narrow bandgap, BiFeO_3 and tuned oxygen defects have synergetic effect on its enhanced performance. Photoelectrochemical study has been performed to understand the charge transfer mechanism in the heterostructure interface. A potential gradient at the interface of two semiconductors generates a built-in-electric field facilitating charge transfer as reflected in lower R_{ct} value, reduces the charge recombination facilitating gas sensing behaviour. Moreover, presence of oxygen defect creates myriads of active sites for H_2S adsorption which significantly enhanced response value. This study provides a route for designing bandgap-engineered $\alpha\text{-MoO}_3/\text{BiFeO}_3$ -heterostructure with enriched oxygen defects to address the need for environmental air quality monitoring.

In **Chapter 6**, $\text{NaTb}(\text{MO}_4)_2$ nanoparticles have been explored for its optical property. The effect of oxygen vacancies on band structure of $\text{NaTb}(\text{MO}_4)_2$ nanoparticles has been studied and it revealed that by tuning of oxygen vacancy (V_O) and introducing disorder in the system induced green emission in the system. Presence of V_O in $\text{NaTb}(\text{MO}_4)_2$ leads to formation of new energy states within the forbidden gap, induces disorder in the system and modifies the bond lengths. The oxygen vacancies are created in the system during controlled synthesis by using ethylenediaminetetraacetic acid (EDTA) which regulates the nucleation and

growth of $\text{NaTb}(\text{MO}_4)_2$ nanomaterials and created deformation near Tb^{3+} ions. Moreover, gas sensing measurement of $\text{NaTb}(\text{MO}_4)_2$ revealed that $\text{NaTb}(\text{MO}_4)_2$ can detect toxic gas formaldehyde with excellent sensitivity and resolution. The trapped electrons in V_O serve as active sites for adsorption of atmospheric oxygen facilitating the gas sensing response of $\text{NaTb}(\text{MO}_4)_2$. Ab initio calculation based on density functional theory (DFT) was utilised to visualise the energy band structure of the nanomaterials and calculate the adsorption energy of formaldehyde gas molecule. Therefore, this study can give a new insight to the fabrication and engineering of nanomaterials which exhibits multifunctionality driven by oxygen vacancies.

Chapter 7 is the conclusive chapter of the thesis which contains the summarization of the key findings of the research work. The excellent gas characteristics of the novel- MOS based chemiresistive gas sensors based on $\text{BaFe}_{12}\text{O}_{19}$ and BiFeO_3 are briefly described. The formation of heterojunction with $\text{MoO}_3/\text{BiFeO}_3$ for superior gas sensing mechanism has been delineated. The findings of the optical as well as the gas sensing characteristics of $\text{NaTb}(\text{MO}_4)_2$ nanomaterials have been described. Afterwards, the future direction of the work has been discussed to further highlight the prospect of this thesis work.

1.12. References

- [1] A. Aghababai Beni, H. Jabbari, *Nanomaterials for Environmental Applications*, Results in Engineering 15 (2022) 100467.
- [2] P.K. Panigrahi, B. Chandu, N. Puvvada, *Recent Advances in Nanostructured Materials for Application as Gas Sensors*, ACS Omega (2023).
- [3] K. Hajra, | Dipak Maity, | Sumit Saha, *Recent Advancements of Metal Oxide Nanoparticles and their Potential Applications: A Review*, Adv Mater Lett 15 (2024) 2401–1740.
- [4] N. Baig, I. Kammakakam, W. Falath, I. Kammakakam, *Nanomaterials: A review of synthesis methods, properties, recent progress, and challenges*, Mater Adv 2 (2021) 1821–1871.
- [5] S. Dhall, B.R. Mehta, A.K. Tyagi, K. Sood, *A review on environmental gas sensors: Materials and technologies*, Sensors International 2 (2021) 100116.
- [6] C.H. Kwak, T.H. Kim, S.Y. Jeong, J.W. Yoon, J.S. Kim, J.H. Lee, *Humidity-Independent Oxide Semiconductor Chemiresistors Using Terbium-Doped SnO₂ Yolk-Shell Spheres for Real-Time Breath Analysis*, ACS Appl Mater Interfaces 10 (2018) 18886–18894.
- [7] K.H. Kim, S.J. Kim, H.J. Cho, N.H. Kim, J.S. Jang, S.J. Choi, I.D. Kim, *WO₃ nanofibers functionalized by protein-templated RuO₂ nanoparticles as highly sensitive exhaled breath gas sensing layers*, Sens Actuators B Chem 241 (2017) 1276–1282.
- [8] Y. Li, N. Chen, D. Deng, X. Xing, X. Xiao, Y. Wang, *Formaldehyde detection: SnO₂ microspheres for formaldehyde gas sensor with high sensitivity, fast response/recovery and good selectivity*, Sens Actuators B Chem 238 (2017) 264–273.
- [9] Z. Li, *Supersensitive and superselective formaldehyde gas sensor based on NiO nanowires*, Vacuum 143 (2017) 50–53.
- [10] P. Rai, Y.S. Kim, H.M. Song, M.K. Song, Y.T. Yu, *The role of gold catalyst on the sensing behavior of ZnO nanorods for CO and NO₂ gases*, Sens Actuators B Chem 165 (2012) 133–142.
- [11] V.K. Tomer, S. Devi, R. Malik, S.P. Nehra, S. Duhan, *Highly sensitive and selective volatile organic amine (VOA) sensors using mesoporous WO₃–SnO₂ nanohybrids*, Sens Actuators B Chem 229 (2016) 321–330.
- [12] D. Ju, H. Xu, Q. Xu, H. Gong, Z. Qiu, J. Guo, J. Zhang, B. Cao, *High triethylamine-sensing properties of NiO/SnO₂ hollow sphere P–N heterojunction sensors*, Sens Actuators B Chem 215 (2015) 39–44.
- [13] S. Shi, F. Zhang, H. Lin, Q. Wang, E. Shi, F. Qu, *Enhanced triethylamine-sensing properties of P–N heterojunction Co₃O₄/In₂O₃ hollow microtubes derived from metal–organic frameworks*, Sens Actuators B Chem 262 (2018) 739–749.
- [14] C. Wang, L. Yin, L. Zhang, D. Xiang, R. Gao, *Metal Oxide Gas Sensors: Sensitivity and Influencing Factors*, Sensors (Basel) 10 (2010) 2088.
- [15] Y. Kang, F. Yu, L. Zhang, W. Wang, L. Chen, Y. Li, *Review of ZnO-based nanomaterials in gas sensors*, Solid State Ion 360 (2021) 115544.
- [16] S. Das, S. Mojumder, D. Saha, M. Pal, *Influence of major parameters on the sensing mechanism of semiconductor metal oxide based chemiresistive gas sensors: A review focused on personalized healthcare*, Sens Actuators B Chem 352 (2022) 131066.
- [17] A. Bag, N.E. Lee, *Gas sensing with heterostructures based on two-dimensional nanostructured materials: a review*, J Mater Chem C Mater 7 (2019) 13367–13383.

- [18] P. Ghosh, M.R. Das, P. Mitra, Influence of particle size on H₂ and H₂S sensing characteristics of nanocrystalline zinc ferrite, *Indian Journal of Physics* 90 (2016) 1367–1373.
- [19] S. Tyagi, N. Batra, A.K. Paul, Influence of Temperature on Reducing Gas Sensing Performance of Nanocrystalline Zinc Ferrite, *Transactions of the Indian Institute of Metals* 68 (2015) 707–713.
- [20] W.R. Algar, M. Massey, K. Rees, R. Higgins, K.D. Krause, G.H. Darwish, W.J. Peveler, Z. Xiao, H.Y. Tsai, R. Gupta, K. Lix, M. V. Tran, H. Kim, Photoluminescent Nanoparticles for Chemical and Biological Analysis and Imaging, *Chem Rev* 121 (2021) 9243–9358..
- [21] U. Shukla, S. Bari, Study on the Photoluminescence, *Journal of Pure Applied and Industrial Physics* 8 (2018) 25–31.
- [22] K. Zheng, P. Ma, Recent advances in lanthanide-based POMs for photoluminescent applications, *Dalton Transactions* 53 (2024) 3949–3958.
- [23] S.M. Majhi, A. Mirzaei, H.W. Kim, S.S. Kim, T.W. Kim, Recent advances in energy-saving chemiresistive gas sensors: A review, *Nano Energy* 79 (2021) 105369.
- [24] S. Liang, J. Li, F. Wang, J. Qin, X. Lai, X. Jiang, Highly sensitive acetone gas sensor based on ultrafine α -Fe₂O₃ nanoparticles, *Sens Actuators B Chem* 238 (2017) 923–927.
- [25] C.Y. Lee, S.J. Kim, I.S. Hwang, J.H. Lee, Glucose-mediated hydrothermal synthesis and gas sensing characteristics of WO₃ hollow microspheres, *Sens Actuators B Chem* 142 (2009) 236–242.
- [26] D.B. Patil, V.L. Patil, S.S. Patil, T.D. Dongale, N.D. Desai, P.R. Patil, R.M. Mane, P.N. Bhosale, P.S. Patil, P.M. Kadam, K. V. Khot, Facile synthesis of MoO₃ nanoplates based NO₂ gas sensor: Ultra-selective and sensitive, *Chem Phys Lett* 782 (2021) 139025.
- [27] R.L. Wilson, C.E. Simion, A. Stanoiu, A. Taylor, S. Guldin, J.A. Covington, C.J. Carmalt, C.S. Blackman, Humidity-Tolerant Ultrathin NiO Gas-Sensing Films, *ACS Sens* 5 (2020) 1389–1397.
- [28] B. Lyson-Sypien, M. Radecka, M. Rekas, K. Swierczek, K. Michalow-Mauke, T. Graule, K. Zakrzewska, Grain-size-dependent gas-sensing properties of TiO₂ nanomaterials, *Sens Actuators B Chem* 211 (2015) 67–76.
- [29] S. Vetter, S. Haffer, T. Wagner, M. Tiemann, Nanostructured Co₃O₄ as a CO gas sensor: Temperature-dependent behavior, *Sens Actuators B Chem* 206 (2015) 133–138.
- [30] Z. Wang, T. Zhang, C. Zhao, T. Han, T. Fei, S. Liu, G. Lu, Anchoring ultrafine Pd nanoparticles and SnO₂ nanoparticles on reduced graphene oxide for high-performance room temperature NO₂ sensing, *J Colloid Interface Sci* 514 (2018) 599–608.
- [31] G. Zhu, L. Guo, X. Shen, Z. Ji, K. Chen, H. Zhou, Monodispersed In₂O₃ mesoporous nanospheres: One-step facile synthesis and the improved gas-sensing performance, *Sens Actuators B Chem* 220 (2015) 977–985.
- [32] Y. Masuda, Recent advances in SnO₂ nanostructure based gas sensors, *Sens Actuators B Chem* 364 (2022) 131876..
- [33] C. Gu, L. Shanshan, J. Huang, C. Shi, J. Liu, Preferential growth of long ZnO nanowires and its application in gas sensor, *Sens Actuators B Chem* 177 (2013) 453–459.
- [34] S. Zhao, Y. Shen, X. Yan, P. Zhou, Y. Yin, R. Lu, C. Han, B. Cui, D. Wei, Complex-surfactant-assisted hydrothermal synthesis of one-dimensional ZnO nanorods for high-performance ethanol gas sensor, *Sens Actuators B Chem* 286 (2019) 501–511.
- [35] D. Acharyya, P. Bhattacharyya, Alcohol sensing performance of ZnO hexagonal nanotubes at low temperatures: A qualitative understanding, *Sens Actuators B Chem* 228 (2016) 373–386.

- [36] Q. Zhou, W. Chen, L. Xu, S. Peng, Hydrothermal Synthesis of Various Hierarchical ZnO Nanostructures and Their Methane Sensing Properties, *Sensors* 2013, Vol. 13, Pages 6171-6182 13 (2013) 6171–6182.
- [37] R. Chen, J. Wang, L. Xiang, Facile synthesis of mesoporous ZnO sheets assembled by small nanoparticles for enhanced NO₂ sensing performance at room temperature, *Sens Actuators B Chem* 270 (2018) 207–215.
- [38] Y. Hou, A.H. Jayatissa, Influence of laser doping on nanocrystalline ZnO thin films gas sensors, *Progress in Natural Science: Materials International* 27 (2017) 435–442.
- [39] F. Cao, C. Li, M. Li, H. Li, X. Huang, B. Yang, Direct growth of Al-doped ZnO ultrathin nanosheets on electrode for ethanol gas sensor application, *Appl Surf Sci* 447 (2018) 173–181.
- [40] Y. Xiao, L. Lu, A. Zhang, Y. Zhang, L. Sun, L. Huo, F. Li, Highly enhanced acetone sensing performances of porous and single crystalline ZnO nanosheets: High percentage of exposed (100) facets working together with surface modification with pd nanoparticles, *ACS Appl Mater Interfaces* 4 (2012) 3797–3804.
- [41] Y. Zhang, C. Liu, F. Gong, B. Jiu, F. Li, Large scale synthesis of hexagonal simonkolleite nanosheets for ZnO gas sensors with enhanced performances, *Mater Lett* 186 (2017) 7–11.
- [42] X. Zhang, J. Chen, M. Wen, H. Pan, S. Shen, Solvothermal preparation of spindle hierarchical ZnO and its photocatalytic and gas sensing properties, *Physica B Condens Matter* 602 (2021) 412545.
- [43] N.B. Patil, A.R. Nimbalkar, M.G. Patil, ZnO thin film prepared by a sol-gel spin coating technique for NO₂ detection, *Materials Science and Engineering: B* 227 (2018) 53–60.
- [44] Y. Zou, S. Chen, J. Sun, J. Liu, Y. Che, X. Liu, J. Zhang, D. Yang, Highly efficient gas sensor using a hollow SnO₂ microfiber for triethylamine detection, *ACS Sens* 2 (2017) 897–902.
- [45] L. Cheng, S.Y. Ma, T.T. Wang, X.B. Li, J. Luo, W.Q. Li, Y.Z. Mao, D.J. Gz, Synthesis and characterization of SnO₂ hollow nanofibers by electrospinning for ethanol sensing properties, *Mater Lett* 131 (2014) 23–26.
- [46] J. Pan, R. Ganesan, H. Shen, S. Mathur, Plasma-modified SnO₂ nanowires for enhanced gas sensing, *Journal of Physical Chemistry C* 114 (2010) 8245–8250.
- [47] E. Leblanc, L. Perier-Camby, G. Thomas, R. Gibert, M. Primet, P. Gelin, NO_x adsorption onto dehydroxylated or hydroxylated tin dioxide surface. Application to SnO₂-based sensors, *Sens Actuators B Chem* 62 (2000) 67–72.
- [48] P.G. Choi, Z. Liu, N. Hara, Y. Masuda, Surface Molecular Separator for Selective Gas Sensing, *Ind Eng Chem Res* 59 (2020) 17894–17900.
- [49] Y.X. Li, Z. Guo, Y. Su, X.B. Jin, X.H. Tang, J.R. Huang, X.J. Huang, M.Q. Li, J.H. Liu, Hierarchical Morphology-Dependent Gas-Sensing Performances of Three-Dimensional SnO₂ Nanostructures, *ACS Sens* 2 (2017) 102–110.
- [50] W.S. Chi, C.S. Lee, H. Long, M.H. Oh, A. Zettl, C. Carraro, J.H. Kim, R. Maboudian, Direct Organization of Morphology-Controllable Mesoporous SnO₂ Using Amphiphilic Graft Copolymer for Gas-Sensing Applications, *ACS Appl Mater Interfaces* 9 (2017) 37246–37253.
- [51] Y. Zhang, X. Zheng, T. Zhang, al -, P. Han, C. Lin, X. Zuo, C. Yuan, L. Hou, L. Shen, S. Yan, J. Zhang, Y. Huang, Y. Lu, Preparation of Coral-like SnO₂ Hierarchical Nanostructures and Its Application in Ethanol Gas-sensing Performance, *IOP Conf Ser Mater Sci Eng* 611 (2019) 012039.
- [52] X. Wang, N. Aroonyadet, Y. Zhang, M. Mecklenburg, X. Fang, H. Chen, E. Goo, C. Zhou, Aligned epitaxial SnO₂ nanowires on sapphire: Growth and device applications, *Nano Lett* 14 (2014) 3014–3022.

- [53] W. Yang, L. Feng, S. He, L. Liu, S. Liu, Density Gradient Strategy for Preparation of Broken In₂O₃ Microtubes with Remarkably Selective Detection of Triethylamine Vapor, *ACS Appl Mater Interfaces* 10 (2018) 27131–27140.
- [54] Q. Zheng, J.H. Lee, S.J. Kim, H.S. Lee, W. Lee, Excellent isoprene-sensing performance of In₂O₃ nanoparticles for breath analyzer applications, *Sens Actuators B Chem* 327 (2021) 128892.
- [55] A.M. Al Shboul, R. Izquierdo, Printed Chemiresistive In₂O₃ Nanoparticle-Based Sensors with ppb Detection of H₂S Gas for Food Packaging, *ACS Appl Nano Mater* 4 (2021) 9508–9517.
- [56] J. Cao, N. Zhang, S. Wang, C. Chen, H. Zhang, Researching the crystal phase effect on gas sensing performance in In₂O₃ nanofibers, *Sens Actuators B Chem* 305 (2020) 127475.
- [57] D. Han, L. Zhai, F. Gu, Z. Wang, Highly sensitive NO₂ gas sensor of ppb-level detection based on In₂O₃ nanobricks at low temperature, *Sens Actuators B Chem* 262 (2018) 655–663.
- [58] Y. Ou, G. Zhu, P. Liu, Y. Jia, L. Zhu, J. Nie, S. Zhang, W. Zhang, J. Gao, H. Lu, Y. Huang, X. Shi, M. Hojamberdiev, Anchoring Platinum Clusters onto Oxygen Vacancy-Modified In₂O₃ for Ultraefficient, Low-Temperature, Highly Sensitive, and Stable Detection of Formaldehyde, *ACS Sens* 7 (2022) 1201–1212.
- [59] L.L. Sui, Y.M. Xu, X.F. Zhang, X.L. Cheng, S. Gao, H. Zhao, Z. Cai, L.H. Huo, Construction of three-dimensional flower-like α -MoO₃ with hierarchical structure for highly selective triethylamine sensor, *Sens Actuators B Chem* 208 (2015) 406–414.
- [60] P. Bisht, A. Kumar, I.T. Jensen, M. Ahmad, B.D. Belle, B.R. Mehta, Enhanced gas sensing response for 2D α -MoO₃ layers: Thickness-dependent changes in defect concentration, surface oxygen adsorption, and metal-metal oxide contact, *Sens Actuators B Chem* 341 (2021).
- [61] Y. Mo, Z. Tan, L. Sun, Y. Lu, X. Liu, Ethanol-sensing properties of α -MoO₃ nanobelts synthesized by hydrothermal method, *J Alloys Compd* 812 (2020) 152166.
- [62] N. Sakhuja, R. Jha, N. Bhat, Facile green synthesis of 2D hexagonal MoO₃ for selective detection of ammonia at room temperature, *Materials Science and Engineering: B* 271 (2021) 115249.
- [63] X. Li, H. Yang, X. Hu, Q. Wu, W. Xiong, Z. Qin, C. Xie, D. Zeng, Exposed Mo atoms induced by micropores enhanced H₂S sensing of MoO₃ nanoflowers, *J Hazard Mater* 429 (2022) 128270.
- [64] S. He, W. Li, L. Feng, W. Yang, Rational interaction between the aimed gas and oxide surfaces enabling high-performance sensor: The case of acidic α -MoO₃ nanorods for selective detection of triethylamine, *J Alloys Compd* 783 (2019) 574–582.
- [65] Y. Yu, Y. Xia, W. Zeng, R. Liu, Synthesis of multiple networked NiO nanostructures for enhanced gas sensing performance, *Mater Lett* 206 (2017) 80–83.
- [66] Y. Zhang, W. Zeng, New insight into gas sensing performance of nanoneedle-assembled and nanosheet-assembled hierarchical NiO nanoflowers, *Mater Lett* 195 (2017) 217–219.
- [67] R. Miao, W. Zeng, Q. Gao, SDS-assisted hydrothermal synthesis of NiO flake-flower architectures with enhanced gas-sensing properties, *Appl Surf Sci* 384 (2016) 304–310.
- [68] F. Yang, Z. Guo, Engineering NiO sensitive materials and its ultra-selective detection of benzaldehyde, *J Colloid Interface Sci* 467 (2016) 192–202.
- [69] Y. Du, W. Wang, X. Li, J. Zhao, J. Ma, Y. Liu, G. Lu, Preparation of NiO nanoparticles in microemulsion and its gas sensing performance, *Mater Lett* 68 (2012) 168–170.
- [70] J. Zhang, D. Zeng, Q. Zhu, J. Wu, K. Xu, T. Liao, G. Zhang, C. Xie, Effect of Grain-Boundaries in NiO Nanosheet Layers Room-Temperature Sensing Mechanism under NO₂, *Journal of Physical Chemistry C* 119 (2015) 17930–17939.

- [71] V.T. Duong, C.T. Nguyen, H.B. Luong, D.C. Nguyen, H.L. Nguyen, Ultralow-detection limit ammonia gas sensors at room temperature based on MWCNT/WO₃ nanocomposite and effect of humidity, *Solid State Sci* 113 (2021) 106534.
- [72] L. Parellada-Monreal, S. Gherardi, G. Zonta, C. Malagù, D. Casotti, G. Cruciani, V. Guidi, M. Martínez-Calderón, I. Castro-Hurtado, D. Gamarra, J. Lozano, L. Presmanes, G.G. Mandayo, WO₃ processed by direct laser interference patterning for NO₂ detection, *Sens Actuators B Chem* 305 (2020) 127226.
- [73] J.W. Yoon, J.K. Choi, J.H. Lee, Design of a highly sensitive and selective C₂H₅OH sensor using p-type Co₃O₄ nanofibers, *Sens Actuators B Chem* 161 (2012) 570–577.
- [74] Z. Wen, L. Zhu, W. Mei, L. Hu, Y. Li, L. Sun, H. Cai, Z. Ye, Rhombus-shaped Co₃O₄ nanorod arrays for high-performance gas sensor, *Sens Actuators B Chem* 186 (2013) 172–179.
- [75] S.F. Shen, M.L. Xu, D.B. Lin, H.B. Pan, The growth of urchin-like Co₃O₄ directly on sensor substrate and its gas sensing properties, *Appl Surf Sci* 396 (2017) 327–332.
- [76] C. Sun, X. Su, F. Xiao, C. Niu, J. Wang, Synthesis of nearly monodisperse Co₃O₄ nanocubes via a microwave-assisted solvothermal process and their gas sensing properties, *Sens Actuators B Chem* 157 (2011) 681–685.
- [77] K. Il Choi, H.R. Kim, K.M. Kim, D. Liu, G. Cao, J.H. Lee, C₂H₅OH sensing characteristics of various Co₃O₄ nanostructures prepared by solvothermal reaction, *Sens Actuators B Chem* 146 (2010) 183–189.
- [78] S. Deng, X. Liu, N. Chen, D. Deng, X. Xiao, Y. Wang, A highly sensitive VOC gas sensor using p-type mesoporous Co₃O₄ nanosheets prepared by a facile chemical coprecipitation method, *Sens Actuators B Chem* 233 (2016) 615–623.
- [79] N. Chen, Y. Li, D. Deng, X. Liu, X. Xing, X. Xiao, Y. Wang, Acetone sensing performances based on nanoporous TiO₂ synthesized by a facile hydrothermal method, *Sens Actuators B Chem* 238 (2017) 491–500.
- [80] H.G. Pozos, K.T.V. Krishna, M. de la Luz Olvera Amador, Y. Kudriavtsev, A.M. Alvarez, TiO₂ thin film based gas sensors for CO-detection, *Journal of Materials Science: Materials in Electronics* 29 (2018) 15829–15837.
- [81] S.T. Navale, Z.B. Yang, C. Liu, P.J. Cao, V.B. Patil, N.S. Ramgir, R.S. Mane, F.J. Stadler, Enhanced acetone sensing properties of titanium dioxide nanoparticles with a sub-ppm detection limit, *Sens Actuators B Chem* 255 (2018) 1701–1710.
- [82] X. Li, X. Li, J. Wang, S. Lin, Highly sensitive and selective room-temperature formaldehyde sensors using hollow TiO₂ microspheres, *Sens Actuators B Chem* 219 (2015) 158–163.
- [83] Z.P. Tshabalala, K. Shingange, B.P. Dhonge, O.M. Ntwaeaborwa, G.H. Mhlongo, D.E. Motaung, Fabrication of ultra-high sensitive and selective CH₄ room temperature gas sensing of TiO₂ nanorods: Detailed study on the annealing temperature, *Sens Actuators B Chem* 238 (2017) 402–419.
- [84] G. Zhao, J. Xuan, Q. Gong, L. Wang, J. Ren, M. Sun, F. Jia, G. Yin, B. Liu, In Situ Growing Double-Layer TiO₂ Nanorod Arrays on New-Type FTO Electrodes for Low-Concentration NH₃ Detection at Room Temperature, *ACS Appl Mater Interfaces* 12 (2020) 8573–8582.
- [85] X. Zhou, Z. Wang, X. Xia, G. Shao, K. Homewood, Y. Gao, Synergistic Cooperation of Rutile TiO₂ {002}, {101}, and {110} Facets for Hydrogen Sensing, *ACS Appl Mater Interfaces* 10 (2018) 28199–28209.
- [86] Z. Zhu, S.J. Lin, C.H. Wu, R.J. Wu, Synthesis of TiO₂ nanowires for rapid NO₂ detection, *Sens Actuators A Phys* 272 (2018) 288–294.

- [87] W. Ge, S. Jiao, Z. Chang, X. He, Y. Li, Ultrafast Response and High Selectivity toward Acetone Vapor Using Hierarchical Structured TiO₂ Nanosheets, *ACS Appl Mater Interfaces* 12 (2020) 13200–13207.
- [88] H. Zhang, T. Tao, X. Li, Y. Bao, X. Xia, M. Lourenço, K. Homewood, Z. Huang, Y. Gao, Extending the detection range and response of TiO₂ based hydrogen sensors by surface defect engineering, *Int J Hydrogen Energy* 45 (2020) 18057–18065.
- [89] Z. Wu, Z. Li, H. Li, M. Sun, S. Han, C. Cai, W. Shen, Y. Fu, Ultrafast Response/Recovery and High Selectivity of the H₂S Gas Sensor Based on α -Fe₂O₃ Nano-Ellipsoids from One-Step Hydrothermal Synthesis, *ACS Appl Mater Interfaces* 11 (2019) 12761–12769.
- [90] N.D. Cuong, D.Q. Khieu, T.T. Hoa, D.T. Quang, P.H. Viet, T.D. Lam, N.D. Hoa, N. Van Hieu, Facile synthesis of α -Fe₂O₃ nanoparticles for high-performance CO gas sensor, *Mater Res Bull* 68 (2015) 302–307.
- [91] Q.Z. Zeng, S.Y. Ma, W.X. Jin, H.M. Yang, H. Chen, Q. Ge, L. Ma, Hydrothermal synthesis of monodisperse α -Fe₂O₃ hollow microspheroids and their high gas-sensing properties, *J Alloys Compd* 705 (2017) 427–437.
- [92] Y. Wang, J. Cao, S. Wang, X. Guo, J. Zhang, H. Xia, S. Zhang, S. Wu, Facile synthesis of porous α -Fe₂O₃ nanorods and their application in ethanol sensors, *Journal of Physical Chemistry C* 112 (2008) 17804–17808.
- [93] Y. Huang, W. Chen, S. Zhang, Z. Kuang, D. Ao, N.R. Alkurd, W. Zhou, W. Liu, W. Shen, Z. Li, A high performance hydrogen sulfide gas sensor based on porous α -Fe₂O₃ operates at room-temperature, *Appl Surf Sci* 351 (2015) 1025–1033.
- [94] J. Zhang, J. Liu, Q. Peng, X. Wang, Y. Li, Nearly monodisperse Cu₂O and CuO nanospheres: Preparation and applications for sensitive gas sensors, *Chemistry of Materials* 18 (2006) 867–871.
- [95] A. Umar, A.A. Ibrahim, U.T. Nakate, H. Albargi, M.A. Alsaiani, F. Ahmed, F.A. Alharthi, A. Ali Alghamdi, N. Al-Zaqri, Fabrication and characterization of CuO nanoplates based sensor device for ethanol gas sensing application, *Chem Phys Lett* 763 (2021) 138204.
- [96] F. Wang, H. Li, Z. Yuan, Y. Sun, F. Chang, H. Deng, L. Xie, H. Li, A highly sensitive gas sensor based on CuO nanoparticles synthesized via a sol–gel method, *RSC Adv* 6 (2016) 79343–79349.
- [97] X. Wan, J. Wang, L. Zhu, J. Tang, Gas sensing properties of Cu₂O and its particle size and morphology-dependent gas-detection sensitivity, *J Mater Chem A Mater* 2 (2014) 13641–13647.
- [98] N. Gogurla, A.K. Sinha, S. Santra, S. Manna, S.K. Ray, Multifunctional Au-ZnO Plasmonic Nanostructures for Enhanced UV Photodetector and Room Temperature NO Sensing Devices, *Scientific Reports* 2014 4:1 4 (2014) 1–9.
- [99] H.R. Yousefi, B. Hashemi, A. Mirzaei, H. Roshan, M.H. Sheikhi, Effect of Ag on the ZnO nanoparticles properties as an ethanol vapor sensor, *Mater Sci Semicond Process* 117 (2020) 105172.
- [100] Y. Wang, Y. Wang, J. Cao, F. Kong, H. Xia, J. Zhang, B. Zhu, S. Wang, S. Wu, Low-temperature H₂S sensors based on Ag-doped α -Fe₂O₃ nanoparticles, *Sens Actuators B Chem* 131 (2008) 183–189.
- [101] M.R. Modabberi, R. Rooydell, S. Brahma, A.A. Akande, B.W. Mwakikunga, C.P. Liu, Enhanced response and selectivity of H₂S sensing through controlled Ni doping into ZnO nanorods by using single metal organic precursors, *Sens Actuators B Chem* 273 (2018) 1278–1290.
- [102] C. Zou, F. Liang, S. Xue, Synthesis and oxygen vacancy related NO₂ gas sensing properties of ZnO:Co nanorods arrays grown by a hydrothermal method, *Appl Surf Sci* 353 (2015) 1061–1069.
- [103] N.M. Vuong, N.D. Chinh, B.T. Huy, Y.I. Lee, CuO-Decorated ZnO Hierarchical Nanostructures as Efficient and Established Sensing Materials for H₂S Gas Sensors, *Scientific Reports* 2016 6:1 6 (2016) 1–13.

- [104] H.A. Varudkar, G. Umadevi, P. Nagaraju, J.S. Dargad, V.D. Mote, Fabrication of Al-doped ZnO nanoparticles and their application as a semiconductor-based gas sensor for the detection of ammonia, *Journal of Materials Science: Materials in Electronics* 31 (2020) 12579–12585.
- [105] L. Zhu, Y. Li, W. Zeng, Enhanced ethanol sensing and mechanism of Cr-doped ZnO nanorods: Experimental and computational study, *Ceram Int* 43 (2017) 14873–14879.
- [106] S.W. Choi, S.S. Kim, Room temperature CO sensing of selectively grown networked ZnO nanowires by Pd nanodot functionalization, *Sens Actuators B Chem* 168 (2012) 8–13.
- [107] A.T. Güntner, M. Righettoni, S.E. Pratsinis, Selective sensing of NH₃ by Si-doped α -MoO₃ for breath analysis, *Sens Actuators B Chem* 223 (2016) 266–273.
- [108] N. Bhardwaj, A. Pandey, B. Satpati, M. Tomar, V. Gupta, S. Mohapatra, Enhanced CO gas sensing properties of Cu doped SnO₂ nanostructures prepared by a facile wet chemical method, *Physical Chemistry Chemical Physics* 18 (2016) 18846–18854.
- [109] Y. Xu, W. Zheng, X. Liu, L. Zhang, L. Zheng, C. Yang, N. Pinna, J. Zhang, Platinum single atoms on tin oxide ultrathin films for extremely sensitive gas detection, *Mater Horiz* 7 (2020) 1519–1527.
- [110] X. Song, Q. Xu, T. Zhang, B. Song, C. Li, B. Cao, Room-temperature, high selectivity and low-ppm-level triethylamine sensor assembled with Au decahedrons-decorated porous α -Fe₂O₃ nanorods directly grown on flat substrate, *Sens Actuators B Chem* 268 (2018) 170–181.
- [111] K. Suematsu, Y. Shin, Z. Hua, K. Yoshida, M. Yuasa, T. Kida, K. Shimanoe, Nanoparticle cluster gas sensor: Controlled clustering of SnO₂ nanoparticles for highly sensitive toluene detection, *ACS Appl Mater Interfaces* 6 (2014) 5319–5326.
- [112] H. Fu, Z. Wu, X. Yang, P. He, X. An, S. Xiong, D. Han, Ultra-high sensitivity and selectivity of Au nanoparticles modified MoO₃ nanobelts towards 1-butylamine, *Appl Surf Sci* 542 (2021) 148721.
- [113] J. Bai, Y. Kong, Z. Liu, H. Yang, M. Li, D. Xu, Q. Zhang, Ag modified Tb-doped double-phase In₂O₃ for ultrasensitive hydrogen gas sensor, *Appl Surf Sci* 583 (2022) 152521.
- [114] B.Y. Kim, J.W. Yoon, J.K. Kim, Y.C. Kang, J.H. Lee, Dual Role of Multiroom-Structured Sn-Doped NiO Microspheres for Ultrasensitive and Highly Selective Detection of Xylene, *ACS Appl Mater Interfaces* 10 (2018) 16605–16612.
- [115] K.G. Krishna, G. Umadevi, S. Parne, N. Pothukanuri, Zinc oxide based gas sensors and their derivatives: a critical review, *J Mater Chem C Mater* 11 (2023) 3906–3925.
- [116] L. Liu, Y. Wang, Y. Liu, S. Wang, T. Li, S. Feng, S. Qin, T. Zhang, Heteronanostructural metal oxide-based gas microsensors, *Microsystems & Nanoengineering* 2022 8:1 8 (2022) 1–22.
- [117] A. Katoch, J.H. Kim, Y.J. Kwon, H.W. Kim, S.S. Kim, Bifunctional sensing mechanism of SnO₂-ZnO composite nanofibers for drastically enhancing the sensing behavior in H₂ gas, *ACS Appl Mater Interfaces* 7 (2015) 11351–11358.
- [118] D.X. Ju, H.Y. Xu, Z.W. Qiu, Z.C. Zhang, Q. Xu, J. Zhang, J.Q. Wang, B.Q. Cao, Near Room Temperature, Fast-Response, and Highly Sensitive Triethylamine Sensor Assembled with Au-Loaded ZnO/SnO₂ Core-Shell Nanorods on Flat Alumina Substrates, *ACS Appl Mater Interfaces* 7 (2015) 19163–19171.
- [119] C. Han, X. Li, C. Shao, X. Li, J. Ma, X. Zhang, Y. Liu, Composition-controllable p-CuO/n-ZnO hollow nanofibers for high-performance H₂S detection, *Sens Actuators B Chem* 285 (2019) 495–503.
- [120] Y. Li, M. Jiao, H. Zhao, M. Yang, High performance gas sensors based on in-situ fabricated ZnO/polyaniline nanocomposite: The effect of morphology on the sensing properties, *Sens Actuators B Chem* 264 (2018) 285–295.

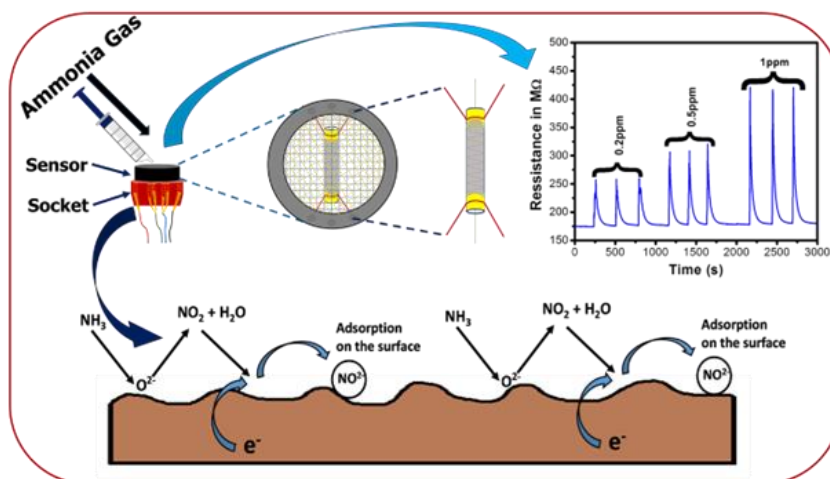
- [121] J. Hu, Y. Sun, X. Wang, L. Chen, W. Zhang, Y. Chen, Synthesis and gas sensing properties of molybdenum oxide modified tungsten oxide microstructures for ppb-level hydrogen sulphide detection, (2017).
- [122] X. Gao, C. Li, Z. Yin, Y. Chen, Synthesis and H₂S sensing performance of MoO₃/Fe₂(MoO₄)₃ yolk/shell nanostructures, *RSC Adv* 5 (2015) 37703–37709.
- [123] K.P. Yuan, L.Y. Zhu, J.H. Yang, C.Z. Hang, J.J. Tao, H.P. Ma, A.Q. Jiang, D.W. Zhang, H.L. Lu, Precise preparation of WO₃@SnO₂ core shell nanosheets for efficient NH₃ gas sensing, *J Colloid Interface Sci* 568 (2020) 81–88.
- [124] H. Bi, Y. Shen, S. Zhao, P. Zhou, S. Gao, B. Cui, D. Wei, Y. Zhang, K. Wei, Synthesis of NiO-In₂O₃ heterojunction nanospheres for highly selective and sensitive detection of ppb-level NO₂, *Vacuum* 172 (2020) 109086.
- [125] H. Xu, J. Ju, W. Li, J. Zhang, J. Wang, B. Cao, Superior triethylamine-sensing properties based on TiO₂/SnO₂ n–n heterojunction nanosheets directly grown on ceramic tubes, *Sens Actuators B Chem* 228 (2016) 634–642.
- [126] L. Guo, C. Wang, X. Kou, N. Xie, F. Liu, H. Zhang, X. Liang, Y. Gao, Y. Sun, X. Chuai, G. Lu, Detection of triethylamine with fast response by Al₂O₃/α-Fe₂O₃ composite nanofibers, *Sens Actuators B Chem* 266 (2018) 139–148.
- [127] M.M. Arafat, A.S.M.A. Haseeb, S.A. Akbar, M.Z. Quadir, In-situ fabricated gas sensors based on one dimensional core-shell TiO₂-Al₂O₃ nanostructures, *Sens Actuators B Chem* 238 (2017) 972–984.
- [128] Z. Ling, C. Leach, The effect of relative humidity on the NO₂ sensitivity of a SnO₂/WO₃ heterojunction gas sensor, *Sens Actuators B Chem* 102 (2004) 102–106.
- [129] L. Liu, Y. Wang, Y. Dai, G. Li, S. Wang, T. Li, T. Zhang, S. Qin, In Situ Growth of NiO@SnO₂ Hierarchical Nanostructures for High Performance H₂S Sensing, *ACS Appl Mater Interfaces* 11 (2019) 44829–44836.
- [130] K. Yuan, C.Y. Wang, L.Y. Zhu, Q. Cao, J.H. Yang, X.X. Li, W. Huang, Y.Y. Wang, H.L. Lu, D.W. Zhang, Fabrication of a Micro-Electromechanical System-Based Acetone Gas Sensor Using CeO₂ Nanodot-Decorated WO₃ Nanowires, *ACS Appl Mater Interfaces* 12 (2020) 14095–14104.
- [131] J. Hu, Y. Sun, Y. Xue, M. Zhang, P. Li, K. Lian, S. Zhuiykov, W. Zhang, Y. Chen, Highly sensitive and ultra-fast gas sensor based on CeO₂-loaded In₂O₃ hollow spheres for ppb-level hydrogen detection, *Sens Actuators B Chem* 257 (2018) 124–135.
- [132] H. Mei, S. Zhou, M. Lu, Y. Zhao, L. Cheng, Construction of pine-branch-like α-Fe₂O₃/TiO₂ hierarchical heterostructure for gas sensing, *Ceram Int* 46 (2020) 18675–18682.
- [133] R. Zhang, C. Qin, H. Bala, Y. Wang, J. Cao, Recent Progress in Spinel Ferrite (MFe₂O₄) Chemiresistive Based Gas Sensors, *Nanomaterials* 2023, Vol. 13, Page 2188 13 (2023) 2188.
- [134] J. Zhang, J.M. Song, H.L. Niu, C.J. Mao, S.Y. Zhang, Y.H. Shen, ZnFe₂O₄ nanoparticles: Synthesis, characterization, and enhanced gas sensing property for acetone, *Sens Actuators B Chem* 221 (2015) 55–62.
- [135] Y. Cao, H. Qin, X. Niu, D. Jia, Simple solid-state chemical synthesis and gas-sensing properties of spinel ferrite materials with different morphologies, *Ceram Int* 42 (2016) 10697–10703.
- [136] L. Zhang, W. Jiao, The effect of microstructure on the gas properties of NiFe₂O₄ sensors: Nanotube and nanoparticle, *Sens Actuators B Chem* 216 (2015) 293–297.
- [137] Y. Zhang, C. Jia, Q. Wang, Q. Kong, G. Chen, H. Guan, C. Dong, Highly Sensitive and Selective Toluene Sensor of Bimetallic Ni/Fe-MOFs Derived Porous NiFe₂O₄ Nanorods, *Ind Eng Chem Res* 58 (2019) 9450–9457.

- [138] S. Zhang, W. Jiang, Y. Li, X. Yang, P. Sun, F. Liu, X. Yan, Y. Gao, X. Liang, J. Ma, G. Lu, Highly-sensitivity acetone sensors based on spinel-type oxide (NiFe₂O₄) through optimization of porous structure, *Sens Actuators B Chem* 291 (2019) 266–274.
- [139] X. Yang, S. Zhang, Q. Yu, P. Sun, F. Liu, H. Lu, X. Yan, X. Zhou, X. Liang, Y. Gao, G. Lu, Solvothermal synthesis of porous CuFe₂O₄ nanospheres for high performance acetone sensor, *Sens Actuators B Chem* 270 (2018) 538–544.
- [140] A. Singh, A. Singh, S. Singh, P. Tandon, Fabrication of copper ferrite porous hierarchical nanostructures for an efficient liquefied petroleum gas sensor, *Sens Actuators B Chem* 244 (2017) 806–814.
- [141] J.Y. Patil, M.S. Khandekar, I.S. Mulla, S.S. Suryavanshi, Combustion synthesis of magnesium ferrite as liquid petroleum gas (LPG) sensor: Effect of sintering temperature, *Current Applied Physics* 12 (2012) 319–324.
- [142] R. V. Godbole, P. Rao, P.S. Alegaonkar, S. Bhagwat, Influence of fuel to oxidizer ratio on LPG sensing performance of MgFe₂O₄ nanoparticles, *Mater Chem Phys* 161 (2015) 135–141.
- [143] S.S. Patil, B.M. Babar, D.Y. Nadargi, F.I. Shaikh, J.D. Nadargi, B.R. Sankapal, I.S. Mulla, M.S. Tamboli, N.T. Nguyen Truong, S.S. Suryavanshi, La-Fe-O Perovskite Based Gas Sensors: Recent Advances and Future Challenges, *ACS Omega* 9 (2024) 29994–30014.
- [144] Z. Dai, C.S. Lee, B.Y. Kim, C.H. Kwak, J.W. Yoon, H.M. Jeong, J.H. Lee, Honeycomb-like periodic porous LaFeO₃ thin film chemiresistors with enhanced gas-sensing performances, *ACS Appl Mater Interfaces* 6 (2014) 16217–16226.
- [145] Q. Rong, Y. Zhang, J. Hu, K. Li, H. Wang, M. Chen, T. Lv, Z. Zhu, J. Zhang, Q. Liu, Design of ultrasensitive Ag-LaFeO₃ methanol gas sensor based on quasi molecular imprinting technology, *Sci Rep* 8 (2018).
- [146] W. Wei, S. Guo, C. Chen, L. Sun, Y. Chen, W. Guo, S. Ruan, High sensitive and fast formaldehyde gas sensor based on Ag-doped LaFeO₃ nanofibers, *J Alloys Compd* 695 (2017) 1122–1127.
- [147] H. Ji, L. Zhang, R. Zhang, Gas sensitive performance and mechanism of multiferroic BiFeO₃ under thermal-magnetic synergetic excitation, *Inorg Chem Commun* 150 (2023) 110491.
- [148] Q. Yu, Y. Zhang, Y. Xu, Hierarchical hollow BiFeO₃ microcubes with enhanced acetone gas sensing performance, *Dalton Transactions* 50 (2021) 6702–6709.
- [149] X.L. Yu, Y. Wang, Y.M. Hu, C.B. Cao, H.L.W. Chan, Gas-Sensing Properties of Perovskite BiFeO₃ Nanoparticles, *Journal of the American Ceramic Society* 92 (2009) 3105–3107.
- [150] P. Xu, X. Han, M. Wang, Synthesis and magnetic properties of BaFe₁₂O₁₉ hexaferrite nanoparticles by a reverse microemulsion technique, *Journal of Physical Chemistry C* 111 (2007) 5866–5870.
- [151] V.A. Morozov, S.M. Posokhova, S.Y. Istomin, D. V. Deyneko, A.A. Savina, B.S. Redkin, N. V. Lyskov, D.A. Spassky, A.A. Belik, B.I. Lazoryak, K₂Tb(MoO₄)₂ Green Phosphor with K⁺-Ion Conductivity: Derived from Different Synthesis Routes, *Inorg Chem* 60 (2021) 9471–9483.
- [152] J.V.B. Moura, C. Luz-Lima, G.S. Pinheiro, P.T.C. Freire, Temperature-induced isostructural phase transition on NaCe(MoO₄)₂ system: A Raman scattering study, *Spectrochim Acta A Mol Biomol Spectrosc* 208 (2019) 229–235.
- [153] C. Xia, Y. Chen, X. He, B. Zeng, J. Yang, C. Cui, S. Xie, Y. Guo, X. Liu, L. Li, Evidence and Practical Applications of Site Occupancy Theory (SOT) of Eu³⁺ in Scheelite Compounds, *Inorg Chem* 63 (2024) 8863–8878.
- [154] V.A. Morozov, A. V. Arakcheeva, P. Pattison, K.W. Meert, P.F. Smet, D. Poelman, N. Gauquelin, J. Verbeeck, A.M. Abakumov, J. Hadermann, K₂Eu(MoO₄)₂: Polymorphism, Structures, and Luminescent Properties, *Chemistry of Materials* 27 (2015) 5519–5530.

- [155] Z. Wang, H. Liang, Q. Wang, L. Luo, M. Gong, Luminescent properties of Tb³⁺ activated double molybdates and tungstates, *Materials Science and Engineering: B* 164 (2009) 120–123.
- [156] L. Zhou, S. Hu, X. Zhou, J. Tang, J. Yang, One-step surfactant-free synthesis of Eu³⁺-activated NaTb(MoO₄)₂ microcrystals with controllable shape and their multicolor luminescence properties, *CrystEngComm* 18 (2016) 7590–7600.
- [157] V.A. Morozov, A. V. Arakcheeva, P. Pattison, K.W. Meert, P.F. Smet, D. Poelman, N. Gauquelin, J. Verbeeck, A.M. Abakumov, J. Hadermann, KEu(MoO₄)₂: Polymorphism, Structures, and Luminescent Properties, *Chemistry of Materials* 27 (2015) 5519–5530.
- [158] Y. Hua, S. Khaja Hussain, J.S. Yu, Samarium(III) and terbium(III) ion-doped NaLa(MoO₄)₂ phosphors for versatile applications, *New Journal of Chemistry* 43 (2019) 10645–10657.
- [159] J.V.B. Moura, C. Luz-Lima, G.S. Pinheiro, P.T.C. Freire, Temperature-induced isostructural phase transition on NaCe(MoO₄)₂ system: A Raman scattering study, *Spectrochim Acta A Mol Biomol Spectrosc* 208 (2019) 229–235.
- [160] L. Xu, X. Yang, Z. Zhai, X. Chao, Z. Zhang, W. Hou, EDTA-mediated hydrothermal synthesis of NaEu(MoO₄)₂ microrugbies with tunable size and enhanced luminescence properties, *CrystEngComm* 13 (2011) 4921–4929.
- [161] Y. Li, G. Wang, K. Pan, W. Zhou, C. Wang, N. Fan, Y. Chen, Q. Feng, B. Zhao, Controlled synthesis and luminescence properties of rhombic NaLn(MoO₄)₂ submicrocrystals, *CrystEngComm* 14 (2012) 5015–5020.
- [162] S.S. Perera, H.N. Munasinghe, E.N. Yatooma, F.A. Rabuffetti, Microwave-assisted solid-state synthesis of NaRE(MO₄)₂phosphors (RE = La, Pr, Eu, Dy; M = Mo, W), *Dalton Transactions* 49 (2020) 7914–7919.
- [163] Z. Xu, P. Du, Q. Zhu, X. Li, X. Sun, J.G. Li, KLn(MoO₄)₂micro/nanocrystals (Ln = La-Lu, Y): Systematic hydrothermal crystallization, structure, and the performance of doped Eu³⁺for optical thermometry, *Dalton Transactions* 50 (2021) 17703–17715.
- [164] X. Jiang, X. Wang, X. Shi, H. Sha, W. Yang, W. Yang, Z. Leng, H. Lin, Z. Su, C. Li, F. Zeng, Effect of Mn⁴⁺ ions on the structure and luminescence properties of NaY(MoO₄)₂: Yb³⁺/Er³⁺ phosphor, *Opt Mater (Amst)* 113 (2021).

CHAPTER 2

Novel Barium Hexaferrite based Highly Selective and Stable Trace Ammonia Sensor for Detection of Renal Disease by Exhaled Breath Analysis



This work is published in “Sensors & Actuators B: Chemical 325 (2020) 128765”

2.1. Introduction

Recently, exhaled breath analysis for the detection of disease and monitoring human health has become a rapidly growing field owing to the major advances in the analytical tools, and the advent of nanotechnology [1-6]. It offers non-invasive, point of care, cost-effective, real time, qualitative/quantitative, and painless diagnosis. Exhaled breath comprises of more than 1000 gases and volatile organic compounds (VOCs) some of which have been detected as breath biomarkers of different diseases. Ammonia is the breath biomarker of kidney malfunction /renal diseases [7,8]. The average exhaled breath ammonia concentration for an otherwise healthy human being is around 250ppb [9]. However, this concentration escalates with the inception of renal/kidney related diseases and may increase up to 4880ppb in end stage renal disease (ESRD) [10].

Different analytical techniques, viz. Gas Chromatography-Mass Spectrometry (GC-MS), Proton Transfer Reaction-Mass Spectrometry (PTR-MS), Selected mass flow tube mass spectrometry (SIFT-MS) have been successfully employed to correlate various diseases with breath biomarker concentrations [11-16]. However, these techniques are costly, cumbersome, and require trained operators and pathological laboratory visitations. Therefore, researchers are progressively taking recourse to chemoresistive sensors owing to their small size, low cost, ruggedness, low power consumption and maintenance requirements etc. We have enlisted some of the salient and most encouraging results from the existing literature reports in [Table 2.1](#). It seems that α -molybdenum oxide (α -MoO₃), and tungsten oxide (WO₃) are the most suitable candidates for developing sensors for trace ammonia detection. However, a commercial sensor/device is yet to hit the market and this opens up the window for investigating into other chemoresistive oxides.

Barium Hexaferrite (BaFe₁₂O₁₉) is one of the most well-studied permanent magnetic materials owing to its high saturation magnetization, large coercivity, good chemical stability, and large magneto-crystalline anisotropy [32-34]. It has a hexagonal crystal structure (space group: P6₃/mmc) [35-36] and finds multitudes of applications in microwave devices, electromagnetic wave absorbers, high density magnetic recording media, phase shifter applications etc. [37-39]. However, there is no report on barium hexaferrite based chemoresistive ammonia sensor until now.

In this paper we report for the first time, barium hexaferrite based highly sensitive and selective trace ammonia sensor. Barium hexaferrite nanoparticles were prepared by a facile

solid-state reaction route. The as prepared nanopowders were characterized by multiple sophisticated techniques, viz. X-ray diffraction (XRD), field emission scanning electron microscopy (FESEM), transmission electron microscopy (TEM), energy dispersive X-ray (EDX), X-ray photoelectron spectroscopy (XPS), and BET surface analysis. The as prepared nanopowders were used to prepare a thick film, chemoresistive, Taguchi type sensor by employing a customized drop coating set up. The sensor shows excellent p-type response towards low-ppm ammonia. Further, it exhibits negligible cross-sensitivity, fast response and recovery times, and long-term stability. Owing to the excellent sensing performance, long-term stability, and repeatability this sensor is a promising candidate for the detection of kidney malfunction /renal diseases from exhaled breath analysis.

Table 2.1 Detection of trace NH_3 by chemoresistive sensors.

Nanomaterial	Morphology	Lowest Concentration of NH_3 Detected
Spin coated MoO_3	NA	50ppb [17]
α - MoO_3	Nanosheets	500ppb [18]
α - MoO_3	Ion beam deposited	3ppm [19]
α - MoO_3	Nanoribbons	280ppt [20]
Si doped α - MoO_3	Needle like morphology	400ppb [10]
2wt% Cr doped WO_3	Mesoporous nanoparticle	5ppm [21]
rGO/ WO_3 nanocomposite	Porous nanosheets with nano-spherical WO_3	1.14ppm [22]
SnO_2	nano-shell	5ppm [23]
ZnO/MoS_2	Self-assembled	500ppb [24]
WO_3	Nanowire	1500ppm [25]
Pure & Cr and Pt doped WO_3	Macroporous	6.2ppm [26]
$\text{W}_{18}\text{O}_{49}$	Nanowire	100ppb [27]
Polypyrrole - WO_3 composite	Nanofiber	1ppm [28]
PANI/ WO_3 composite	NA	10ppm [29]
rGO/ WS_2 heterojunction	NA	10 ppm [30]
Flexible graphene based wearable gas sensor	NA	ppt level [31]

2.2. Experimental Section

2.2.1. Materials

Barium (II) carbonate (BaCO_3 , Mw = 197.34 g/mol, Merck Millipore), Iron(III) oxide (Fe_2O_3 , Mw = 159.69 g/mol, <50nm particle size by BET analysis, Sigma-Aldrich), Isopropyl alcohol ($\text{C}_3\text{H}_8\text{O}$, Mw = 60.1 g/mol, E-merck), acetone ($\text{C}_3\text{H}_6\text{O}$, Mw = 58.08g/mol, E-merck) were used as procured without further purification. Conducting gold paste (Ted-Pella), nichrome wire, Platinum wire, and custom-made plastic sensor cases were used in different processes involved in the synthesis and fabrication of the sensor module.

2.2.2. Synthesis of Barium Hexaferrite nanopowder

$\text{BaFe}_{12}\text{O}_{19}$ nanopowders were prepared by a solid-state reaction route. 9.5g Fe_2O_3 , and 2g of BaCO_3 were ground with acetone in an agate mortar-pestle for 1h to achieve a homogeneous mixture. The mixture was pre-fired at 600 °C for 1h to achieve a precursor compound which was further pestled with acetone in an agate mortar-pestle for 30 mins to achieve fineness. The fine powders were calcined at 1000 °C for 2h. The as prepared nanopowders were used for further characterization and sensing studies. The synthesis process is schematically illustrated in Fig. 2.1 for more clarity.

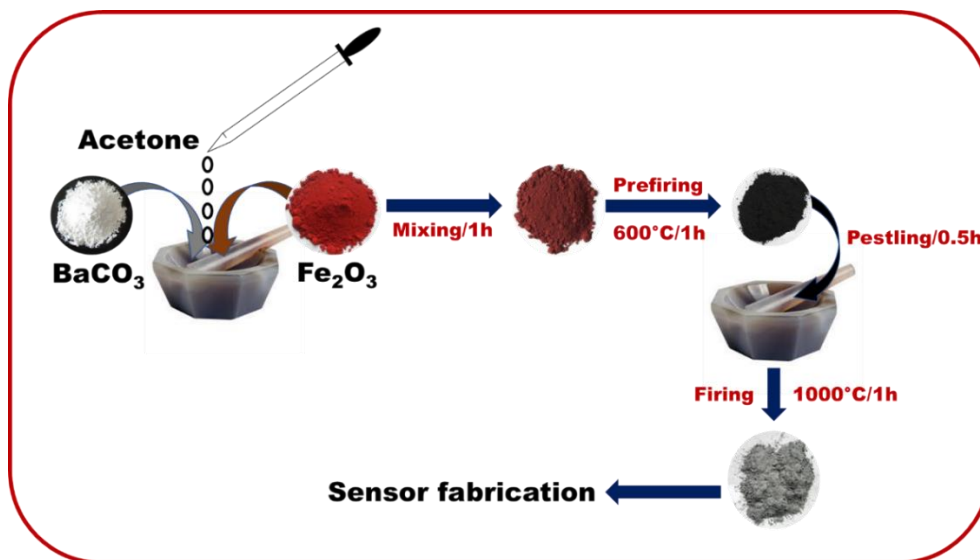


Fig. 2.1. Schematic illustration of the synthesis process of $\text{BaFe}_{12}\text{O}_{19}$ nanopowder.

2.2.3. Fabrication on Barium Hexaferrite nanopowder based sensor

Taguchi type sensor module was fabricated using the as prepared $\text{BaFe}_{12}\text{O}_{19}$ nanopowders. Firstly, a 3.5 mm long sensor substrate was cut from a long, hollow, and cylindrical α -alumina tube (1mm outer diameter, and 0.5mm inner diameter). The substrate was cleaned sequentially with hydrochloric acid (35%, E-Merck), DI water and, acetone and dried thereafter. Then, the substrate was electroded. Conducting gold paste was applied on its two ends and Pt wire as lead wires were connected to these electrodes. The electrodes were then cured at 900 °C for 1h. The distance between two electrodes was kept as 3mm. The substrate thus prepared was hooked to a drop coater (ref. Fig. 2.2c) which can rotate the sensor around its axis at an rpm of 10. Meanwhile, 0.5g of the as prepared $\text{BaFe}_{12}\text{O}_{19}$ nanopowder was pestled with IPA into an agate mortar until drop coating consistency was achieved (ref. Fig. 2.2(c-d)). Thereafter, 5 μL of the paste was dropped onto the rotating α -alumina substrate. The rotating motion uniformly coats the drop onto the substrate surface (ref. Fig. 2.2d). Then a nichrome wire (resistance 24 Ω) was inserted into the hollow core of the sensor (ref. Fig. 2.2e) and the sensor was mounted on a six-pin plastic socket by spot-welding the Pt electrode leads and the heater to these six pins (ref. Fig. 2.2f). Finally, a plastic cap with double mesh (200 mesh each) was push-fitted on this socket (ref. Fig. 2.2h). This sensor module ((ref. Fig. 2.2h) was used for all the sensor measurements.

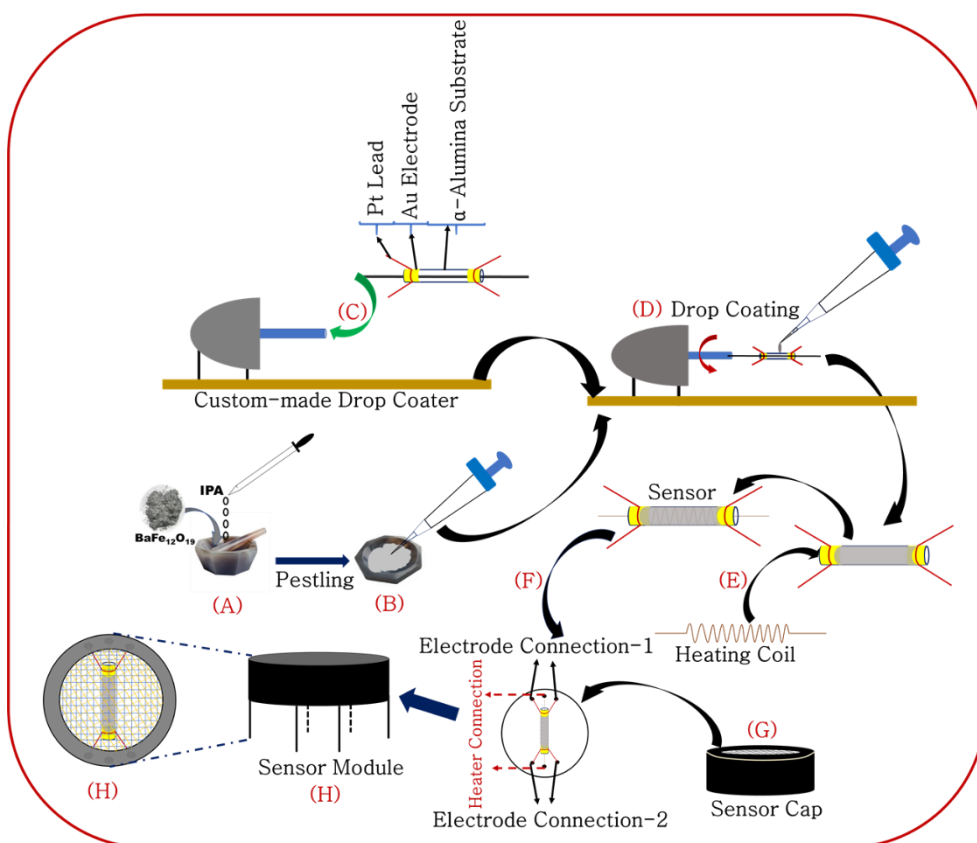


Fig. 2.2. Schematic illustration of the step by step fabrication of $\text{BaFe}_{12}\text{O}_{19}$ nanopowder based Taguchi type chemoresistive sensor: (a) Addition and pestling of $\text{BaFe}_{12}\text{O}_{19}$ nanopowder with IPA in an agate mortar pestle, (b) Pipetting out $5\mu\text{L}$ of the nanopowder paste, (c) Hooking the electroded sensor substrate to the motor of a custom-made drop coater, (d) Drop coating, (e) Insertion of heating coil, (f) Spot-welding the sensor into a socket, (g) Mounting the sensor cap, and (h) Complete sensor module.

2.2.4. Preparation of trace ammonia vapor and sensor measurement setup

After several measurements it was confirmed that the resistance of the as prepared $\text{BaFe}_{12}\text{O}_{19}$ sensor changes in response to trace ammonia gas in a repeatable fashion. Trace ammonia gas of different concentrations, viz. 100 ppm, 50 ppm, 10 ppm, 1 ppm, 0.5 ppm, and 0.2 ppm were prepared by desiccator dilution method. A high concentration of ammonia gas was prepared in a large desiccator. Small volumes of high concentration ammonia gas were syringed out of it and syringed into different smaller desiccators. Thereafter, we waited for 24h to allow homogeneous mixing of the ammonia gas inside the desiccators. Thus, different lower concentrations of ammonia gas, ranging from 0.2 ppm-100 ppm are prepared. The desiccator dilution technique is governed by eq. (1) given as following,

$$V_1 \times C_1 = v_2 \times c_2 \quad (1)$$

where V_1 is the volume of the mother desiccator, C_1 is the concentration of ammonia gas in the mother desiccator, v_2 is the volume of the small desiccator, and c_2 is the concentration of ammonia gas in the small desiccator.

The as prepared sensor was mounted on a sensor base which connects the heating coil to a DC voltage source (Agilent make, E3630A) and the electrodes to a digital multimeter (34461A, Agilent make). Different DC voltages were applied across the heating coil to heat up the sensor to various elevated temperatures. The multimeter measures the resistance of the sensor and the change of it. The sensor was allowed to achieve a stable base resistance before data recording at a particular temperature. A data logging software allied to the multimeter records the change in resistance of the sensor and a graphical user interface allows the visualization of the change. A schematic illustration of the measurement set up is shown in Fig. 2.3.

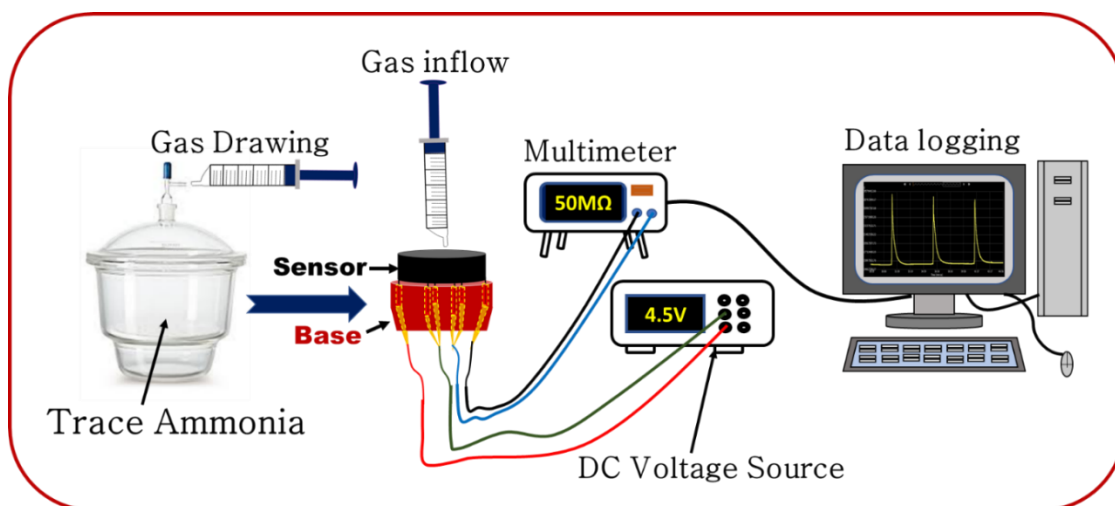


Fig. 2.3. Schematic representation of the BaFe₁₂O₁₉ sensor-based trace ammonia measurement setup

2.2.5. Characterization

X-ray diffraction (XRD), Field emission scanning electron microscopy (FESEM), Transmission electron microscopy (TEM), X-ray photoelectron spectroscopy (XPS), and Brunauer–Emmett–Teller (BET) surface area studies were conducted to have an insight into the microstructure and chemical composition of the sensing material. X-ray diffraction pattern (XRD) was recorded from 10 to 90 (2θ/deg) at a step of 0.05° by using a PANanalytical make diffractometer (X'pert pro) fitted with Cu-K_α target (wavelength ~ 1.5418Å) and nickel filter. FESEM was conducted using a Carl Zeiss make Supra 35 VP microscope. 50mg BaFe₁₂O₁₉

nanopowder was dispersed in acetone by a Rivotek make ultrasonic bath (250W) and 500 μL of the dispersed powder was drop coated on a 3mm x 3mm biological grade glass slide to prepare sample for FESEM. 10 mg $\text{BaFe}_{12}\text{O}_{19}$ nanopowder was dispersed in acetone and 100 μL of the dispersed powder was drop coated on a Ted-Pella make carbon coated copper grid (300mesh) to perform TEM and HRTEM studies. TEM and HRTEM micrographs were recorded by a Tecnai G2 30 ST (FEI) electron microscope operating at 300kV. Energy dispersive X-ray (EDX) study was conducted using the same instrument. XPS study was conducted by a PHI 5000 Versa Probe II scanning XPS microprobe (ULVAC-PHI, U.S) with monochromatic $\text{AlK}\alpha$ ($h\nu = 1486.6 \text{ eV}$) radiations with a beam size of 100 μm and resolution of about 0.7 eV. BET study (NovaWin, Quantachrome Instruments) was conducted to determine the specific surface area of the nanopowder. Thermal imaging of the sensor surface was performed by a Fluke Ti27 infrared camera to determine the accurate operating temperature. Current-Voltage (I-V) measurements were conducted by an Agilent B2901A precision source/measure unit to investigate into the ohmic nature of the prepared sensor. An Agilent 34461A digital multimeter was used to measure the sensitivity of the sensor in terms of change in resistance of the functional material in response to various analytes.

2.3. Results and Discussion

2.3.1. Structural Characterization

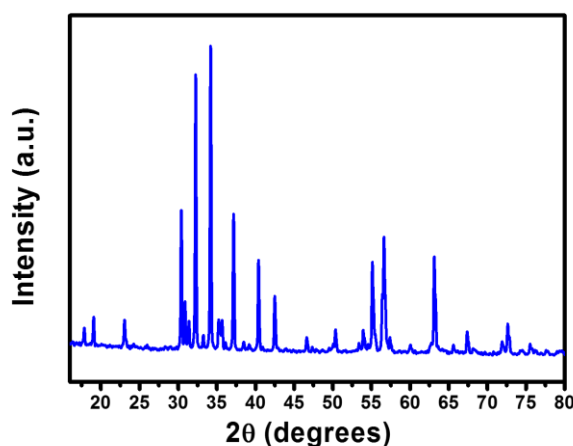


Fig. 2.4. XRD pattern of $\text{BaFe}_{12}\text{O}_{19}$ nanopowder.

The X-ray diffraction pattern of prepared BaFe₁₂O₁₉ nanopowder is shown in Fig. 2.4. It is clear from the XRD pattern that there are several peaks at various 2θ values. All the peaks match well with the standard data of BaFe₁₂O₁₉ (JCPDS-Card no. 39-1433). No extra peak for any impurity was observed. This suggests that the as synthesized material is phase pure BaFe₁₂O₁₉. The average crystallite size was calculated to be 53.05 nm using the Debye Scherer's formula given by,

$$D = \frac{k\lambda}{\beta \cos\theta} \quad (2)$$

where D is crystallite size, k is shape factor, λ is X-ray wavelength (here, 1.54Å), β is the FWHM (full width at half maxima), and θ is the Bragg angle. The sharp and narrow peaks indicate high degree of crystallinity in the as synthesized nanopowder.

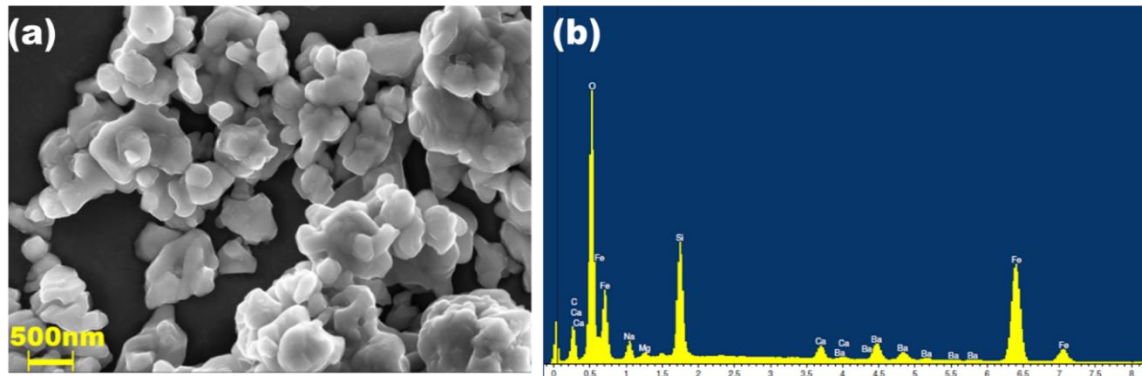


Fig. 2.5. (a) FESEM image, and (b) EDX study of BaFe₁₂O₁₉ nanopowder.

FESEM study was conducted to determine the particle size and morphology of the as prepared BaFe₁₂O₁₉ nanoparticles. Fig. 2.5a shows a typical micrograph at a magnification of 50,000. It appears that the particles are almost spherical in shape and the particle size is in the range of 100-500nm. However, due to agglomeration it is rather difficult to accurately determine the particle size and morphology from this image. Further, the contrast between the particles and the background is appreciable suggesting that the particles are dense in nature. Fig. 2.5b shows the EDX spectrum of the as prepared nanopowder. It clearly shows the presence of Ba, Fe, and O as should be present in barium hexaferrite. The presence of C is attributed to a conducting carbon thin film that was sputtered on the oxide film to avoid charging while carrying out FESEM and peaks of Ca, Mg, Na, and Si originate from the glass slide on which the oxide film was coated for conducting FESEM and EDX.

To have further insight into the microstructure of the $\text{BaFe}_{12}\text{O}_{19}$ nanopowders TEM study was conducted. A typical TEM image is shown in Fig. 2.6a. A marked image of Fig. 2.6a is presented in Fig. 2.6b for the facile understanding of the particle size and morphology. It is clearly observed from Fig. 2.6b that the particles are ovoid in shape and the particle size ranges from 200nm to 500nm. This result corroborates the observations of FESEM study. Fig. 2.6c shows a typical HRTEM image in which a set of parallel crystalline planes are clearly visible. This signifies that the nanoparticles are well crystalline. From the calculations of interplanar distance this plane has been detected as (218) of $\text{BaFe}_{12}\text{O}_{19}$. The inset of Fig. 2.6c shows the selected area diffraction (SAED) pattern of the particle. Large white dots are visible therein signifying highly crystalline nature. Therefore, both HRTEM study, and SAED pattern indicate the growth of highly crystalline $\text{BaFe}_{12}\text{O}_{19}$ nanoparticles. Fig. 2.6d shows the reduced FFT pattern of the HRTEM image in Fig. 2.6c. Presence of three different crystalline planes, viz. (218), (205), and (102) has been observed therein. This further corroborates the crystalline nature of the as prepared $\text{BaFe}_{12}\text{O}_{19}$ nanopowders.

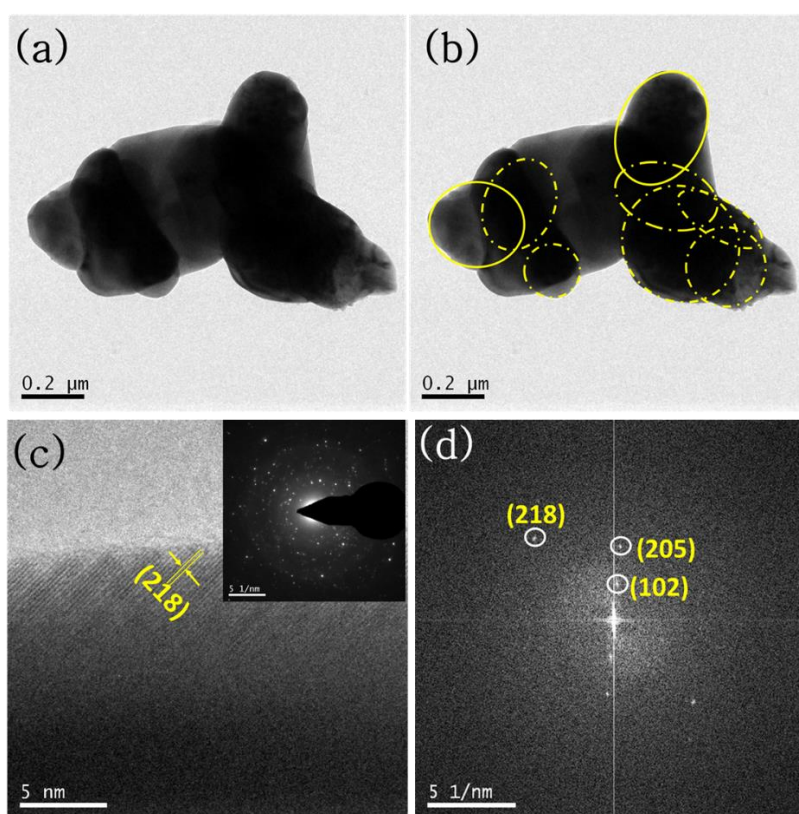


Fig. 2.6. (a) TEM image, (b) Marked TEM image, (c) HRTEM image (inset shows SAED pattern), and (d) Reduced FFT pattern of $\text{BaFe}_{12}\text{O}_{19}$ nanopowder.

XPS study of the BaFe₁₂O₁₉ nanopowders was conducted to determine the ionic states of Ba, Fe, and O. Fig. 2.7a shows the survey scan spectra of the material and reveals the presence of the peaks corresponding to Fe 3s, C 1s, O 1s, Fe 2p, Ba 3d, and O KLL. O KLL is an auger peak. When a photoelectron is emitted from the K shell of an oxygen atom/ion a hole is generated. This hole can be filled up by an electron from the L shell resulting into a release of energy which can further knock out an L shell electron. This auger electron is responsible for the O KLL peak in the XPS spectrum. Adventitious carbon that occurs due to the exposure of the sample to the atmosphere, leads to the generation of C1S peak at ~284.8 eV [40]. Fig. 2.7b shows the XPS spectra of Ba 3d. It was deconvoluted using Gaussian function with sufficient accuracy to yield two peaks at binding energies 778.9eV and 793.84eV which can be attributed to Ba 3d_{5/2} and Ba 3d_{3/2}, respectively [41]. These two peaks are typical of BaO suggesting the presence of Ba²⁺ in the sample. Fig. 2.7c shows the XPS spectra of Fe 2p. This was also deconvoluted using Gaussian function and fitted with two peaks centered at 710.5eV and 723.9eV which correspond to Fe 2p_{3/2}, and Fe 2p_{1/2}, respectively. Further, a satellite peak is present at 718eV which along with the other two peaks indicate the presence of Fe³⁺ state [42]. The O1s peak centered at 529.3eV (ref. Fig. 2.7d) confirms the presence of O²⁻. In summary, XPS study (ref. Fig. 2.7(a-d)) of the BaFe₁₂O₁₉ nanopowder suggests the presence of Ba²⁺, Fe³⁺, and O²⁻.

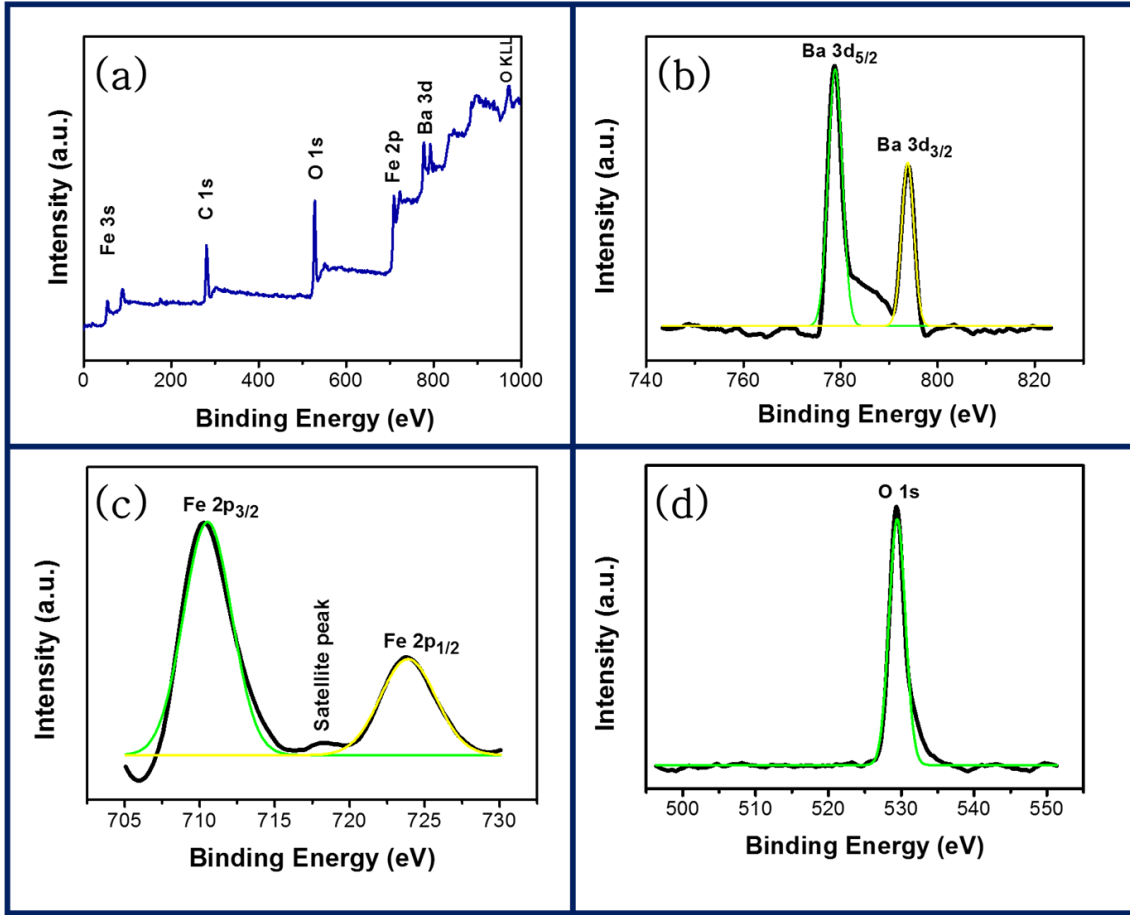


Fig. 2.7. XPS spectra of (a) survey scan, (b) Ba 3d, (c) Fe 2p, and (d) O 1s of BaFe₁₂O₁₉ nanopowder

It is essential for a gas sensor to have a high specific surface area in order to exhibit high sensitivity. High surface area ensures that effective sites of adsorption for the target analyte molecules is also high and this in turn increases sensitivity. BET surface area study of the BaFe₁₂O₁₉ nanopowders were conducted in order to investigate into the specific surface area of the sensor. Fig. 2.8 shows the Langmuir isotherm plot for the sample. The curve is sufficiently linear and therefore could be fitted linearly with high accuracy (Adjusted R² = 0.99931). The slope and Y-axis intercept derived from the linear fitting are 1583 g⁻¹ and 3.8 g⁻¹, respectively. The BET specific surface area is calculated by the following equation,

$$S_{\text{BET}} = \frac{Ns}{V(A+I)a} \quad (3)$$

where, N is Avogadro's number, s is adsorption cross-section of the adsorbing species (here nitrogen), V is molar volume of the adsorbate gas, A is the slope of the fitted straight line, I is the Y-intercept of the fitted straight line, and a is the mass of the adsorbent (here the nanopowder sample). Putting the requisite values in eq. (3), we have S_{BET} = 5.16 m²/g. This is

an appreciable specific surface area indeed and suggests that the sensor should have high sensitivity in general.

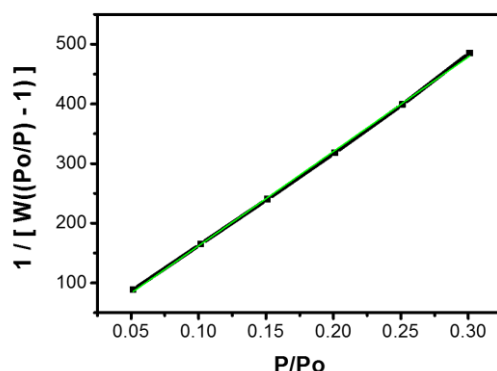


Fig. 2.8. Langmuir isotherm plot of BaFe₁₂O₁₉ nanopowder

2.3.2. Electrical Characterization

A chemoresistive gas sensor should have ohmic properties, i.e. the current flowing through the sensor should always be directly proportional to the voltage applied across it. Current-voltage (I-V) measurements at four different operating temperatures, viz. 270 °C, 300 °C, 350 °C, and 400 °C were conducted to investigate whether or not the BaFe₁₂O₁₉ sensor shows ohmic properties. The corresponding I-V plots (ref. Fig. 2.9) delineates that for all the four temperatures the current vs voltage curve remained perfectly linear. This suggests that the sensor indeed exhibits ohmic properties at elevated operating temperatures. Also, the slopes of the lines corresponding to different temperatures increased with increasing temperature, suggesting decrease in resistance of the sensor with increase in temperature. This is characteristic of a semiconductor metal oxide based chemoresistive sensor.

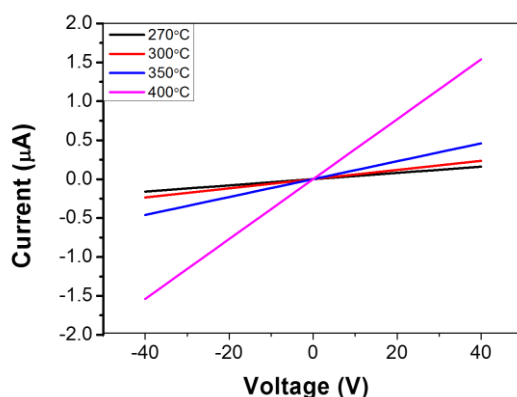


Fig. 2.9. I-V plots of barium hexaferrite sensor at 270 °C, 300 °C, 350 °C, and 400 °C.

2.3.3. Sensitivity Study

Different DC voltages were applied across the heating coil inside the sensor to generate these operating temperatures. Thermal imaging of the sensor surface was conducted to determine the accurate temperature. Fig. 2.10(a-i) show the thermal images of the sensor surface when different voltages ranging from 1.5V-5.5V were applied across the heating coil. It is observed that the surface temperature of the sensor varies from ~70 °C to 390 °C.

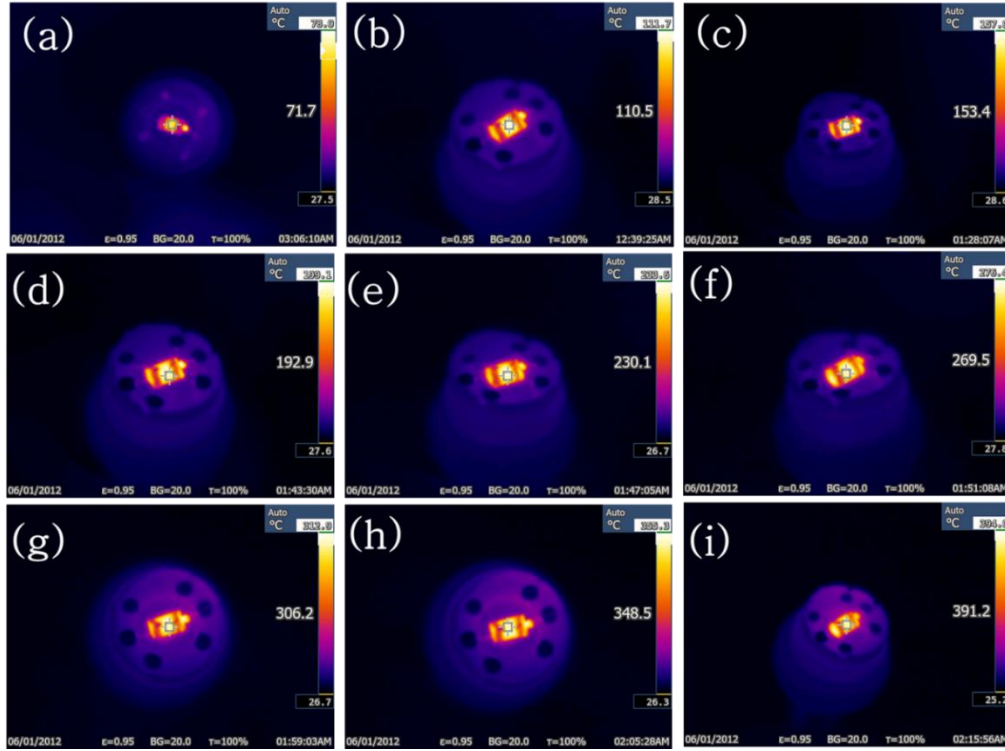


Fig. 2.10. Thermal images of barium hexaferrite sensor surface at (a) 1.5V, (b) 2V, (c) 2.5V, (d) 3V, (e) 3.5V, (f) 4V, (g) 4.5V, (h) 5V, (i) 5.5V.

It is of utmost importance that the operating temperature of a chemoresistive gas sensor is optimized carefully. The as prepared barium hexaferrite sensor showed a p-type response towards ammonia vapor at different operating temperatures ranging from 260 °C to 400 °C. The sensitivity, S of the sensor at a particular operating temperature is given by,

$$S = \frac{R_{NH_3}}{R_{air}} \quad (4)$$

where R_{NH_3} is the resistance of the sensor when exposed to ammonia gas and R_{air} is the resistance of the sensor in air. Fig. 2.11 shows the sensitivity of the sensor towards 1ppm ammonia at different operating temperatures ranging from 260 °C to 400 °C. It is observed that maximum sensitivity is obtained at 306 °C. Below this temperature the number of conduction

band electrons at the sensor surface available for trapping by the atmospheric oxygen is low for an appreciable sensitivity. However, above this temperature the desorption rate of the target analyte supersedes the adsorption rate of it resulting in reduction in sensitivity. Therefore, 306 °C (4.5V across the heating coil, ref. Fig. 2.10) is the optimum operating temperature for the sensor.

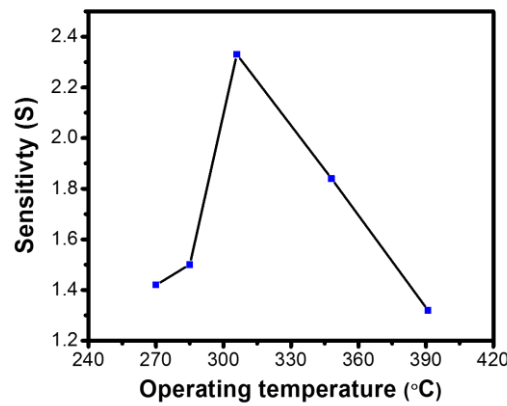


Fig. 2.11. Operating temperature vs Sensitivity plot of the barium hexaferrite sensor

Fig. 2.12a shows the sensor response to 0.2ppm to 100ppm ammonia gas at an operating temperature of 306 °C. It is observed that the sensor response almost saturates at 10ppm and completely saturates at 50ppm. There is virtually no difference in the sensor response to 50ppm and 100 ppm ammonia gas. This might be attributed to the saturation of the active sensing sites on the sensor surface beyond 50ppm of ammonia gas [43]. The sensitivity to 0.2ppm ammonia is 1.46 folds, which is appreciably high. Such high sensitivity might be attributed to the high surface area of the sensor (5.16 m²/g) (ref. Fig. 2.8) as it ensures the presence of myriads of active sites at the sensor surface. As a greater number of ammonia molecules are oxidized, change in resistance increases, thereby increasing the sensitivity.

Alongside high sensitivity complete and fast recovery of the sensor is also important. That would ensure that the sensor can be used to test multiple samples in real time. This necessitates that the target analyte (here ammonia vapor) should be physisorbed and not chemisorbed on the sensor surface. To determine the nature of interaction between the ammonia gas molecules and the sensor surface, Freundlich absorption isotherm model has been employed [44]. Freundlich absorption isotherm equation is given by,

$$S = \alpha C^{\beta} \quad (5)$$

or,
$$\log S = \log \alpha + \beta \log C \quad (6)$$

where S is sensitivity, α is the proportionality constant, C is the concentration of ammonia vapor, and β is the exponent [45]. The value of β determines the nature/strength of interaction between the adsorbent (sensor surface) and the adsorbed species (ammonia vapor). The log-log plot of S vs C was fitted by two straight lines with reasonable accuracy (R^2 values for the blue line and the red line are 0.90 and 0.97, respectively) (ref. Fig. 2.12b). The β values for the blue and the red line derived from the fitting were estimated to be 0.29 and 0.035, respectively. Since, both these β values are less than 1, it is evident that the interaction of ammonia molecules with the sensor surface is weak and physisorption is taking place [46]. Therefore, a complete and reasonably fast recovery may be expected. Also, the linear fitting of the experimental data ensures reversible gas sensing ability [45, 47]. Further, it is observed from Fig. 2.12b that the slope of the blue line is much higher than the red line. This indicates that the ammonia molecules interact relatively strongly with the sensor surface at lower vapor concentrations (≤ 1 ppm). However, this strength of interaction decreases by 1 order of magnitude at higher ammonia concentrations (≥ 10 ppm). This observation corroborates our previous assumption that the sensor surface gets saturated at higher concentrations of ammonia (> 2.18 ppm).

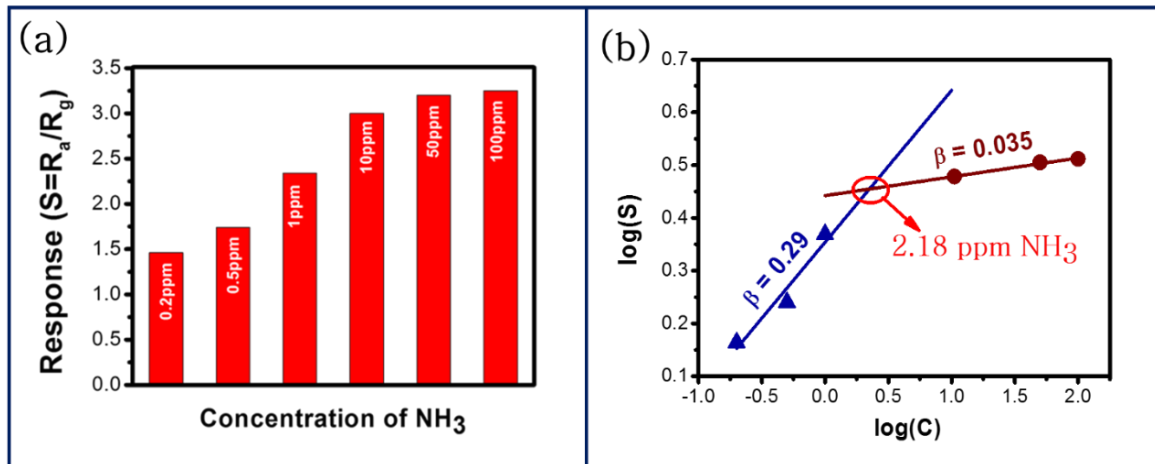


Fig. 2.12. (a) Response (S) of the barium hexaferrite sensor to different trace concentrations (C) of ammonia ranging from 0.2ppm to 100ppm, and (b) fitting of $\log(S)$ vs $\log(C)$ experimental data using Freundlich absorption isotherm equation with linear regression at 306 °C.

Fig. 2.13 shows the dynamic response curve of the sensor to various trace concentrations of ammonia vapor ranging from 0.2 ppm to 1 ppm. The sensor exhibited response of 1.46, 1.74, and 2.34 folds to 0.2 ppm, 0.5 ppm, and 1 ppm ammonia gas, respectively at 306 °C. Clearly, the resolution (difference) in sensitivity towards trace concentrations of ammonia is excellent. It might be recalled that the concentration of ammonia in healthy human breath is 250 ppb and in case of renal diseases it escalates. Therefore, good resolution in sensitivity around the 200 ppb concentration is essential and it is from this point of view that the result shown in Fig. 2.13 is important. Further, to test the repeatability of the sensor three consecutive measurements were taken at each concentration of ammonia, viz. to 0.2 ppm, 0.5 ppm, and 1 ppm.

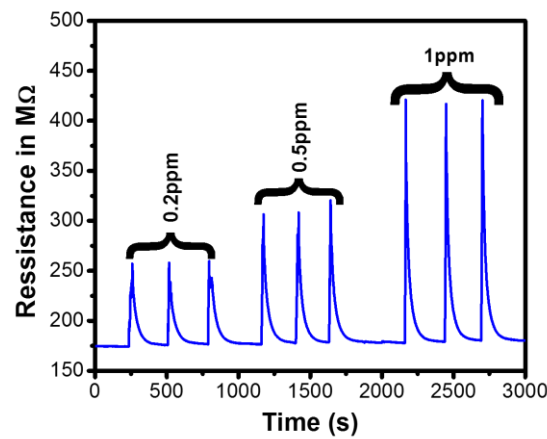


Fig. 2.13. Dynamic response curve of the barium hexaferrite sensor to various trace concentrations of ammonia viz. 0.2 ppm, 0.5 ppm, and 1 ppm at 306 °C.

From Fig. 2.13 it can be clearly seen that the three response peaks corresponding to each concentration match well. This confirms repeatability of the sensor. Further, the sensor exhibits fast response and recovery time, rendering it suitable for real time application. Fig. 2.14 shows the transient conductance curve of barium hexaferrite sensor for 1ppm ammonia vapor at 306 °C. The conduction transient has two parts, viz. response, and recovery. To determine the response and recovery times the conduction transient was fitted by single-site Langmuir adsorption model [48-50]. Accordingly, the transient conductance ($G(t)$) of the sensor for the response process at a constant temperature (306 °C) and at a particular instant t is given by,

$$G(t) = G_0(t) + G_1 e^{\frac{-t}{\tau_{\text{response}}}} \quad (7)$$

where, $G_0(t)$ is the base conductance, and τ_{response} is the response time. Similarly, the transient conductance $G'(t)$ for the recovery process at 306 °C is given by,

$$G'(t) = G'_0(t) + G'_1 \left(1 - e^{\frac{-t}{\tau_{\text{recovery}}}} \right) \quad (8)$$

where, $G'_0(t)$ is the conductance at the end of the response process, and τ_{recovery} is the recovery time of the sensor. The response and recovery times (τ_{response} and τ_{recovery}) obtained by fitting the transient conductance curve by eq. (7) and eq. (8) are $\sim 2.88\text{s}$ and $\sim 39.4\text{s}$, respectively. Such fast response is attributed to high surface area (ref. Fig. 2.8) and elevated operating temperature. Due to high surface area ample number of active sites are present at the sensor surface. Therefore, the molecules of the target analyte (ammonia) do not have to compete with each other for interacting with the surface. Further, the elevated operating temperature boosts the kinetics of reaction between the gas molecules and the surface adsorbed oxygen species. Collectively, the response time is reduced. The fast recovery time however is attributed only to the elevated surface temperature which ensures fast desorption of the reaction products from the surface. Further, it may be recollected that the Freundlich adsorption isotherm modelling of the sensor response (ref. Fig. 2.12b) predicted a complete and fast recovery. This is exactly what has been observed here.

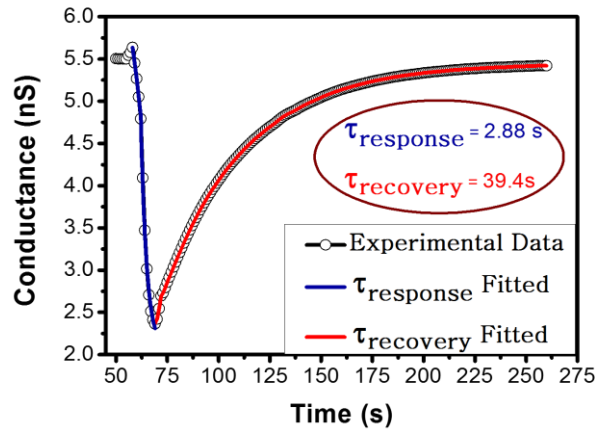


Fig. 2.14. Fitting of transient conductance curve of barium hexaferrite sensor for 1ppm ammonia vapor at 306 °C using single-site Langmuir adsorption model

The performance study of a sensor is incomplete without the discussion of cross-sensitivity to other gases than the target analyte. The choice of interfering gases while measuring cross-sensitivity should be based on the final application intended for the sensor. The targeted application of this sensor is detection of kidney malfunction/ renal diseases by exhaled breath analysis. Therefore, cross-sensitivity towards other major interfering exhaled breath gases and volatiles should be measured. Hence, we have chosen 1ppm acetone vapor, 1ppm ethanol vapor, and saturated moisture vapor. These concentrations have been chosen according to their

average concentrations in healthy human breath. Fig. 2.15 shows the cross-sensitivity plot of the sensor. It is observed that as compared to the response of the sensor towards 1ppm ammonia, the sensitivity towards 1ppm acetone vapor, 1ppm ethanol vapor, and saturated moisture vapor are negligible. This shows the excellent selectivity of the sensor towards trace ammonia.

The ammonia molecules and the other interfering molecules react with the surface adsorbed oxygen species and the energy of the reactions is provided by the surface of the sensor. Evidently, different energy is required for different molecules. At the optimized operating temperature of 306 °C, the polycrystalline barium hexaferrite nanoparticles at the sensor surface possess a particular energy. According to quantum mechanics, the reaction requiring energy closest to this surface energy will be preferred. Plausibly, the energy requirement for the degradation of ammonia molecules by the surface adsorbed oxygen species matches best with the surface energy of the sensor at 306 °C. This could be the prime reason for the observed selectivity. Secondly, the ammonia molecules can access most of the active sites at the surface and at the surface pores owing to its small size. Acetone and ethanol molecules are larger in size, hence the active sites available to those are lesser. This can be another plausible reason for the selectivity of the sensor towards ammonia. Water molecules do not absorb well on surfaces having temperature more than 100 °C and that explains the reason for inferior humidity sensitivity of the sensor at 306 °C.

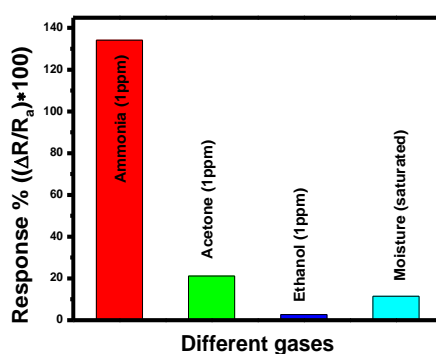


Fig. 2.15. Cross-sensitivity plot of barium hexaferrite sensor towards other major breath volatiles at 306 °C.

Fig. 2.16 shows the stability plot of the sensor for 3months (90 days). It is observed that the sensitivity of the sensor towards 1ppm ammonia remains virtually same over this period of time. Such appreciable stability further bolsters its suitability for plausible commercial use.

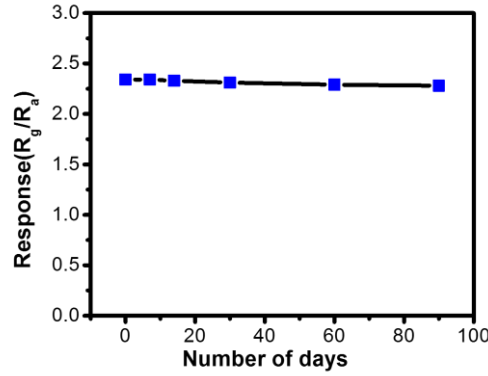
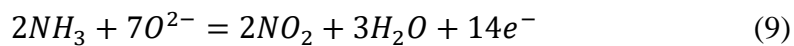


Fig. 2.16. Long-term stability graph of the barium hexaferrite sensor.

2.3.4. Sensing Mechanism

Having discussed about the excellent sensing behavior of the barium hexaferrite sensor towards trace ammonia, it is only ordinate that a plausible sensing mechanism now be proposed. When the temperature of the sensor is stabilized at 306 °C some of the electrons trapped in the donor type defect bands generated during the synthesis and consequent annealing of the sensor, jump to the conduction band of the material. The conductivity of the sensor increases as a result. The ambient atmosphere is fraught with myriads of oxygen which traps the conduction electrons at the sensor surface owing to its high electron affinity. As a result, an electron depletion layer (EDL) is developed at the sensor surface, thereby increasing the resistance of the sensor. Eventually, the sensor attains steady state resistance which is termed as the base resistance of the sensor or resistance in air (R_a, ref. [eq. \(4\)](#)). It may be recollected from [eq. \(4\)](#) that all the sensitivity calculations are conducted on the basis of this base resistance.

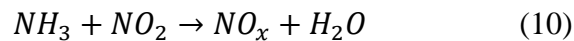
When ammonia gas molecules are injected onto the sensor surface, they are oxidized by the surface adsorbed negatively charged oxygen species (O²⁻). Taking cue from the existing literature [51,52] the interaction can be summarized as follows,



It is well known that NO₂ has a very high electron affinity. Therefore, the NO₂ molecules produced by the oxidation of ammonia molecules trap some electrons from the conduction band of the electron and get adsorbed on the sensor surface (ref. [Fig. 2.17](#) (STEP-1)). Therefore, the resistance of the sensor starts to increase (ref. [Fig. 2.13](#)).

As a greater number of ammonia molecules are oxidized at the sensor surface increasing number of NO₂ molecules are formed and gradually adsorb at the sensor surface trapping more conduction electrons from the sensor surface thereby, progressively increasing the resistance of the sensor (ref. Fig. 2.13). However, the NO₂ molecules have to compete with the atmospheric oxygen molecules to have a share of the conduction electrons and to get adsorbed at the sensor surface. At this stage ammonia is continually oxidized at sensor surface generating fresh NO₂ molecules and therefore, the local concentration of NO₂ molecules in the close proximity of the sensor surface surpasses the oxygen molecule concentration there. These triggers preferred adsorption of NO₂ molecules over oxygen molecules on the sensor surface. Even then, the oxidation of the ammonia molecules is a comparatively faster process. Therefore, the rate of generation of NO₂ molecules is faster than the rate of its adsorption at the sensor surface. This leads to the accumulation of NO₂ molecules near the sensor surface (ref. Fig. 2.17(STEP-2)).

Eventually, a considerable number of NO₂ molecules accumulate near the sensor surface, thereby creating a cloud/multilayer of NO₂ molecules there. Any ammonia molecule that is now injected onto the sensor head cannot directly interact with the sensor surface. It has to pass through the NO₂ multilayer. Incidentally, NO₂ is an oxidizing gas. Therefore, it oxidizes the ammonia molecules passing through it as follows,



These NO_x molecules gradually get oxidized to NO₂ as they percolate through the NO₂ multilayer (ref. Fig. 2.17(STEP-3)). Meanwhile adsorption of NO₂ molecules on the sensor surface continues resulting in further increase in resistance until there are no more active surface state to access. When the ammonia flow on the sensor head is stopped, the NO₂ molecules accumulated near the surface are desorbed first. Then the surface adsorbed NO₂ molecules desorb from the sensor surface leaving the electrons that they trapped to the conduction band. This is the recovery phase where the resistance of the sensor decreases again until the base resistance is reached (ref. Fig. 2.17(STEP-4)).

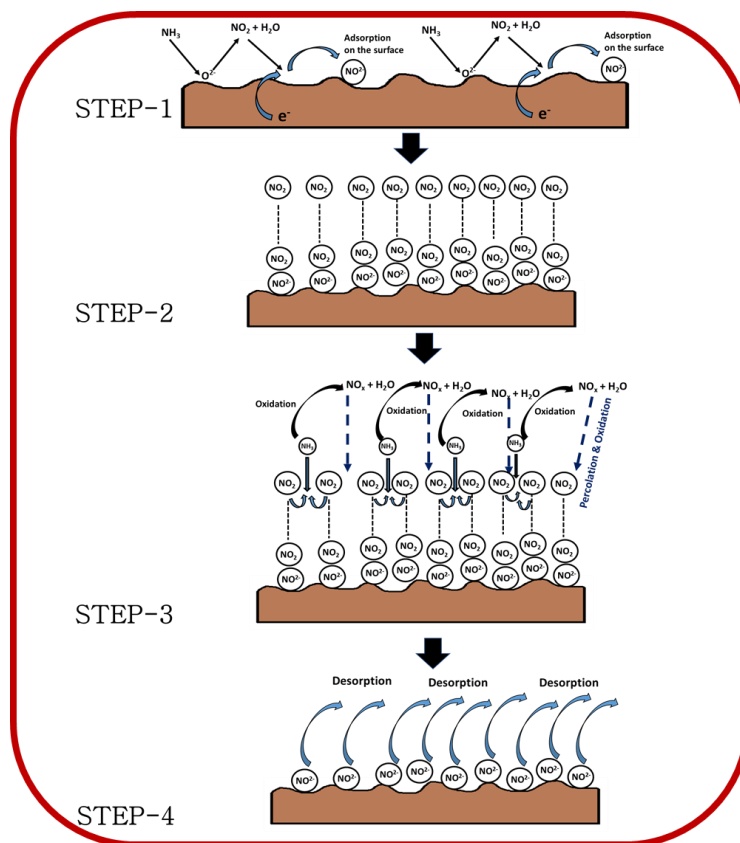


Fig. 2.17. Schematic illustration of the ammonia sensing mechanism of barium hexaferrite sensor.

2.4. Conclusion

In summary, we have achieved trace ammonia sensing capability with high sensitivity and selectivity using barium hexaferrite nanoparticles ($BaFe_{12}O_{19}$) synthesized by a facile solid-state route. The developed sensor is p-type in nature and showed high sensitivity to different trace concentrations of ammonia vapor, viz. ~ 2.34 folds to 1ppm ammonia vapor, and ~ 1.46 folds to 0.2ppm ammonia. It also exhibited fast response (2.88s) and recovery times (39.4s) along with negligible cross-sensitivities towards other major interfering breath volatiles, viz. acetone, ethanol, and saturated moisture vapor. Such excellent sensing properties were attributed to high specific surface area, optimized operating temperature, and small size of ammonia molecule. In totality the superior sensing properties of the prepared sensor towards trace ammonia makes it a promising candidate for the detection of renal diseases by exhaled breath analysis.

2.5. References

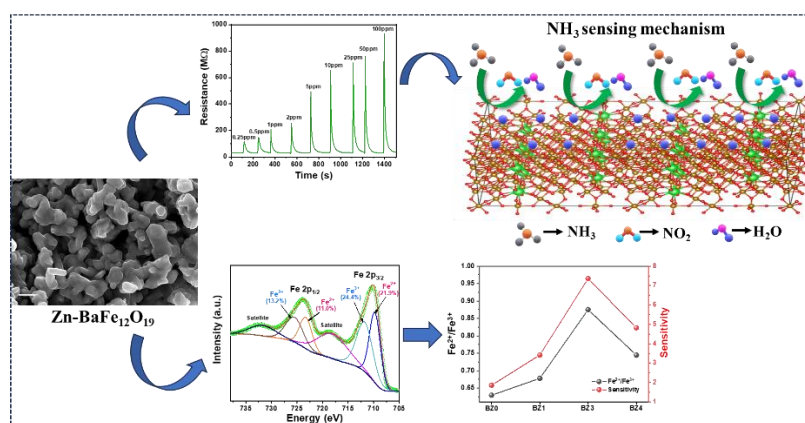
- [1] M. Giardina, and S. V. Olesik, Application of low-temperature glassy carbon coated macrofibers for solid-phase microextraction analysis of simulated breath volatiles, *Anal. Chem.* 75 (2003) 1604-1614.
- [2] M. Phillips, and J. Greenberg, Method for the collection and analysis of volatile compounds in the breath, *J. Chromatogr. Biomed. Appl.* 564 (1991) 242-249.
- [3] J. Schmutzhard, J. Rieder, M. Deibl, I. M. Schwentner, S. Schmid, P. Lirk, I. Abraham, and A. R. Gunkel, Pilot study: volatile organic compounds as a diagnostic marker for head and neck tumors, *Head Neck* 30 (2008) 743-749.
- [4] A. Boschetti, F. Biasioli, M. van Opbergen, C. Warneke, A. Jordan, R. Holzinger, P. Prazeller, T. Karl, A. Hansel, and W. Lindinger, PTR-MS real time monitoring of the emission of volatile organic compounds during postharvest aging of berry fruit, *Postharvest Biol. Technol.* 17 (1999) 143-151.
- [5] S. M. Abbott, J. B. Elder, P. Spanel, and D. Smith, Quantification of acetonitrile in exhaled breath and urinary headspace using selected ion flow tube mass spectrometry, *Int. J. Mass spectrom.* 228 (2003) 655-665.
- [6] D. Vaira, J. Holton, C. Ricci, C. Basset, L. Gatta, F. Perna, A. Tampieri, and M. Miglioli, *Helicobacter pylori* infection from pathogenesis to treatment: a critical reappraisal, *Alimentary Pharmacol. Therapeut.*, 16((Suppl. 4)) (2002) 105-113.
- [7] I. O. Essiet, Diagnosis of kidney failure by analysis of the concentration of ammonia in exhaled human breath, *J. Emerg. Trends Eng. Appl. Sci.* 4 (2013) 859-862.
- [8] D. J. Kearney, T. Hubbard, and D. Putnam, Breath ammonia measurement in *Helicobacter pylori* infection, *Dig. Dis. Sci.* 47 (2002) 2523-2530.
- [9] S. Das, and M. Pal, Review—Non-Invasive Monitoring of Human Health by Exhaled Breath Analysis: A Comprehensive Review, *J. Electrochem. Soc.* 167 (2020) 037562.
- [10] A. T. Günter, M. Righettoni, and S. E. Pratsinis, Selective sensing of NH_3 by Si doped $\alpha\text{-MoO}_3$ for breath analysis, *Sens. Actuators B* 223 (2016) 266-273.
- [11] J. M. Sanchez, and R. D. Sacks, GC analysis of human breath with a series coupled column ensemble and a multibed sorption trap, *Anal. Chem.* 75 (2003) 2231-2236.
- [12] H. Lord, Y. F. Yu, A. Segal, and J. Pawliszyn, Breath analysis and monitoring by membrane extraction with sorbent interface, *Anal. Chem.* 74 (2002) 5650-5657.
- [13] A. Amann, G. Poupart, S. Telser, M. Ledochowski, A. Schmid, and S. Mechtcheriakov, Applications of breath gas analysis in medicine, *Int. J. Mass Spectrom.* 239 (2004) 227-233.
- [14] T. Karl, P. Prazeller, D. Mayr, A. Jordan, J. Rieder, R. Fall, and W. Lindinger, Human breath isoprene and its relation to blood cholesterol levels: new measurements and modeling. *J. Appl. Physiol.* 91 (2001) 762-770.
- [15] P. Spanel, S. Davies, and D. Smith, Quantification of breath isoprene using the selected ion flow tube mass spectrometric analytical method, *Rapid Commun. Mass Spectrom.* 13 (1999) 1733-1738.
- [16] A. M. Diskin, P. Spanel, and D. Smith, Time variation of ammonia, acetone, isoprene and ethanol in breath: A quantitative SIFT-MS study over 30 days, *Physiol. Meas.* 24 (2003) 107-119.
- [17] P. Gouma, K. Kalyanasundaram, X. Yun, M. Stanacevic, and L. Wang, Nanosensor and breath analyzer for ammonia detection in exhaled human breath, *IEEE Sensors J.* 10 (2010) 49-53.

- [18] G. Jodhani, J. Huang, and P. Gouma, Flame spray synthesis and ammonia sensing properties of pure α - MoO_3 nanosheets, *J. Nanotechnol.* 2016 (2016) 7016926_1-7016926_5.
- [19] A. K. Prasad, D. J. Kubinski, and P. I. Gouma, Comparison of sol-gel and ion beam deposited MoO_3 thin film gas sensors for selective ammonia detection, *Sens. Actuators B* 93 (2003) 25-30.
- [20] D. Kwak, M. Wang, K. J. Koski, L. Zhang, H. Sokol, R. Maric, and Y. Lei, Molybdenum trioxide (α - MoO_3) nanoribbons for ultrasensitive ammonia (NH_3) gas detection: integrated experimental and density functional theory simulation studies, *ACS Appl. Mater. Interfaces* 11 (2019) 10697-10706.
- [21] C. Zamani, O. Casals, T. Andreu, J. R. Morante, and A. Romano-Rodriguez, Detection of amines with chromium-doped WO_3 mesoporous material, *Sens. Actuators B* 140 (2009) 557-562.
- [22] G. Jeevitha, R. Abhinayaa, D. Mangalaraj, N. Ponpandian, P. Meena, V. Mounasamy, and S. Madanagurusamy, Porous reduced graphene oxide (rGO)/ WO_3 nanocomposites for the enhanced detection of NH_3 at room temperature, *Nanoscale Adv.* 1 (2019) 1799-1811.
- [23] H. Wu, Z. Ma, Z. Lin, H. Song, S. Yan, and Y. Shi, High-sensitive ammonia sensors based on tin monoxide nanoshells, *Nanomaterials (Basel)* 9 (2019) E388 (1-9).
- [24] D. Zhang, C. Jiang, and Y. Sun, Room-temperature high-performance ammonia gas sensor based on layer-by-layer self-assembled molybdenum disulfide/zinc oxide nanocomposite film, *J. Alloys Compd.* 698 (2017) 476-483.
- [25] N. V. Hieu, V. V. Quang, N. D. Hoa, and D. Kim, Preparing large-scale WO_3 nanowire-like structure for high sensitivity NH_3 gas sensor through a simple route, *Curr. Appl. Phys.* 11 (2011) 657-661.
- [26] M. D'Arienzo, L. Armelao, C. M. Mari, S. Polizzi, R. Ruffo, R. Scotti, and F. Morazzoni, Macroporous WO_3 thin films active in NH_3 sensing: role of the hosted Cr isolated centers and Pt nanoclusters, *J. Am. Chem. Soc.* 133 (2011) 5296-5304.
- [27] Y. M. Zhao, and Y. Q. Zhu, Room temperature ammonia sensing properties of $\text{W}_{18}\text{O}_{49}$ nanowires, *Sens. Actuators B* 137 (2009) 27-31.
- [28] T. A. Ho, T. S. Jun, and Y. S. Kim, Material and NH_3 -sensing properties of polypyrrole coated tungsten oxide nanofibers, *Sens. Actuators B* 185 (2013) 523-529.
- [29] S. Li, P. Lin, L. Zhao, C. Wang, D. Liu, F. Liu, P. Sun, X. Liang, F. Liu, X. Yan, Y. Gao, and G. Lu, The room temperature gas sensor based on Polyaniline@flower-like WO_3 nanocomposites and flexible PET substrate for NH_3 detection, *Sens. Actuators B* 259 (2018) 505-513.
- [30] X. Wang, D. Gu, X. Li, S. Lin, S. Zhao, M. N. Rumyantseva, and A. M. Gaskov, Reduced graphene oxide hybridized with WS_2 nanoflakes based heterojunctions for selective ammonia sensors at room temperature, *Sens. Actuators B* 282 (2019) 290-299.
- [31] E. Singh, M. Meyyappan, and H. S. Nalwa, Flexible graphene-based wearable gas and chemical sensors, *ACS Appl. Mater. Interfaces* 9 (2017) 34544-34586.
- [32] D.H. Choi, S.Y. An, S.W. Lee, I. Shim, and C.S. Kim, Site occupancy and anisotropy distribution of Al substituted Ba-ferrite with high coercivity, *Phys. Stat. Sol.* 241(7) (2004) 1736-1739.
- [33] M. C. Dimri, S. C. Kashyap, and D.C. Dube, Electrical and magnetic properties of barium hexaferrite nanoparticles prepared by citrate precursor method, *Ceram. Int.* 30 (2004) 1623-1626.
- [34] D. Sriram, R.L. Snyder, and V.R.W. Amarakoon, Anisotropic thermal expansion of barium hexaferrite using dynamic high-temperature X-ray diffraction, *Mater. Res. Soc.* 15(6) (2000) 1349-1353.
- [35] H. Kojima in: E.P. Wohlfarth (Ed.), *Ferromagnetic Materials*, 1982, p. 305. North-Holland, Amsterdam.

- [36] R.A. McCurrie, *Ferromagnetic Materials: Structure and Properties*, Academic Press, London, UK, 1994.
- [37] [N. Dishovski](#), [A. Petkov](#), [I. Nedkov](#), and [I. Razkazov](#), Hexaferrite contribution to microwave absorbers characteristics, *IEEE Trans. Magn.* 30(2) (1994) 969-971.
- [38] S. E. Jacobo, L. Civale, and M. A. Blesa, Evolution of the magnetic properties during the thermal treatment of barium hexaferrite precursors obtained by coprecipitation from barium ferrate (VI) solutions, *J. Magn. Magn. Mater.* 260 (2003) 37-41.
- [39] A.T. Wise, J. Rocks, D.E. Laughlin, M.E. McHenry, S.D. Yoon, C. Vittoria, and V.G. Harris, M-type barium hexaferrite synthesis and characterization for phase shifter applications, *J. Appl. Phys.* 109 (2011) 07E535-1-4.
- [40] J. Liu, Y. Mao, E. Lan, D. R. Banatao, G. J. Forse, J. Lu, H. Blom, T. O. Yeates, B. Dunn, and J. P. Chang, Generation of oxide nanopatterns by combining self-assembly of S-Layer proteins and area-selective atomic layer deposition, *J. Am. Chem. Soc.* 130 (2008) 16908–16913.
- [41] L. Wang, J. Zhang, Q. Zhang, N. Xu, and J. Song, XAFS and XPS studies on site occupation of Sm^{3+} ions in Sm doped M-type $\text{BaFe}_{12}\text{O}_{19}$, *J. Magn. Magn. Mater.* 377 (2015) 362–367.
- [42] T. Fujii, F. de Groot, G. A. Sawatzky, F. C. Voogt, T. Hibma, and K. Okada, In situ XPS analysis of various iron oxide films grown by NO_2 -assisted molecular-beam epitaxy, *Phys. Rev. B: Condens. Matter Mater. Phys.* 59 (1999) 3195–3202.
- [43] D.R. Patil, L.A. Patil, and D.P. Amalnerkar, Ethanol gas sensing properties of Al_2O_3 -doped ZnO thick film resistors, *Bull. Mater. Sci.* 30 (2007) 553-559.
- [44] S. Chakraborty, and M. Pal, Highly selective and stable acetone sensor based on chemically prepared bismuth ferrite nanoparticles, *J. Alloys Compd.* 787 (2019) 1204-1211.
- [45] M. Sinha, R. Mahapatra, B. Mondal, T. Maruyama, and R. Ghosh, Ultra-fast and reversible gas sensing properties of ZnO nanowire arrays grown by hydrothermal technique, *J. Phys. Chem. C* 120(5) (2016) 3019-3025.
- [46] S.M. Ahmed, Md R. Taha, and O.M.E. Taha, Kinetics and isotherms of dichlorodiphenyltrichloroethane (DDT) adsorption using soil-zeolite mixture, *Nanotechnol. Environ. Eng.* 3:4 (2018) 1-20.
- [47] S. Chakraborty, and M. Pal, Improved sensitivity of CdS nanoparticles by virtue of calcium doping: Promising candidate for monitoring alcohol in exhale human breath, *Mater. Des.* 126 (2017) 18-28.
- [48] N. M. Vuong, N. D. Chinh, B. T. Huy, and Y. Lee, CuO-decorated ZnO hierarchical nanostructures as efficient and established sensing materials for H_2S gas sensors, *Sci. Rep.* 6: 26736 (2016) 1-13.
- [49] D. Majumder, A. Datta, M. K. Mitra, and S. Roy, Kinetic analysis of low concentration CO detection by Au-loaded cerium oxide sensors, *RSC Adv.* 6 (2016) 92989-92995.
- [50] S. Chakraborty, and M. Pal, Highly efficient novel carbon monoxide gas sensor based on bismuth ferrite nanoparticles for environmental monitoring, *New J. Chem.* 42 (2018) 7188-7196.
- [51] Y. Takao, K. Miyazaki, Y. Shimizu, and M. Egashira, High ammonia sensitive semiconductor gas sensors with double-layer structure and interface electrodes, *J. Electrochem.* 141 (1994) 1028–1034.
- [52] G. K. Mani, and J. B. B. Rayappan, A highly selective room temperature ammonia sensor using spray deposited zinc oxide thin film, *Sens. Actuators B* 183 (2013) 459– 466.

CHAPTER 3

Enhanced ammonia sensing performance of barium hexaferrite enabled through Zn doping: Mechanistic study considering modulation of $\text{Fe}^{2+}/\text{Fe}^{3+}$ ratio and oxygen vacancy



This work is published in “Sensors and Actuators B: Chemical 406 (2024) 135358”

3.1. Introduction

Rapid development of industries has resulted in wide usage of ammonia (NH_3), a toxic gas, in production of fertilizers, refrigerants, textile and food industries etc. [1,2]. According to the report of occupational safety and health administration (OSHA), threshold limit of exposure concentration of NH_3 for human being is 25 ppm within 8 h and 35 ppm within 15 mins. Prolonged exposure to NH_3 , can cause irritation of skin, eyes, lung swelling, dyspnea and even cancer [3–6]. On the other hand, NH_3 in human exhaled breath is acknowledged as the key breath-biomarker for impaired kidney function. Elevated level in exhaled breath is the indicative of hepatic dysfunction, halitosis and bacterial infection by *Helicobacter pylori* [7–9]. In exhaled-breath of healthy individuals, NH_3 concentration varies from 50-1500 ppb [10]. Whereas, in patients with end stage renal disease (ESRD) exhaled NH_3 level rises to ~5 ppm. Breath analysis could play key role in early detection of disease by recognizing abnormal pattern of exhaled NH_3 . Therefore, selective monitoring of ammonia in patients has become a necessity for real-time health monitoring [11–13]. Various methods viz. gas chromatography mass spectroscopy (GC–MS), selected ion flow tube mass spectrometry (SIFT-MS) and photoacoustic laser spectroscopy (LPAS) have been employed to detect NH_3 gas. However, these systems are bulky, confined in laboratory facility and require experienced manpower that makes them impractical for daily use [14–17]. Thus, metal oxide semiconductors (MOSs) based chemiresistive sensors have gained attention for its low-cost operating system, feasibility and durability [18]. Several MOSs viz, SnO_2 , ZnO , NiO , Co_3O_4 , WO_3 , CuO have been reported for gas detection [19–25]. These materials have several drawbacks such as low selectivity, effect of humidity and inability to detect low concentration of gas. Hence, demand for alternative materials for MOS based chemiresistive gas sensing is rising.

Ferrites have gained recognition for their extensive applications in magnetic materials, photocatalytic activity for degradation of dyes, water splitting for hydrogen generation, water purification etc. M-type barium hexaferrite ($\text{BaFe}_{12}\text{O}_{19}$) is new in sensing field with hardly any detailed report on its NH_3 sensing behaviour [26]. Amidst effective strategies, doping with suitable metals is identified as fruitful way to enhance stability and gas response of the sensing materials. Wang et al. synthesized Zn-doped NiO sensor with by hydrothermal controllable route for enhanced ammonia sensing [27]. Yang et al. prepared Zn doped MoO_3 nanobelts for effective improvement of ethanol response [28]. Hemalatha et al. have reported Zn doping in CuO plays key role in enhancement of acetone sensing [29]. Even though there are reports of

Zn doping to enhance magnetic properties in ferrite materials [30], substitution of Fe^{3+} with Zn^{2+} was seldom used as an approach to influence oxygen defects in $\text{BaFe}_{12}\text{O}_{19}$ to enhance gas sensing property.

In this work, we are reporting ammonia sensing property of solid-state route-derived Zn doped $\text{BaFe}_{12}\text{O}_{19}$ samples. Zn was used as strategic dopant in the $\text{BaFe}_{12}\text{O}_{19}$ to alter $\text{Fe}^{2+}/\text{Fe}^{3+}$ ratio and modulate the oxygen defects. The substitution of Fe^{3+} by Zn^{2+} proves to be beneficial in improving NH_3 sensing performance and effectively reducing operating temperature of the host material. NH_3 response, response/recovery time and selectivity of the as-prepared sensors (BZ3) was observed to be improved after doping and proved to be superior than previously reported ferrite based NH_3 sensors. Table 3.1 displays the comparison data of NH_3 sensing properties of different MOS based sensors in reports. The mechanism behind improved gas response has been discussed and confirmed with subsequent X-ray photoelectron spectroscopy (XPS) analysis. The sensor has been employed to detect wide range of NH_3 concentration, which opens up its application in human exhaled breath analysis for health monitoring and trace NH_3 detection in ambient to ensure quality of life.

Table 3.1 Comparison of ammonia sensing performance between Zn doped barium hexaferrite base sensor and other ammonia sensors reported in literature.

Material	Operating temp. (°C)	t_{response} (s)	t_{recovery} (s)	Lower detection limit	Response /Conc. (ppm)	Ref.
ZnO	250	3-15s	5-14s	-	80%/ 3 ppm	[31]
SnS/CQD	RT	7s	103s	100 ppb	5.72/ 10 ppm	[32]
$\text{SnO}_2@\text{MoS}_2$	25	6s	121s		8.6/ 100 ppm	[33]
TiO_2	RT	30.3s	31.0s	0.1 ppm	~7.8/ 5 ppm	[34]
NiO-PANI	RT	149s	257s	-	43%/ 10 ppm	[35]
$\text{Ti}_3\text{C}_2\text{T}_x/\text{V}_2\text{O}_5/\text{CuWO}_4$	RT	10s	5s	0.3 ppm	6.4/ 5 ppm	[36]
Ce- TiO_2	25	25s	272s	140 ppb	23.99/ 20 ppm	[37]
rGO/ WO_3	RT	18s	24s	1.14 ppm	8.03/ 40 ppm	[38]
$\text{BaFe}_{12}\text{O}_{19}$	300	2.88s	39.40s	0.2 ppm	2.34/ 1 ppm	[26]
Zn- $\text{BaFe}_{12}\text{O}_{19}$	250	2.66s	35.25s	150 ppb	7.36/ 1 ppm	Current work

For p-type gas sensors response $S = R_{\text{gas}}/R_{\text{air}}$, For n-type gas sensors response, $S\% = ((R_{\text{air}} - R_{\text{gas}})/R_{\text{air}}) * 100$

3.2. Experimental section

3.2.1. Materials and reagents

Barium carbonate (BaCO_3), iron (II) oxide (Fe_2O_3), zinc nitrate hexahydrate ($\text{Zn}(\text{NO}_3)_2 \cdot 6\text{H}_2\text{O}$), acetone ($\text{C}_3\text{H}_6\text{O}$) were purchased from Merck India and used without further purification.

3.2.2. Synthesis of Zn doped $\text{BaFe}_{12}\text{O}_{19}$ samples

Pure and Zn-doped $\text{BaFe}_{12}\text{O}_{19}$ was synthesized by solid state route. BaCO_3 and Fe_2O_3 of molar ratio 1:6 were mixed well in a mortar pestle using acetone for 1 hr. until both the powders were homogeneously mixed. $\text{Zn}(\text{NO}_3)_2 \cdot 6\text{H}_2\text{O}$ was added to the mixture to prepare Zn (wt%=1%, 2%, 3%, 4%) doped $\text{BaFe}_{12}\text{O}_{19}$ samples. After grinding thoroughly for 1 hr, the powder was pre-heated in a furnace at 600 °C temperature for 1 hr to achieve a precursor compound which is then pestled again with acetone for about half an hour. Finally, the mixture is calcined at 1000 °C for 1 hr. The as-synthesized Zn (wt%=0%, 1%, 2%, 3%, 4%) doped $\text{BaFe}_{12}\text{O}_{19}$ samples were labelled as BZ0, BZ1, BZ2, BZ3, BZ4. The samples were dark brown in colour and were taken for further characterization. The synthesis procedure is illustrated in Fig. 3.1.

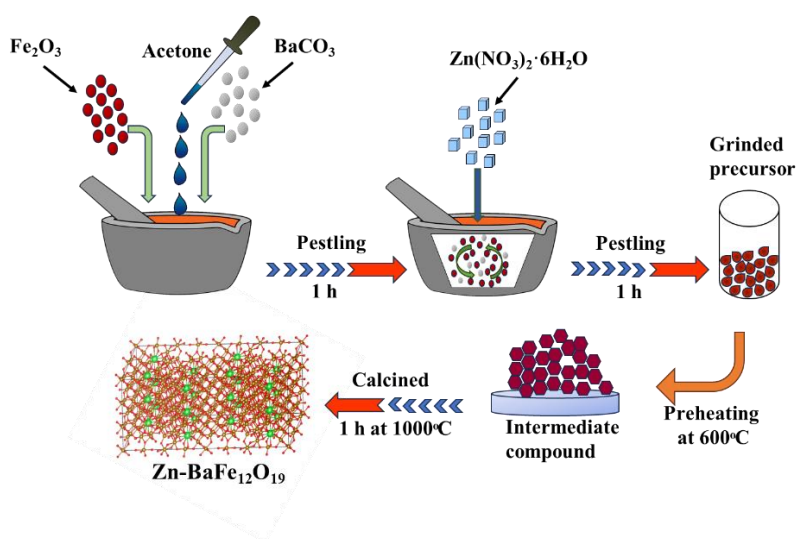


Fig. 3.1. Schematic diagram of solid-state synthesis of Zn-doped $\text{BaFe}_{12}\text{O}_{19}$.

3.2.3. Characterization of materials

Crystallographic structure of as-prepared materials was conducted using X-ray diffraction (XRD) instrument (X'pert Pro MPD XRD PANalytical diffractometer) with nickel filtered $\text{Cu-K}\alpha_1$ radiation ($\lambda=0.15404\text{nm}$). The morphology of the samples was examined using field-emission scanning electron microscopy (FESEM) (Carl Zeiss make Supra 35 VP microscope)

operated with an accelerating voltage of 10 kV and high-resolution transmission electron microscopy (HRTEM) (Tecnai G² 30ST (FEI) operating at 300kV. For elemental characterization of as-prepared samples, energy dispersive X-ray spectroscopy (EDS) equipped with FESEM was used. To understand chemical state, X-ray photoelectron spectroscopy (XPS) was conducted (PHI 5000 Versa Probe II scanning XPS microprobe ULVAC-PHI, U.S) with monochromatic AlK α (h ν =1486.6 eV) source and C 1s peak at 284.6 eV was used as an internal standard. The optical band gap of the materials was measured using UV-vis-NIR spectrometer (Shimadzu, UV-3600). Room temperature photoluminescence (PL) spectra was performed using Horiba FluoroMax-4 spectrometer. The current-voltage characteristics of the materials were measured using Agilent source meter B2901A. Agilent 34461A digital multimeter was used for the gas sensing measurements. For measurement of relative humidity (%RH) Bombay engineering company made relative humidity indicator (model: 2D/RH-100C) was used.

3.2.4. Fabrication of prototype chemiresistive sensor

The gas sensors were fabricated by drop-coating slurry paste of as-prepared samples on a Taguchi type cylindrical α -alumina substrates. Pt wires were attached as electrodes on each side of the sensor modules with conducting gold paste [26]. After coating, the sensor substrates were dried in a furnace overnight at 120 °C for removal of solvent. Ni-Cr wire was inserted inside the hollow tube to use as a heating element. Following the same fabrication method identical sensors (namely BZ0, BZ1, BZ2, BZ3, BZ4) were developed comprising of pure and 1%, 2%, 3% and 4% Zn-doped BaFe₁₂O₁₉ samples, respectively, for their gas sensing performance comparison. The gas sensing set up is given in Fig. 3.2.

3.2.5. Gas preparation procedure

NH₃ gas sensing measurement in this work was performed by using commercially available nitrogen balanced dry NH₃ gas cylinders. For the particular ppm concentration of gas flow, Alicat made mass flow controller (MFC) meter was used to dilute the gas using N₂ gas mixture. Similarly, cross-sensing response of the sensors was checked using gas cylinders of acetone, formaldehyde, CO₂, CO, NO₂, NO, SO₂, H₂S of 100 ppm concentration balanced in nitrogen. For preparation of ethanol, benzene, toluene, isopropyl alcohol of required concentration, we have used desiccator dilution method. The dilution formula used as following eq. (1),

$$U = \frac{V \times M \times C}{22.4 \times d \times p} \times 10^{-6} \quad (1)$$

U refers to the injected volume of the liquid (μl), V is volume of the test chamber (ml), M is liquid molecular weight (g), C is liquid-vapor concentration (ppm), d is liquid specific gravity (g/cm^3) and p is the purity of the gas liquid.

3.2.6. Study of effect of relative humidity on gas sensing property

The influence of relative humidity (at 27°C) on the response of the BZ3 sensor at optimum working temperature of the sensor 250°C was conducted in an indigenously developed measurement chamber using a lower portion of a glass desiccator and air-tight lid. Different background atmosphere were created containing specific relative humidity (%RH) at 27°C in normal atmospheric pressure inside a sealed chamber. The chamber was covered by an air-tight lid using vacuum grease. Saturated aqueous solutions of different inorganic salts, to generate various %RH inside the desiccator, were kept at the bottom of the desiccator and covered by air-tight lid. The total chamber was kept untouched for few hours to set the desired relative humidity percentage. A commercially available humidity measuring meter (Model: 2D/RH-100C) was placed inside the chamber. Study of response of BZ3 sensor at different relative humidity (%RH) was carried out keeping the prepared sensor at its optimum working temperature (250°C). The sensor was placed on a base that delivered DC voltage to set the sensor's working temperature. The multimeter, which measured the sensor's transient resistance, was attached to additional electrodes. The humidity-controlled sensing setup is shown schematically in Fig. 3.2 given below for better clarity.

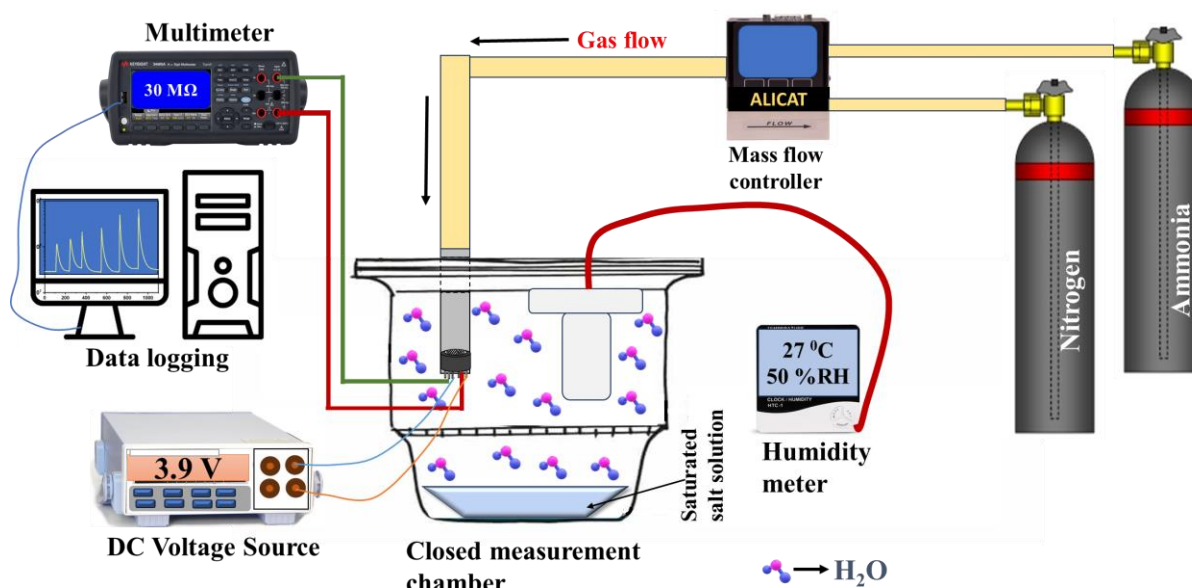


Fig. 3.2. Schematic diagram of gas measurement set up.

3.3. Results and discussion

3.3.1. Crystallographic structure and morphological analysis

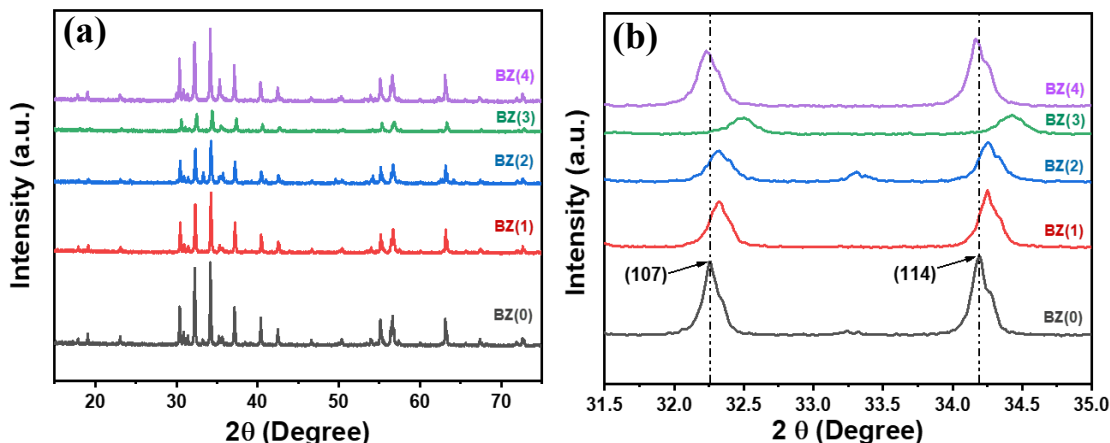


Fig. 3.3. (a) XRD spectra of pure BaFe₁₂O₁₉ and Zn-doped BaFe₁₂O₁₉ samples, (b) correspondingly magnified XRD patterns.

Fig. 3.3a shows the X-ray diffraction (XRD) pattern of as-prepared samples. Analysis with Expert High Score Plus software (ICDD card number 00-007-0276) reveals that all the prepared materials have well-formed hexagonal BaFe₁₂O₁₉ crystal structure with P6₃/mmc space group. The absence of any impurity phase indicates the formation of pure M-phase BaFe₁₂O₁₉. A gradual shift of XRD peaks towards higher 2θ is observed with increase in Zn doping concentration up to 3% wt. The magnified view of two highest intensity peaks (107) and (114) is shown in Fig. 3.3b. The shifting of the peaks to higher 2θ is indicative of lattice contraction attributed to larger ionic radii of Zn²⁺ (0.74Å) compared to that of Fe³⁺ (0.64Å) [39]. Increase in Full Width at Half Maxima (FWHM) with increase in doping concentration indicate that Zn²⁺ has been included in the BaFe₁₂O₁₉ matrix by replacing Fe³⁺ ions. Average crystallite size of as-prepared materials Debye-Scherrer formula (equation (1)) are ~49 nm, 39 nm, 35 nm, 33 nm and 31 nm for pure and 1%, 2%, 3% and 4% Zn doped BaFe₁₂O₁₉, respectively.

$$D = \frac{K\lambda}{\beta \cos \theta} \dots\dots\dots (1)$$

Where, D represents crystallites size, K is shape factor (0.89), λ is the wavelength of the X-ray source (here, 0.15406nm), β is FWHM for the diffraction angle 2θ, and θ is the Bragg angle

[26]. Lattice parameters (a,c) and unit cell volume (V) of the as-prepared samples were calculated using the eq.(2-4) following equations [40–42],

$$n\lambda = 2d_{hkl} \sin \theta \quad (2)$$

$$\frac{1}{d_{hkl}^2} = \frac{4}{3} \left(\frac{h^2 + hk + k^2}{a^2} \right) + \frac{l^2}{c^2} \quad (3)$$

$$V = 0.866a^2c \quad (4)$$

Where d_{hkl} refers to spacing between (114) and (107) planes, h,k and l are Miller's indices, $\lambda=1.5406 \text{ \AA}$, “n” is an integer, θ is the angle of incidence. The values of lattice parameters of pure and Zn doped $\text{BaFe}_{12}\text{O}_{19}$ as calculated from XRD data are shown in Table 3.2. It is evident that both lattice parameters “a” and “c” have decreased monotonously with increase in Zn doping concentration. This is attributed to the substitution of smaller sized Fe^{3+} (0.64 \AA) ions with larger sized Zn^{2+} (0.74 \AA). The volume of unit cell also decreased accordingly up to BZ3. This observation indicates the substitution of Fe with Zn [43,44]. However, for BZ4 it increased again, which indicates that for higher Zn doping concentration, rather than replacing the Fe^{3+} ions, Zn^{2+} ions are taking interstitial positions in the lattice.

Table 3.2 Lattice parameter related to prepared samples:

Sample	a (\AA)	c(\AA)	V(\AA^3)	c/a
BZ0	5.8741	23.1431	691.5560	3.9398
BZ1	5.8640	23.1031	687.9804	3.9398
BZ2	5.8638	23.1005	687.8560	3.9395
BZ3	5.8334	22.9944	677.6363	3.9418
BZ4	5.8775	23.1610	692.8973	3.9406

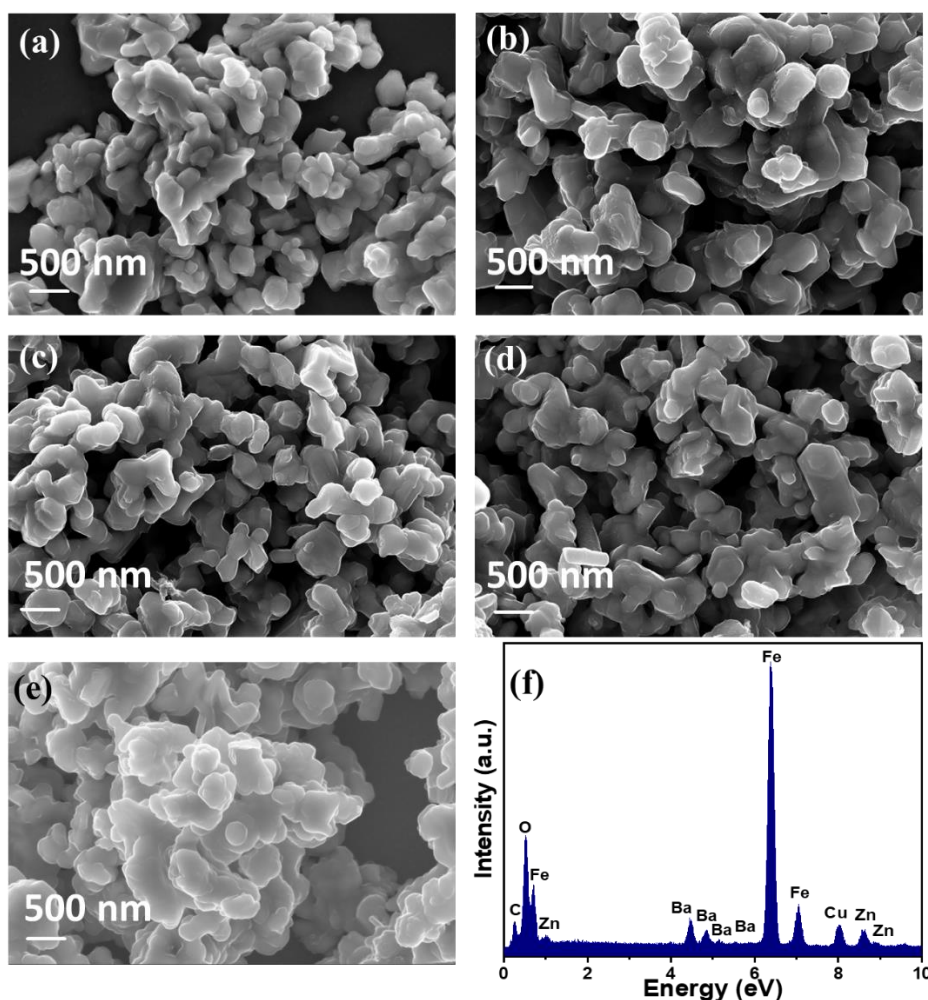


Fig. 3.4. FESEM micrographs of (a) pure $\text{BaFe}_{12}\text{O}_{19}$, (b) 1%, (c) 2%, (d) 3% and (e) 4% Zn doped $\text{BaFe}_{12}\text{O}_{19}$ samples, (f) EDS spectroscopy of BZ3.

The microstructures of the as-prepared samples were examined using FESEM. The Fig. 3.4(a-e) displays the FESEM micrograph corresponding to BZ0, BZ1, BZ2, BZ3 and BZ4 samples, respectively. The images reveal the existence of agglomerated non-uniform structure. While Zn concentration goes to 3% (BZ3), the hexagonal platelet like morphology started to appear but not much prominent due to agglomeration. Fig. 3.4f represents the energy dispersive X-ray spectroscopy (EDS) of BZ3 which confirms the presence of Ba, Fe, O and Zn in the sample.

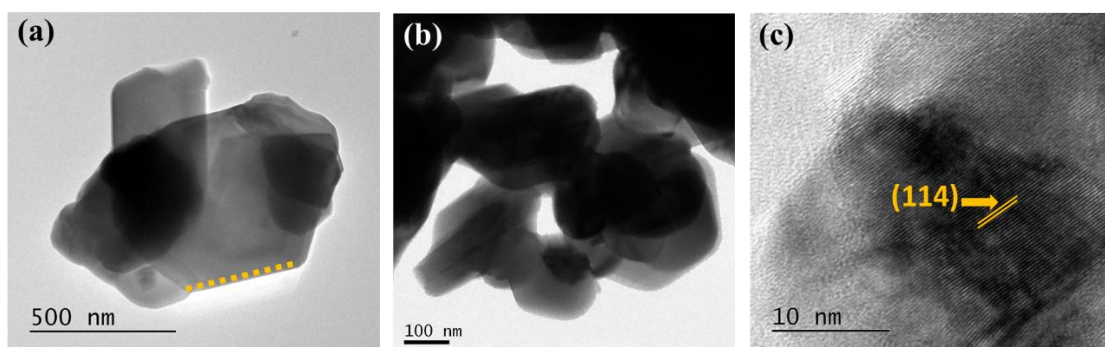


Fig. 3.5. TEM images of BZ3, (a) 1000 nm, (b) 500 nm, (c) High resolution-TEM image of BZ3.

To further explore the morphology of BZ3 sample transmission electron microscopy (TEM) studies were conducted (Fig. 3.5). In Fig. 3.5 (a-b), at both 500 nm and 100 nm, agglomerated particles of hexagonal platelet-like shape were observed, which matched well with the FESEM image of the BZ3 sample. High resolution transmission electron micrograph (HRTEM) (Fig. 3.5c) shows the lattice fringes of BZ3 to be 0.265 nm corresponding to the (114) lattice plane of hexagonal $\text{BaFe}_{12}\text{O}_{19}$ crystal structure. Fig. 3.6(a-s) displays elemental mapping of the prepared samples. It is evident that, Ba, Fe, O are present in all samples. Zn is present in all doped samples (BZ1, BZ3, BZ4). It is clear from the elemental mapping that all the elements in the as-synthesised samples are distributed homogeneously.

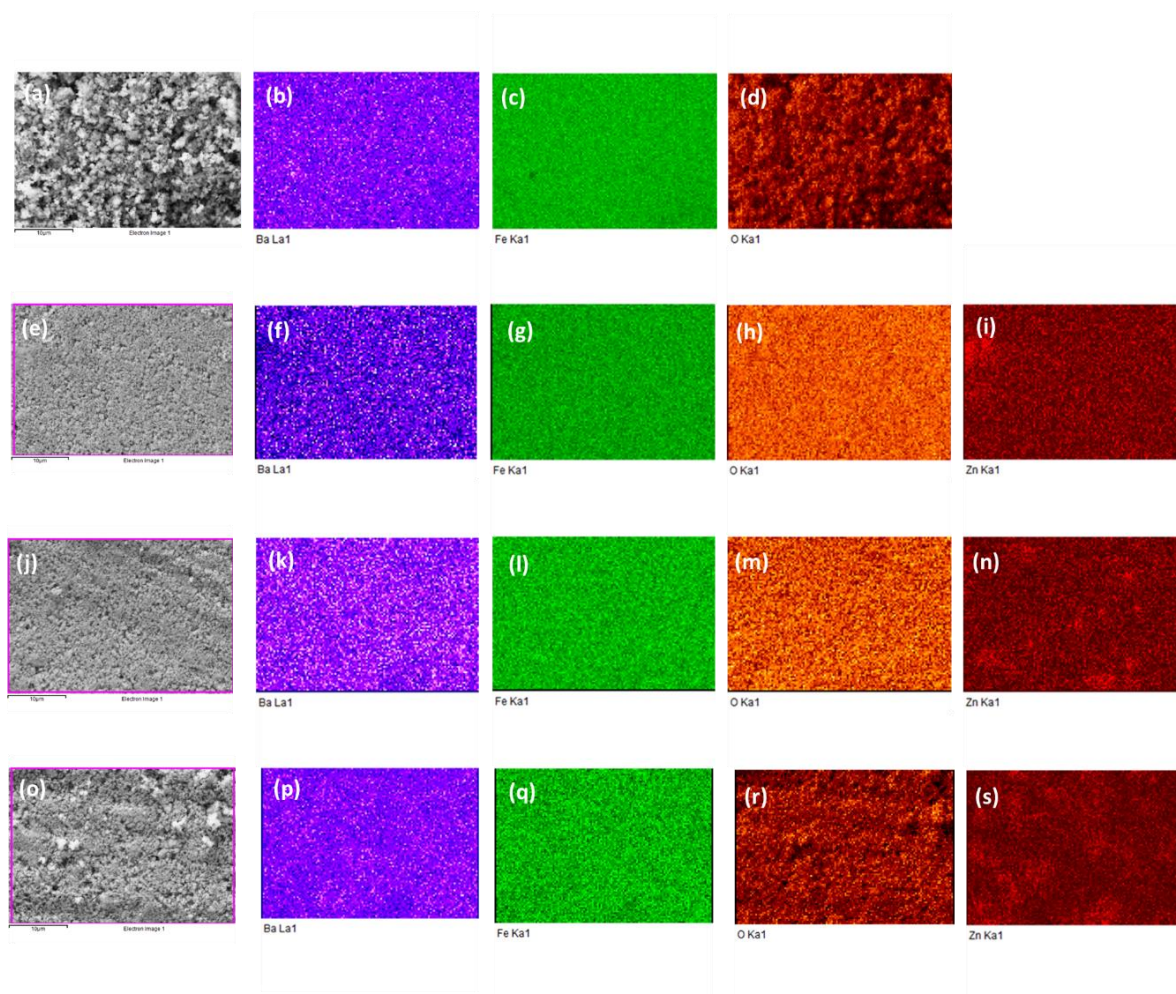


Fig. 3.6. Elemental distribution mapping images of samples: (b,f,k,p) Ba element, (c,g,l,q) Fe element, (d,h,m,r) O element in BZ0, BZ1, BZ3 and BZ4, respectively, (i,n,s) Zn element in BZ1, BZ3 and BZ4, respectively.

3.3.2. Chemical state and surface area analyses

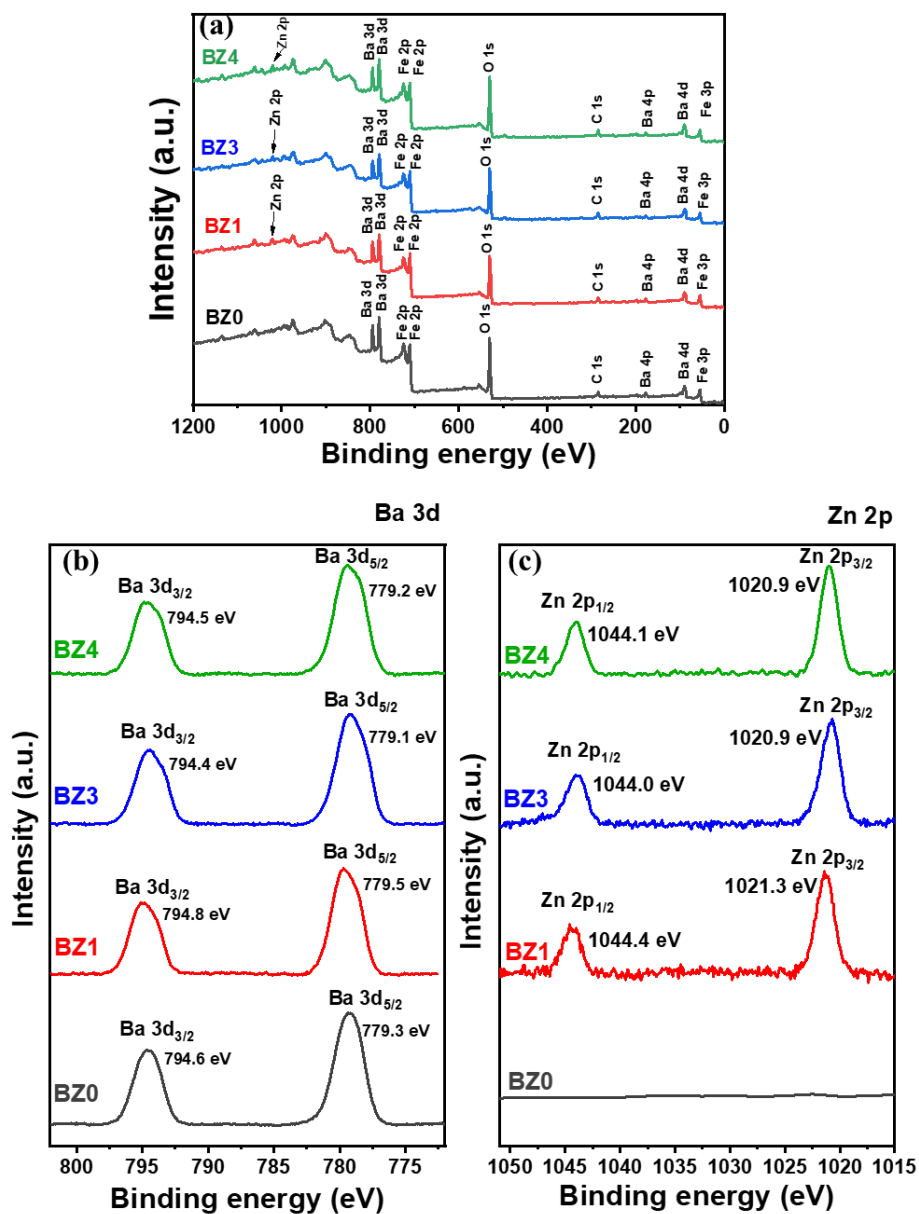


Fig. 3.7. (a) XPS wide scan spectra of all (BZ0, BZ1, BZ3, BZ4) samples, respectively. High resolution XPS spectra of (b) Ba 3d (c) Zn 2p of the BZ0, BZ1, BZ3, BZ4 samples.

Table 3.3 XPS analysis of Fe 2p peaks of BZ, BZ1, BZ3 and BZ4.

Samples	Fe species		Binding energy (eV)	Percentage of area	Fe ²⁺ /Fe ³⁺
BZ0	Fe 2p _{3/2}	Fe ²⁺	710.1	18.81	0.6294
		Fe ³⁺	711.9	24.67	
	Fe 2p _{1/2}	Fe ²⁺	723.6	10.20	
		Fe ³⁺	725.7	21.43	
BZ1	Fe 2p _{3/2}	Fe ²⁺	710.1	20.05	0.6779
		Fe ³⁺	711.9	25.74	
	Fe 2p _{1/2}	Fe ²⁺	723.7	9.76	
		Fe ³⁺	725.8	18.24	
BZ3	Fe 2p _{3/2}	Fe ²⁺	709.7	21.92	0.8750
		Fe ³⁺	711.8	24.39	
	Fe 2p _{1/2}	Fe ²⁺	723.3	11.00	
		Fe ³⁺	725.5	13.23	
BZ4	Fe 2p _{3/2}	Fe ²⁺	709.9	20.50	0.7446
		Fe ³⁺	711.7	24.12	
	Fe 2p _{1/2}	Fe ²⁺	723.4	9.30	
		Fe ³⁺	725.3	15.90	

XPS study was performed to detect the surface composition of prepared samples. Fig. 3.7a shows the survey scan spectra of BZ0, BZ1, BZ3 and BZ4 samples revealing peaks of Ba 3d, Fe 2p, O 1s in all samples and peaks of Zn 2p in doped samples. To calibrate the binding energy the adventitious carbon peak located at 284.8 eV was used as reference. Fig. 3.7(b-c) shows the narrow-scan spectra of Ba 3d and Zn 2p of the samples. Two doublet peaks centred at ~ 779.3 eV and ~794.6 eV indicates the presence of Ba 3d_{5/2} and Ba 3d_{3/2} peaks, respectively, which conforms 2+ oxidation state of Ba in all samples [45]. In narrow-scan spectra of Zn 2p (Fig.3.7b), peaks at ~1021.3 eV and ~1044.4 eV correspond to Zn 2p_{3/2} and Zn 2p_{1/2}, respectively, which confirmed the Zn²⁺ oxidation state in all doped samples [46]. Characteristic peaks of core level Fe 2p spectra of all samples is represented in Fig. 3.8a. The major peaks located at ~710.0 eV and ~723.6 eV correspond to Fe 2p_{3/2} and Fe 2p_{1/2} doublets. Existence of two satellite peaks at ~718.2 eV and at ~732.6 eV confirmed the presence of Fe³⁺ oxidation state [47]. The asymmetric Fe 2p peaks were fitted with gaussian peaks with Shirley

background. The major Fe 2p_{3/2} peak was deconvoluted into two subpeaks at ~710.1 eV and ~711.9 eV, related to Fe²⁺ and Fe³⁺ state, respectively. Similarly, major Fe 2p_{1/2} peak was deconvoluted into two subpeaks at ~723.6 eV and ~725.7 eV which corresponds to Fe²⁺ and Fe³⁺ state, respectively [48]. Details of fitting of Fe 2p peaks are given in Table 3.3. Fig. 3.8b shows narrow scan core level spectra of O 1s of the samples. The asymmetric O 1s peaks were fitted with three gaussian subpeaks corresponding to three oxygen species on the surface, namely: lattice oxygen (O_L) peak (~529.2 eV) ascribed to the O²⁻ ions in the metal oxides; defect oxygen (O_D) peak (~529.9 eV) attributed to the O²⁻ ions in the oxygen deficient regions caused by oxygen interstitials; and chemisorbed oxygen (O_C) peak (~530.80 eV) corresponds to the chemisorbed or dissociated oxygen species (O⁻) on the surface of the materials [49]. The summary of O 1s XPS analysis of samples are presented in Table 3.4. Specific surface area of the samples was obtained using Brunauer-Emmett-Teller (BET) method. BET plots of all the samples are given in Fig. 3.9, which indicate that specific surface area has increased slightly after incorporation of Zn.

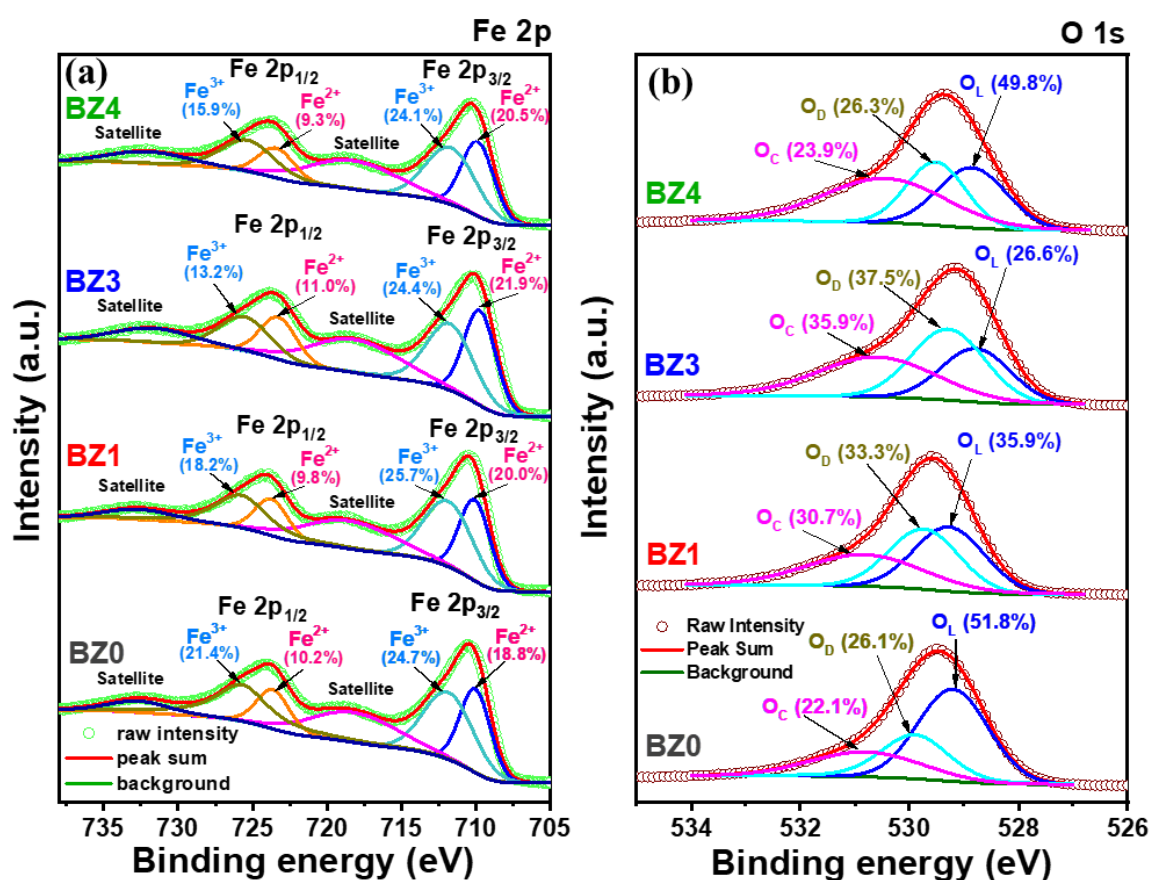


Fig. 3.8. High resolution core level deconvoluted spectra of (a) Fe 2p (b) O 1s of the BZ0, BZ1, BZ3, BZ4 samples.

Table 3.4 Analysis of XPS results of O 1s and Fe 2p peaks of BZ, BZ1, BZ3 and BZ4.

Samples	Oxygen species	Binding energy of oxygen species (eV)	Percentage of oxygen species
BZ0	O _L	529.2	51.75
	O _D	529.9	26.14
	O _C	530.8	22.09
BZ1	O _L	529.3	35.92
	O _D	529.7	33.34
	O _C	530.8	30.72
BZ3	O _L	528.2	26.55
	O _D	529.3	37.53
	O _C	530.6	35.92
BZ4	O _L	529.1	49.84
	O _D	529.8	26.25
	O _C	530.9	23.90

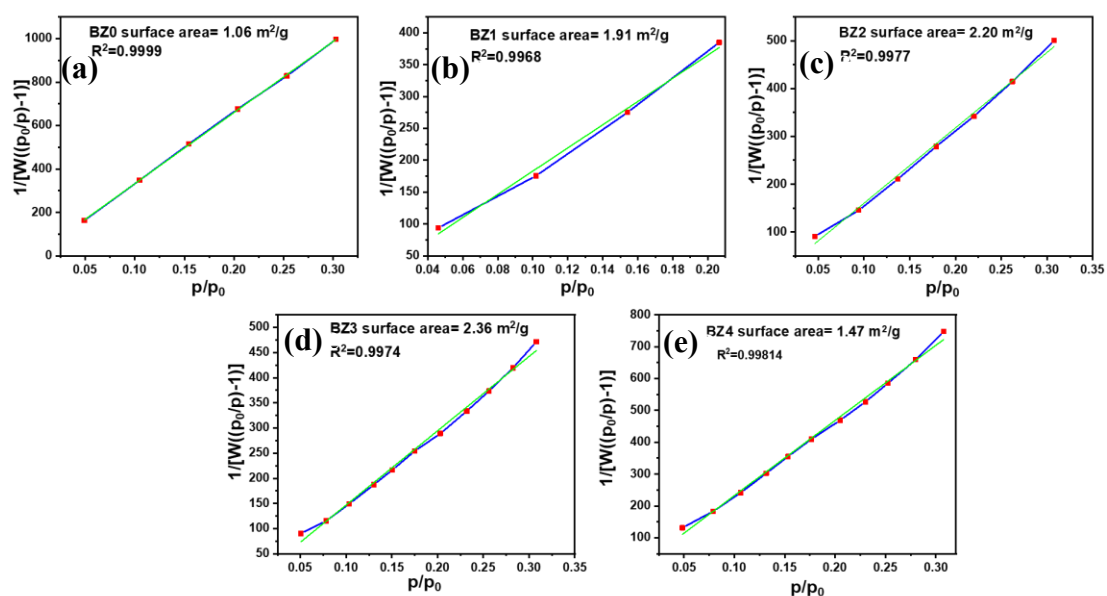


Fig. 3.9. Linear fitting of Brunauer–Emmett–Teller (BET) surface area analysis plot of BZ0, BZ1, BZ2, BZ3 and BZ4, respectively.

3.3.3. Optical properties

The bandgap (E_g) of the samples was measured by Tauc plot using UV-vis spectroscopy at room temperature. The relation between absorption coefficient (α) and the incident photon energy ($h\nu$) in a direct-band semiconductor can be written as,

$$\alpha h\nu = C(h\nu - E_g)^{1/2} \quad (5)$$

Fig. 3.10(a-e) displays the Tauc plots of all samples and the corresponding bandgap values (E_g) are given in bar diagram, Fig. 3.11a. As ZnO ($E_g \sim 3.33$ eV) is doped in barium hexaferrite having narrow bandgap ($E_g \sim 1.35$ eV), the bandgap of the doped materials increased gradually with increasing Zn doping concentration. Moreover, after Zn doping decrease in crystallite size was observed (as calculated from XRD spectra of samples). The crystallite size and band gap energy have inverse relationship due to quantum confinement effect. This decrease in crystallite size can also contribute to increase in bandgap energy.[50–52].

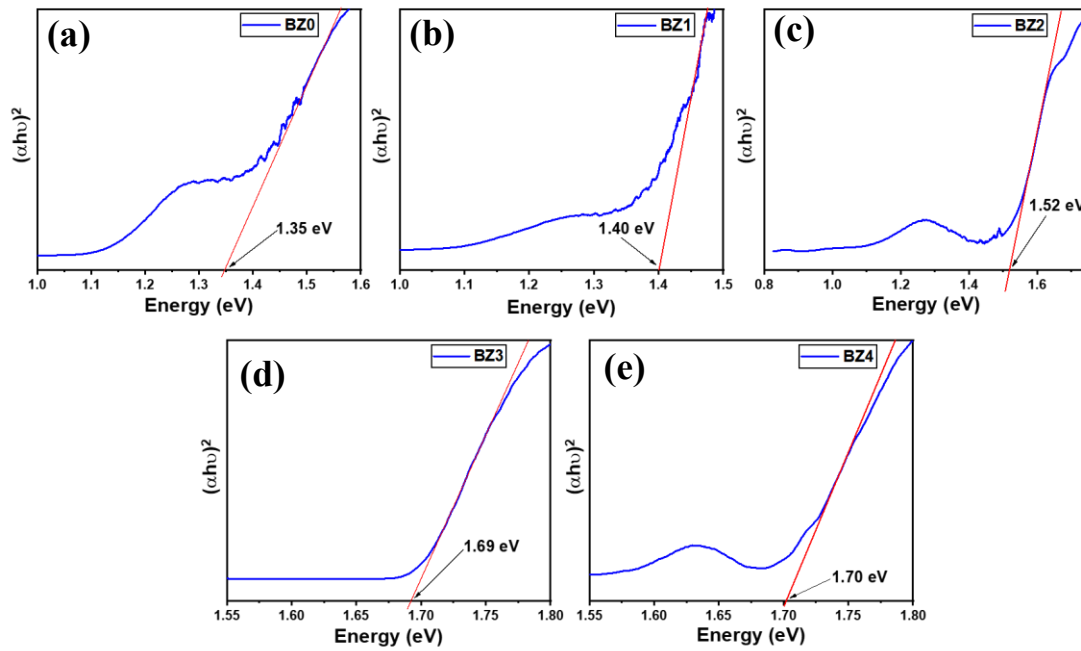


Fig. 3.10. Tauc plot of the as-synthesized (a) BZ0, (b) BZ1, (c) BZ2, (d) BZ3 and (e) BZ4 samples, respectively.

To understand charge separation efficiency, photoluminescence (PL) spectra of the materials were measured at room temperature as presented in Fig. 3.11b. It shows normalized PL emission peaks of the materials at excitation wavelength, $\lambda = 350$ nm. All the samples showed PL emission peak at wavelength region from 400–450 nm. Significant quenching of

PL emission intensity was observed in doped samples compared to BZ0. Among all the doped samples BZ3 showed lowest PL emission peak intensity, which is ascribed to better charge separation achieved by Zn doping [46]. Due to rapid recombination of photocharges pure sample BZ0 showed highest PL intensity. On the other hand, lower PL intensity of Zn doped samples is attributed to increased carrier density induced by decrease of recombination centres and increase in charge transfer efficiency [53,54].

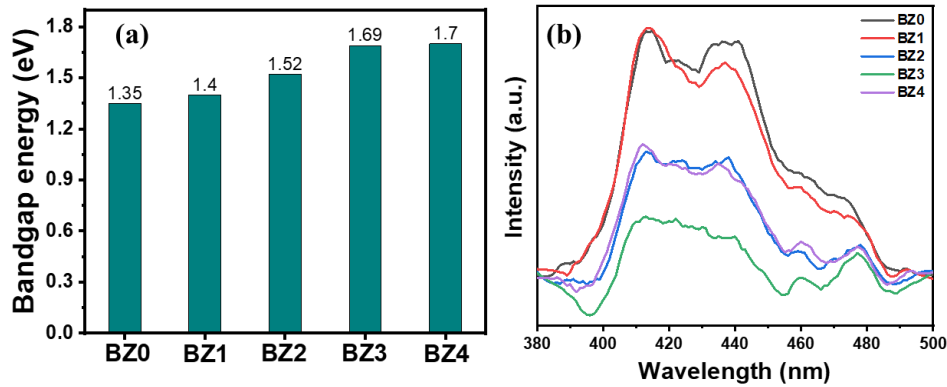


Fig. 3.11. (a) Room temperature PL spectra of samples at $\lambda=350$ nm. (b) Bandgap energy values of all samples.

3.3.4. Gas sensing properties for ammonia

Gas response of MOS is tested by measuring the change in conductivity of the material while exposing it to target gas. Here ammonia gas cylinder balanced in air was used as target gas. Dynamic response of the as-prepared sensors to different concentration of ammonia revealed p-type semiconductor behaviour where the response (S) is calculated using the formula $S = \frac{R_{gas}}{R_{air}}$, where R_{air} and R_{gas} represent resistance of the sensor in air and in the presence of target gas, respectively. As gas response of MOS depends on their operating temperature, estimation of optimum operating temperature of the sensors was performed by exposing the sensors to 1 ppm NH_3 in the operating temperature range from 200- 400 °C (Fig. 3.12a). All the curves showed “increase-maximum-decrease” trend of response with increase in operating temperature. At low operating temperature, target gas can not react with adsorbed oxygen on the surface because of low activation energy. After reaching maximum response, with further increase in operating temperature the gas response decreased as carrier concentration on the surface of the material saturates [55,56]. The optimum operating temperature of BZ0, BZ1, BZ2, BZ3, BZ4 were 310 °C, 250 °C, 250 °C, 250°C and 210 °C,

respectively. All the Zn-doped materials had lower optimum temperature than that of pure material. This indicates that, doping BaFe₁₂O₁₉ with Zn provides positive catalytic effect on adsorption of NH₃. Fig. 3.12b shows change of R_{air} of all the sensors with operating temperature. With increasing operating temperature R_{air} values of all sensors have gradually decreased. As the prepared sensing materials are all semiconducting in nature, at lower operating temperature lower number of charge carriers are available for conduction, hence R_{air} is high at low operating temperature for all samples. Increasing operating temperature leads to increase in number of majority charge carrier concentration. Gradual decrease in R_{air} with increasing operating temperature is the indicative of the improved conductivity of the samples which delineates semiconducting nature of this active sensing material [57].

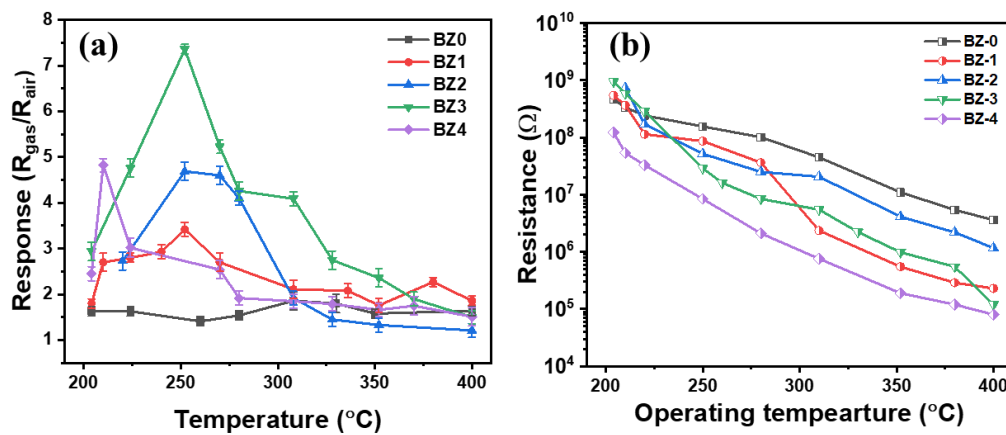


Fig. 3.12. (a) Response of all sensors to 1 ppm NH₃ at 200-400 °C operating temperature, (b) The base resistance (R_{air}) values of the sensors in air as a function of operating temperature in the range 200-400 °C.

Fig. 3.13a displays the response of all sensors to 1-100 ppm NH₃ at their respective optimum operating temperatures which clearly indicates the response of doped samples are higher than the pure one. The response of BZ3 for 100 ppm ammonia was S= 32.62 which is ~7 times higher than BZ0 (S= 4.8). Moreover, sensor BZ3 tend to saturate beyond 100 ppm of NH₃ concentration, whereas other sensors saturated much lower NH₃ concentration.

The relationship between the response (S) and NH₃ concentration (C) can be expressed using Freundlich adsorption isotherm equation as follows [58],

$$S = \alpha C^\beta \quad (6)$$

Or,

$$\log(S) = \log(\alpha) + \beta \log(C) \quad (7)$$

Where, C represents the concentration of NH₃ (in ppm), S represents the response of the sensor to NH₃, α is proportionality constant, β is the exponent [52,59]. The fitting with linear regression of the log (S) vs log (C) based on obtained response data of BZ0 and BZ3 sensors are displayed in Fig. 3.13b. The correlation coefficient (R^2) for BZ3 is 0.97 which indicates strong linear dependence between sensor response and NH₃ concentration. The values of β , as obtained from the slope of the fittings, are 0.37 and 0.21 for BZ3 and BZ0, respectively, indicating the adsorption process of NH₃ on the surface is physisorption ($\beta < 1$) [60]. Based on the fitting (Fig. 3.13b), theoretical limit of detection (LOD) of BZ3 is 150 ppb with S=1.4 whereas that of BZ0 sensor was 600 ppb. Zn-doping can deliver excellent sensing performance even at very low NH₃ concentration. Fig. 3.13(c-d) represents real-time dynamic resistance curve of BZ3 to NH₃ concentration range from 0.25-10 ppm and from 25-100ppm at 250 °C, respectively. Linear scale version of dynamic response-recovery curve (0.25-100ppm) is displayed in the Fig. 3.13c. The sensor's response-recovery curve to 0.5 ppm, 1 ppm, 2 ppm, 5 ppm NH₃ for three consecutive measurements is shown in Fig. 3.13e. Inset shows linear scale on y-axis version of the figure. It is clear that, the BZ3 sensor exhibits outstanding resolution in detecting different concentrations of NH₃.

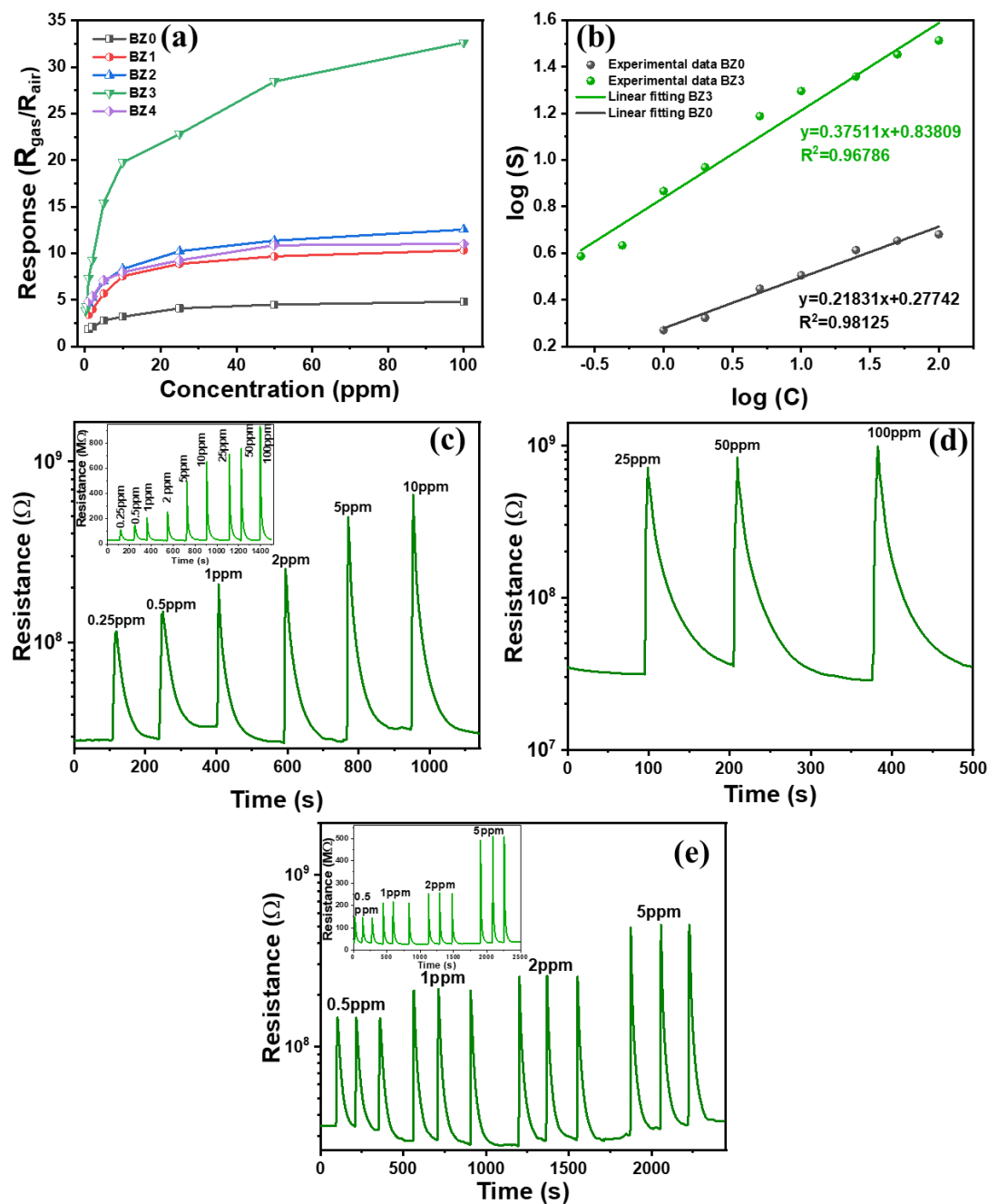


Fig. 3.13. (a) The response of all the sensors to 1-100 ppm NH_3 at their corresponding optimum operating temperatures; (b) Fitting of experimental data of sensing response of BZ0 and BZ3 sensors to NH_3 (1-100ppm) using Freundlich isotherm equation; Real time dynamic response-recovery curves of BZ3 sensor at 250 °C for NH_3 in the concentration range (c) 0.25-10ppm with log scale on y-axis (inset with linear scale) and (d) from 25-100ppm in log scale; (e) Response transient curves of BZ3 sensor for repeated cycles towards 0.5 ppm, 1 ppm, 2 ppm, 5 ppm NH_3 at 250 °C with log scale on y-axis (inset with linear scale).

Current-voltage (I-V) characteristics of the fabricated sensor was measured. Fig. 3.14a represents current vs voltage graph of BZ3 measured by varying the applied voltage from -40 V to +40 V for different operating temperatures of the sensor (200°C, 250 °C, 300°C, 350°C and 400 °C). It was observed that current and applied voltage maintains ohmic law implying ohmic contact has been formed. The sensor showed similar behaviour for all the operating temperatures which indicates that the sensor is able to perform well in the given temperature range. I-V measurements suggest that the material is semiconducting in nature as the conductivity of the sample increases with temperature. The current-voltage (I-V) characteristics under various concentrations of NH₃ gas has been measured to validate the p-type chemiresistive sensing performance of BZ3 sensor as shown in Fig. 3.14b. It is clearly visible from the I-V curve that as concentration of ammonia increases resistance of the sensor increases which exactly matches with the sensing data.

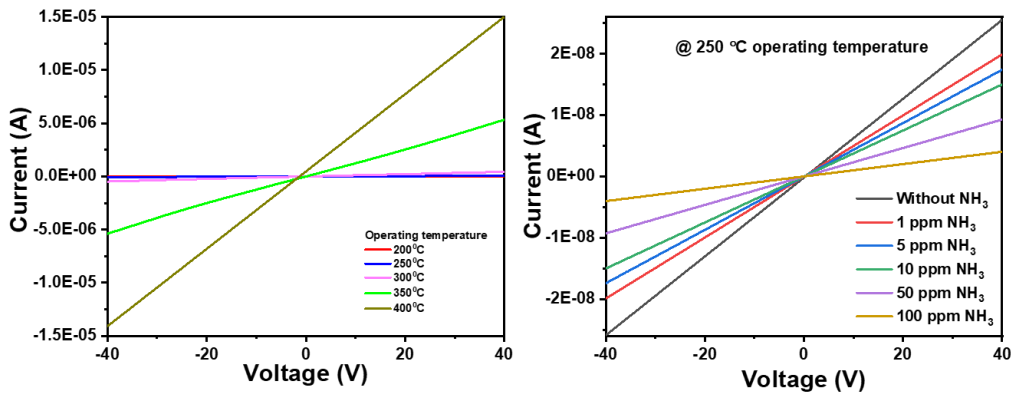


Fig. 3.14. (a) Current-voltage (I-V) characteristics of BZ3 sensor at operating temperatures 200 °C, 250 °C, 300 °C, 350 °C and 400 °C, respectively. (b) Current-voltage (I-V) characteristics of BZ3 sensor in presence of different concentration of NH₃ at operating temperature 250 °C.

Multiexponential transient conductance model is employed to calculate transient response and recovery times of BZ3 sensor at 250 °C (ref. Fig. 3.15a). According to the Langmuir adsorption model the response transient conductance $G(t)$ and the recovery transient conductance $G'(t)$ at a constant temperature can be expressed as follows [49],

$$G(t) = G_0 + G_1 [\exp(-t/\tau_{\text{response}})] \quad (8)$$

$$G'(t) = G_0' + G_1' [1 - \exp(-t/\tau_{\text{recovery}})] \quad (9)$$

Here, G_0 is conductance in presence of air, also known as base conductance, $\tau_{response}$ is the time constant of NH_3 adsorption, G_0' is conductance at stable response value and $\tau_{recovery}$ is the time constant of NH_3 desorption. Response/recovery time for 1 ppm NH_3 at 250 °C are 2.66 s/35.25 s indicating rapid adsorption and desorption process. Fig. 3.15b represents short-term stability of BZ3 sensor tested for 1 ppm NH_3 for nine consecutive response-recovery cycles, which showed excellent repeatability in response data. Also, the long-term stability (Fig. 3.15b) of BZ3 was tested against 1 ppm NH_3 for 100 days. The deviation in long-term stability data is insignificant (<2%), which indicates the sensor's suitability for practical application. Selectivity of the as-fabricated sensors was tested against various relevant interfering gasses i.e. acetone, ethanol, formaldehyde, benzene, toluene, isopropyl alcohol, CO_2 , CO, NO_2 , NO, SO_2 , H_2S , that are present in human exhaled breath and outdoor air. As shown in the Fig. 3.15c, all the Zn doped sensors showed highest response to 1ppm ammonia compared to the other gases. These results reveal that among all other sensors BZ3 sensor showed enhanced selectivity to NH_3 which makes the sensor applicable for both breath analysing and environment monitoring.

To observe the influence of humidity on the sensing property of BZ3, the sensing performance was tested under different relative humidity ranging from 30%-98% RH (at 27 °C) while the sensor was kept at 250 °C operating temperature as shown in Fig. 3.15d. It was observed that variation of base resistance (R_{air}) with increase in RH % is negligible which is presented in Fig. 3.15d. The response of the sensor has increased by <3% with increase in RH from 30% to 98%. This result may be attributed to the promotion of reaction of NH_3 molecules with the sensor surface in the due to the abundance of high relative humidity in the environment [61]. The sensing result showed effect of humidity is very low on sensing performance of BZ3 sensor.

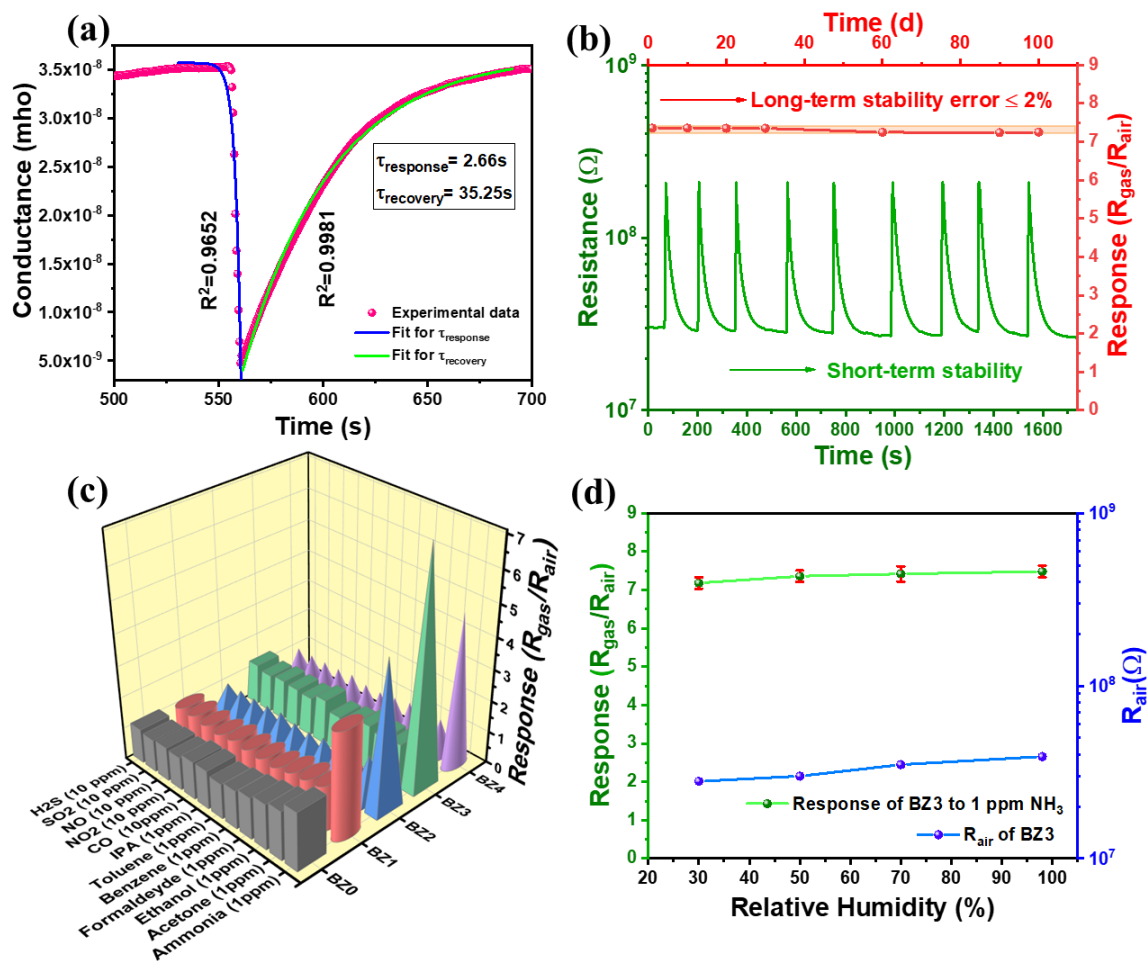


Fig. 3.15. (a) Fitting of conductance transient for response and recovery of BZ3 sensor to 1 ppm NH₃ at 250 °C; (b) Cyclic response and recovery curves and long-term stability of the BZ3 sensor for 100 days to 1 ppm NH₃ at 250 °C; (c) The response of all sensors to different gases showing selectivity of the sensors at their corresponding optimum operating temperatures, (d) Response and R_{air} values of BZ3 sensor to 1 ppm NH₃ at different RH % (at 27 °C) at operating temperature 250 °C.

3.3.5. Simulation of breath analysis

To investigate the performance of Zn-BaFe₁₂O₁₉ based sensor as a breath analyzer, simulated breath study was performed. Healthy human exhaled breaths were collected and required amount of ammonia vapor was mixed with it using desiccator dilution method to prepare simulated breath with different concentrations of NH₃ (0.5 ppm, 1 ppm, 1.5 ppm, 3 ppm), separately. Real time simulated breath study was conducted using healthy breath and simulated breath containing different ammonia concentration. Fig. 3.16 shows response recovery curve of BZ3 sensor to the simulated breath samples. The sensor's response to healthy

human breath (H.B.) was 4.04 which could be due to the presence of 0.25 ppm NH_3 in healthy breath. The sensor showed 5.61, 7.53, 887, 11.85 response towards simulated breath with 0.5 ppm, 1 ppm, 1.5 ppm, 3 ppm additional NH_3 , respectively. The data shows that the sensor can distinguish between different simulated breaths and detect low ppm concentrations of NH_3 in exhaled breath, making the BZ3 sensor a suitable choice for breath analysis.

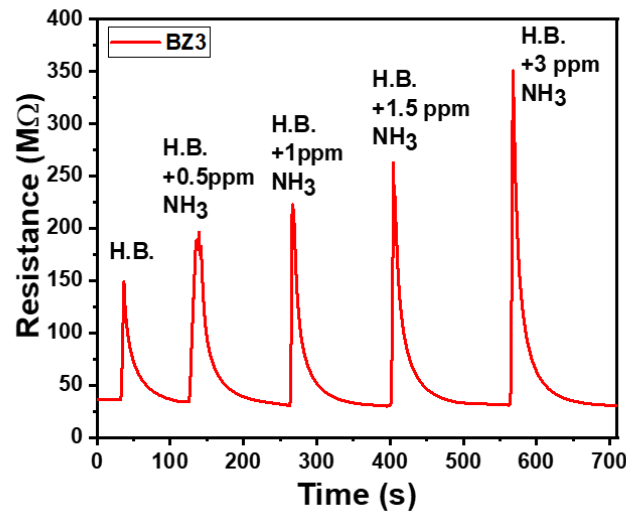
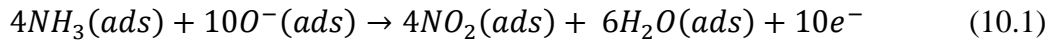


Fig. 3.16. Sensing responses of BZ3 sensor prototype to healthy exhaled breath and simulated exhaled breath mixed with different NH_3 concentrations at 250 °C.

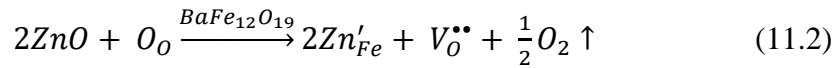
3.3.6. Mechanism of NH_3 sensing

Gas sensing is a surface phenomenon where interaction takes place between the target gas and the exposed surface of the sensing material. Mechanism of gas sensing of $\text{BaFe}_{12}\text{O}_{19}$, which showed a typical p-type semiconductor sensing behaviour, can be explained by oxygen adsorption theory. When sensor surface is exposed to air, the oxygen molecules from atmosphere gets adsorbed on the surface and converted to different ions i.e. O_2^- , 2O^- , O^{2-} depending upon temperature by capturing electrons from the conduction band of the material [47,62]. Accordingly, a hole accumulation layer (HAL) will be created at the surface of $\text{BaFe}_{12}\text{O}_{19}$ whose thickness will depend on the adsorption capability of the material. Since operating temperature of BZ3 is 250 °C oxygen mainly exist in the form of O^- . When the material is exposed to NH_3 it reacts with the adsorbed oxygen species and gives the previously captured electrons back to the conduction band. That in turn decreases the hole concentration and causes thinning of HAL (eq.10.1-10.2). In this process, the resistance of the sensor increases which is measured as response of the sensor. When NH_3 gas flow is removed, the

atmospheric oxygen gets re-adsorbed on the sensor surface and NH_3 is desorbed from the sensor surface and HAL is restored which results in complete recovery of the sensor. The corresponding reaction with ammonia is given by following equation [63,64],



The enhancement of NH_3 sensing properties of by Zn doping in $\text{BaFe}_{12}\text{O}_{19}$, may be influenced by the following factors. Firstly, substitution of Zn having valence state 2+ can lead to following defect reactions,



It suggests that Zn doping in $\text{BaFe}_{12}\text{O}_{19}$ can create hole or oxygen vacancies [65]. The R_{air} values of the sensors when measured at 250 °C are 156 M Ω , 86 M Ω , 52 M Ω , 29 M Ω , 8.5 M Ω for BZ0, BZ1, BZ2, BZ3 and BZ4, respectively, indicating the conductivity of the materials have increased after doping with Zn. Therefore, it can be inferred that substitution of Zn in Fe site results in occurrence of the firstly mentioned process (eq. 11.1). The excess holes (h^\bullet) will contribute to the majority charge carrier concentration which increased with increase in Zn doping concentration. This will enhance the p-type sensing behaviour of the material.

Secondly, intensity of PL emission spectra reflects the charge separation efficiency of electron-holes in semiconductors. Lower PL emission intensity means higher charge separation efficiency, therefore more electrons will be available in conduction band, which benefits the ionization of atmospheric oxygen and gas sensing. As displayed in Fig. 3.11b pure sample BZ0 showed highest PL emission peak and BZ3 showed lowest emission peak. This indicates BZ3 has higher electron-hole separation which helps to improve sensing behaviour. Moreover, oxygen vacancies generated during the substitution process of Fe with Zn have improved charge transfer and reduces bulk recombination. This in turn improved the charge separation efficiency of the Zn doped samples [66,67]. This corroborated with XPS O1s spectra analysis.

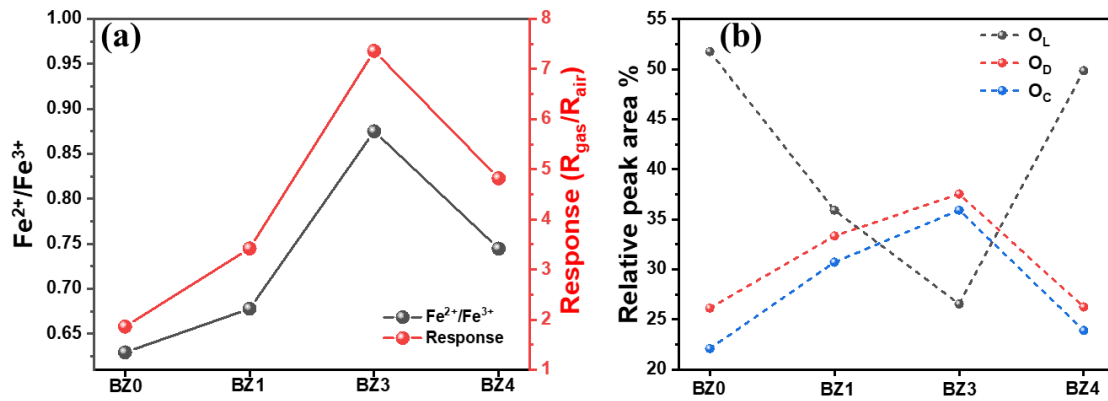


Fig. 3.17. (a) Change in $\text{Fe}^{2+}/\text{Fe}^{3+}$ ratio and corresponding response of BZ0, BZ1, BZ3 and BZ4; (b) Variation of concentration of oxygen species on the surface of BZ0, BZ1, BZ2, BZ3 and BZ4.

Thirdly, Fe^{2+} ion content increased from 29.01% in BZ0 to 32.92% in BZ3 (ref. Table 3.3). Therefore, it may be concluded that substitution of Fe with Zn facilitates coexistence of Fe^{2+} and Fe^{3+} in the Zn doped $\text{BaFe}_{12}\text{O}_{19}$ samples. BZ3 exhibited highest Fe^{2+} content among the doped samples. The increase-maximum-decrease trend of the $\text{Fe}^{2+}/\text{Fe}^{3+}$ ratio with increasing Zn doping exactly reflects the trajectory of the enhanced response of the corresponding samples, as shown in Fig. 3.17a. To maintain the charge neutrality during the ionic substitution process (ref. equation 11.2), Fe^{2+} ion content rises and contributes to the formation of increased oxygen vacancy content on the surface which plays an important role in enhancement of gas response [65,68–71]. It was observed, the percentage of lattice oxygen (O_L) is lowest for BZ3 (ref. Table 3.4). Additionally, with increase in Zn doping concentration the percentage of O_D and O_C showed increase-maximum-decrease trend, and maximum value was reached for BZ3 sample (Fig. 3.17b), which exhibited best NH_3 sensing property among all the samples. The lattice oxygen species (O_L) can not react with any target analytes and the target gas molecules interact with defect oxygen sites and chemisorbed oxygen species on the surface as they act as active sites for sensing. Therefore, with increase in the surface chemisorbed oxygen species the gas sensing response of the materials also increases. This study establishes a correlation of the material's improved ammonia sensing ability with the coexistence of Fe^{2+} and Fe^{3+} states and increased oxygen vacancy concentration. However, BZ4 exhibited lower concentration of O_D and O_C . Also, as conferred from calculation of lattice parameter (ref. Table 3.2) that, for higher doping concentration in BZ4, Zn^{2+} ions are taking interstitial positions in the lattice. Therefore, Fe^{2+} content decreased in BZ4 compared to BZ3, which is responsible for lower sensing

performance of BZ4. The gas sensing mechanism of Zn doped $\text{BaFe}_{12}\text{O}_{19}$ is represented in Fig. 3.18. The highly selective nature of Zn doped $\text{BaFe}_{12}\text{O}_{19}$ samples toward ammonia may explained in terms of bond dissociation energy. The bond dissociation energy of N-H (391 kJ/mol) in ammonia is lower than that of O-H (458.8 kJ/mol) in ethanol, and C=O (798.9 kJ/mol) in acetone and HCHO. The reaction activity of ammonia with Zn doped $\text{BaFe}_{12}\text{O}_{19}$ is higher as it is easier to dissociate ammonia molecules due to its lower dissociation energy [62,72].

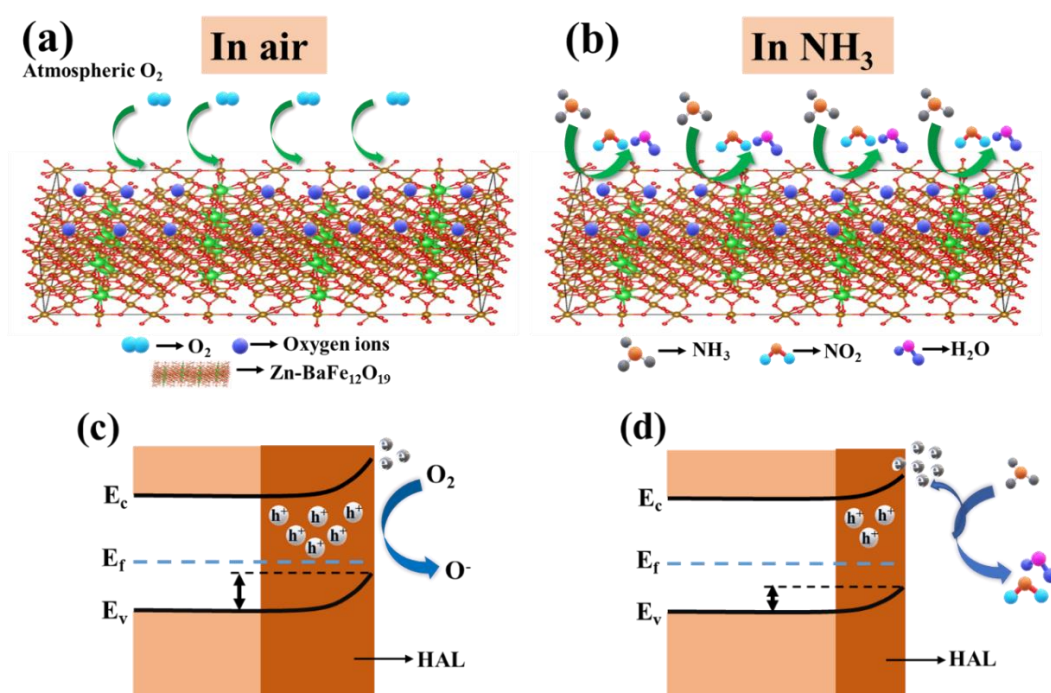


Fig. 3.18. Schematic diagram of sensing mechanism of Zn doped $\text{BaFe}_{12}\text{O}_{19}$ based sensor (a,c) in air and (b,d) in NH_3 .

3.4. Conclusion

In summary, we have demonstrated that, ammonia sensing performance of $\text{BaFe}_{12}\text{O}_{19}$ can be improved significantly by doping with Zn. 3% Zn-doped $\text{BaFe}_{12}\text{O}_{19}$ -based sensor exhibited greater selectivity toward ammonia with negligible effect of humidity, enhanced response ($R_{\text{gas}}/R_{\text{air}} = 7.36$) towards 1 ppm NH_3 at 250 °C, lower detection limit of 150 ppb, fast response/recovery times 2.66s/35.25s. Enhanced response was attributed to the modulation of the surface oxygen defect and active gas-adsorption sites by introducing Zn^{2+} in the system in place of Fe^{3+} , as validated from XPS analysis. This work is significant for fabrication of ammonia sensor that can be used in health monitoring and prevention of workplace hazard by environmental surveillance.

3.5. References

- [1] S. Singh, J. Deb, U. Sarkar, S. Sharma, MoSe₂/multiwalled carbon nanotube composite for ammonia sensing in natural humid environment, *J Hazard Mater* 435 (2022) 128821.
- [2] A.H. Assen, O. Yassine, O. Shekhah, M. Eddaoudi, K.N. Salama, MOFs for the Sensitive Detection of Ammonia: Deployment of fcu-MOF Thin Films as Effective Chemical Capacitive Sensors, *ACS Sens* 2 (2017) 1294–1301.
- [3] H.Y. Li, C.S. Lee, D.H. Kim, J.H. Lee, Flexible Room-Temperature NH₃ Sensor for Ultrasensitive, Selective, and Humidity-Independent Gas Detection, *ACS Appl Mater Interfaces* 10 (2018) 27858–27867.
- [4] X. Xing, L. Du, D. Feng, C. Wang, Y. Tian, Z. Li, H. Liu, D. Yang, Twistable and tailorable V₂O₅/PANI/GO nanocomposites textile for wearable ammonia sensing, *Sens Actuators B Chem* 351 (2022) 130944.
- [5] M. Jagannathan, D. Dhinasekaran, A.R. Rajendran, B. Subramaniam, Selective room temperature ammonia gas sensor using nanostructured ZnO/CuO@graphene on paper substrate, *Sens Actuators B Chem* 350 (2022) 130833.
- [6] D. Zhang, Z. Kang, X. Liu, J. Guo, Y. Yang, Highly sensitive ammonia sensor based on PSS doped ZIF-8-derived porous carbon/polyaniline hybrid film coated on quartz crystal microbalance, *Sens Actuators B Chem* 357 (2022) 131419.
- [7] A.T. Güntner, S. Abegg, K. Königstein, P.A. Gerber, A. Schmidt-Trucksäss, S.E. Pratsinis, Breath Sensors for Health Monitoring, *ACS Sens* 4 (2019) 268–280.
- [8] H.Y. Li, C.S. Lee, D.H. Kim, J.H. Lee, Flexible Room-Temperature NH₃ Sensor for Ultrasensitive, Selective, and Humidity-Independent Gas Detection, *ACS Appl Mater Interfaces* 10 (2018) 27858–27867.
- [9] L.A. Panes-Ruiz, M. Shaygan, Y. Fu, Y. Liu, V. Khavrus, S. Oswald, T. Gemming, L. Baraban, V. Bezugly, G. Cuniberti, Toward Highly Sensitive and Energy Efficient Ammonia Gas Detection with Modified Single-Walled Carbon Nanotubes at Room Temperature, *ACS Sens* 3 (2018) 79–86.
- [10] G. Song, D. Jiang, J. Wu, X. Sun, M. Deng, L. Wang, C. Hao, J. Shi, H. Liu, Y. Tian, M. Chen, An ultrasensitive fluorescent breath ammonia sensor for noninvasive diagnosis of chronic kidney disease and helicobacter pylori infection, *Chemical Engineering Journal* 440 (2022) 135979.
- [11] F. Ranjbar, S. Hajati, M. Ghaedi, K. Dashtian, H. Naderi, J. Toth, Highly selective MXene/V₂O₅/CuWO₄-based ultra-sensitive room temperature ammonia sensor, *J Hazard Mater* 416 (2021) 126196.
- [12] Z. Liu, T. He, H. Sun, B. Huang, X. Li, Layered MXene heterostructured with In₂O₃ nanoparticles for ammonia sensors at room temperature, *Sens Actuators B Chem* 365 (2022) 131918.
- [13] G. Song, D. Jiang, J. Wu, X. Sun, M. Deng, L. Wang, C. Hao, J. Shi, H. Liu, Y. Tian, M. Chen, An ultrasensitive fluorescent breath ammonia sensor for noninvasive diagnosis of chronic kidney disease and helicobacter pylori infection, *Chemical Engineering Journal* 440 (2022) 135979.
- [14] A.M. Diskin, P. Španěl, D. Smith, Time variation of ammonia, acetone, isoprene and ethanol in breath: a quantitative SIFT-MS study over 30 days, *Physiol Meas* 24 (2003) 107.
- [15] L.R. Narasimhan, W. Goodman, C.K.N. Patel, Correlation of breath ammonia with blood urea nitrogen and creatinine during hemodialysis, *Proc Natl Acad Sci U S A* 98 (2001) 4617–4621.

- [16] G. Song, D. Jiang, J. Wu, X. Sun, M. Deng, L. Wang, C. Hao, J. Shi, H. Liu, Y. Tian, M. Chen, An ultrasensitive fluorescent breath ammonia sensor for noninvasive diagnosis of chronic kidney disease and helicobacter pylori infection, *Chemical Engineering Journal* 440 (2022) 135979.
- [17] N. Tang, C. Zhou, L. Xu, Y. Jiang, H. Qu, X. Duan, A Fully Integrated Wireless Flexible Ammonia Sensor Fabricated by Soft Nano-Lithography, *ACS Sens* 4 (2019) 726–732.
- [18] S. Pandey, K.K. Nanda, Au Nanocomposite Based Chemiresistive Ammonia Sensor for Health Monitoring, *ACS Sens* 1 (2016) 55–62.
- [19] X. Liu, N. Chen, B. Han, X. Xiao, G. Chen, I. Djerdj, Y. Wang, Nanoparticle cluster gas sensor: Pt activated SnO₂ nanoparticles for NH₃ detection with ultrahigh sensitivity, *Nanoscale* 7 (2015) 14872–14880.
- [20] N. Kumar, A.K. Srivastava, R. Nath, B.K. Gupta, G.D. Varma, Probing the highly efficient room temperature ammonia gas sensing properties of a luminescent ZnO nanowire array prepared via an AAO-assisted template route, *Dalton Transactions* 43 (2014) 5713–5720.
- [21] H.I. Chen, C.Y. Hsiao, W.C. Chen, C.H. Chang, T.C. Chou, I.P. Liu, K.W. Lin, W.C. Liu, Characteristics of a Pt/NiO thin film-based ammonia gas sensor, *Sens Actuators B Chem* 256 (2018) 962–967.
- [22] Z. Li, Z. Lin, N. Wang, J. Wang, W. Liu, K. Sun, Y.Q. Fu, Z. Wang, High precision NH₃ sensing using network nano-sheet Co₃O₄ arrays based sensor at room temperature, *Sens Actuators B Chem* 235 (2016) 222–231.
- [23] V. Srivastava, K. Jain, Mechanism of enhancement in NH₃ sensing for surface functionalized WO₃ film, *RSC Adv* 5 (2015) 56993–56997.
- [24] G. Chaloeipote, R. Prathumwan, K. Subannajui, A. Wisitsoraat, C. Wongchoosuk, 3D printed CuO semiconducting gas sensor for ammonia detection at room temperature, *Mater Sci Semicond Process* 123 (2021).
- [25] Y. Tu, C. Kyle, H. Luo, D.W. Zhang, A. Das, J. Briscoe, S. Dunn, M.M. Titirici, S. Krause, Ammonia Gas Sensor Response of a Vertical Zinc Oxide Nanorod-Gold Junction Diode at Room Temperature, *ACS Sens* 5 (2020) 3568–3575.
- [26] T. Das, S. Das, M. Karmakar, S. Chakraborty, D. Saha, M. Pal, Novel barium hexaferrite based highly selective and stable trace ammonia sensor for detection of renal disease by exhaled breath analysis, *Sens Actuators B Chem* 325 (2020) 128765.
- [27] J. Wang, X. Wei, P. Wangyang, Gas-Sensing Devices Based on Zn-Doped NiO Two-Dimensional Grainy Films with Fast Response and Recovery for Ammonia Molecule Detection, *Nanoscale Res Lett* 10 (2015) 1–9.
- [28] S. Yang, Y. Liu, T. Chen, W. Jin, T. Yang, M. Cao, S. Liu, J. Zhou, G.S. Zakharova, W. Chen, Zn doped MoO₃ nanobelts and the enhanced gas sensing properties to ethanol, *Appl Surf Sci* 393 (2017) 377–384.
- [29] T. Hemalatha, S. Akilandeswari, T. Krishnakumar, S.G. Leonardi, G. Neri, N. Donato, Comparison of Electrical and Sensing Properties of Pure, Sn-and Zn-Doped CuO Gas Sensors, *IEEE Trans Instrum Meas* 68 (2019) 903–912.
- [30] S.K. Godara, V. Kaur, K. Chuchra, S.B. Narang, G. Singh, M. Singh, A. Chawla, S. Verma, G.R. Bhadu, J.C. Chaudhari, P.D. Babu, A.K. Sood, Impact of Zn²⁺-Zr⁴⁺ substitution on M-type Barium Strontium Hexaferrite's structural, surface morphology, dielectric and magnetic properties, *Results Phys* 22 (2021) 103892.
- [31] S. Kanaparthi, S. Govind Singh, Highly sensitive and ultra-fast responsive ammonia gas sensor based on 2D ZnO nanoflakes, *Mater Sci Energy Technol* 3 (2020) 91–96.

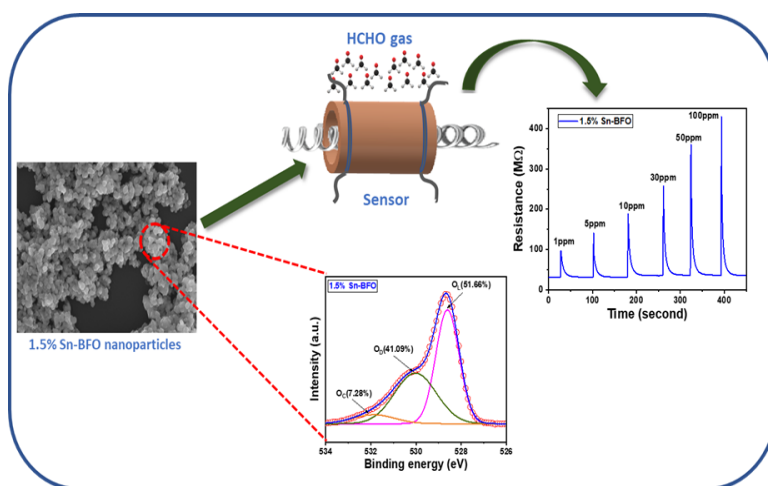
- [32] Y. Qin, X. Liu, J. Xie, Humidity-enhanced NH₃ sensor based on carbon quantum dots-modified SnS, *Appl Surf Sci* 634 (2023) 157612.
- [33] J. Bai, Y. Shen, S. Zhao, Y. Chen, G. Li, C. Han, D. Wei, Z. Yuan, F. Meng, Flower-like MoS₂ hierarchical architectures assembled by 2D nanosheets sensitized with SnO₂ quantum dots for high-performance NH₃ sensing at room temperature, *Sens Actuators B Chem* 353 (2022) 131191.
- [34] S. Suriyawong, J. Khumphon, R. Rattanakam, P. Chaopanich, S. Thongmee, S. Youngjan, P. Khemthong, S. Kityakarn, Engineering three-dimensionally ordered mesoporous structure of TiO₂ for the fast responsive NH₃ gas sensor at ambient conditions, *Colloids Surf A Physicochem Eng Asp* 666 (2023) 131281.
- [35] Q. Hu, Z. Wang, J. Chang, P. Wan, J. Huang, L. Feng, Design and preparation of hollow NiO sphere-polyaniline composite for NH₃ gas sensing at room temperature, *Sens Actuators B Chem* 344 (2021).
- [36] F. Ranjbar, S. Hajati, M. Ghaedi, K. Dashtian, H. Naderi, J. Toth, Highly selective MXene/V₂O₅/CuWO₄-based ultra-sensitive room temperature ammonia sensor, *J Hazard Mater* 416 (2021) 126196.
- [37] K. Wu, M. Debligny, C. Zhang, Room temperature gas sensors based on Ce doped TiO₂ nanocrystals for highly sensitive NH₃ detection, *Chemical Engineering Journal* 444 (2022).
- [38] G. Jeevitha, R. Abhinayaa, D. Mangalaraj, N. Ponpandian, P. Meena, V. Mounasamy, S. Madanagurusamy, Porous reduced graphene oxide (rGO)/WO₃ nanocomposites for the enhanced detection of NH₃ at room temperature, *Nanoscale Adv* 1 (2019) 1799–1811.
- [39] D.A. Vinnik, A.S. Semisalova, L.S. Mashkovtseva, A.K. Yakushechkina, S. Nemrava, S.A. Gudkova, D.A. Zhrebtsov, N.S. Perov, L.I. Isaenko, R. Niewa, Growth, structural and magnetic characterization of Zn-substituted barium hexaferrite single crystals, *Mater Chem Phys* 163 (2015) 416–420.
- [40] S. Mesdaghi, M. Yousefi, M. Hossaini Sadr, A.R. Mahdavian, Effect of Sn⁴⁺-Zn²⁺-Co²⁺ doping on structural and magnetic properties of M-Type barium hexaferrites, *IEEE Trans Magn* 55 (2019).
- [41] S.K. Nandi, S.K. Nath, A.K.M.A. Hossain, J.U. Khan, Effect of Zn Doping on Structural and Magnetic Properties of Ba₄Ni_{2-x}Zn_xFe₃₆O₆₀ Hexaferrites, *J Supercond Nov Magn* 27 (2014) 2655–2662.
- [42] S.S.S. Afghahi, A. Shokuhfar, Two step synthesis, electromagnetic and microwave absorbing properties of FeCo@C core-shell nanostructure, *J Magn Mater* 370 (2014) 37–44.
- [43] R.D. Shannon, IUCr, Revised effective ionic radii and systematic studies of interatomic distances in halides and chalcogenides, *Urn:Issn:0567-7394* 32 (1976) 751–767.
- [44] D.A. Vinnik, D.A. Zhrebtsov, L.S. Mashkovtseva, S. Nemrava, A.S. Semisalova, D.M. Galimov, S.A. Gudkova, I. V. Chumanov, L.I. Isaenko, R. Niewa, Growth, structural and magnetic characterization of Co- and Ni-substituted barium hexaferrite single crystals, *J Alloys Compd* 628 (2015) 480–484.
- [45] V. V. Atuchin, D.A. Vinnik, T.A. Gavrilova, S.A. Gudkova, L.I. Isaenko, X. Jiang, L.D. Pokrovsky, I.P. Prosvirin, L.S. Mashkovtseva, Z. Lin, Flux Crystal Growth and the Electronic Structure of BaFe₁₂O₁₉ Hexaferrite, *Journal of Physical Chemistry C* 120 (2016) 5114–5123.
- [46] J. Wang, Q. Zhang, F. Deng, X. Luo, D.D. Dionysiou, Rapid toxicity elimination of organic pollutants by the photocatalysis of environment-friendly and magnetically recoverable step-scheme SnFe₂O₄/ZnFe₂O₄ nano-heterojunctions, *Chemical Engineering Journal* 379 (2020) 122264.
- [47] W. Qin, Z. Yuan, Y. Shen, R. Zhang, F. Meng, Phosphorus-doped porous perovskite LaFe_{1-x}PxO_{3-δ} nanosheets with rich surface oxygen vacancies for ppb level acetone sensing at low temperature, *Chemical Engineering Journal* 431 (2022) 134280.
- [48] C. Li, D. Ma, S. Mou, Y. Luo, B. Ma, S. Lu, G. Cui, Q. Li, Q. Liu, X. Sun, Porous LaFeO₃ nanofiber with oxygen vacancies as an efficient electrocatalyst for N₂ conversion to NH₃ under ambient conditions, *Journal of Energy Chemistry* 50 (2020) 402–408.

- [49] T. Das, S. Mojumder, S. Chakraborty, D. Saha, M. Pal, Beneficial effect of Sn doping on bismuth ferrite nanoparticle-based sensor for enhanced and highly selective detection of trace formaldehyde, *Appl Surf Sci* 602 (2022) 154340.
- [50] E.O. Filatova, A.S. Konashuk, Interpretation of the Changing the Band Gap of Al₂O₃ Depending on Its Crystalline Form: Connection with Different Local Symmetries, *Journal of Physical Chemistry C* 119 (2015) 20755–20761.
- [51] T. Kaur, S. Kumar, B.H. Bhat, A.K. Srivastava, Enhancement in physical properties of barium hexaferrite with substitution, *J Mater Res* 30 (2015) 2753–2762.
- [52] S. Mojumder, T. Das, S. Das, N. Chakraborty, D. Saha, M. Pal, Y and Al co-doped ZnO-nanopowder based ultrasensitive trace ethanol sensor: A potential breath analyzer for fatty liver disease and drunken driving detection, *Sens Actuators B Chem* 372 (2022) 132611..
- [53] W. Guo, L. Huang, X. Liu, J. Wang, J. Zhang, Enhanced isoprene gas sensing performance based on p-CaFe₂O₄/n-ZnFe₂O₄ heterojunction composites, *Sens Actuators B Chem* 354 (2022) 131243.
- [54] J. Wang, Q. Zhang, F. Deng, X. Luo, D.D. Dionysiou, Rapid toxicity elimination of organic pollutants by the photocatalysis of environment-friendly and magnetically recoverable step-scheme SnFe₂O₄/ZnFe₂O₄ nano-heterojunctions, *Chemical Engineering Journal* 379 (2020) 122264.
- [55] J. Yang, W. Han, J. Ma, C. Wang, K. Shimanoe, S. Zhang, Y. Sun, P. Cheng, Y. Wang, H. Zhang, G. Lu, Sn doping effect on NiO hollow nanofibers based gas sensors about the humidity dependence for triethylamine detection, *Sens Actuators B Chem* 340 (2021) 129971.
- [56] H. Fang, S. Li, H. Zhao, J. Deng, D. Wang, J. Li, Enhanced NO₂ gas sensing performance by hierarchical CuO–Co₃O₄ spheres, *Sens Actuators B Chem* 352 (2022) 131068.
- [57] M. Yang, J. Lu, X. Wang, H. Zhang, F. Chen, J. Sun, J. Yang, Y. Sun, G. Lu, Acetone sensors with high stability to humidity changes based on Ru-doped NiO flower-like microspheres, *Sens Actuators B Chem* 313 (2020) 127965.
- [58] M. Sinha, R. Mahapatra, B. Mondal, T. Maruyama, R. Ghosh, Ultrafast and Reversible Gas-Sensing Properties of ZnO Nanowire Arrays Grown by Hydrothermal Technique, *Journal of Physical Chemistry C* 120 (2016) 3019–3025.
- [59] S. Mojumder, T. Das, M. Mukherjee, D. Saha, A. Datta, M. Pal, Development of highly sensitive and selective trace acetone sensor using perovskite yttrium ferrite: Mechanism, kinetics and phase dependence study, *Chemical Engineering Journal* 477 (2023) 146855.
- [60] S. Chakraborty, M. Pal, Highly selective and stable acetone sensor based on chemically prepared bismuth ferrite nanoparticles, *J Alloys Compd* 787 (2019) 1204–1211.
- [61] S. Li, Y. Diao, Z. Yang, J. He, J. Wang, C. Liu, F. Liu, H. Lu, X. Yan, P. Sun, G. Lu, Enhanced room temperature gas sensor based on Au-loaded mesoporous In₂O₃ nanospheres@polyaniline core-shell nanohybrid assembled on flexible PET substrate for NH₃ detection, *Sens Actuators B Chem* 276 (2018) 526–533.
- [62] X. Zhu, X. Chang, S. Tang, X. Chen, W. Gao, S. Niu, J. Li, Y. Jiang, S. Sun, Humidity-Tolerant Chemiresistive Gas Sensors Based on Hydrophobic CeO₂/SnO₂ Heterostructure Films, *ACS Appl Mater Interfaces* 14 (2022) 25680–25692.
- [63] Z. Liu, T. He, H. Sun, B. Huang, X. Li, Layered MXene heterostructured with In₂O₃ nanoparticles for ammonia sensors at room temperature, *Sens Actuators B Chem* 365 (2022) 131918.
- [64] J. Zawadzki, M. Wiśniewski, K. Skowrońska, Heterogeneous reactions of NO₂ and NO–O₂ on the surface of carbons, *Carbon N Y* 41 (2003) 235–246.
- [65] F.J. Meng, X.M. Guo, Tuning the oxygen defects and Fermi levels via In³⁺ doping in SnO₂-In₂O₃ nanocomposite for efficient CO detection, *Sens Actuators B Chem* 357 (2022) 131412.

- [66] S. Corby, L. Francàs, A. Kafizas, J.R. Durrant, Determining the role of oxygen vacancies in the photoelectrocatalytic performance of WO₃ for water oxidation, *Chem Sci* 11 (2020) 2907–2914.
- [67] J. Huang, Y. Wang, X. Liu, Y. Li, X. Hu, B. He, Z. Shu, Z. Li, Y. Zhao, Synergistically enhanced charge separation in BiFeO₃/Sn:TiO₂ nanorod photoanode via bulk and surface dual modifications, *Nano Energy* 59 (2019) 33–40.
- [68] Z. Dong, Q. Hu, H. Liu, Y. Wu, Z. Ma, Y. Fan, R. Li, J. Xu, X. Wang, 3D flower-like Ni doped CeO₂ based gas sensor for H₂S detection and its sensitive mechanism, *Sens Actuators B Chem* 357 (2022) 131227.
- [69] M. Yang, J. Lu, X. Wang, H. Zhang, F. Chen, J. Sun, J. Yang, Y. Sun, G. Lu, Acetone sensors with high stability to humidity changes based on Ru-doped NiO flower-like microspheres, *Sens Actuators B Chem* 313 (2020) 127965.
- [70] J. Yang, W. Han, J. Ma, C. Wang, K. Shimanoe, S. Zhang, Y. Sun, P. Cheng, Y. Wang, H. Zhang, G. Lu, Sn doping effect on NiO hollow nanofibers based gas sensors about the humidity dependence for triethylamine detection, *Sens Actuators B Chem* 340 (2021) 129971.
- [71] G.N. Gerasimov, V.F. Gromov, M.I. Ikim, O.J. Ilegbusi, S.A. Ozerin, L.I. Trakhtenberg, Structure and gas-sensing properties of SnO₂-In₂O₃ nanocomposites synthesized by impregnation method, *Sens Actuators B Chem* 320 (2020) 128406.
- [72] L. Zhang, J. Zhao, H. Lu, L. Li, J. Zheng, J. Zhang, H. Li, Z. Zhu, Highly sensitive and selective dimethylamine sensors based on hierarchical ZnO architectures composed of nanorods and nanosheet-assembled microspheres, *Sens Actuators B Chem* 171–172 (2012) 1101–1109.

CHAPTER 4

Beneficial effect of Sn doping on bismuth ferrite nanoparticle-based sensor for enhanced and highly selective detection of trace formaldehyde



This work is published in “Applied Surface Science 602 (2022) 154340”

4.1. Introduction

Among various air pollutants formaldehyde (HCHO) is very common due to its wide usage in chemical production, wooden and plastic furniture, adhesives, flooring materials, coating and insulating materials, cosmetics and rubber production etc. [1,2]. Long term exposure to formaldehyde at concentration 0.4-1.0 ppm can cause serious health problems such as mucosal inflammation, throat pain, vomiting, nausea, pulmonary edema, bronchospasm, encephaloma and so on, commonly referred as sick building syndrome [3]. Exposure to higher concentration of formaldehyde (above 3ppm) can damage immune system and the central nervous system [4,5]. Moreover, exposure to concentration above 6ppm can even cause nasopharyngeal and myeloid leukemia and pulmonary damage [6,7]. Due to its high toxicity, formaldehyde has been categorized as a potent carcinogenic agent [8,9]. Therefore, it has become a necessity to develop high performance, stable and very selective formaldehyde sensors to monitor indoor and outdoor air quality.

Chemiresistive gas sensors are known to be one of the most cost effective and low maintenance ways for the detection of formaldehyde concentration in air. Numerous efforts have been made over the past several years to find formaldehyde detecting material suitable for practical application. Various metal oxide semiconductor-based sensors have been reported in literature viz. SnO_2 [10,11], NiO [12], ZnO [13], In_2O_3 [14] to detect formaldehyde in indoor environments. Several approaches such as, changing the morphology [15,16], developing heterojunctions [17,18], loading with noble metal as catalysts [19], extrinsic doping with suitable metals [20-24] have been made to achieve better sensitivity and selectivity of the metal oxide semiconductor (MOS) formaldehyde sensors. Among these approaches, doping with suitable metal oxide in the MOS structure demonstrated plausible results. Study revealed that, doping NiO with Sn can improve HCHO sensing performance by electron compensation mechanism [4].

In the recent years, trinary metal oxides have emerged as excellent gas sensors owing to their excellent stability and reliability in gas sensing properties compared to conventional binary metal oxide gas sensors [25]. BiFeO_3 (BFO) is a well-known multiferroic perovskite ferrite which has gained increasing attention due to its application in different areas such as memory, spintronics and magnetoelectronic sensor devices [26]. However, despite its multifunctional use in different fields, gas sensing properties of BFO has not been explored widely. BFO exhibits p-type semiconducting properties with a bandgap 2.2-2.8 eV. Of late,

due to its tunable bandgap, excellent thermal stability and transport property, BFO has emerged as very promising gas sensing material. As of now, BFO has been investigated for its reasonably high response to various gases viz. CO, acetone, ethanol, LPG, SO₂ etc. [27-31].

Surface electronic state modification by means of doping is known to be an effective approach in improving gas sensing properties and selectivity of metal oxides. For example, significant increase in ethanol sensing capability has been observed by doping BFO with barium [32]. Another work by Waghmare et al. also demonstrated H₂ and NO₂ sensing property of W doped BFO nanocrystalline thin films [33]. Sn is a widely known dopant with a strong proficiency in activating and catalysing surface reaction process of gas sensing materials and consequently improving its performance. Sn doping approach has been adopted in various reports in order to modify different gas (viz. TMA, xylene, ethanol, hydrogen) sensing properties of metal oxide nanomaterials. The reports demonstrate that, a great enhancement in xylene sensing property have been observed upon modifying the structure of NiO with Sn dopant [34,35]. Therefore, we have undertaken our investigation of effect of Sn doping on formaldehyde sensing properties of BFO nanoparticles. A comparison of formaldehyde sensing performance of different sensing materials as reported in literature is listed in Table 4.1. On the basis of literature survey, we have found out that although there are many formaldehyde sensors reported in literature the greatest challenge for the sensors for monitoring indoor air quality is their slow response/recovery time [11, 15-23, 36-45]. Long-time stability measurement of the sensors for over six months is rarely studied [11, 15-18, 20, 23, 41,43]. Most of the sensors are unable to detect formaldehyde gas concentration down to the range of ppb [36-39,42-43]. Achieving good selectivity against relevant interfering volatile organic compounds (VOCs) present in indoor air which act as hinderance to the sensor while detecting HCHO is still a problem [11, 21].

In the present work, we are reporting the effect of doping the Fe-site of BFO with Sn on its gas sensing property, using formaldehyde as target gas. The pure BFO and Sn-doped BFO nanoparticles were synthesised via facile sol-gel technique with an aim to investigate its formaldehyde sensing properties. Compared to pure BFO nanoparticles-based sensor, we were able to achieve much higher response, rapid response/recovery time and good selectivity to sub-ppm level concentration of formaldehyde, with very low interference from VOCs viz, ammonia, ethanol, acetone, methanol, benzene, toluene and xylene. Influence of different concentration of Sn doping on sensing property has been studied. The enhanced formaldehyde sensing property of the as-synthesized Sn doped BFO nanoparticles-based sensors was

explained by doping induced modification of surface electronic states and hole concentration in accumulation layer.

Table 4.1 Comparison of formaldehyde gas sensing performance of sensors based of different materials.

Material	Operating temp. (°C)	Response time	Recovery time	Lower detection limit	Response (R_g/R_a)	Ref
SnO ₂	200	2.5s	52s	—	13 (20 ppm)	[10]
SnO ₂	230	53s	60s	1ppm	2.5 (1ppm)	[11]
Co ₃ O ₄ /CoFe ₂ O ₄	139	4s	9s	300 ppb	12.7 (10 ppm)	[15]
Co ₃ O ₄ –ZnO	220	6s	9s	—	~5.1 (100 ppm)	[16]
NiO–SnO ₂	100	44s	7s	0.5ppm	2.4 (0.5ppm)	[17]
SnO ₂ /NiO	230	107s	10s	1ppm	3.072 (5ppm)	[18]
Ag–LaFeO ₃	70	65s	60s	1ppm	25(1ppm)	[19]
Y-doped SnO ₂	180	8s	25s	1ppm	18 (50 ppm)	[20]
Zn-doped NiO	200	9min	13min	74ppb	~140 (1.4 ppm)	[21]
Y–ZnO	300	4s	6s	—	65.7 (50 ppm)	[22]
CdO activated Sn–ZnO	200	5min	—	1ppm	10 (1 ppm)	[23]
In ₂ O ₃	230	100s	70s	—	80 (100 ppm)	[36]
Zn–LaFeO ₃	250	100s	100s	100ppm	38 (100ppm)	[37]
La–Bi–Fe–O	100	5s	30s	5ppm	23.3(50ppm)	[38]
Co ₃ O ₄	170	46s	98s	10ppm	12 (100ppm)	[39]
α -Fe ₂ O ₃	300	63s	395s	50ppb	5.2 (1ppm)	[40]
Ag@Pt@ZnO nanowires	280	162s	225s	3.5 ppb	0.262 (240ppb)	[41]
Ca–ZnO	250	—	—	1ppm	5.28 (5ppm)	[42]
ZIF-8/MWCNT	RT	12s	—	4.38 ppm	3.08 (100ppm)	[43]
LaFeO ₃	120	>5min	>5min	50ppb	1.35 (1ppm)	[44]
BiFeO ₃	240	20s	14s	2ppm	3.1 (25ppm)	[45]
Sn–BiFeO ₃	280	2.71s	25.22s	100ppb	3.05(1ppm)	Current work

4.2. Experimental section

4.2.1. Materials and reagents

Bismuth nitrate pentahydrate ($\text{Bi}(\text{NO}_3)_3 \cdot 5\text{H}_2\text{O}$), iron (III) nitrate nonahydrate ($\text{Fe}(\text{NO}_3)_3 \cdot 9\text{H}_2\text{O}$), tin (IV) chloride pentahydrate ($\text{SnCl}_4 \cdot 5\text{H}_2\text{O}$), tartaric acid ($\text{C}_4\text{H}_6\text{O}_6$), nitric acid were purchased from Merck India. The chemicals were used as received without further purification for the synthesis.

4.2.2. Synthesis of Sn doped bismuth ferrite nanoparticles

Pure and 1%, 1.5%, 2% Sn-doped BFO nanoparticles were synthesized via sol-gel technique. Stoichiometric amount of bismuth nitrate pentahydrate ($\text{Bi}(\text{NO}_3)_3 \cdot 5\text{H}_2\text{O}$), iron nitrate nonahydrate ($\text{Fe}(\text{NO}_3)_3 \cdot 9\text{H}_2\text{O}$), tin chloride pentahydrate ($\text{SnCl}_4 \cdot 5\text{H}_2\text{O}$) were dissolved in double distilled water individually in separate beaker. Few drops of nitric acid were added to the bismuth nitrate solution. The precursor solution (sol) was prepared by mixing the above three solutions followed by stirring at 80 °C for one hour. Equimolar tartaric acid dissolved in distilled water was added to the mixture and stirred continuously to form a complete homogeneous solution. Then the sol was placed on a hot plate at 120 °C and stirred vigorously for 6h to form a viscous gel. The gel was then placed in an oven at 100 °C overnight to dry completely. Finally, the dried gel was ground well followed by calcination at 600 °C for 2 h in air in an oven. The schematic diagram of the synthesis process is presented in Fig.4.1 for clarity.

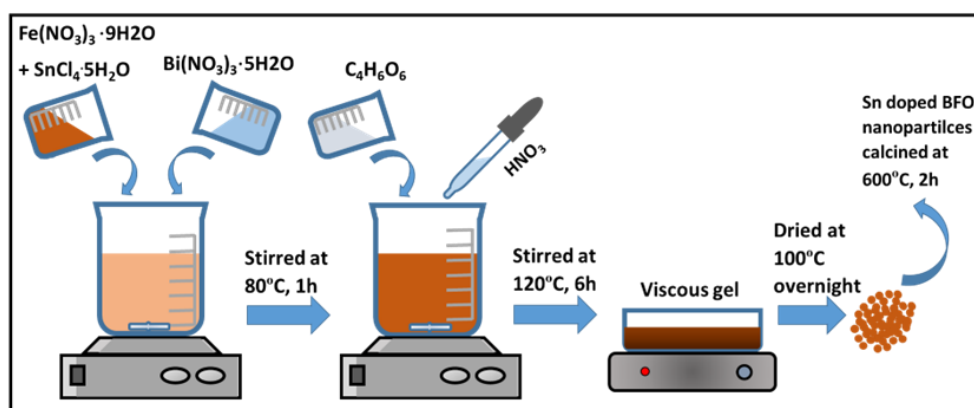


Fig. 4.1. Schematic diagram of Sn doped BFO nanoparticles synthesis process.

4.2.3. Characterization of materials

To study the crystal structure and phase composition of the synthesized powder, X-ray diffraction (XRD) patterns were recorded with an X'pert Pro MPD XRD PANalytical diffractometer using nickel filtered Cu-K α radiation ($\lambda=0.15404\text{nm}$). The surface morphologies of the samples were examined by using field-emission scanning electron microscopy (FESEM) (Carl Zeiss make Supra 35 VP microscope) operated at 10 kV accelerating voltage. Further investigation on particle size and lattice fringe was done using Tecnai G² 30ST (FEI) transmission electron microscope (TEM) and high-resolution transmission electron microscopy (HRTEM) operating at 300kV. Elemental characterisation was done with Energy Dispersive X-ray Spectroscopy (EDS) equipped with TEM. UV-Vis-NIR spectrometer (Shimadzu, UV-3600) was used to measure the optical band gap of the prepared material. Specific surface area of the samples was measured using Brunauer-Emmett-Teller (BET) surface area analysing technique (NovaWin, Quantachrome Instruments). Pore size distribution was evaluated using Barrett–Joyner–Halenda (BJH) method. For X-ray photoelectron spectroscopy (XPS) study of the material PHI 5000 Versa Probe II scanning XPS microprobe (ULVAC-PHI, U.S) with monochromatic AlK α ($h\nu=1486.6\text{ eV}$) radiations with a beam size of 100 μm was used. The current voltage (I-V) characteristics at room temperature was studied using an Agilent source meter B2901A. Presence of different functional bonds in the sample was investigated with Fourier Transform Infrared Spectroscopy (FTIR) (Nicolet 380 FTIR spectrometer). To record Photoluminescence (PL) spectra a fluorescence spectrophotometer (PL, F-7000, Japan) was used. Gas sensing study was performed using Agilent 34461A digital multimeter.

4.2.4. Fabrication of chemiresistive sensor module and gas measurement setup

Taguchi-type gas sensor module was used for sensing study. Cylindrical α -alumina hollow tubes of length 3.5 mm, 1 mm outer diameter, and 0.5 mm inner diameter, with gold electrodes, were used as substrates to fabricate the sensor modules. Pt-wires were attached to the substrate with conducting gold paste as electrodes to make the electrical contact. 0.2g of as-synthesized material was mixed with isopropyl alcohol and grinded in a mortar and pestle to form a homogeneous slurry paste. When the slurry achieved required consistency, the slurry paste was then deposited drop wise on to the tube substrate to form a thick layer of sensing film. The Ni-Cr alloy coil was inserted into the tube substrate to use it as a heater for controlling the operating temperature of the sensor by applying voltage across it. The substrate was then dried in a

furnace at 100°C for 6h to remove the residual organic compounds and solvent. Then the coated substrate was mounted on a six-pin module having double mesh on top (200 mesh each). Following the same procedure, identical sensor modules have been fabricated using prepared nanoparticles (denoted as pure BFO, 1% Sn-BFO, 1.5% Sn-BFO, 2% Sn-BFO) for the ideal comparative study.

Different concentrations of VOCs for gas sensing property measurement were obtained by evaporating the calculated volume of test gas liquids using the formula given in eq. (1) as follows,

$$U = \frac{V \times M \times C}{22.4 \times d \times p} \times 10^{-6} \quad (1)$$

U refers to the injected volume of the liquid (μl), V is volume of the test chamber (ml), M is liquid molecular weight (g), C is liquid-vapor concentration (ppm), d is liquid specific gravity (g/cm³) and p is the purity of the gas liquid [46]. The obtained gas was purged through prepared sensors connected to a Keysight multimeter (34470A) through the base. The variation in sensor resistance was monitored with the multimeter interfaced with data logger software.

4.3. Results and discussion

4.3.1. Crystallographic structure and morphological analysis

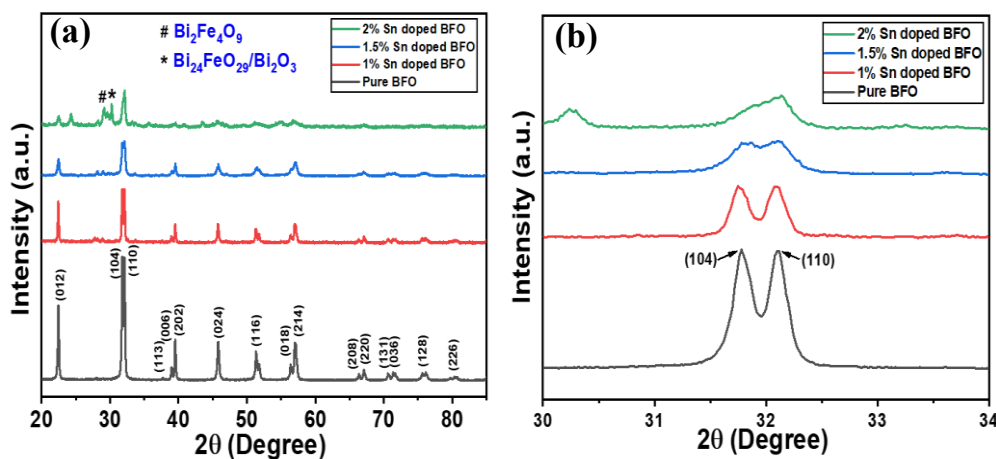


Fig. 4.2. (a) XRD spectra of pure, 1% Sn doped, 1.5% Sn doped, 2% Sn doped BFO nanoparticles, and (b) correspondingly magnified patterns around 2θ=32°.

The identification of crystal structure and crystal phase of the pure BFO and 1%, 1.5%, 2% Sn doped BFO nanoparticles were carried out using XRD technique and the observed

patterns are shown in Fig. 4.2a. All the diffraction peaks of pure BFO corresponding to various planes (hkl) are indexed to be rhombohedral BiFeO₃ with space group R3c (in accordance with JCPDS card no. 01-071-2494), indicating that highly pure crystalline phase was obtained. With low level of Sn doping namely, 1%, 1.5% samples, the diffraction patterns matched well with pure BFO, and no additional peaks belonging to secondary phases or any other impurities were observed, which demonstrates well incorporation of Sn dopant in BFO host. It can be observed that though the crystallographic structure does not change for 1%, 1.5% Sn doped samples yet, the intensity of the peaks is decreasing and FWHM is increasing with increasing Sn content. However, with further increase in Sn content, in 2% Sn doped sample, apart from the main BiFeO₃ peaks, few minor peaks belonging to secondary phases Bi₂Fe₄O₉ and Bi₂₅FeO₂₉ are visible in the 2θ range between 25° and 30°. Average crystallite size for pure and doped BFO nanoparticles was calculated from Debye-Scherrer formula (eq. (2)) using two highest peaks of the XRD spectra.

$$D = \frac{K\lambda}{\beta \cos \theta} \quad (2)$$

Where, D is crystallites size, K is shape factor (0.89), λ is the wavelength of the X-ray source (here, 0.15406nm), β is full width of the diffraction peak at half maximum for the diffraction angle 2θ (FWHM), and θ is the Bragg angle. The values of the average crystallite size of pure BFO and (1%, 1.5%, 2%) Sn-BFO were found to be 33.38nm, 30.04nm, 21.19nm, 22.06nm, respectively. This indicates that Sn substitution could influence grain growth. It is observed that the average crystallite size decreases with the Sn doping concentration, that may be attributed to insertion of Sn⁴⁺ ions (0.69Å) at B-site (Fe³⁺, 0.64Å) of BFO having a slight difference in their radii. In pure BFO peaks corresponding to (104) and (110) are clearly separated. The relative intensity of (012) peak is observed to decrease with increase of Sn doping. Furthermore, for the doped samples it can be seen that, in the vicinity of 2θ around 32°, doublet diffraction peaks corresponding to (104) and (110) merged to a single broad peak and shifted towards higher 2θ value with increasing Sn concentration (shown in Fig. 4.2b), as a result of substitution of Fe³⁺ (0.64Å) ion by Sn⁴⁺ (0.69Å) having a larger ionic radius [47].

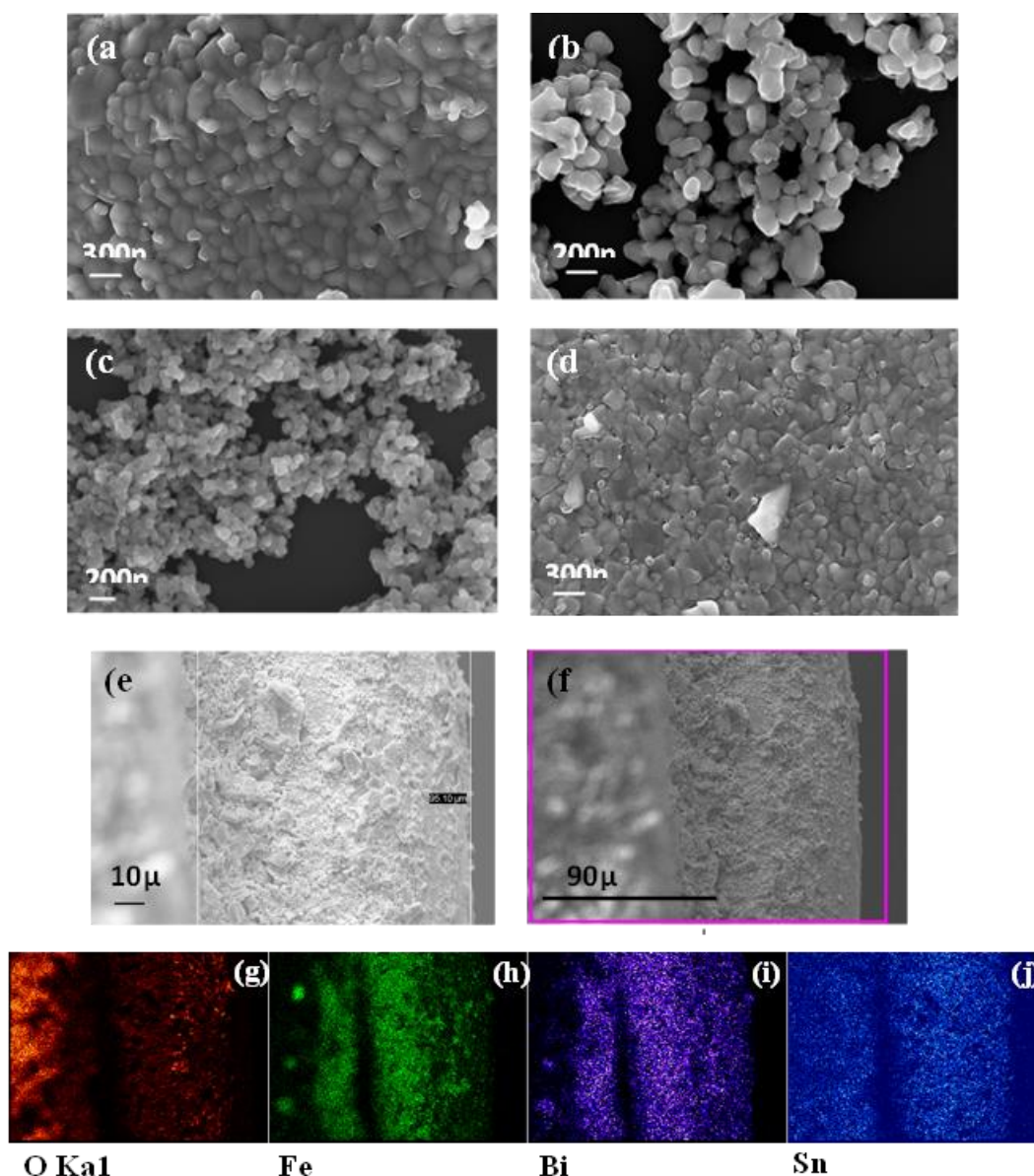


Fig. 4.3. FESEM image of (a) pure BFO, (b) 1% Sn-doped BFO, (c) 1.5% Sn-doped BFO, and (d) 2% Sn-doped BFO nanoparticles; (e) FESEM cross section of the 1.5% Sn-BFO sensor shows that the thickness of the sensing film is $\sim 95.1 \mu\text{m}$; and (f) FESEM image of the selected mapping area and the corresponding EDX colour mapping of (g) O, (h) Fe, (i) Bi, (j) Sn of 1.5% Sn-BFO sensor confirms the uniformity of doping.

Surface microstructure of the prepared samples was evaluated using FESEM. [Fig. 4.3 \(a-d\)](#) displays FESEM images of pure and Sn doped BFO nanoparticles. It is evident from the micrographs that the particles of pure BFO ([Fig. 4.3a](#)) are agglomerated and shape of nanoparticles is irregular and non-uniform. With 1.5% Sn doping ([Fig. 4.3c](#)), BFO nanoparticle appears to be more porous in structure and less agglomerated among all the samples. [Fig. 4.3e](#)

displays the SEM cross-section image of the 1.5% Sn-BFO sensor. It can be observed from the image that the thickness of the sensing film is $\sim 95.1\mu\text{m}$ (as calculated by using ImageJ software). The elemental composition of the sensing film based on 1.5% Sn-BFO is examined from Energy Dispersive X-Ray Spectroscopy (EDX) using FESEM. The EDX colour mapping of 1.5% Sn-BFO thick film sensor, displayed in Fig. 4.3(f-j), indicates that the Sn is distributed uniformly in the sample.

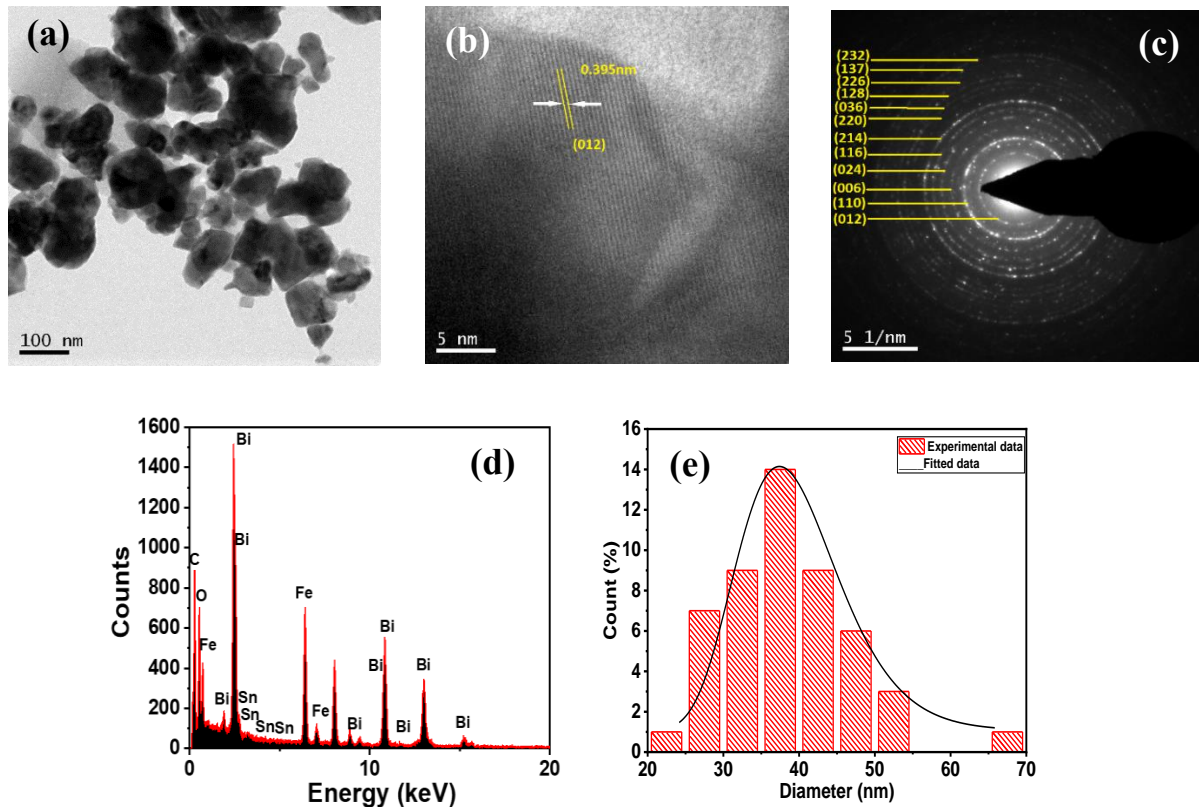


Fig. 4.4. (a) TEM image, (b) High resolution-TEM image, (c) SAED pattern, (d) EDS spectra, and (e) Particle size distribution profile of 1.5% Sn-doped bismuth ferrite nanoparticles.

TEM study of the 1.5% Sn-doped BFO nanoparticles was carried out for further observation on microstructure and size distribution. Fig. 4.4a shows the TEM image of the 1.5% Sn doped BFO nanoparticles. HRTEM image of the sample presented in Fig. 4.4b which delineates clear lattice fringes suggesting good crystallinity of the sample. Interplanar spacing of the lattice plane, calculated from the image, was found to be 0.395 nm which matched well with the (012) lattice plane of pure BFO (card no. 01-071-2494). The selected area electron diffraction (SAED) pattern of the sample is presented in Fig. 4.4c in which diffraction rings corresponding to different lattice planes are visible clearly and indexed. This further signifies high degree of

crystallinity of the 1.5% Sn doped BFO nanoparticles. Energy dispersive spectroscopy (EDS) was conducted to confirm the elemental composition of the sample (Fig. 4.4d). All the elements Bi, Sn, Fe, O are detected in the EDS spectra confirming the purity of the as-prepared sample. The peak of C appears due to the carbon-grid used during TEM experiment. From the particle size distribution profile, shown in Fig. 4.4e, the average particle size is found to be 38nm which corroborates the results of XRD study.

4.3.2. Chemical state and surface area analyses

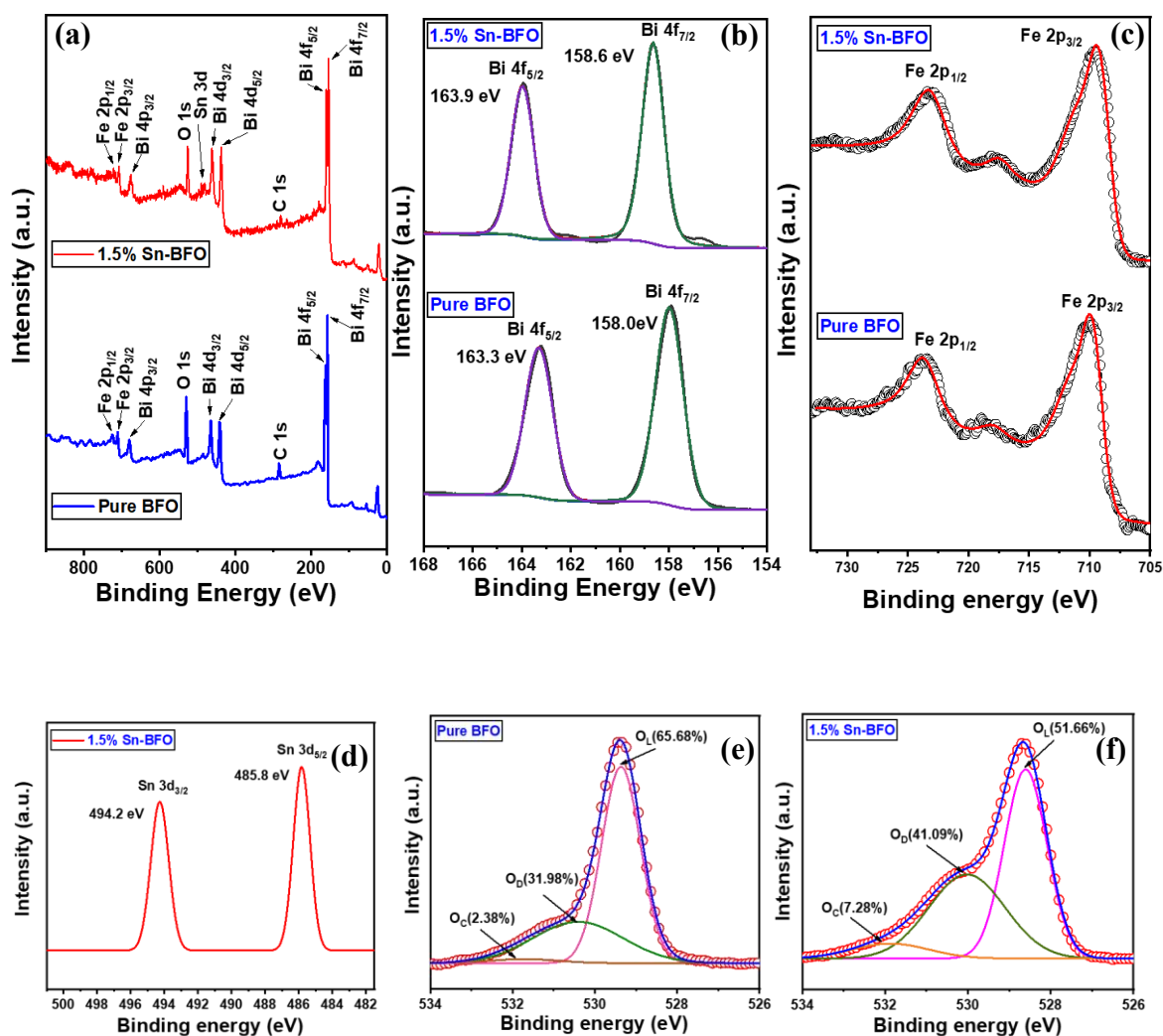


Fig. 4.5. (a) XPS wide scan spectra for pure and 1.5% Sn-doped BFO nanoparticles, respectively. High resolution XPS of (b) Bi 4f and (c) Fe 2p for pure and 1.5% Sn-doped BFO nanoparticles, respectively. (d) Sn 3d of the 1.5% Sn doped BFO nanoparticles. (e)-(f) O 1s core-level XPS spectra for different samples along with fitted peaks and calculated relative percentage of different oxygen sites.

Further study on the valence state and the effect of Sn doping on surface composition of the as-synthesized BFO nanoparticles was conducted using X-ray photoelectron spectroscopy (XPS). Fig. 4.5a represents survey scan spectra of pure and 1.5% Sn doped BFO nanoparticles which reveals the presence of the peaks corresponding to Fe 2p, Bi 4p, O 1s, Bi 4d, C 1s and Bi 4f. All the raw data of XPS were calibrated with respect to carbon (C) peak located at 284.8 eV. Presence of Sn 3d peak in 1.5% BFO XPS wide scan spectra reveals the presence of Sn in the 1.5% Sn doped sample. In Fig. 4.5(b-e) the high resolution XPS spectra of pure and 1.5% Sn doped BFO nanoparticles in the binding energy region of Bi 4f (b), Fe 2p (c), Sn 3d (d), O 1s (e-f) are displayed. In Bi 4f spectra doublet peaks observed at 158.0 eV /158.6 eV and 163.3 eV/163.9 eV can be assigned to the binding energies of Bi 4f_{7/2} and Bi 4f_{5/2}, respectively for both pure BFO and 1.5% Sn-BFO (represented in Fig. 4.5b). This clearly indicates the presence of Bi³⁺ in the samples [48]. The spin orbit splitting energy is 5.3 eV for both of the samples, this is in well agreement with the previous reports [49]. Fig. 4.5c represents the high-resolution spectra of Fe 2p of pure BFO and 1.5% Sn-BFO samples. Two major peaks located at binding energy 709.4 eV/710.0 eV and 723.3 eV/723.7 eV correspond to Fe 2p_{3/2} and Fe 2p_{1/2}, respectively. The presence of satellite peak around 717.5 eV indicates that the element Fe was in Fe³⁺ valence state in the samples [50]. Fe 2p peak shift of 1.5% Sn-BFO sample towards the higher binding energy by ~0.5 eV implies that Sn doping induces interaction between Fe and Sn. Fig. 4.5d displays the XPS spectra of Sn 3d region of 1.5% Sn doped BFO sample. The peaks observed at 485.8 and 494.2 eV correspond to the Sn 3d_{5/2} and Sn 3d_{3/2}, respectively. The distance between these two peaks is ~ 8.4 eV, that corresponds to the 3d binding energy of Sn (IV) ions, indicating that Sn is present in the sample in Sn⁴⁺ form [35]. Thus, XPS results are in well agreement with the EDS result obtained from TEM.

Fig. 4.5(e-f) display the O 1s core-level XPS spectra for pure BFO and 1.5% Sn doped BFO nanoparticles, respectively. The asymmetric O 1s spectra were fitted with Gaussian peaks and it is observed that all O 1s spectra comprised three symmetrical peaks. This indicates that there are three oxygen species present on the surface of the prepared materials; namely lattice oxygen (O_L: ~529.3 eV), oxygen deficient sites (O_D: ~530.1 eV) and surface chemisorbed oxygen (O_C: ~531.8 eV), respectively. The lattice oxygen peak around 529.0 eV can be attributed to the presence of O²⁻ ions in the metal oxides. The O_D peak around 530.0 eV can be attributed to the oxygen deficient regions which arises due to loss of oxygen in the sample. The O_C peak in the vicinity of 532.0 eV is due to the chemisorbed oxygen species (O⁻) at the surface of the metal oxide [35]. The relative lattice oxygen sites (O_L) percentages are 65.68% and 51.66%, the

oxygen deficient sites (O_D) percentages are 31.98% and 41.09%, and the chemisorbed oxygen (O_C) percentages are 2.38 % and 7.28 % in the pure BFO and 1.5% Sn-BFO, respectively (Table 4.3). The formation of oxygen vacancy defect-sites may be attributed to the substitution of Sn^{4+} in the Fe^{3+} site of $BiFeO_3$ as result of maintaining the charge neutrality of the material. The effect of distribution of oxygen species on the sensing property of the material is discussed later in this report.

The porous structure and the surface area of the materials were measured by N_2 adsorption-desorption isotherms using Brunauer-Emmett-Teller (BET) method. The N_2 adsorption-desorption isotherms of all the samples are displayed in Fig. 4.6(a-d). Pore volume of the samples are calculated using Barrett-Joyner-Halenda (BJH) pore size distribution plot. The pore size distribution curves of all samples are displayed in Fig. 4.6(a-d) (inset). BET surface area, pore volume and average pore diameter of the samples are summarized in Table 4.2. Observations reveal that the surface area of BFO has increased after doping with Sn. As shown in Table 4.2, 1.5% Sn-BFO has largest surface area ($10.02 \text{ m}^2/\text{g}$), pore volume ($0.1044 \text{ cm}^3/\text{g}$) and pore diameter (64.43 nm) among all the samples. Compared to the other samples this increase in surface area and pore size of 1.5% Sn-BFO contribute to the enhanced formaldehyde sensing performance by providing more adsorption-desorption sites for the gas molecules. However, the decrease in surface area of 2% Sn-BFO is significant which will lead to its lower sensing performance compared to 1.5% Sn-BFO.

Table 4.2 BET surface area, pore volume (V) and average pore diameter (D) analysis of the samples.

Sample	BET surface area (m^2/g)	Pore volume (cm^3/g)	Average pore diameter (nm)
Pure-BFO	2.06	0.0087	53.32
1% Sn-BFO	8.87	0.1042	53.30
1.5% Sn-BFO	10.02	0.1044	64.43
2% Sn-BFO	4.00	0.0350	38.59

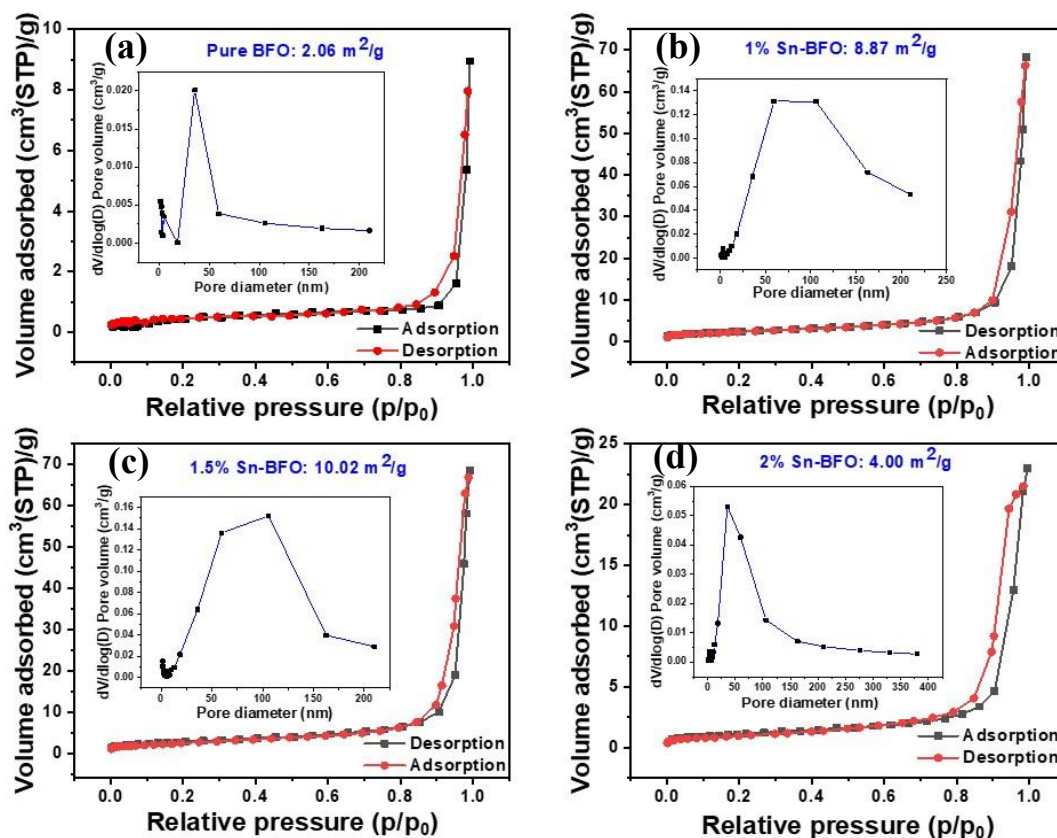


Fig. 4.6. N₂ adsorption-desorption isotherms and corresponding BJH pore size distribution curve (inset) of (a) Pure-BFO, (b) 1% Sn-BFO, (c) 1.5% Sn-BFO and (d) 2% Sn-BFO.

4.3.3. FTIR spectra analysis and band gap measurement

Room temperature FTIR band was recorded in the range of 400–4000 cm⁻¹ in the transmittance mode to investigate the presence of characteristic functional groups and bonds in the synthesized samples. Fig.4.7 displays the FTIR spectra of pure, 1% Sn-doped, 1.5% Sn-doped and 2% Sn-doped BFO nanoparticles. The presence of metal-oxygen bands was observed in the range 400-600cm⁻¹. Strong adsorption peaks were observed at ~555cm⁻¹ and ~435cm⁻¹ for all samples. The band ~555cm⁻¹ corresponds to the characteristic stretching vibration of Fe-O bonds confirming the presence of FeO₆ octahedron and the band near ~435cm⁻¹ ascribes to the Bi-O bonds confirming the presence of BiO₆ octahedral structure in the samples [51]. The band appearing at 1634cm⁻¹ is attributed to C=O vibrations. The band near 1076cm⁻¹ is due to the vibration of carbonate groups [52]. The broad bands in the range from 3000-3600cm⁻¹ arose from anti-symmetric and symmetric stretching of H₂O and O-H bond groups originating from condensed ambient water [53]. No significant shift of absorption bands is observed due to Sn doping.

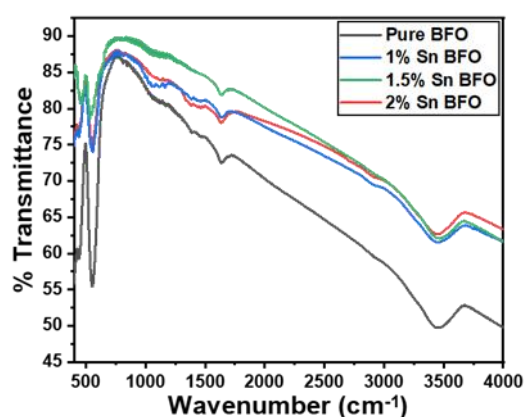


Fig. 4.7. FTIR spectra of pure BFO, and 1%, 1.5%, 2% Sn-doped BFO nanoparticles.

The effect of Sn doping on the optical absorption of BFO was also investigated by using UV-vis spectroscopy at room temperature. Fig. 4.8a displays the absorbance curves of pure and all Sn doped BFO nanoparticles. The absorption band edge of pure BFO nanoparticles was detected at around 607nm. Band gap for all the samples have been estimated from UV-vis spectra. The bandgaps of pure BFO, Sn doped BFO samples are presented in the form of bar diagram Fig. 4.8b. The pure BFO sample had bandgap of 2.04 eV and it increased after doping with Sn. The bandgap was observed to be maximum (2.21 eV) for the 1.5% Sn-doped sample. It shows that the bandgaps initially increase with Sn doping and then decreases after showing maxima at 1.5 % Sn sample. Similar trend was observed in previous reports where doping BFO with Sn increases the bandgap with increase in doping concentration [54]. The increase in bandgap with doping concentration of Sn can be ascribed to decreasing crystallite size of the particles of pure, 1% and 1.5% Sn doped BFO. Therefore, the results of UV spectroscopy analysis corroborate well with the results of FESEM and XRD analysis.

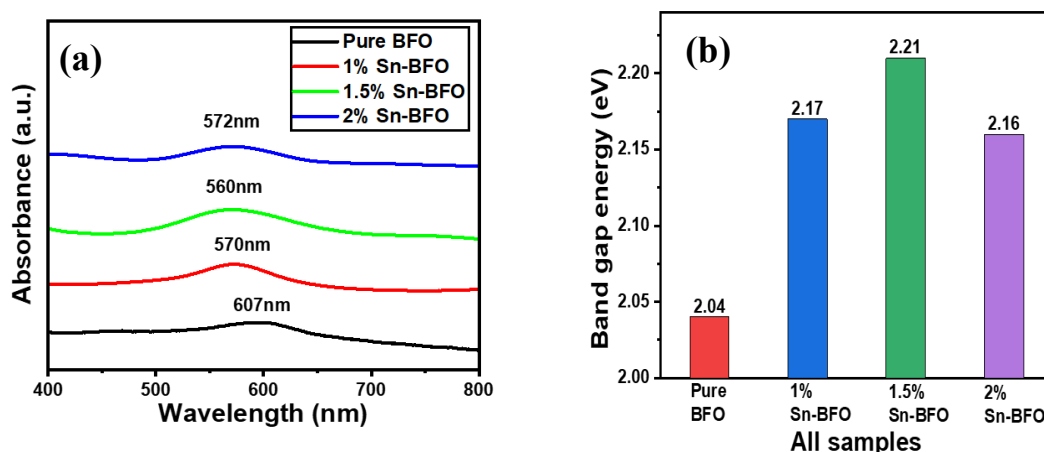


Fig. 4.8. (a) UV-vis absorption spectra of pure, 1%, 1.5%, 2% Sn-doped BFO nanoparticles, and (b) Estimated band gap values of the prepared pure and Sn doped BFO nanoparticles.

4.3.4. Electrical properties

Current-voltage (I-V) characteristics of 1.5% Sn BFO sensor was measured at different operating temperature viz. 260 °C, 280 °C, 300 °C, 350 °C by varying applied voltage from -40V to +40V in normal ambient (Fig. 4.9). It is evident from the linear relationship between the measured current and applied voltage that, ohmic-type contact was formed between the sensing material layer and the gold electrodes. No asymmetry was observed in forward and reverse voltage regions. It can be observed from the slopes of the curves that the conductivity of the material increased with increase in operating temperature that confirms the semiconducting behaviour of the material. The sensor was stable at all operating temperature indicating that the sensor can perform well at elevated temperature.

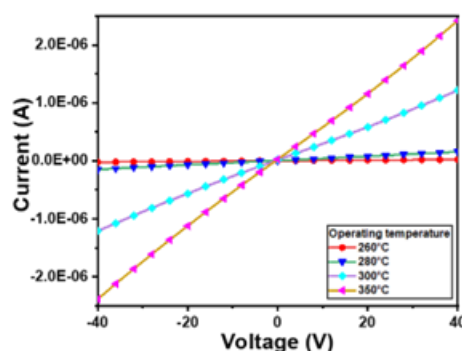


Fig. 4.9. Current-voltage characteristics of 1.5% Sn doped BFO nanoparticles at different operating temperatures.

4.3.5. Gas sensing properties

Semiconductor metal oxide based chemiresistive gas sensing is majorly a kinetically driven series of oxidation and reduction process in which an optimum operating temperature will lead to maximum rate of reaction. The gas sensing characteristics of pure BFO and (1%, 1.5%, 2%) Sn doped BFO nanoparticles-based sensors were measured by exposing the sensors to fixed concentration of target analyte (formaldehyde) while varying the operating temperature from 200 °C to 400 °C. When the sensors were exposed to formaldehyde (HCHO) vapour, the electrical resistance of the sensors increased which demonstrates that the samples possess p-type semiconducting property. The response of the fabricated sensor devices was calculated as a ratio of the resistance of the sensor in gaseous environment (R_{gas}) to that in the air (R_{air}) using the following relation,

$$S = \frac{R_{gas}}{R_{air}} \dots\dots\dots (3)$$

Fig. 4.10a represents variation in sensing response of all four sensors as a function of operating temperature in presence of 1ppm HCHO gas. It was observed that the response of all the sensors increased with the increase in temperature and reached a maximum value at temperature 280 °C. Response started to decrease on further increase in temperature. Further, all the doped samples delineate higher response than the pristine and achieved maximum for 1.5% Sn-BFO nanoparticles-based sensor. Sensing response for 2% Sn-BFO sensor was comparatively lower than that of 1.5% Sn-BFO. This may be due to the agglomerated nature of 2% Sn-BFO nanoparticles as observed from FESEM (Fig. 4.3d). Based on the aforementioned results, 1.5% Sn-BFO sensor was selected for further study at 280 °C operating temperature.

Fig. 4.10b shows dynamic response curves of 1.5% Sn-BFO sensor to various concentrations of HCHO (viz. 0.1, 0.2, 0.5ppm) at 280 °C operating temperature. From Fig. 4.10b it is very clear that the sensor exhibited completely reversible response, excellent reproducibility and good resolution for multiple repeated cycles to different concentrations of HCHO. Prepared sensor can detect HCHO up to 100 ppb with good response ($S=1.44$), which indicates the capability of sensor for monitoring sub ppm concentration of formaldehyde for the monitoring of indoor air quality. Moreover, the stability of the sensor was evaluated by exposing the sensor to 1ppm formaldehyde and continuously turning the gas on and off creating periodic cycles of exposure as shown in Fig. 4.10c. The sensor showed excellent stability towards 1ppm formaldehyde for eight consecutive cycles with a deviation of ± 0.02 in sensitivity ($S=R_g/R_a$), which is really insignificant Fig.4.10d. To further evaluate the sensing performance of 1.5%

Sn-BFO sensor, it was exposed to different concentration of HCHO. The response for various concentration of HCHO at operating temperature 280 °C is presented in Fig. 4.11a. The enhancement in response of 1.5% Sn BFO sensor is attributed to increased absorption efficiency of the material surface corresponding to increased surface area and porous structure of the surface (as shown in Fig. 4.6c).

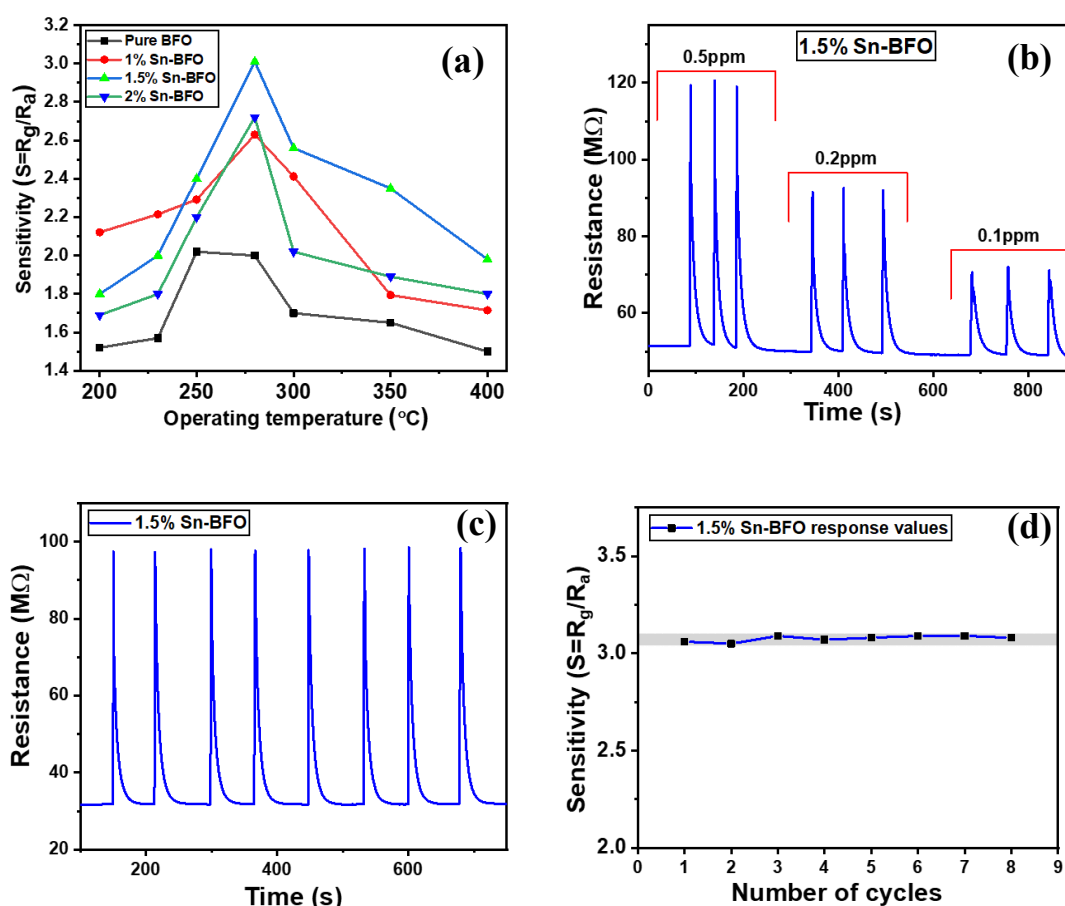


Fig. 4.10. (a) Variation in sensing response of pure BFO, 1% Sn-BFO, 1.5% Sn-BFO, 2% Sn-BFO nanoparticles-based sensors as a function of temperature in presence of 1ppm HCHO; (b) Real-time response transient curve of 1.5% Sn-BFO sensor for repeated cycles towards 0.1ppm, 0.2ppm, 0.5ppm HCHO at operating temperature of 280 °C; (c) Stable response of 1.5% Sn-BFO sensor towards 1ppm formaldehyde at 280 °C operating temperature for eight consecutive cycles and (b) Stability in the sensitivity data of 1.5% Sn-BFO sensor for eight cycles.

A comparison between sensing response of pure BFO and 1.5% Sn-BFO nanoparticles as a function of formaldehyde concentration is displayed in Fig. 4.11b. Upon exposure to 1ppm HCHO, the response magnitude of 1.5% Sn-BFO sensor was 3.05, that is 1.6 times greater than that of pure BFO sensor (which was 1.88). In presence of 100ppm HCHO, 1.5% Sn-BFO exhibited response 12.13 which is 2.4 times higher than that of pure BFO sensor ($S=5.05$). By comparing the response curves, it can be concluded that the 1.5% Sn doping on BFO nanoparticles improved the sensing activity of the material greatly. Moreover, the sensing response of Sn-BFO was observed to increase considerably with increase of HCHO concentration and did not saturate even when it was exposed to 100ppm of HCHO.

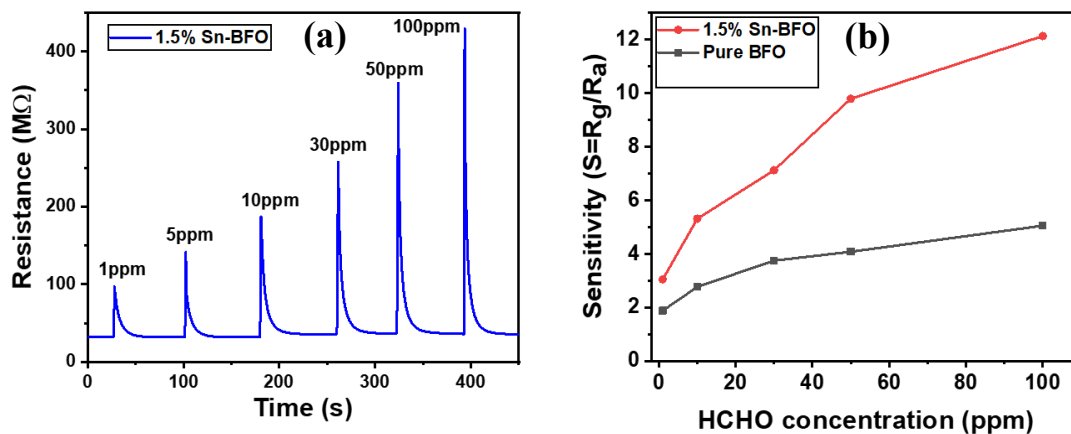


Fig. 4.11. (a) Dynamic response of 1.5% Sn-BFO to different concentrations of HCHO at 280 °C temperature, and (b) Comparison between the sensitivities of pure BFO and 1.5% Sn-BFO sensors to different HCHO concentrations at 280 °C temperature.

To estimate the transient response of the sensor, multi-exponential model of transient conductance is applied [25,28,55]. The transient conductance model considers the adsorption (decrease of conductance) and desorption (increase of conductance) phases of sensor response. The model is described mathematically as follows,

$$G(t) = G_0 + G_1 [\exp(-t/\tau_{response})] \quad \dots\dots\dots (4)$$

Here, G_0 is base conductance, $G(t)$ is the transient conductance of the sensor at a constant temperature, $\tau_{response}$ is the time constant of adsorption of HCHO.

Same model was used for the recovery process of the sensor,

$$G'(t) = G_0' + G_1' [1 - \exp(-t/\tau_{recovery})] \quad \dots\dots\dots (5)$$

G_0' is conductance at stable response value, $G'(t)$ is transient conductance during recovery of the sensor at a constant temperature, $\tau_{recovery}$ is the time constant of desorption of HCHO. From the fitting (shown in Fig. 4.12a), the response and recovery time is obtained as $\tau_{response}=2.71s$ and $\tau_{recovery}=25.22s$ for 1ppm HCHO at 280 °C. This confirms rapid interaction between HCHO and negatively charged oxygen species on the surface of the material. Response time taken by the sensor to 1ppm HCHO gas is relatively smaller compared to previous reports on HCHO sensors (Table 4.1).

The linear fitting of log (response) vs log (HCHO concentration) using Freundlich adsorption isotherm model is shown in Fig. 4.12b Freundlich adsorption isotherm equation is given in eq. (6) and (7) as follows,

$$S = \alpha C^\beta \quad (6)$$

The equation can be rewritten as follows,

$$\log(S) = \log(\alpha) + \beta \log(C) \quad (7)$$

here S is the response, α is the proportionality factor, β is the power law exponent and C is the concentration of formaldehyde (ppm) [28]. The fitting of response vs HCHO concentration with non-linear regression is shown inset of Fig. 4.12b. The correlation coefficient (R^2) is found to be 0.9917 for linear regression and 0.988 for non-linear regression. The fitting has greater R^2 value in linear regression. This demonstrates that, the response of the sensor increases linearly with increase in HCHO concentration and relationship between the response of the sensor and the concentration of formaldehyde is strongly correlated. The value of the correlation coefficient R^2 confirms the validity of the Freundlich isotherm for all concentrations of HCHO at temperature 280 °C. The value of β calculated from the gradient of slope is 0.29. It is known from previous literature that, the value of $\beta < 1$ indicates that the adsorption is dominated by physisorption [56]. The linear dependency between $\log(S)$ and $\log(C)$ implies reversible gas sensing mechanism.

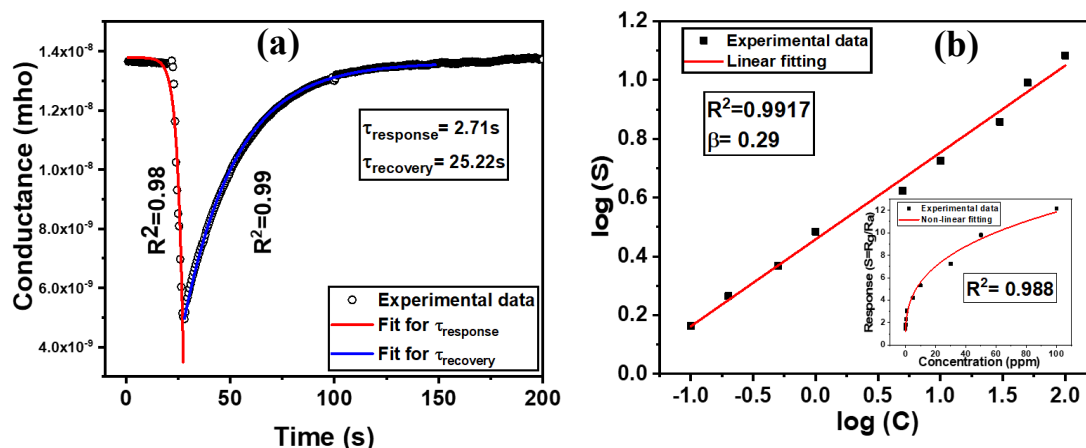


Fig. 4.12. (a) Fitting of conductance transient for response and recovery of 1.5% Sn-BFO sensor to 1 ppm HCHO at 280 °C using single-site Langmuir adsorption model; and (b) Fitting of experimental data of dynamic sensing response of 1.5% Sn-BFO sensor towards different concentration of HCHO (0.5-100ppm) at 280 °C using Freundlich isotherm equation with liner and non-liner (shown in inset) regression.

Selectivity is an important criterion for the evaluation of performance of a gas sensor. In order to verify the potential practical application of the sensor, the selectivity of the Sn-BFO based sensor was evaluated against different analytes such as ethanol, acetone, ammonia, benzene, toluene and xylene. These VOCs are the indoor gases that are produced by alcoholic beverages, cleaning products, leather products, furniture, paints and decorating materials etc. The sensor accomplished high selectivity against the aforementioned gases at 280 °C operating temperature. The very important factor influencing the selectivity of the sensor is bond dissociation energy of the target analytes. When the bond dissociation energy of the main functional groups in the target analyte is less, it promotes the reaction between the gas molecules and the adsorbed oxygen at the surface of the sensing material. The bond dissociation energy of formaldehyde is 364 kJ/mol which is comparatively lower than that of the other interfering analytes such as ethanol (458 kJ/mol), methanol (439 kJ/mol), acetone (393 kJ/mol), ammonia (435 kJ/mol), benzene (431 kJ/mol) and toluene (368 kJ/mol) [57,58]. Therefore, during the adsorption at the surface of the sensing material, formaldehyde is easily broken which leads to highest response of the sensor amongst the other potential interfering gases. It is known from previous studies that humidity affects electrical response of sensors. Therefore, the sensor's response to saturated moisture at 280 °C was measured to be 1.11 that shows the sensor is almost insensitive to moisture. Long term stability test under repeated

cycles were also performed for quite a long time (600 days) for checking the practical applicability of the sensor. Fig. 4.13b depicts that, no significant decrease in sensing performance was observed within first 300days. However, slight decreasing tendency was observed while measurement was conducted after 500 days. Altogether, the sensor exhibited remarkably stable response over long period of time.

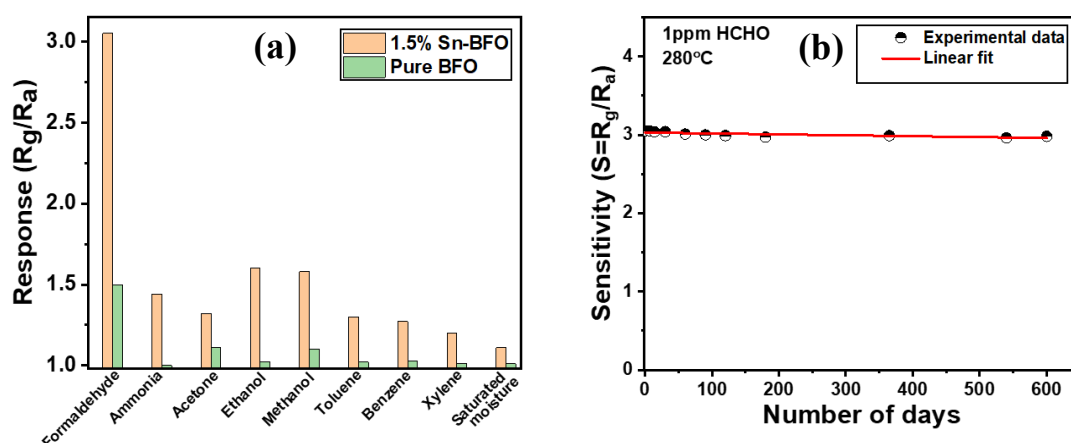


Fig. 4.13. (a) Comparison in the response of pure BFO and 1.5% Sn-BFO sensors to relevant test VOCs of concentration 1ppm and saturated moisture at 280 °C; and (b) Stability of 1.5% Sn-BFO sensor response to 1ppm HCHO at 280 °C within 600 days.

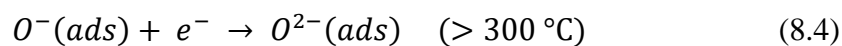
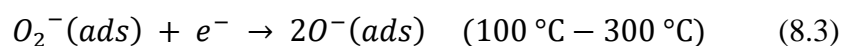
4.3.6. Performance comparison to other chemiresistive formaldehyde gas sensors

A comparison of formaldehyde gas sensing performance of as synthesized Sn doped BFO nanoparticle-based sensor with recently reported sensors are listed in Table 4.1. By comparing the sensing performance of formaldehyde sensors based on different sensing materials represented in Table 4.1, it is observed that the formaldehyde sensor based on BFO doped with Sn reported in this work exhibits excellent sensing properties along with most rapid response/recovery time (2.71s/25.22s) among all the other reported formaldehyde sensors listed in Table 4.1. Lower limit of detection of our sensor is 100 ppb which is remarkably superior to that of other p-type chemiresistive sensors as well. Even though there are a few ppb level sensors reported in literature [21,40,41,44], Sn-BFO sensor reported in this work has comparatively faster response/recovery time. Moreover, the sensor in our work produced long-term stable response data for the longest period of time (600 days) which is hardly seen in any other formaldehyde sensors reported in literature. In brief, notable stability for repetitive measurement, reproducibility of sensing data and impressive selectivity of the sensor for wide

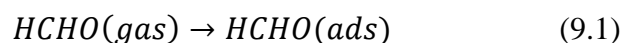
range of interfering gases (viz. ethanol, methanol, ammonia, acetone, toluene, benzene, xylene) shown in our work makes Sn doped BFO nanoparticles a very promising formaldehyde sensing material for indoor air quality monitoring.

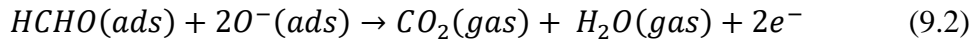
4.3.7. Mechanism of gas sensing

The gas sensing mechanism of semiconductor metal oxides is explained by interaction between the target gas molecules with the adsorbed oxygen species on the surface of the material. The surface interaction results in variation of charge carrier concentration of the semiconductor, that in turn causes change of conductance (or resistance) of the sensor. This interaction mechanism is greatly affected by the temperature of the material surface. When the sensor surface is exposed to air, at lower temperature (<100 °C) oxygen from the atmosphere gets physisorbed on the surface of the material and transforms into O_2^- by transferring holes to the valence band of the p-type semiconductor. When the temperature is relatively higher (100 °C -300 °C), the oxygen gets chemisorbed and transforms into O^- . This chemisorbed oxygen species O^- is more stable and reactive to different gases. When temperature is more than 300 °C, the O^- ions transform into O^{2-} . The oxygen adsorption process creates a hole accumulation layer on the semiconductor surface resulting in upward bending of the energy band near the surface. The adsorption process is described in the following eq. (8.1-8.4) [8,59,60],



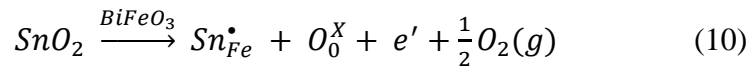
HCHO is known to be a reducing agent. As BFO is a p-type semiconductor, the majority charge transporters are holes. When the sensor surface is exposed to HCHO concentration at temperature 280 °C, reaction between HCHO and surface adsorbed O^- occurs and electrons are generated in the process (eq. 9.2). These electrons then recombine with the holes resulting in decrease conductivity of BFO. Therefore, increase in sensor resistance is observed that determines the gas response of the sensor. The corresponding reaction equations are given in eq. 9.1-9.3 as following [3,8],





When the HCHO gas flow is off, the partial pressure of HCHO decreases at the vicinity of the sensor surface, and fresh atmospheric oxygen molecules get re-adsorbed on the surface of BFO generating holes (h^+) in the valence band of BFO. This results in decrease in resistance of BFO back to its initial value. Thus, complete recovery of the sensor is achieved.

Enhancement of HCHO sensing response in Sn doped BFO sensors may be attributed to the combined action of variation of carrier concentration and defect oxygen species present at the sensor surface. At operating temperature 280 °C the average sensor resistance in air (R_a) of the pure BFO, 1% Sn-BFO, 1.5% Sn-BFO, 2% Sn-BFO sensors were observed as 30.5Mohm, 39Mohm, 45.2Mohm, 60.3Mohm, respectively. The response of the above sensors to 1ppm HCHO at 280 °C was 2, 2.63, 3.01 and 2.72, respectively. This increase in R_a and enhancement of sensing activity is closely related to the electronic compensation mechanism involved during the substitution of Sn. The substitution process of Sn^{4+} at the site of Fe^{3+} can be explained by the electronic compensation mechanism given in eq. (10) as following,



Where Sn_{Fe} represents Sn substituted in Fe site, O_0^X is oxygen ion with neutral charge [4,35,45]. In electronic compensation, one electron is generated to compensate the replacement of one Fe^{3+} by one Sn^{4+} . These electrons will recombine with holes and decrease carrier concentration, resulting in increase of resistance of the Sn-BFO sensors in air (R_a). Increase of R_a upon Sn doping corroborates with experimental results for Sn doped BFO. Oxygen molecules that are formed (as explained in eq. (10)) during electronic compensation mechanism are converted into negatively charged surface oxygen or interstitial oxygen [61].

As reported in literature [4,35], the gas response of the p-type sensor can be expressed as,

$$S = \frac{R_{gas}}{R_{air}} = \frac{p_{air}}{p_{gas}} = \frac{p_{air}}{p_{air}-\Delta p} = \frac{\Delta p}{p_{air}-\Delta p} + 1 \quad (11)$$

Here, p_{air} and p_{gas} are the hole concentration in the presence of air and test gas, respectively. $\Delta p = (p_{air} - p_{gas})$ is the change in hole concentration upon exposure to analyte (formaldehyde) gas. From eq. (11) it is evident that when the hole concentration in hole accumulation layer is lower, a higher sensing response of the Sn-BFO sensor towards formaldehyde gas can be achieved. For same number of electrons injected during the sensing

process, lower hole concentration in the hole accumulation layer in presence of air leads to larger variation in sensing resistance resulting in enhanced chemiresistive sensitivity of the sensor [4,35,61]. This happens due to the fact that carrier concentration is inversely proportional to mobility of the charge carriers. High carrier mobility is beneficial for the reaction between formaldehyde gas and chemisorbed oxygen on the surface and it helps in promoting the reaction between formaldehyde gas and the adsorbed oxygen on the surface [4]. This explains enhanced sensitivity of Sn doped BFO sensor compared to undoped BFO sensor. A schematic diagram of the formaldehyde sensing mechanism of pure and Sn doped BFO nanoparticles is presented in Fig. 4.14 a and b, respectively.

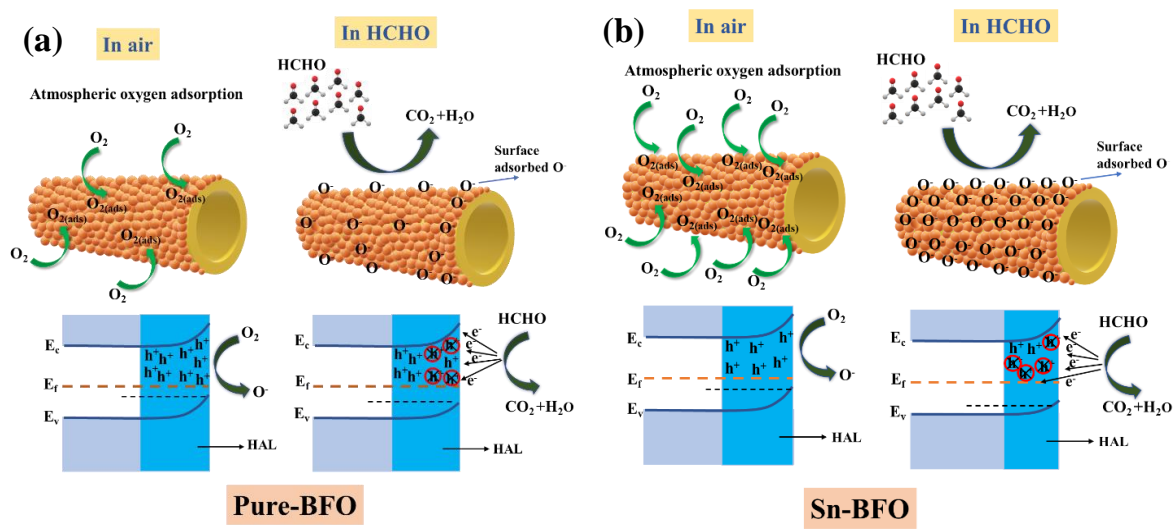


Fig. 4.14. Schematic illustration of the formaldehyde sensing mechanism of (a) pure BFO and (b) Sn doped BFO nanoparticles.

Table 4.3 Fitting results of O1s XPS spectra of pure BFO and 1.5% Sn-BFO samples.

Sample	Oxygen species	Binding energy (eV)	Percentage (%)
Pure BFO	O _L	529.4	65.68
	O _D	530.1	31.98
	O _C	531.0	2.38
1.5% Sn doped BFO	O _L	528.6	51.66
	O _D	530.0	41.09
	O _C	531.8	7.28

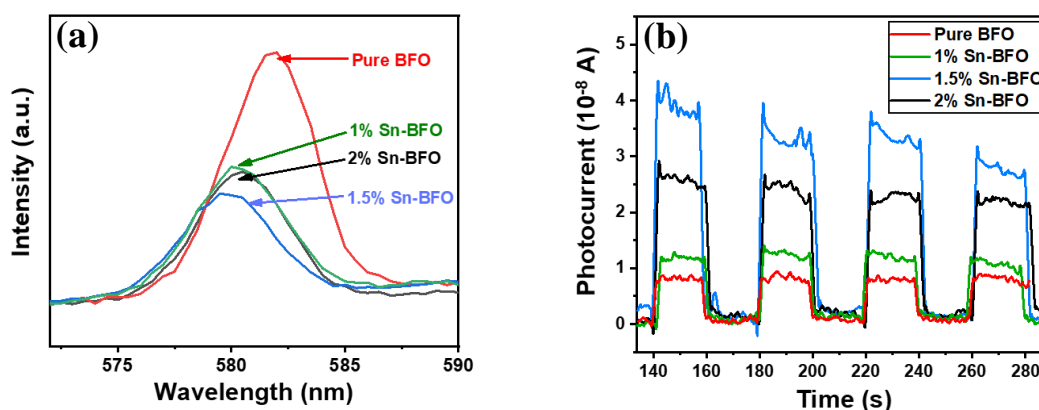


Fig. 4.15. (a) Room temperature PL spectra of the samples at excitation wavelength 425 nm, and (b) Transient photocurrent response of pure BFO, 1% Sn-BFO, 1.5% Sn-BFO and 2% Sn-BFO nanoparticles.

The effect of Sn doping on charge separation was verified using photoluminescence (PL) emission spectra and transient photocurrent response studies. To investigate the recombination efficiency of the electron-holes room temperature photoluminescence (PL) emission spectra was measured. As reported in literature, lower PL emission intensity is the indication of higher separation efficiency of photogenerated electron-hole pairs [62,63]. Room temperature PL spectra of pure BFO and doped BFO samples are shown in Fig. 4.15a. It is observed that intensity of the peaks decreased while Sn is incorporated in BFO. Which suggests that Sn doping is beneficial for promoting separation of electron-holes. The PL peak intensity decreased successively in the following order: pure BFO > 1% Sn-BFO > 2% Sn-BFO > 1.5% Sn-BFO. Accordingly, 1.5% Sn-BFO exhibits lowest PL peak intensity compared to other samples which demonstrates that it is most efficient in maintaining electron-hole separation and which gives rise to its highest sensitivity. In case of 2% Sn-BFO sample, PL emission intensity was higher which indicates its higher recombination rate than 1.5% Sn-BFO. The charge separation of photogenerated electron-holes in the materials was reconfirmed by transient photocurrent response studies shown in Fig. 4.15b. It is observed that Pure BFO demonstrates low output photocurrent which confirms its rapid electron-hole recombination. The photocurrents increased after Sn is introduced to the system and shows highest photocurrent response intensity for 1.5% Sn-BFO. This further indicates that 1.5% Sn-BFO possessed highest photoinduced charge separation efficiency [62].

Also, the charge difference between Sn^{4+} and Fe^{3+} will create many oxygen defects. Defect oxygen species will increase with increase in Sn concentration. These defects act as active sites

on the surface of the sensor and increases oxygen adsorption, that leads to higher sensing response. This can be further established by analysing O 1s core-level XPS spectra for pure BFO and 1.5% Sn doped BFO nanoparticles. By comparing the area ratio of the fitted peaks in Fig. 4.5(d-e), it was observed that, the relative intensity of the three oxygen species O_L , O_D and O_C changed in Sn doped BFO nanoparticles compared to that of the pure BFO nanoparticles. Change in percentage of different oxygen species is listed in Table 4.3. It is clear from the results that concentration of defect oxygen species (O_D) increased with increase in doping concentration. Doping BFO with Sn influences the generation of oxygen defects on the surface of the material. The ratio of relative percentage of chemisorbed oxygen species in pure BFO to 1.5% Sn-BFO was 2.38%: 7.28%. When the surface of the material is exposed to the target gas, the chemisorbed oxygen interacts with the gas molecules that enhances the gas sensing activity of Sn-BFO [19]. The relative percentage of oxygen defect sites (O_D) were 31.98% in pure BFO and was observed to increase to a value of 41.09% in 1.5% Sn-BFO sample. It is evident from the result of XPS analysis that, the oxygen defect sites increased and the lattice oxygen content decreased with increase in Sn doping concentration compared to the undoped BFO sample. Therefore, 1.5% Sn-BFO has highest defect oxygen concentration, which results in highest response towards formaldehyde. However, when the Sn doping content was increased by 2%, the surface layer of the BFO nanoparticles gets covered by Sn ions, which reduces the active sites. This explains decrease in sensing activity of 2% Sn-BFO sensor compared to 1.5% Sn-BFO sensor. Moreover, with increase in Sn doping concentration to 1.5%, the surface morphology of the nanoparticles changed. The average crystallite size was observed to decrease with increase in doping content. According to previous reports, sensitivity increases if average particle size decreases. As shown in Table 4.2, for 1.5% Sn-BFO increased surface area ($10.02 \text{ m}^2/\text{g}$) and pore volume ($0.1044 \text{ cm}^3/\text{g}$) contributed in enhancement of sensing property of the sensor by providing more active sites on the surface, that in turn enhanced formaldehyde gas response of the sensor. For 2% Sn-BFO significant decrease in surface area ($4.00 \text{ m}^2/\text{g}$) and pore volume ($0.0350 \text{ cm}^3/\text{g}$) explains its lower sensing performance compared to 1.5% Sn-BFO.

4.4. Conclusion

Pure and Sn-doped BFO nanoparticles have been synthesized using sol-gel route and their formaldehyde gas sensing performances have been investigated. It was observed that both pristine and Sn-doped BFO nanoparticles delineates p-type sensing and sensitivity enhances

more than 2.4 times towards formaldehyde gas when doped with Sn. As synthesised 1.5% Sn doped BFO nanoparticles-based sensor showed response around 3.01 towards 1ppm formaldehyde gas at 280 °C operating temperature, with a fast response/recovery time of 2.71s/25.22s, good selectivity, resolution, detection limit down to 100ppb and exceptional 600 days stability. Experimental results suggest that creation of more oxygen defects and extra electron due to Sn doping is responsible for enhanced sensing activity. The observations showed that, Sn-doped BFO nanoparticles-based sensor is a promising candidate for development of high-performance formaldehyde sensing device for the monitoring of indoor air quality.

4.5. References

- [1] K. Kawamura, K. Kerman, M. Fujihara, N. Nagatani, T. Hashiba, E. Tamiya, Development of a novel hand-held formaldehyde gas sensor for the rapid detection of sick building syndrome, *Sens. Actuators B: Chem.*, 105 (2005) 495–501.
- [2] W. Wei, S. Guo, C. Chen, L. Sun, Y. Chen, W. Guo, S. Ruan, High sensitive and fast formaldehyde gas sensor based on Ag-doped LaFeO₃ nanofibers, *J. Alloys Compd.*, 695 (2017) 1122–1127.
- [3] D. Kukkar, K. Vellingiri, R. Kaur, S. K. Bhardwaj, A. Deep, and K. H. Kim, Nanomaterials for sensing of formaldehyde in air: Principles, applications, and performance evaluation, *Nano Research*, 12(2) (2019) 225–246.
- [4] Z. Wang, H. Zhou, D. Han and F. Gu, Electron compensation in p-type 3DOM NiO by Sn doping for enhanced formaldehyde sensing performance, *J. Mater. Chem. C*, 5 (2017) 3254–3263.
- [5] X. Wang, Y. Si, J. Wang, B. Ding, J. Yu, S. S. Al-Deyab, A facile and highly sensitive colorimetric sensor for the detection of formaldehyde based on electro-spinning/netting nano-fiber/nets, *Sens. Actuators B: Chem.*, 163 (2012) 186–193.
- [6] M. Hauptmann, J. H. Lubin, P. A. Stewart, R. B. Hayes, A. Blair, Mortality from Solid Cancers among Workers in Formaldehyde Industries, *Am. J. Epidemiol.* 159 (12) (2004) 1117–1130.
- [7] M. Hauptmann, P. A. Stewart, J. H. Lubin, L. E. Beane Freeman; R. W. Hornung, R. F. Herrick, R. N. Hoover, J. F. Fraumeni, A. Blair, R. B. J. Hayes, Mortality From Lymphohematopoietic Malignancies and Brain Cancer Among Embalmers Exposed to Formaldehyde, *Natl. Cancer Inst.* 101 (24) (2009) 1696–1708.
- [8] Z. Han, Y. Qi, Z. Yang, H. Han, Y. Jiang, W. Du, X. Zhang, J. Zhang, Z. Dai, L. Wu, C. Fletcher, Z. Wang, J. Liu, G. Lud and F. Wang, Recent advances and perspectives on constructing metal oxide semiconductor gas sensing materials for efficient formaldehyde detection, *J. Mater. Chem. C*, 8 (2020) 13169–13188.
- [9] A. T. Güntner, V. Koren, K. Chikkadi, M. Righettoni, and S. E. Pratsinis, E-Nose Sensing of Low-ppb Formaldehyde in Gas Mixtures at High Relative Humidity for Breath Screening of Lung Cancer?, *ACS Sens.* 1 (2016) 528–535.
- [10] T. Yang, M. Zhu, K. Gu, C. Zhai, Q. Zhao, Xi. Yang and M. Zhang, Facile synthesis of SnO₂ nanoparticles for improved formaldehyde detection, *New J. Chem.*, 42 (2018) 13612–13618.
- [11] L. Gao, H. Fu, J. Zhu, J. Wang, Y. Chen and H. Liu, Synthesis of SnO₂ nanoparticles for formaldehyde detection with high sensitivity and good selectivity, *J. Mater. Res.*, 35 (2020) 2208–2217.
- [12] C. Y. Lee, C. M. Chiang, Y. H. Wang, R. H. Ma, A self-heating gas sensor with integrated NiO thin-film for formaldehyde detection, *Sens. Actuators B: Chem.*, 122 (2007) 503–510.
- [13] J. Liu, Y. Chen and H. Zhang, Study of Highly Sensitive Formaldehyde Sensors Based on ZnO/CuO Heterostructure via the Sol-Gel Method, *Sensors*, 21 (2021) 4685.
- [14] J. Liu, L. Zhang, B. Cheng, J. Fan, J. Yu, A high-response formaldehyde sensor based on fibrous Ag-ZnO/In₂O₃ with multi-level heterojunctions, *J. Hazard. Mater.*, 413 (2021) 125352.
- [15] N. Zhang, S. Ruan, F. Qu, Y. Yin, X. Li, S. Wen, S. Adimi and J. Yin, Metal–organic framework-derived Co₃O₄/CoFe₂O₄ double-shelled nanocubes for selective detection of sub-ppm-level formaldehyde, *Sens. Actuators B: Chem.*, 298 (2019) 126887.
- [16] X. Gao, F. Li, R. Wang and T. Zhang, A formaldehyde sensor: significant role of p-n heterojunction in gas-sensitive core-shell nanofibers, *Sens. Actuators B: Chem.*, 258 (2018) 1230–1241.

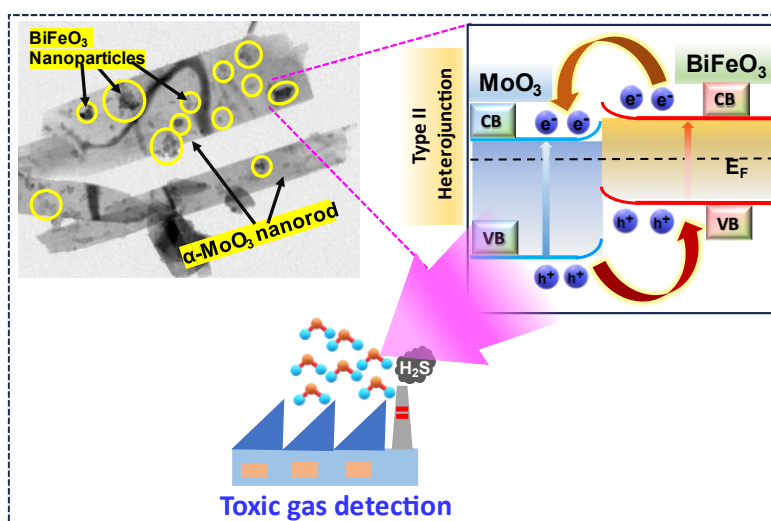
- [17] G. Zhang, X. Han, W. Bian, J. Zhan and X. Ma, Facile synthesis and high formaldehyde-sensing performance of NiO–SnO₂ hybrid nanospheres, *RSC Adv.*, 6 (2016) 3919.
- [18] L. Xu, M. Ge, F. Zhang, H. Huang, Y. Sun, D. He, Nanostructured of SnO₂/NiO composite as a highly selective formaldehyde gas sensor *L. J. Mater. Res.*, 35 (2020) 3079-3090.
- [19] Y.M. Zhang, Y.T. Lin, J.L. Chen, J. Zhang, Z.Q. Zhu and Q.J. Liu, A high sensitivity gas sensor for formaldehyde based on silver doped lanthanum ferrite, *Sens. Actuators B: Chem.*, 190 (2014) 171-176.
- [20] K. Zhu, S. Ma, Y. Tie, Q. Zhang, W. Wang, S. Pei and X. Xu, Highly sensitive formaldehyde gas sensors based on Y-doped SnO₂ hierarchical flower-shaped nanostructures, *J. Alloys Compd.*, 792 (2019) 938–944.
- [21] R. L. Fomekong, H. M. T. Kamta, J. N. Lambi, D. Lahem, P. Eloy, M. Debliquy, A. Delcorte, A sub-ppm level formaldehyde gas sensor based on Zn-doped NiO prepared by a coprecipitation route, *J. Alloys Compd.*, 731 (2018) 1188-1196.
- [22] W. Guo, T. Liu, R. Sun, Y. Chen, W. Zeng and Z. Wang, Hollow, porous, and yttrium functionalized ZnO nanospheres with enhanced gas-sensing performances, *Sens. Actuators B: Chem.*, 178 (2013) 53-62.
- [23] N. Han, X. Wu, D. Zhang, G. Shen, H. Liu and Y. Chen, CdO activated Sn-doped ZnO for highly sensitive, selective and stable formaldehyde sensor, *Sens. Actuators B: Chem.*, 152 (2011) 324–329.
- [24] D. Liu, J. Pana, J. Tanga, W. Liua, S. Bai, R. Luo, Ag decorated SnO₂ nanoparticles to enhance formaldehyde sensing properties, *J. Phys. Chem. Solids*, 124 (2019) 36–43.
- [25] T. Das, S. Das, M. Karmakar, S. Chakraborty, D. Saha, M. Pal, Novel barium hexaferrite based highly selective and stable trace ammonia sensor for detection of renal disease by exhaled breath analysis, *Sens. Actuators B: Chem.*, 325 (2020) 128765.
- [26] M. Dziubaniuka, R. B. Koronska, J. Suchanicz, J. Wyrwaa, M. Rekas, Application of bismuth ferrite protonic conductor for ammonia gas detection, *Sens. Actuators B: Chem.*, 188 (2013) 957-964.
- [27] S. Chakraborty and M. Pal, Highly efficient novel carbon monoxide gas sensor based on bismuth ferrite nanoparticles for environmental monitoring, *New J. Chem.*, 42 (2018) 7188-7196.
- [28] S. Chakraborty, M. Pal, Highly selective and stable acetone sensor based on chemically prepared bismuth ferrite nanoparticles, *J. Alloys Compd.*, 787 (2019) 1204-1211.
- [29] H. Xu, J. Xu, H. Li, W. Zhang, Y. Zhang, Z. Zhai, Highly sensitive ethanol and acetone gas sensors with reduced working temperature based on Sr-doped BiFeO₃ nanomaterial, *J. Mater. Res. Technol.*, 17 (2022) 1955-1963.
- [30] S. D. Waghmare, V. V. Jadhav, S. K. Gore, S. J. Yoon, S. B. Ambade, B.J. Lokhande, R. S. Mane, S. H. Han, Efficient gas sensitivity in mixed bismuth ferrite micro (cubes) and nano (plates) structures, *Mater. Res. Bull.*, 47 (2012) 4169-4173.
- [31] S. Das, S. Rana, Sk. Md. Mursalin, P. Rana, Sonochemically prepared nanosized BiFeO₃ as novel SO₂ sensor, *Sens. Actuators B: Chem.*, 218 (2015) 122-127.
- [32] G. Dong, H. Fan, H. Tian, J. Fang and Q. Li, Gas-sensing and electrical properties of perovskite structure p-type barium substituted bismuth ferrite, *RSC Adv.*, 5 (2015) 2961.
- [33] S. D. Waghmare, V. V. Jadhav, S. F. Shaikh, R. S. Mane, J. H. Rhee, [C. O'Dwyer](#), Sprayed tungsten-doped and undoped bismuth ferrite nanostructured films for reducing and oxidizing gas sensor applications, *Sens. Actuators A: Physical*, 271 (2018) 37-43.

- [34] H. Gao, D. Wei, P. Lin, C. Liu, P. Sun, K. Shimanoe, N. Yamazoe, G. Lu, The design of excellent xylene gas sensor using Sn-doped NiO hierarchical nanostructure, *Sens. Actuators B: Chem.*, 253 (2017) 1152-1162.
- [35] J. Yang, W. Han, J. Ma, C. Wang, K. Shimanoe, S. Zhang, Y. Sun, P. Cheng, Y. Wang, H. Zhang, G. Lu, Sn doping effect on NiO hollow nanofibers based gas sensors about the humidity dependence for triethylamine detection, *Sens. Actuators B: Chem.*, 340 (2021) 129971.
- [36] F. Gu, C. Li, D. Han and Z. Wang, Manipulating the Defect Structure (VO) of In₂O₃ Nanoparticles for Enhancement of Formaldehyde Detection, *ACS Appl. Mater. Interfaces*, 10 (2018) 933–942.
- [37] J. Zhang, Y. Zhang, C. Hu, Z. Zhu and Q. Liu, A formaldehyde gas sensor based on zinc doped lanthanum ferrite, *Adv. Mat. Res.*, 873 (2014) 304-310.
- [38] Q. Ruan and W. Zhang, Preparation and gas sensing properties of p-type La-Bi-Fe-O nanorods, *Mater. Lett.*, 62 (2008) 4303.
- [39] W. Zhou, Y. P. Wu, J. Zhao, W. W. Dong, X. Q. Qiao, D. F. Hou, X. Bu, and D. S. Li, Efficient Gas-Sensing for Formaldehyde with 3D Hierarchical Co₃O₄ Derived from Co₅-Based MOF Microcrystals, *Inorg. Chem.* 56 (2017) 14111-14117.
- [40] H. J. Park, S. Y. Hong, D. H. Chun, S. W. Kang, J. C. Park, D. S. Lee, A highly susceptible mesoporous hematite microcube architecture for sustainable P-type formaldehyde gas sensors, *Sens. Actuators B: Chem.*, 287 (2019) 437-444.
- [41] D. Xu, P. Xu, X. Wang, Y. Chen, H. Yu, D. Zheng and X. Li, Pentagon-Shaped Ag@Pt Core-Shell Nanostructures as High-Performance Catalysts for Formaldehyde Detection, *ACS Appl. Mater. Interfaces*, 12 (2020) 8091–8097.
- [42] S. Jaballah, M. Benamara, H. Dahman, D. Lahem, M. Debliquy and L. El Mir, Formaldehyde sensing characteristics of calcium-doped zinc oxide nanoparticles-based gas sensor, *J. Mater. Sci.: Mater. Electron.*, 31 (2020) 8230–8239.
- [43] N. Jafari, S.h Zeinali, Highly Rapid and Sensitive Formaldehyde Detection at Room Temperature Using a ZIF-8/MWCNT Nanocomposite, *ACS Omega*, 5 (2020) 4395-4402.
- [44] J. Hu, X. Chen, Y. Zhang, Batch fabrication of formaldehyde sensors based on LaFeO₃ thin film with ppb-level detection limit, *Sens. Actuators B: Chem.*, 349 (2021) 130738.
- [45] K.M. Zhu, S.Y. Ma, S.T. Pei, Y. Tie, Q.X. Zhang, W.Q. Wang, X.L. Xu, Preparation, characterization and formaldehyde gas sensing properties of walnut-shaped BiFeO₃ microspheres, *Mater. Lett.*, 246 (2019) 107–110.
- [46] Q. Zhu, Y.M. Zhang, J. Zhang, Z.Q. Zhu, Q.J. Liu, A new and high response gas sensor for methanol using molecularly imprinted technique, *Sens. Actuators B: Chem.*, 207 (2015) 398-403.
- [47] X. Deng, Z. Zeng, R. Gao, Z. Wang, G. Chen, W. Cai, C. Fu, Study of structural, optical and enhanced multiferroic properties of Ni doped BFO thin films synthesized by sol-gel method, *J. Alloys Compd.*, 831 (2020) 154857.
- [48] D. Chen, F. Niu, L. Qin, S. Wang, N. Zhang, Y. Huang, Defective BiFeO₃ with surface oxygen vacancies: Facile synthesis and mechanism insight into photocatalytic performance, *Sol. Energy Mater. Sol. Cells*, 171 (2017) 24-32.
- [49] X. Ou, Y. Shuai, W. Luo, P.F. Siles, R. Kogler, J. Fiedler, H. Reuther, S. Zhou, R. Hubner, S. Facsko, M. Helm, T. Mikolajick, O.G. Schmidt, H. Schmidt, Forming-free resistive switching in multiferroic BiFeO₃ thin films with enhanced nanoscale shunts, *ACS Appl. Mater. Interfaces*, 5 (2013) 12764-12771.
- [50] Q. Yu, Y. Zhang, Y. Xu, Hierarchical hollow BiFeO₃ microcubes with enhanced acetone gas sensing performance, *D. Transactions.*, 50 (2021) 6702-6709.

- [51] H. Wu, P. Xue, Y. Lu, X. Zhu, Microstructural, optical and magnetic characterizations of BiFeO₃ multiferroic nanoparticles synthesized via a sol-gel process, *J. Alloys Compd.*, 731 (2018) 471-477.
- [52] A. Mukherjee, Sk. M. Hossain, M. Pal, S. Basu, Effect of Y-doping on optical properties of multiferroics BiFeO₃ nanoparticles, *Appl. Nanosci.*, 2 (2012) 305-310.
- [53] A.C. Tas, P.J. Majewski, F. Aldinger, Chemical preparation of pure and strontium- and/or magnesium-doped lanthanum gallate powders, *J. Am. Ceram. Soc.*, 83 (2000) 2954-2960.
- [54] S. Irfan, S. Rizwan, Y. Shen, L. Li, Asfandiyar, S. Butt, C. Nan, The Gadolinium (Gd³⁺) and Tin (Sn⁴⁺) Co-doped BiFeO₃ Nanoparticles as New Solar Light Active Photocatalyst, *Sci. Rep.*, 7 (2017) 42493.
- [55] S. Chakraborty, M. Pal, Mater. Des., Improved sensitivity of CdS nanoparticles by virtue of calcium doping: promising candidate for monitoring alcohol in exhale human breath, 126 (2017) 18-28.
- [56] N. MinhVuong, N. DucChinh, B. T. Huy, Y. Lee, CuO-Decorated ZnO Hierarchical Nanostructures as Efficient and Established Sensing Materials for H₂S Gas Sensors, *Sci. Rep.*, 6 (2016) 26736.
- [57] C. Zhang, J. Wang*, R. Hu, Q. Qiao, X. Li, Synthesis and gas sensing properties of porous hierarchical SnO₂ by grapefruit exocarp biotemplate, *Sens. Actuators B: Chem.*, 222 (2016) 1134-1143.
- [58] Y. Li, N. Chen, D. Deng, X. Xing, X. Xiao, Y. Wang, Formaldehyde detection: SnO₂ microspheres for formaldehyde gas sensor with high sensitivity, fast response/recovery and good selectivity, *Sens. Actuators B: Chem.*, 238 (2017) 264-273.
- [59] T. P. Mokoena, H. C. Swart, K. T. Hillie, Z. P. Tshabalala, M. Jozela, J. Tshilongo, D. E. Motaung, Enhanced propanol gas sensing performance of p-type NiO gas sensor induced by exceptionally large surface area and crystallinity, *Appl. Surf. Sci.*, 517 (2022) 151121.
- [60] M. S. Choi, M. Y. Kim, A. Mirzaei, H. S. Kim, S. Kim, S.H. Baek, D. W. Chunh, C. Jin, K. H. Lee, Selective, sensitive, and stable NO₂ gas sensor based on porous ZnO nanosheets, *Appl. Surf. Sci.*, 568 (2021) 150910.
- [61] H. Gao, D. Wei, P. Lin, C. Liu, P. Sun, K. Shimanoe, N. Yamazoe, G. Lu, The design of excellent xylene gas sensor using Sn-doped NiO hierarchical nanostructure, *Sens. Actuators B: Chem.*, 253 (2017) 1152-1162.
- [62] W. Guo, L. Huang, X. Liu, J. Wang, J. Zhang, Enhanced isoprene gas sensing performance based on p-CaFe₂O₄/ n-ZnFe₂O₄ heterojunction composites, *Sens. Actuators B: Chem.* 354 (2022) 131243.
- [63] G. Murali, M. Reddeppa, Ch. S. Reddy, S. Park, T. Chandrakalavathi, M. D. Kim, and I. In, Enhancing the Charge Carrier Separation and Transport via Nitrogen-Doped Graphene Quantum Dot-TiO₂ Nanoplate Hybrid Structure for an Efficient NO Gas Sensor, *ACS Appl. Mater. Interfaces*, 12 (2020) 13428-13436.

CHAPTER 5

n-n type α -MoO₃/BiFeO₃ heterostructure for enhanced charge transfer induced H₂S gas sensing



This work is under communication

5.1. Introduction

Environmental air quality degradation is one of the major threats to sustainability of humankind. Due to rapid development of human civilization, excessive emission of toxic gasses from the industrial facilities has given rise to concerning environmental issues such as increasing air pollution. Emission of toxic pollutants in environment from the industries, mills has led to declining of air quality and caused health damage. Among various industrial exhaust hazardous gases, hydrogen sulphide (H_2S) is a malodorous, colourless poisonous gas commonly emitting from factories, paper production mills, sewage and faecal sludge treatment plants [1,2]. Exposure to H_2S from 50-100 ppm of concentration can possess threat to human health by causing nausea, dizziness, chest distress and it can even be fatal when exposed to higher concentration [3,4]. Therefore, fast operating, highly sensitive sensor material for real-time detection of H_2S exposure is thoroughly needed for human health safety issue and monitoring of environment air quality.

Amidst numerous metal oxide semiconductors (MOS) based gas sensors that have been employed for the detection of hazardous gases in the environment MoO_3 is widely known for its sensing activities to variety of gases, such as ethanol, ammonia, trimethyl amine and NO_2 . [5–8]. However, owing to several disadvantages such as low selectivity, unsatisfactory detection limit and slow response/recovery times, the efficiency of bare MoO_3 is insufficient for practical use [9]. Recently, in order to overcome these shortcomings, various methods have been adopted. Shen et al have reported the decoration of MoO_3 with active catalyst Ag which has improved its gas sensing property. [10] On the other hand, metal oxide heterostructures have been employed to minimize the potential energy barriers of gas adsorption on the sensor surface. Gao et al have reported detection of H_2S with $\text{MoO}_3/\text{SnO}_2$ junction with improved sensing properties compared to their individual counterparts [11]. As reported in another study by Gao et al., the change in barrier height between the contacted interfaces when exposed to target analytes resulted in enhanced H_2S sensing properties in $\text{MoO}_3/\text{Fe}_2(\text{MoO}_4)_3$ nanostructures [12]. Thus, heterostructure have gained extensive interest due to the synergetic effect from their constituent MOS sensing materials in favor of the improvement of gas sensing properties. Hence, a new composition of $\text{MoO}_3/\text{BiFeO}_3$ heterostructures has been designed to overcome these traditional issues.

In this work, we have developed α -MoO₃/BiFeO₃ heterostructure for real-time monitoring of hazardous H₂S in environment. Novel α -MoO₃/BiFeO₃ heterojunction is a portable, cost-effective H₂S sensor that can rapidly detect low concentration of H₂S in environment with high-precision and selectivity. A Type II heterojunction was constructed between n-type MoO₃ and n-type BiFeO₃ as synthesised via hydrothermal route. Experimental results proved that among various compositions of BiFeO₃, optimized 9% BiFeO₃ loaded α -MoO₃/BiFeO₃ heterostructure (MBF3) exhibited the highest photocurrent density and low charge transfer resistance. Strategic tuning of oxygen defects in MBF3 facilitated charge trapping sites in order to minimize e^-/h^+ recombination. The origin of enhanced photoelectrochemical performance as well as H₂S sensing performance of α -MoO₃/BiFeO₃ heterostructure has been inspected on the basis of band edge position by measuring UV-Vis DRS and Mott-Schottky analysis. The concentration of oxygen vacancies of α -MoO₃/BiFeO₃ heterostructure was extensively studied through XPS, EPR and PL analysis techniques. The results indicate that the heterostructure interface of MBF3 provides more active sites for H₂S gas adsorption which is attributed to its greater concentration of defect oxygen on the material surface. This work provides a new understanding of surface activity driven mechanism H₂S gas sensing of the α -MoO₃/BiFeO₃ heterostructure. The comparison between the H₂S gas sensing behaviour of different MoO₃-based heterostructure has been given in [Table 5.1](#).

Table 5.1 Comparison table of H₂S sensing properties in this work with MoO₃ based materials reported in previous works.

Sensor materials	Measuring range (ppm)	Response (%)	Response/recovery time (s)	References
2D-MoO ₃	0.5-30	~84% (30 ppm)	-	[9]
Ag/ α - MoO ₃	0.1-100	~80% (50 ppm)	8s/340s	[10]
MoO ₃ /SnO ₂	0.5-100	~90% (50 ppm)	22s/10s	[11]
MoO ₃ /Fe ₂ (MoO ₄) ₃	1-50	1.7 (1 ppm) (R _g /R _a)	20s/70s	[12]
MoO₃/BiFeO₃	1-100	98.02% (100 ppm)	5.7s/7.5s (1 ppm)	This work

5.2. Experimental Section

5.2.1. Chemicals

Bismuth nitrate pentahydrate ($\text{Bi}(\text{NO}_3)_3 \cdot 5\text{H}_2\text{O}$), iron (III) nitrate nonahydrate ($\text{Fe}(\text{NO}_3)_3 \cdot 9\text{H}_2\text{O}$), tartaric acid ($\text{C}_4\text{H}_6\text{O}_6$), ammonium heptamolybdate tetrahydrate ($(\text{NH}_4)_7\text{Mo}_7\text{O}_{24} \cdot 4\text{H}_2\text{O}$), Sodium nitrate (NaNO_3), nitric acid (HNO_3) were purchased from Sigma Aldrich. Deionized water (DI water) was used to wash the synthesized samples and as a solvent.

5.2.2. Synthesis of BiFeO_3

BiFeO_3 was synthesized via sol-gel synthesis technique as reported earlier with few modifications [13]. Equimolar amount of Bismuth nitrate pentahydrate ($\text{Bi}(\text{NO}_3)_3 \cdot 5\text{H}_2\text{O}$) and iron (III) nitrate nonahydrate ($\text{Fe}(\text{NO}_3)_3 \cdot 9\text{H}_2\text{O}$) was dissolved in 50 ml distilled water separately and stirred continuously for homogeneous mixing. Now both solutions were mixed and stirred well while concentrated HNO_3 was being added dropwise to the solution to maintain pH at 2. After this, precalculated amount of tartaric acid was mixed in 50 ml distilled water and added to the above solution. The mixture of solutions was then ultrasonicated for 1 h. Then, the solution was placed on a hot plate at 120°C and vigorously stirred for 8 h until it formed a thick gel. The gel was left in the oven for 24 h at 100°C to dry up completely. Finally, the dried gel was calcined at 600°C for 2 h and desired bismuth ferrite was obtained.

5.2.3. Synthesis of bare $\alpha\text{-MoO}_3$ and $\alpha\text{-MoO}_3/\text{BiFeO}_3$ heterostructure

$\alpha\text{-MoO}_3/\text{BiFeO}_3$ heterostructure were synthesized via hydrothermal synthesis technique. 1 mmol ammonium heptamolybdate tetrahydrate ($(\text{NH}_4)_7\text{Mo}_7\text{O}_{24} \cdot 4\text{H}_2\text{O}$) and 10 mmol NaNO_3 were dissolved in 30 ml and 10 ml distilled water, respectively, and stirred continuously. The above two solutions were added together and mixed using magnetic stirrer while HNO_3 was added dropwise to the solution to maintain the pH of the solution at 2. The calculated amount of pre-prepared BiFeO_3 was added to the solution and stirred for 30 minutes to obtain homogeneity. The homogenous solution was then transferred to a 50 ml Teflon-lined stainless-steel autoclave. The autoclave was put into a furnace at 180°C for 30 h. After the white product was collected from the autoclave, it was filtered and washed with deionized water repeatedly and kept in 80°C oven overnight. The prepared $\alpha\text{-MoO}_3/\text{BiFeO}_3$ heterostructures were marked as MBF1 ($\alpha\text{-MoO}_3/\text{BiFeO}_3=1:0.03$), MBF2 ($\alpha\text{-MoO}_3/\text{BiFeO}_3=1:0.06$), MBF3 ($\alpha\text{-MoO}_3/\text{BiFeO}_3=1:0.09$), MBF4 ($\alpha\text{-MoO}_3/\text{BiFeO}_3=1:0.12$).

Bare α -MoO₃ was prepared hydrothermally following the same procedure without adding BiFeO₃ to the solution. Details of the weight percentage used for synthesis are given in [Table 5.2](#).

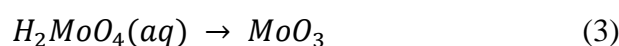
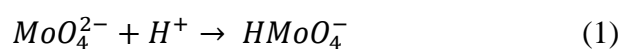
Table 5.2 Details of weight percent of as-synthesized α -MoO₃/BiFeO₃ heterostructures.

Name of sample	α -MoO ₃	BiFeO ₃	α -MoO ₃ /BiFeO ₃ (wt %)
MBF1	1.0075g	0.03128g (0.1 mmol)	α -MoO ₃ /BiFeO ₃ -3%
MBF2	1.0075g	0.06256g (0.2 mmol)	α -MoO ₃ /BiFeO ₃ -6%
MBF3	1.0075g	0.09384g (0.3 mmol)	α -MoO ₃ /BiFeO ₃ -9%
MBF4	1.0075g	0.12512g (0.4 mmol)	α -MoO ₃ /BiFeO ₃ -12%

5.2.4. Growth mechanism of α -MoO₃ nanorods α -MoO₃/BiFeO₃ heterostructures

The growth mechanism of α -MoO₃ nanorods and BiFeO₃ nanoparticles decorated α -MoO₃ nanorods heterostructures is demonstrated utilizing Ostwald ripening method. Proposed steps of growth mechanism is given as follows:

An intermediate compound H₂MoO₄ is formed as a result of interaction between ammonium heptamolybdate ((NH₄)₇Mo₇O₂₄) and HNO₃. During the increased pressure and temperature treatment in hydrothermal reaction sufficient energy is created which helps decomposition of H₂MoO₄ and oxidation process of MoO_x. Afterwards initializes the formation of MoO₃ crystal nuclei which grows into nanocrystals. Acidity of the medium due to the presence of HNO₃ in the precursor yields the formation of MoO₃ nanocrystals. The reaction during the formation of MoO₃ crystals can be described by [eq. \(1-3\)](#) as follows [14],



At first, with reaction time, anisotropic growth of nanocrystals takes place in a preferred direction. Initially condensation and nucleation process take place and the MoO₃ grows in size and nuclei started to get bigger in size. With increased reaction time those bigger nanocrystals turned into sheet-like structure of MoO₃. After reaction time was longer, the nanosheets added up with one another and grew into nanorods which later sized up following Ostwald ripening method to grow in diameter and length. The addition of NaNO₃ played crucial role in formation

on MoO_3 nanorods. It influences the growth kinetics of MoO_3 nanorods, preventing the formation of nanoplates or nanoslabs. Furthermore, the interaction between Na^+ and NO_3^- ions with the MoO_3 nuclei works in favour of anisotropic growth mechanism. NO_3^- ions facilitates the oxidation environment of MoO_x to MoO_3 while the metal ion Na^+ help in formation of microrods. Aggregation of nanoparticles into formation of nanorods is to minimize the surface energy[15]. The addition of BiFeO_3 nanoparticles during the formation of MoO_3 nanorods in the hydrothermal process helps in formation of heterostructure interface. The BiFeO_3 being smaller sized than MoO_3 nanorods, they are self-decorated on the surface of the rods. Presence of BiFeO_3 nanoparticles during the formation of MoO_3 nanorods, hinders the increase in length of the nanorods. In this case, along with the interaction of Na^+ with MoO_3 nuclei, interaction between BiFeO_3 nanoparticles and MoO_3 simultaneously takes place. As a result, formation of nanorods in shorter length and also formation of $\alpha\text{-MoO}_3/\text{BiFeO}_3$ interface occurs. The growth technique is schematically presented in Fig. 5.1.

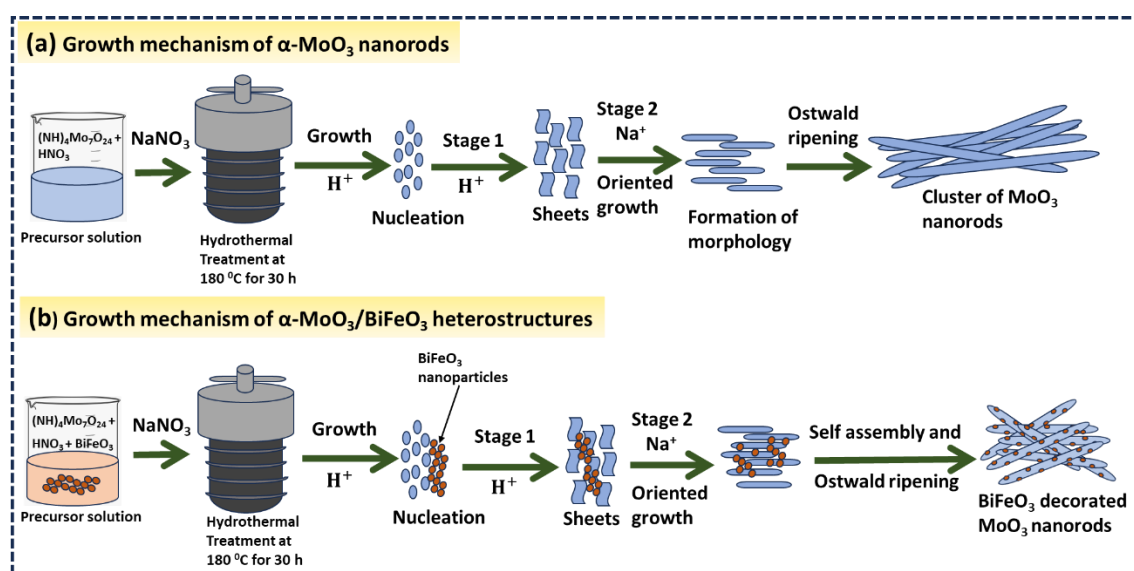


Fig. 5.1. Schematic illustration of growth technique of (a) $\alpha\text{-MoO}_3$ microrods and (b) BiFeO_3 nanoparticles decorated $\alpha\text{-MoO}_3$ nanorod heterostructures.

5.2.5. Characterization of heterostructures

Crystal structure of as-synthesized materials was characterized via X-ray diffraction (XRD) patterns using X'pert Pro MPD XRD PANalytical diffractometer using nickel filtered $\text{Cu-K}\alpha$ radiation ($\lambda=0.15404\text{nm}$). The morphologies and particle distributions of the $\alpha\text{-MoO}_3/\text{BiFeO}_3$ heterostructures were studied by field-emission scanning electron microscopy (FESEM) (Carl Zeiss make Supra 35 VP microscope) operated at 10 kV accelerating voltage

and high-resolution transmission electron microscopy (HRTEM) (Tecnai G² 30ST (FEI) operating at 300kV. Elemental characterization was performed by high angle annular dark field (HAADF) scanning transmission electron microscope (STEM) detector (Fischione, Model 3000) and energy dispersive X-ray spectroscopy (EDS). Specific surface area of the samples was measured by (BET) surface area analysing technique (NovaWin, Quantachrome Instruments). Barrett–Joyner–Halenda (BJH) method was employed for evaluation of pore size distribution. Elemental composition and oxidation state of the elements were determined using X-ray photoelectron spectroscopy (XPS) (PHI 5000 Versa Probe II scanning XPS microprobe ULVAC-PHI, U.S) with monochromatic AlK α (h ν =1486.6 eV) source and C 1s peak at 284.6 eV was used as standard for charge correction. Photoluminescence (PL) spectra was recorded using fluorescence spectrophotometer (PL, F-7000, Japan). Electron paramagnetic resonance (EPR) study was performed using Bruker A300-9.5/12/S/W instrument. UV-vis-NIR spectrometer (Shimadzu, UV-3600) was used to record room-temperature UV–visible diffuse reflectance spectra (DRS) of the α -MoO₃ and α -MoO₃/BiFeO₃ heterostructures.

5.2.6. Photoelectrochemical measurements

The thin films of the materials have been prepared on FTO coated glass substrate (1 cm \times 1cm) by spin coating method (catalyst concentration 2 mg/mL). A potentiostat - galvanostat (ZIVE, SP1) was used to perform the photoelectrochemical (PEC) measurements. A three-electrode set-up has been used where a Pt electrode is a counter electrode, an Ag/AgCl electrode is the reference electrode, a thin film-coated FTO substrate is a working electrode, and 0.1M Na₂SO₄ is the electrolyte. The Xenon light source with intensity of 150 mW/cm² was employed for all measurement. Linear sweep voltammogram (LSV) was performed in the range of voltage 0V to 1V vs Ag/AgCl at 20 mVs⁻¹ scan rate. Later on, photostability was checked *via* transient photocurrent at 0.26V vs Ag/AgCl under chopped conditions. The charge transfer resistance at the electrode-electrolyte interface has been calculated by measuring Electrochemical Impedance Spectroscopy (EIS) from 100KHz to 0.1Hz. All the EIS data were collected and fitted *via* ZMAN 2.5 software to find the charge transfer (R_{ct}) resistance and junction capacitance (C_{ct}). A mott-Schottky (MS) study has been performed to calculate the flat band potential and charge carrier density of as prepared photoanodes. The potential vs Ag/AgCl (E_{Ag/AgCl}) can be converted to a reference hydrogen electrode (RHE) by Nernst equation (eq. 4), as follows:

$$E_{\text{RHE}} = (E_{\text{Ag/AgCl}} + 0.059 \times \text{pH}) \text{ (at } 25^{\circ}\text{C)} + 0.197 \quad (4)$$

Theoretically, photoelectrochemical H_2 generation has been calculated from transient photocurrent spectra by determined amount of charge (Q) that passes through the photoanode. Amount of charge can be calculated from integrating current passes through the photoanode over time and the moles of H_2 is equal to $\frac{Q}{2F}$, where F is the faraday constant ($F = 96500$).

5.2.7. Gas sensors fabrication

Bare MoO_3 and $\alpha-MoO_3/BiFeO_3$ heterostructures were mixed with isopropanol and pestled using a mortar pestle to form a homogeneous paste. After the slurry reached required consistency, it was drop coated on cylindrical alumina substrate ($3.5mm \times 1mm \times 0.5mm$) with platinum electrodes attached with conducting gold paste to fabricate Taguchi type gas sensor modules. Then the alumina substrates coated with sensing materials were dried overnight at $120^\circ C$ to get rid of the residue solvent. Afterwards, Ni-Cr wire was inserted inside the hollow alumina substrate as a heating element to provide the necessary working temperature of the sensors. By changing the current flowing through the Ni-Cr wire, the working temperature of the sensors can be changed. Sensor prototypes based on $\alpha-MoO_3/BiFeO_3$ heterostructures were fabricated namely MBF0, MBF1, MBF2, MBF3 and MBF4 sensors. The gas sensing measurement set up is elaborated in detail in our previous works [13,16]. The gas response of the sensor was defined in eq. (5) as,

$$S = \frac{R_{air} - R_{gas}}{R_{air}} \times 100\% \quad (5)$$

Where R_{air} and R_{gas} refer to the resistance of the sensors in presence of air and in presence of target gas, respectively. The response time and recovery time of the sensor was defined by time taken by the sensor resistance change to reach 90% of the equilibrium state resistance value after the target gas in and out, respectively.

5.3. Results and discussion

5.3.1. Structure and morphology

Powder X-ray crystallography was carried out to understand the phase purity and crystallographic structure of $\alpha-MoO_3$ and $\alpha-MoO_3/BiFeO_3$ heterostructures and corresponding patterns are displayed in Fig. 5.2. XRD patterns of bare MoO_3 and $BiFeO_3$ match well with orthorhombic MoO_3 of space group Pbnm (JCPDS card number 05-0508) and rhombohedral $BiFeO_3$ of space group R3c (JCPDS card number 01-071-2494), respectively. The characteristics peaks of MoO_3 at 2θ of indexed to 23.34, 25.65, 27.25, 29.31, 33.80, 35.32,

38.89, 42.98, 46.50, 48.82, 55.94, 58.68 indexed to (110), (040), (021), (130), (111), (041), (060), (141), (210), (002), (042) and (081) planes, respectively, were detected in the α - $\text{MoO}_3/\text{BiFeO}_3$ heterostructures which matched well with the α - MoO_3 XRD pattern (JCPDS card number 05-0508). Diffraction peaks of α - $\text{MoO}_3/\text{BiFeO}_3$ heterostructures exhibit characteristic peaks of BiFeO_3 at 2θ of 31.76, 37.84, 45.32, 51.62 indexed to (104), (110), (024) and (116) planes, respectively, matched well with the rhombohedral BiFeO_3 (JCPDS card number 01-071-2494). The presence of characteristics peaks of BFO indicates the formation of the heterostructure.

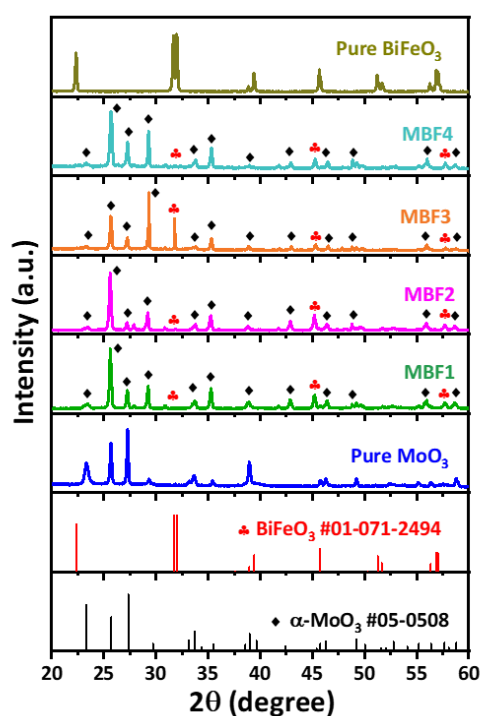


Fig. 5.2. XRD patterns of α - MoO_3 and BiFeO_3 JCPDS cards, as-synthesized bare samples and α - $\text{MoO}_3/\text{BiFeO}_3$ heterostructures.

The morphologies and microstructure of bare α - MoO_3 nanorods and α - $\text{MoO}_3/\text{BiFeO}_3$ heterostructures were investigated using FESEM. Fig. 5.3(a-d) exhibits the FESEM micrograph of bare α - MoO_3 and α - $\text{MoO}_3/\text{BiFeO}_3$ heterostructures, respectively. As-synthesized bare MoO_3 exhibited a well-developed nanorod-shaped structure. The bare MoO_3 nanorods were ~ 150 nm of diameter and 2-3 μm of length as calculated using ImageJ software (ref. Fig. 5.3a). When BiFeO_3 was introduced to the system the length of the nanorods started to decrease. The length of the nanorods were observed for sample MBF1 was 400 nm- 800 μm (Fig. 5.3b). Sample MBF2 exhibited shortened nanorods with average length of ~ 250 nm (Fig.

5.3c). MBF3 sample exhibited abundant of BiFeO_3 nanoparticles with few MoO_3 nanorods of length ~ 150 nm (Fig. 5.3d). This observation showed that with increase of BiFeO_3 in the system the microstructure of the nanorods have reduced in length and spherical shaped BiFeO_3 nanoparticles adhered to the surface of the nanorods by self-assembly method (ref Fig. 5.1).

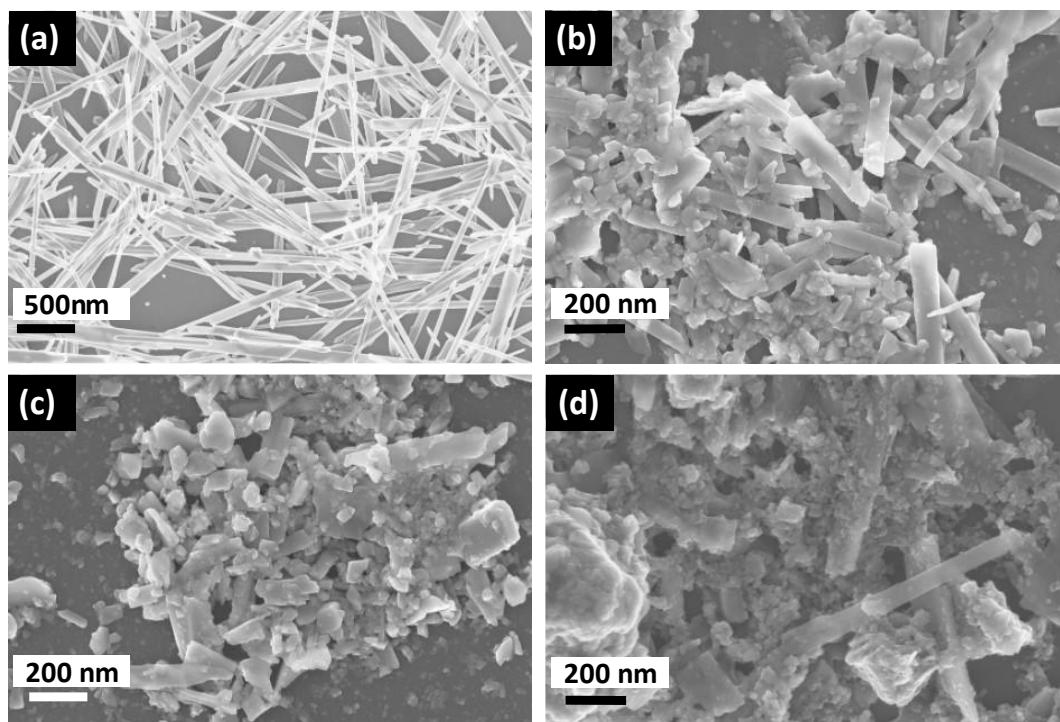


Fig. 5.3. FESEM micrograph of (a) bare MoO_3 (MBF0), (b) MBF1, (c) MBF2, (d) MBF3.

To further analyze the lattice fringe of the samples TEM was carried out on bare MoO_3 and MBF3. From TEM image in Fig. 5.4a, it was evident that bare MoO_3 (MBF0) exhibited nanorod structures of diameter ranging from 150 nm- 300 nm as calculated using ImageJ software. This result is consistent with the FESEM results. Fig. 5.4b displays the HRTEM image of the lattice fringe with d-spacing of 0.229 nm which is consistent with (060) crystalline plane of orthorhombic MoO_3 . This result corroborates with the diffraction peaks of XRD pattern of bare MoO_3 (ref. Fig. 5.2). Fig. 5.4c represents the TEM image of MBF3 sample in which the shortened nanorod structure of MoO_3 and BiFeO_3 nanoparticles adhered to the MoO_3 nanorods are clearly visible. HRTEM of MBF3 lattice fringe (displayed in Fig. 5.4d) exhibits clear image of lattice fringes of α - $\text{MoO}_3/\text{BiFeO}_3$ heterostructure (MBF3). In this image, the lattice spacing of 0.279 nm is distinctly visible, which corresponds to (110) lattice plane of BiFeO_3 (JCPDS card no. 01-071-2494) and the lattice fringe with d-spacing of 0.348 nm corresponds to (040) lattice plane of orthorhombic MoO_3 (JCPDS card no. 05-0508). As the HRTEM analysis of MBF3 confirms the presence of both MoO_3 and BiFeO_3 crystal planes,

this observation indicates the successful formation of α -MoO₃/BiFeO₃ heterostructure. This result is also consistent with the XRD peak pattern of MBF3 (ref. Fig. 5.2). This confirms that BiFeO₃ nanoparticles are sitting on the MoO₃ nanorods retaining the nanostructure of underlying α -MoO₃.

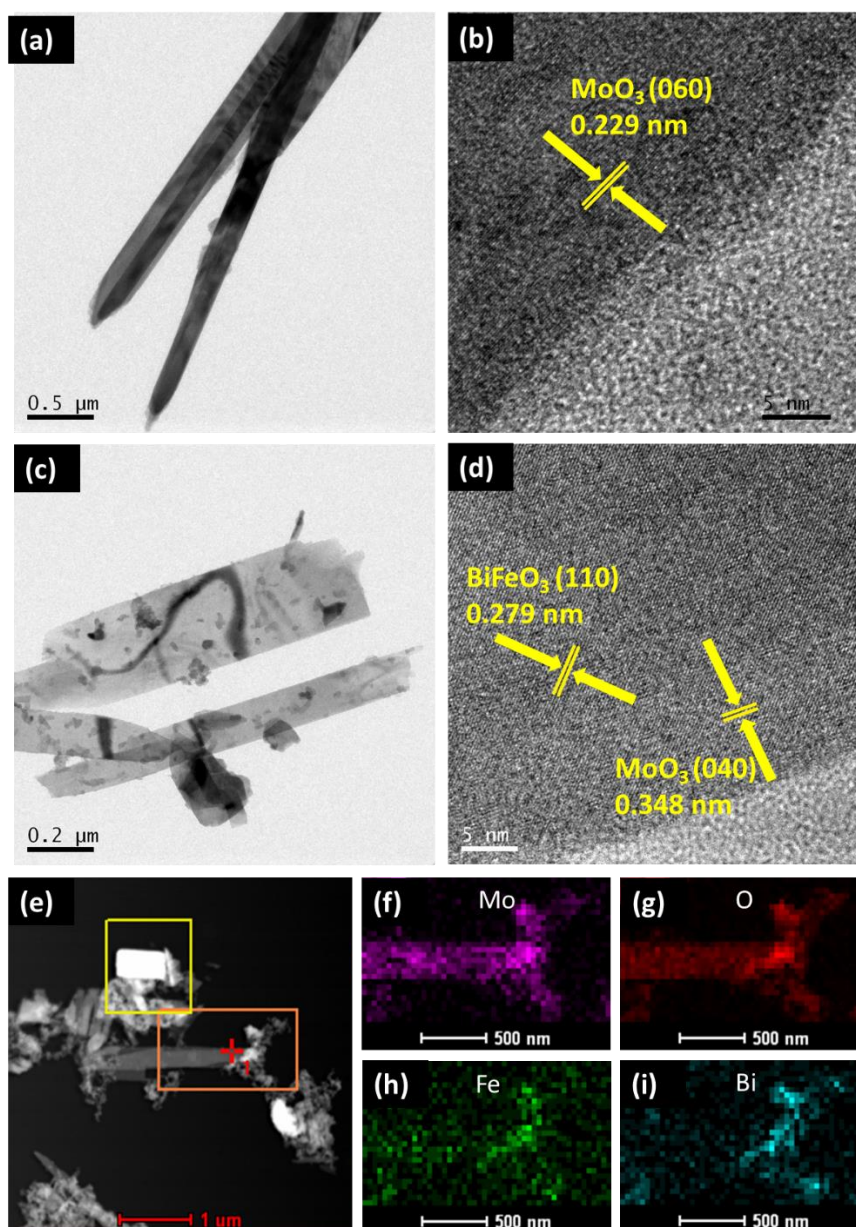


Fig. 5.4. (a,c) TEM images and (b,d) HRTEM micrographs of bare α -MoO₃ (MBF0) and α -MoO₃/BiFeO₃ heterostructure (MBF3), respectively. (e) The high-angle annular dark-field scanning TEM (HAADF-STEM) image of MBF3. Elemental mapping of (f) Mo, (g) O, (h) Fe and (i) Bi of MBF3.

Elemental mapping of sample MBF3 was analyzed with the help of scanning transmission electron microscopy (STEM) demonstrated in pattern in Fig. 5.4(e-i). Fig. 5.4e

represents the high-angle annular dark-field scanning TEM (HAADF-STEM) image of MBF3 and corresponding colour mapping of elements Mo, O, Fe, Bi are shown in Fig. 5.4(f-i), respectively. The results of elemental mapping confirm uniform distribution of Mo, O, Bi and Fe elements in the MBF3 structure. Energy dispersive X-ray (EDX) analysis at different regions of MBF3 was conducted to confirm the elements present and uniform distribution of the elements in the sample. Fig. 5.5 represents the EDX spectra of MBF3 where peaks of only Mo and O are detected in regions 1 and 2, whereas, presence of Mo, O along with Bi and Fe are detected in region 3, which indicates spherical BFO nanoparticles are grown over the MoO₃ nanorods.

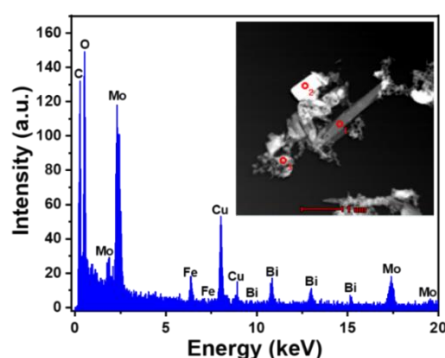


Fig. 5.5. EDX spectra of MBF3 acquired from HAADF-STEM.

Specific surface area and porous structure of the materials were analysed by N₂ adsorption-desorption employing Brunauer-Emmett-Teller (BET) method. The pore volume (V) and pore diameter (D) of the samples were analysed using Barrett-Joyner-Halenda (BJH) pore size distribution plot. The summary of BET surface area analysis, pore volume and average pore size of bare α -MoO₃ (MBF0) and α -MoO₃/BiFeO₃ heterostructures (MBF1, MBF2, MBF3 and MBF4) are given in Table 5.1. The adsorption-desorption isotherms exhibited typical type IV hysteresis curve (ref. Fig. 5.6(a-e)). The BJH pore size distribution curve (insets of Fig. 5.6) indicates porous structure of the samples. This observation reveals that introduction BiFeO₃ to the system enhanced the surface area of MoO₃ nanorods and MBF3 exhibited largest pore volume (6.75 cm³/g) and average pore size (21.18 nm) among all the α -MoO₃/BiFeO₃ heterostructures. This observation reveals that introduction BiFeO₃ to the system enhanced the surface area of α -MoO₃/BiFeO₃ heterostructures. However, for the heterostructure, surface area variation was not so prominent. With increase of BiFeO₃ concentration, the pore size of the samples gradually increases and becomes maximum for MBF3 sample. A larger surface area and pore volume are beneficial for the enhancement of

gas sensing properties as they can provide abundant active sites for surface activity and also help promote photocatalytic applications.

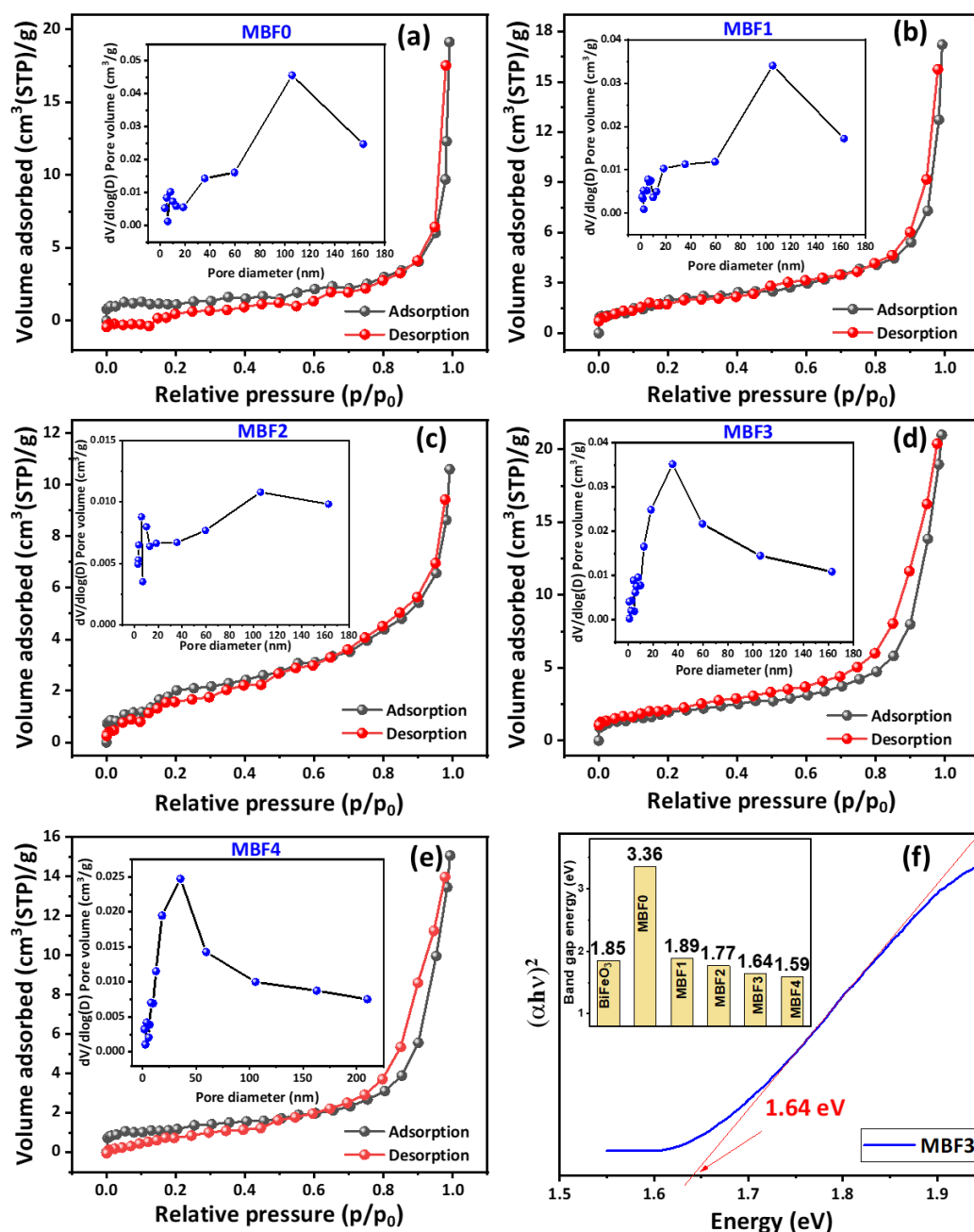


Fig. 5.6. N₂ adsorption–desorption isotherms and (inset: corresponding BJH pore size distribution curve) of (a) MBF0, (b) MBF1, (c) MBF2 and (d) MBF3 and (e) MBF4. (f) Tauc plot obtained from UV-vis DRS of MBF3 (inset: Band gap energy of all samples).

5.3.2. Optical and surface electronic properties

UV-vis diffuse reflectance spectra (DRS) was employed to study the optical absorption of the prepared α -MoO₃/BiFeO₃ heterostructures. The band gap energy of the as-prepared materials was calculated using Kubelka-Munk equation, (eq. 6), as follows,

$$(\alpha h\nu) = C(h\nu - E_g)^n \quad (6)$$

Where α represents linear absorption coefficient, $h\nu$ is energy of the photon, C is proportionality constant, n is the exponent that depends on the nature of electronic transition of the material. The value of n is 2 in the case of direct allowed transition. Fig. 5.7(a-e) and 5.6(f) display the Tauc-plot of bare BiFeO₃, MoO₃ and MoO₃/BiFeO₃ heterostructures. The calculated band gap energy of the samples is given in inset of Fig. 5.6f and listed in Table 5.1. As evident from the results that, bare α -MoO₃ usually possessed large band gap of 3.36 eV, which gradually have reduced while α -MoO₃/BiFeO₃ heterostructure was formed. This observation shows that the presence of BiFeO₃ in the system effectively reduces the band gap of MoO₃ and promotes ability of visible region photon absorption. Therefore, BiFeO₃ can play a significant role in bandgap energy tuning of MoO₃ nanostructure by facilitating electron transition.

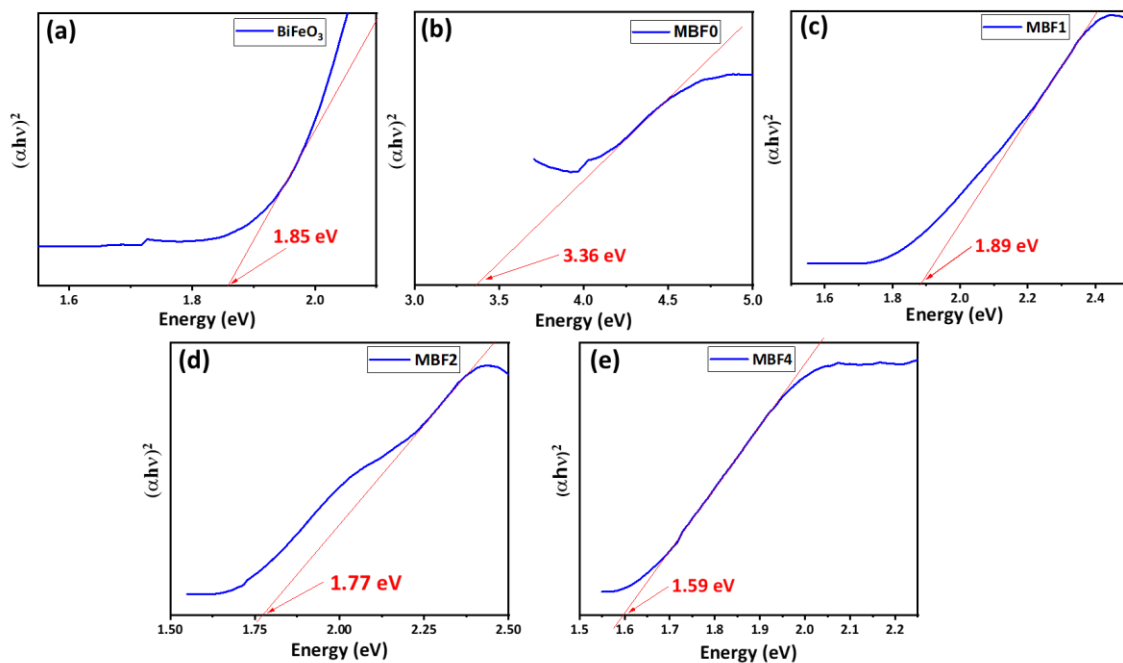


Fig. 5.7. Tauc plot obtained from UV-vis DRS of bare BiFeO₃, MBF0, MBF1, MBF2 and MBF4 samples.

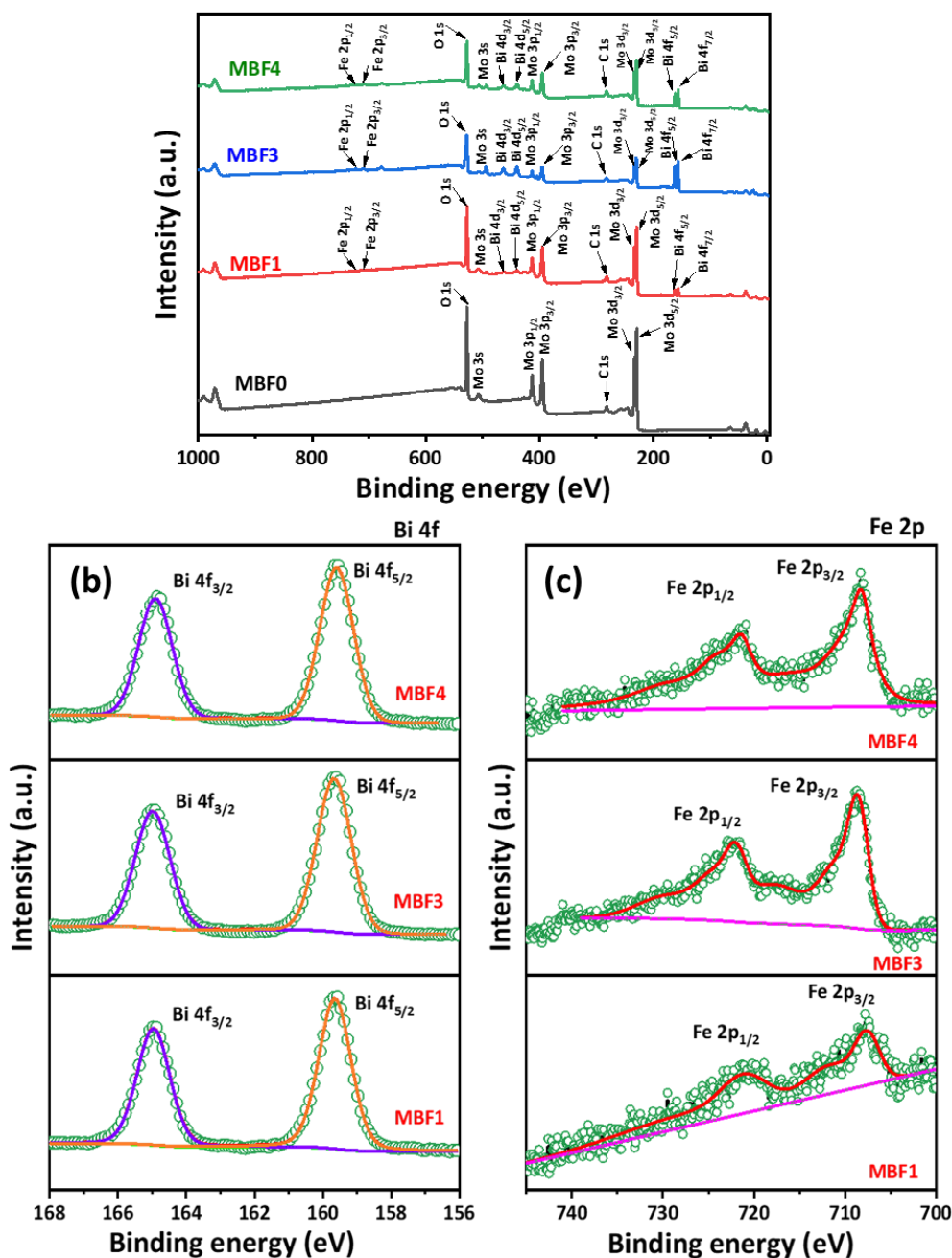


Fig. 5.8. (a) XPS survey spectra of bare MoO₃ (MBF0) and α -MoO₃/BiFeO₃ heterostructures (MBF1, MBF3 and MBF4). High magnification core level (b) Bi 4f, (c) Fe 2p XPS spectra of α -MoO₃/BiFeO₃ heterostructures (MBF1, MBF3 and MBF4, respectively).

Surface chemical composition and valence state of the samples were characterized by X-ray photoelectron spectroscopy (XPS). Fig. 5.8a represents the wide scan XPS spectra of bare MoO₃ and α -MoO₃/BiFeO₃ heterostructures (MBF1, MBF3 and MBF4). Binding energy peaks corresponding to Mo 3d, C 1s, Mo 3p, Mo 3s, O 1s were observed for both bare MoO₃ (MBF0) and α -MoO₃/BiFeO₃ heterostructures (MBF1, MBF3 and MBF4). Whereas, along

with the aforementioned Mo 3d, C 1s, O 1s peaks, additional peaks of Bi 4f, Bi 4d, Fe 2p peaks were detected in XPS spectra of MBF1, MBF3 and MBF4 samples, which confirmed the presence of Bi, Fe in the α -MoO₃/BiFeO₃ heterostructures. The signal peak of C 1s is caused by external impurity of the measuring instrument. High-magnification XPS spectra was used to detect the chemical states of the elements of the samples. In high resolution XPS spectra of Bi 4f of MBF1, MBF3 and MBF4, (depicted in Fig. 5.8b), doublet peaks observed at around 162.07 eV and 156.75 eV are ascribed to Bi 4f_{3/2} and Bi 4f_{5/2}, respectively, indicating presence of Bi³⁺ oxidation state. The intensity of peaks of Bi 4f and Fe 2p have gradually increased with increase in BiFeO₃ concentration. The oxidation state of Fe was confirmed by XPS spectra of Fe 2p depicted in Fig. 5.8c. Fe 2p spectrum of α -MoO₃/BiFeO₃ heterostructures (MBF1, MBF3 and MBF4) reveal two peaks at around 724.22 eV and 708.491 eV attributed to Fe 2p_{1/2} and Fe 2p_{3/2}, respectively. The presence of two satellite peaks located at binding energy around 717.72 eV and 729.25 eV confirmed the valence state of Fe to be Fe⁺³.

In Fig. 5.9a high resolution XPS spectra of Mo 3d of MBF0, MBF1, MBF3, MBF4 reveal two doublet peaks centered around 236.0 eV and 232.8 eV, which are attributed to Mo 3d_{3/2} and Mo 3d_{5/2}, respectively. However, the peaks are asymmetric in nature. Hence, these two peaks can be resolved with an intensive doublet ascribed to Mo⁶⁺ and a weak doublet ascribed to Mo⁵⁺. The doublet peaks centered at around 232.9 eV and 236.0 eV are ascribed to 3d_{5/2} and 3d_{3/2} orbital electrons of Mo⁶⁺ and similarly, the doublet peaks centered at around 231.9 eV and 234.8 eV correspond to 3d_{5/2} and 3d_{3/2} orbital electrons of Mo⁵⁺ [17,18]. It was observed that, the area percentage of Mo⁵⁺ has increased from 7.60% in MBF0 to 10.67% in MBF1 and 12.29% in MBF3. Then again, the same has decreased to 11.20% in MBF4. Therefore, the calculated ratio of Mo⁵⁺/Mo⁶⁺ in bare α -MoO₃ (MBF0) and α -MoO₃/BiFeO₃ heterostructures (MBF0, MBF1, MBF3, MBF4) are 0.0822, 0.1194, 0.1401 and 0.1261, respectively. A summary of the analysis is given in Table 5.4. When the α -MoO₃/BiFeO₃ heterostructures were formed some amount of Mo⁶⁺ in α -MoO₃ was reduced to Mo⁵⁺ and gave rise to Mo bivalency in the system and oxygen vacancies (as the XPS O 1s spectra analysis indicated) [19]. The presence of Mo bivalency in the α -MoO₃/BiFeO₃ heterostructures system promotes the intrinsic conductivity of the whole system. As reported in the literature, partially reduced α -MoO₃ with abundant oxygen vacancies in the heterostructure system promotes electrochemical performance compared to that of bare α -MoO₃[17]. Therefore, BiFeO₃ as a modifier to α -MoO₃ system is a strategy to enhance electrochemical property of α -MoO₃. From the result it was observed that Mo⁵⁺/Mo⁶⁺ is maximum for MBF3 sample, which explains its

best electrochemical performance compared to other α -MoO₃/BiFeO₃ heterostructures. This indicates, 9% BiFeO₃ is the optimum concentration to sensitize the α -MoO₃. The O 1s spectra of MBF0, MBF1, MBF3 and MBF4 are depicted in Fig. 5.9b. The O 1s peak of the samples showed asymmetric nature, hence, were resolved into two peaks, namely O_L: lattice oxygen and O_D: defect oxygen. The peak corresponding to lattice oxygen O_L (around 530.7 eV) can be attributed to O²⁻ in metal-oxygen bonds. The O_D peak (around 531.1 eV) ascribed to O²⁻ ions near oxygen deficient sites [20,21]. The percentage of two components of O 1s is summarized in Table 5.4. It is observed that, with concentration of BiFeO₃ in the system, percentage of O_D has gradually increased from 17.05% in MBF0 to 21.49%, 40.01% in MBF1, MBF3, respectively. The sample MBF3 has highest O_D percentage (40.01%) than that of other heterostructures MBF1 (21.49%) and MBF4 (22.12%). The percentage of oxygen content in the samples corroborates with the ratio of Mo⁵⁺/Mo⁶⁺ as obtained from Mo 3d peaks. These oxygen defects contribute in improving the conductivity of the heterostructures and in turn promote rapid transport of electrons. Higher percentage of O_D provides higher number of active sites for gas adsorption on the surface to enhance sensing activity of the material.

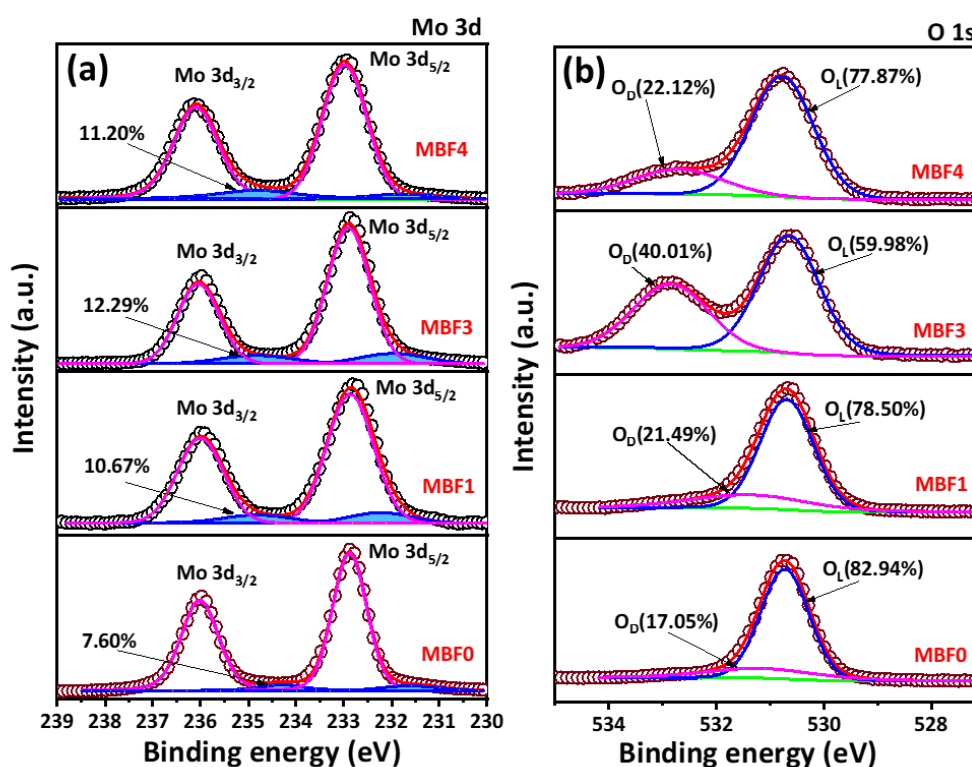


Fig. 5.9. (a) Mo 3d, (b) O 1s XPS spectra of bare MoO₃ (MBF0) and α -MoO₃/BiFeO₃ heterostructures (MBF1, MBF3 and MBF4), respectively.

Electron paramagnetic resonance (EPR) spectroscopy was carried out to further confirm the presence of oxygen vacancies. As shown in Fig. 5.10a no signal was observed for MoO₃ (MBF0), whereas α -MoO₃/BiFeO₃ heterostructures exhibited strong characteristic signal at g value of 2.04, which is the direct evidence of oxygen vacancies on the surface of α -MoO₃/BiFeO₃. [22] The intensity of the g=2.04 corresponding to oxygen vacancies on the surface of the heterostructures increased gradually with increasing BiFeO₃ loading percentage and reached maximum value for MBF3 sample and the decreased again for MBF4 sample. This indicates MBF3 comprises of optimum amount of BiFeO₃ loading concentration which results in enhancement of photocatalytic activity as well as H₂S response due to increase of active sites. The result of EPR spectra corroborates with XPS results.

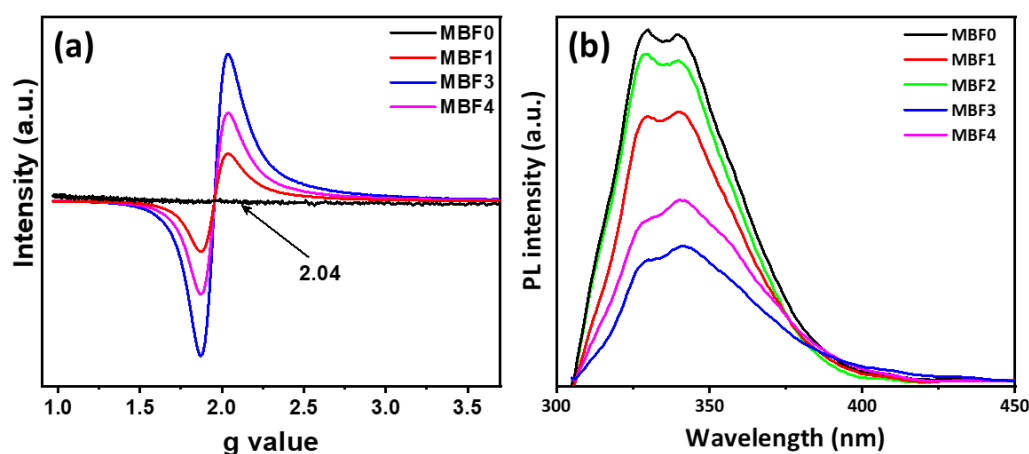


Fig. 5.10. (a) EPR spectra of MB0, MB1, MB3 and MB4 samples. (b) PL spectra of bare α -MoO₃ (MBF0) and α -MoO₃/BiFeO₃ heterostructures (MBF1, MBF3 and MBF4) excited at 290 nm.

PL spectra of bare MoO₃ and α -MoO₃/BiFeO₃ heterostructures were recorded (shown in Fig. 5.10b) at room temperature at 290 nm (4.27 eV) excitation energy that is greater than the band gap (3.36-1.59 eV) of the materials so that the electrons in the valence band can easily jump to the conduction band [23]. It was observed that the concentration of BiFeO₃ in the system affected the PL peak intensity of the samples. The bare MoO₃ exhibited strongest PL peak intensity and the peaks intensities decreased in the α -MoO₃/BiFeO₃ heterostructures. The sample MBF3 exhibited the lowest peak intensity. PL intensity of the as-prepared samples in ascending order is: MBF3, MBF4, MBF1, MBF2 and MBF0. PL emission spectra reflects the photogenerated e^-h^+ recombination. Higher PL emission intensity indicates higher recombination efficiency of photogenerated e^-h^+ [13,24]. Therefore, the observation indicates

that when BiFeO₃ increased to 9% in the sample MBF3 the corresponding PL peak exhibited the lowest intensity. This result indicates the highest charge separation of photogenerated e⁻-h⁺ of the sample MBF3 which in turn promotes charge transfer and PEC activity that is beneficial for sensing activity also [25].

5.3.3. Photoelectrochemical properties

Photocatalytic activity depends on the band edge positions of semiconductors, free photoexcited charge carrier density, and charge transfer resistance in the semiconductor-electrolyte interface, which can be performed by photoelectrochemical measurement. A series of photoelectrochemical measurements were performed using as-synthesized materials. The LSV curve of bare BiFeO₃, MoO₃, and MoO₃/BiFeO₃ heterostructures, as shown in Fig. 5.11a and Fig. 5.12a, indicates the formation of heterostructure effectively enhanced the current density compared to pristine semiconductor current density, leads towards an increase in free charge carrier mobility, reduction of electron-hole recombination rate and high charge carrier concentration through the interfaces. It has been observed that MBF3 has nearly 8.3 times higher current density than bare MoO₃ at 0.6V vs Ag/AgCl. Fig. 5.11b and Fig. 5.12b showed photostability of the anodes which measured by transient photocurrent. The MBF3 displayed the highest photocurrent density and stability compared to the other compositions and bare semiconductors, which is consistent with the LSV result and also the PL result.

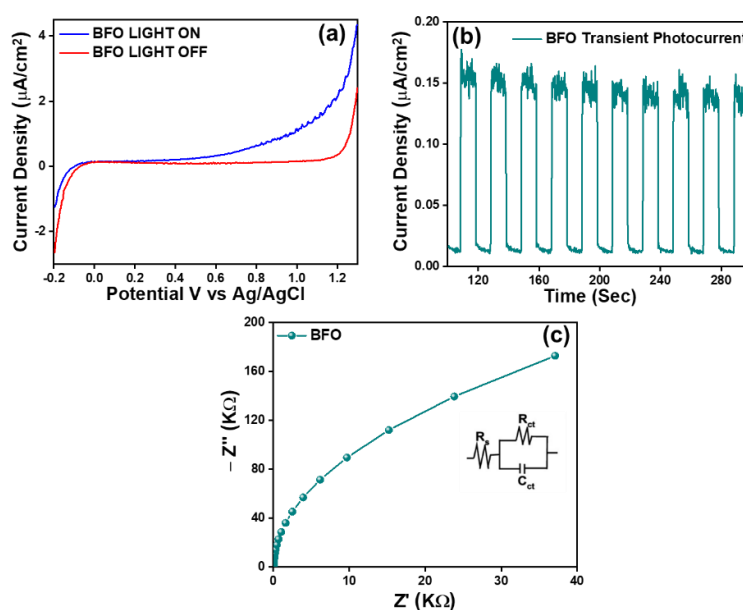


Fig. 5.11. (a) LSV curve of BiFeO₃ at light on/off state. (b) Transient photocurrent spectra of BiFeO₃. (c) Electrochemical impedance spectra of BiFeO₃.

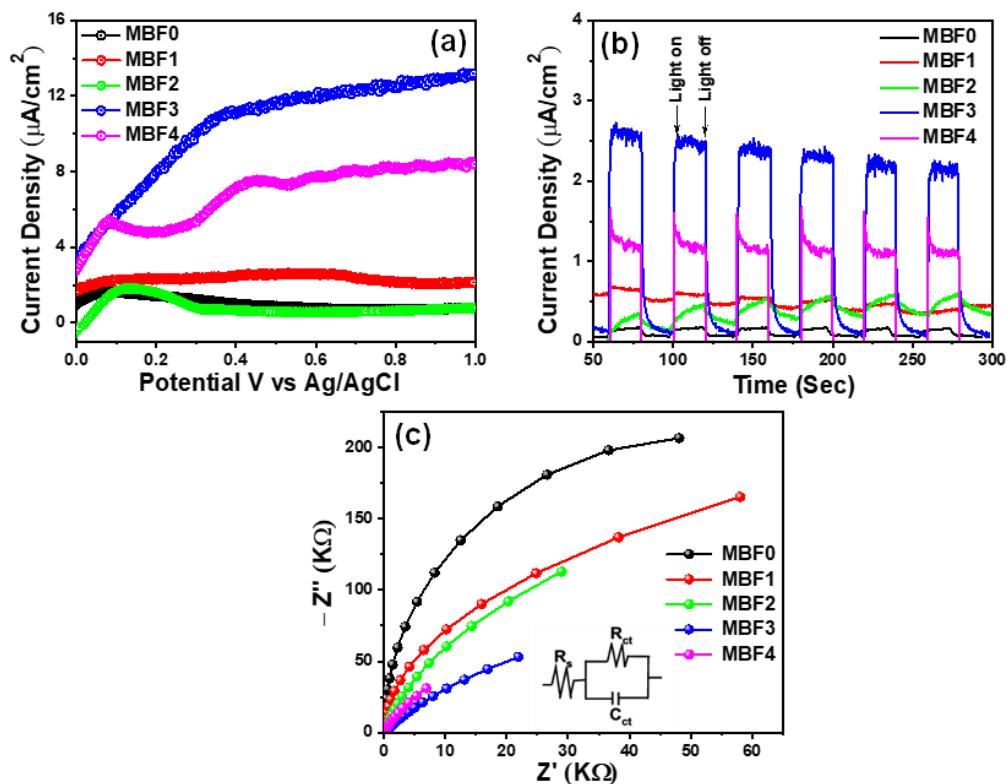


Fig. 5.12. (a) LSV curves, (b) Transient photocurrent spectra, and (c) Photoelectrochemical impedance spectra of MBF0, MBF1, MBF2, MBF3, and MBF4, respectively. Inset: The equivalent circuit parameters.

To understand the charge transfer at the heterostructure-electrolyte interfacial, charge transfer resistance is an important parameter that can be followed by electrochemical impedance spectroscopy (EIS). The Nyquist plots of MBF0 and heterostructure with varied loading of BiFeO₃ indicate quite higher charge transfer resistance for bare MBF0 (~94.2 K Ω), whereas MBF3 shows the lowest charge transfer resistance (~35 K Ω) with a semi-circular arc compared to the other compositions and pristine semiconductors as shown in Fig. 5.11c and Fig. 5.12c. This semi-circular path suggests the charge transfer resistance and junction capacitance at the heterostructure-electrolyte interface.[26,27] Notably, low charge transfer resistance indicates an effective charge diffusion from electrolyte to semiconductor and increases their mobility which enhances the electrical conductivity of the semiconductor. The EIS spectrum of all the semiconductors has been fitted with junction capacitance and charge transfer resistance in parallel circuits connecting with solution resistance in series, as shown in the inset of Fig. 5.11c. The charge transfer resistance (R_{ct}) of the materials has been tabulated in Table 5.4.

The M-S plots of as-synthesized bare materials MBF0 and BiFeO₃ shows positive slope as shown in Fig. 5.13 (a, b), means typically they are n-type semiconductor in nature with flat band potential (E_{fb}) $-0.37V$, $-0.40V$ vs Ag/AgCl for MBF0 and BFO respectively.[28] The E_{fb} of the heterostructures are $-0.47V$, $-0.36V$, $-0.46V$ and $-0.43V$ vs Ag/AgCl for MBF1, MBF2, MBF3 and MBF4, respectively (Fig. 5.13c-f). Value of E_{fb} vs RHE has been determined by using eq. (4). The position of conduction band (CB) edges has been calculated by using eq. (7) as follows: [29]

$$CB = E_{fb} \text{ vs RHE} - 0.2V \quad (7)$$

The position of valance band (VB) edges has been determined by using band gap data which measured from UV-Vis DRS spectra by eq. (8) as follows:

$$VB - CB = E_g \quad (8)$$

The calculated value of E_{fb} , and free charge carrier/donor density has tabulated in Table 5.4. The free charge carrier concentration of the pristine semiconductor and the heterostructures has been calculated from E_{fb} by eq. (9) as follows:[30]

$$\frac{1}{C^2} = \frac{2}{eN_d\epsilon\epsilon_0} \left(E - E_{fb} - \frac{K_B T}{e} \right) \quad (9)$$

Where C is the space charge capacitance at the junction of the semiconductor-electrolyte interface, N_d is the free charge carrier concentration, e is the charge of the electron, ϵ is the dielectric constant of the semiconductor, ϵ_0 is permittivity of the free space, K_B is the Boltzmann constant and T is the temperature. Table 5.4 shows donor density (N_d) value of MBF3 is 78 times and 1.4 times higher than MBF0 and BiFeO₃, respectively, which directly implies MBF3 perform better photocatalytic activity than others. Comparison of the photo current density of MoO₃/BiFeO₃ with other heterostrcutre-based semiconductors reported in literature is given in Table 5.3. As can be seen from the table MoO₃/BiFeO₃ exhibited higher current density than other reported heterostructures.

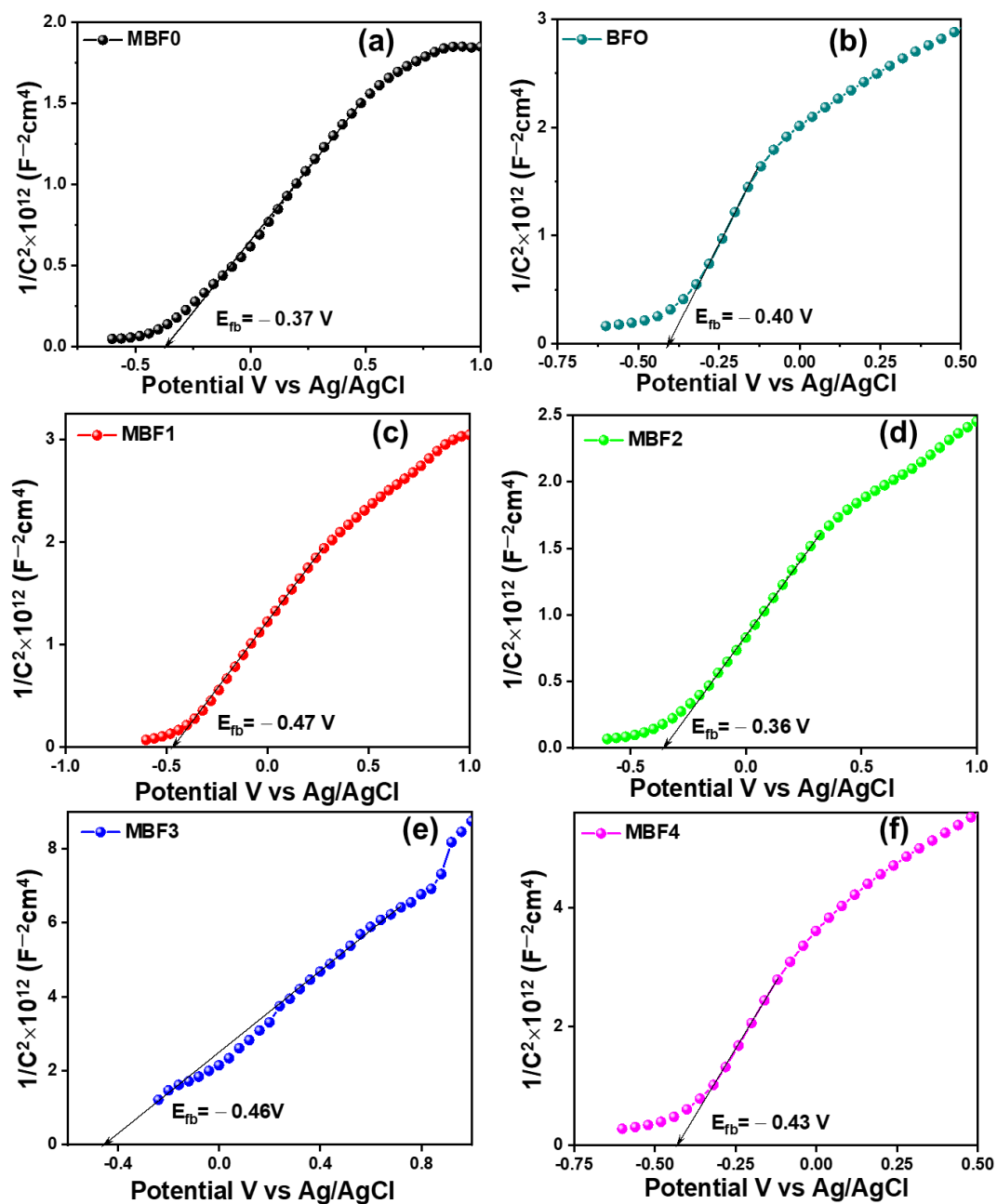


Fig. 5.13. M-S plot of all samples.

Table 5.3 Comparison table of photoelectrochemical applications of MoO₃ based materials.

Material	Light Source	Electrolyte	Current density ($\mu\text{A cm}^{-2}$) (vs RHE)	References
MoO _{3-x} /g-C ₃ N ₄	—	0.5M Na ₂ SO ₄	3.3	6
α -MoO ₃ @MoS ₂	150W mercury lamp	0.1M Na ₂ SO ₄	0.09	7
MoO ₃ /PI	—	0.5M Na ₂ SO ₄	2.5	9
MoS ₂ /MoO ₃	—	0.5M H ₂ SO ₄	10	10
amine- CdS/MoO ₃	300FW xenon lamp	0.25M Na ₂ SO ₃	1.5	11
Er-Yb: TiO ₂ /MoO _{3-x}	300-W Xenon lamp	0.2 mol/L of Na ₂ SO ₄	0.64	12
α - MoO ₃ /BiFeO ₃	150 W Xenon light	0.1 M Na ₂ SO ₄	12	This work

5.3.4. H₂S sensing properties

Measurement of hazardous H₂S gas sensing property of the MoO₃/BiFeO₃ heterostructure based sensors were studied in detail. Gas sensing property of MOS depends on the operating temperature of the sensor. To optimize the operating temperature, the sensors were exposed to 100 ppm H₂S at an operating temperature ranging from 120 °C -350 °C (Fig. 5.14a). With increasing operating temperature, the response of the sensors was observed to increase and reached its maximum value at 210 °C. Beyond this optimum temperature, the response value decreased gradually. At higher operating temperature, rate of desorption of the H₂S gas molecules was higher than their reaction with the oxygen species on the surface of the sensing material, which causes lower sensitivity. When the operating temperature was lower than the optimum, the H₂S molecules lacked the activation energy needed to react with the adsorbed oxygen. At optimum operating temperature, these two processes were balanced, which explains the increase-maximum-decrease trend of the sensing performance of the sensors [33,34]. Fig. 5.14b shows that with increasing BiFeO₃ concentration, the response of the sensors has increased gradually from MBF0 to MBF3, but again decreased with further increase of BiFeO₃ concentration in MBF4. MBF3 sensor has highest response to 100 ppm H₂S (~98%) that is

about 130% higher than that of bare MoO₃ based sensor (~39%). Additionally, all the α-MoO₃/BiFeO₃ heterostructures-based sensors exhibited reduced operating temperature of 210 °C compared to bare α-MoO₃ based sensor (350 °C). This observation proves that modification of α-MoO₃ with BiFeO₃ has a positive effect on H₂S response of the material. Fig. 5.14b displays the resistance of the sensors in air (R_{air}) as a function of operating temperature. The resistance of the sensors decreased gradually with increase in temperature which indicates the semiconducting nature of the sensing materials. Fig. 5.14c shows the H₂S gas response values of the sensors when exposed to different concentration of the gas starting from 1 ppm – 100 ppm. The responses of the sensors increase rapidly with increase in H₂S concentration. The MBF3 sensor showed highest response to H₂S among all the sensors. The logarithm of sensitivity vs logarithm of H₂S concentration plots (inset of Fig. 5.14c) exhibit good linearity with the correlation coefficient (R²) values 0.98896, 0.99487, 0.99150, 0.99174, 0.98722 for MBF0, MBF1, MBF2, MBF3, MBF4 sensors, respectively. The linear trend follows the conductance model of the semiconductor represented by empirical equation given in eq. (10) as follows,

$$S_g(\%) = A_g P_g^\beta \quad (10)$$

Where P_g^β is the partial pressure of the target analyte which is proportional to the concentration of the gas (C_g), A_g corresponds to the prefactor, β is the response exponent that depends on the adsorbed oxygen species on the surface, $S_g(\%)$ is the sensitivity toward the target gas. The value of β is usually between 0.5-1. When the value of β is 0.5, the adsorbed oxygen species is O²⁻, and when it is nearest to 1, the oxygen species changes to O⁻. Here, the value of β for MBF3 sensor, as obtained from the slope of the fitting plot, is 0.47, which indicates that the interaction between H₂S and MoO₃/BiFeO₃ is a surface phenomenon and adsorption of H₂S happens through physisorption. [33,35] The response comparison of all bare α-MoO₃ and α-MoO₃/BiFeO₃ heterostructures-based sensors to 50 ppm H₂S gas at their optimum operating temperatures of 300 °C (MBF0) and 210 °C (MBF1, MBF2, MBF3, MBF4), respectively, is shown in Fig. 5.14d. This shows that incorporation of BiFeO₃ in the system enhances the H₂S response and it is highest for MBF3 sample (ref. Table 5.1).

Table 5.4 Summary of BET surface area analysis, XPS spectra analysis, calculated charge transfer resistance (R_{ct}), bandgap (E_g), flat band potentials (E_{fb}), donor density (N_d), and H₂S response of the as-synthesized materials.

Samples		BiFeO ₃	MBF0	MBF1	MBF2	MBF3	MBF4
BET surface area (m ² /g)		—	4.18	7.58	6.70	6.75	4.28
Pore volume (cm ³ /g)		—	2.9189E-02	2.5416E-02	1.6059E-02	6.7529E+00	2.2659E-02
Pore diameter (nm)		—	27.93	13.41	9.57	21.18	19.06
Area percentage of oxygen species	O _L	—	82.94%	78.50%	—	60.80%	77.87%
	O _D	—	17.05%	21.49%	—	39.91%	22.12%
Mo ⁵⁺ /Mo ⁶⁺		—	0.0822	0.1194	—	0.1401	0.1261
R _{ct} (KΩ)		—	94.2	53.3	64.7	35.0	39.9
Band gap (eV)		1.85	3.36	1.89	1.77	1.64	1.59
Type of Material from MS plot		n-type	n-type	n-type	n-type	n-type	n-type
E_{fb} (V) vs Ag/AgCl		− 0.40	− 0.37	− 0.47	− 0.36	− 0.46	− 0.43
Donor density (N _d) (cm ³)		6.20 × 10 ²²	1.12 × 10 ²¹	1.16 × 10 ²¹	7.23 × 10 ²¹	8.80 × 10 ²²	3.15 × 10 ²²
Response to 50 ppm H ₂ S (%)		—	39.45	52.98	76.06	88.12	68.20

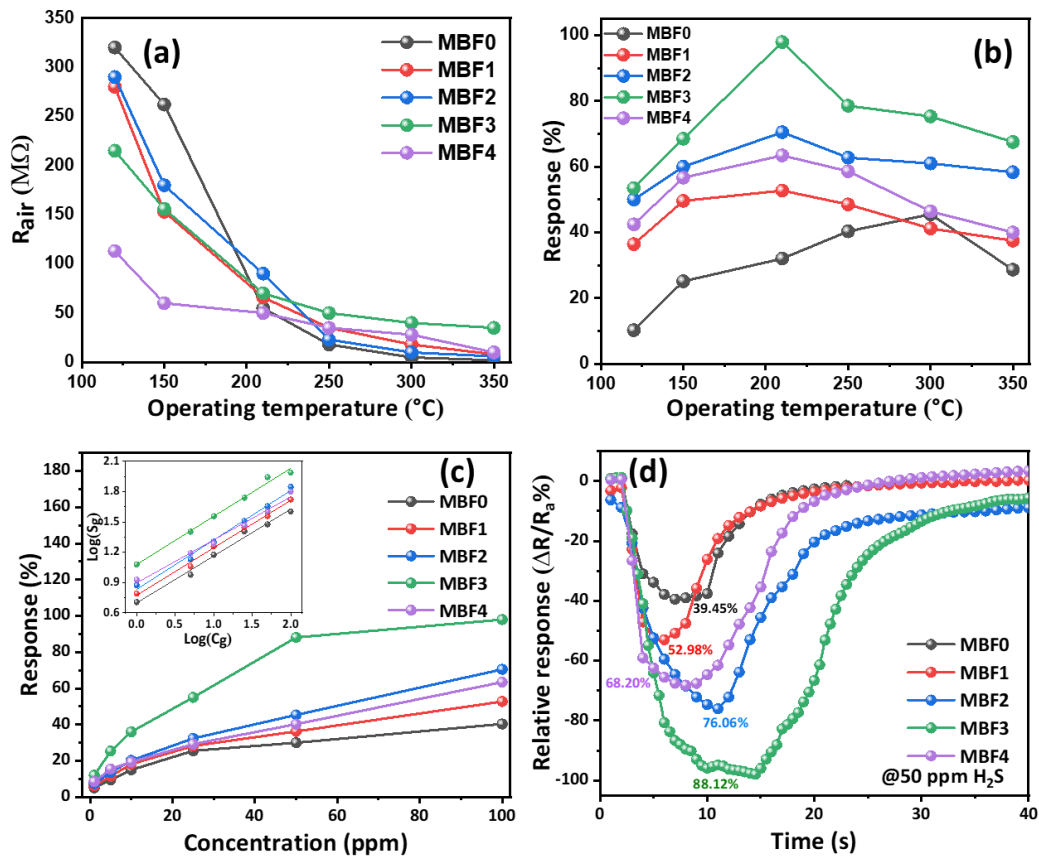


Fig. 5.14. (a) The R_{air} values of bare α - MoO_3 and α - MoO_3 / $BiFeO_3$ heterostructures-based sensors at 200-430 °C temperature. (b) Response (%) of the sensors based on bare α - MoO_3 and α - MoO_3 / $BiFeO_3$ heterostructures-based sensors to 100 ppm H_2S gas in the operating temperature range from 120-350 °C. (c) Response (%) of the bare α - MoO_3 (at 300 °C) and α - MoO_3 / $BiFeO_3$ heterostructures-based sensors as a function of H_2S gas concentration at 210 °C operating temperature. (d) Response comparison of bare α - MoO_3 and α - MoO_3 / $BiFeO_3$ heterostructures-based sensors to 50 ppm H_2S at at their optimum operating temperatures.

Fig. 5.15a represents the dynamic response curve of the MBF3 to different concentration of H_2S from 1-100 ppm at 210 °C. It shows the typical n-type sensing behaviour of the sensors. The lower limit of H_2S detection of the MBF3 sensor is 1 ppm ($S=12.02\%$). The sensor's response tends to saturate after 100 ppm of H_2S concentration. From the dynamic response curve of MBF3 it is evident that the sensor possesses excellent resolution in detecting different concentrations of H_2S , which makes it a reliable sensing material for real-time application. Fig. 5.15b represents the short-time stability of MBF3 sensor, showing response-recovery curves for six consecutive cycles of H_2S gas exposure at 210 °C. The sensor shows remarkable stability exhibiting the same response value for every cycle. The response data of the MBF3 sensor to

100 ppm H₂S was taken in intervals for more than 300 days, which showed only <0.35% stability error, indicating superior long-term stability of the sensor (ref. Fig. 5.15b). As shown in Fig. 5.15c, the selectivity of the sensors to 100 ppm of different interfering target gases such as SO₂, NO, NO₂, CO, isopropyl alcohol, toluene, benzene, formaldehyde, ethanol, acetone, ammonia was investigated. It is clear that the loading with BiFeO₃ benefitted the selectivity of the sensors toward H₂S. All the α -MoO₃/BiFeO₃ heterostructures-based sensors show highly selective response to H₂S which is important for the practical use of the sensor. The reason behind selectivity maybe attributed to bond dissociation energy of H₂S at this temperature is evidently lower than that of C–C (345 kJ/mol) in isopropanol, O–H (458.8 kJ/mol) in ethanol, N–H (391 kJ/mol) in ammonia, and C=O (798.9 kJ/mol) in acetone and HCHO. [36] Fig. 5.15d displays dynamic response transient of MBF3 sensor to 1 ppm H₂S at 210 °C. The response and recovery times (t_{res} and t_{rec}) of the MBF3 sensor to 1 ppm H₂S is 5.7s and 7.5s, respectively. All the sensing performance result of MBF3 altogether proves it to be better than other MoO₃ heterostructure-based H₂S sensors reported in literature (Table 5.1). Fig. 5.16 represents response/recovery time of MBF3 sensor to 100 ppm concentration of H₂S. The fast response/recovery of the sensor makes it suitable for practical application in environmental air quality monitoring.

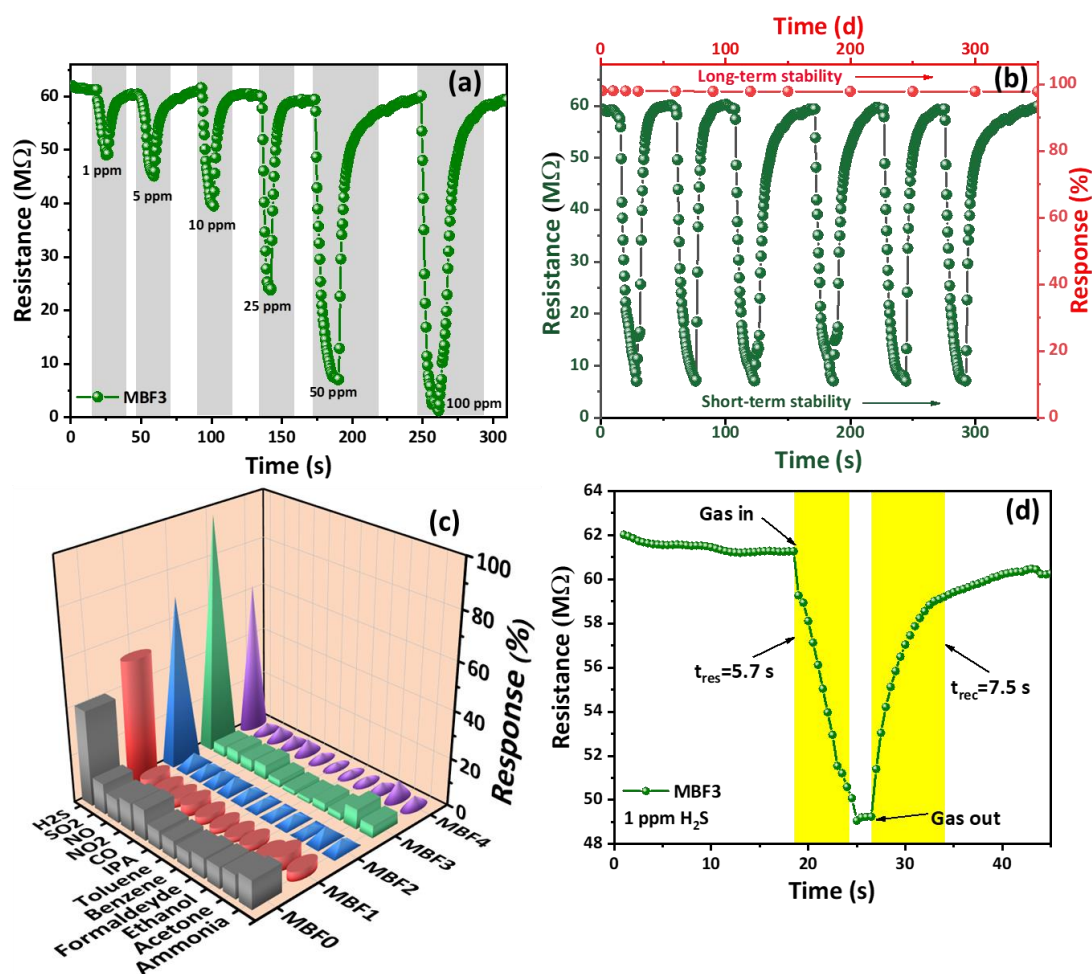


Fig. 5.15. (a) Dynamic response curve of the MBF3 sensor to H₂S concentration (1-100 ppm) at 210 °C. (b) Short-term curves of MBF3 sensor to 50 ppm H₂S for six consecutive cycles at 210 °C and long-term stability data of MBF3 sensor to 100 ppm H₂S at 210 °C taken over 350 days. (c) Gas responses of all the sensors on exposure to 100 ppm concentration of different target analytes at 210 °C. (d) Dynamic response transient of MBF3 based sensor to 1 ppm H₂S at 210 °C.

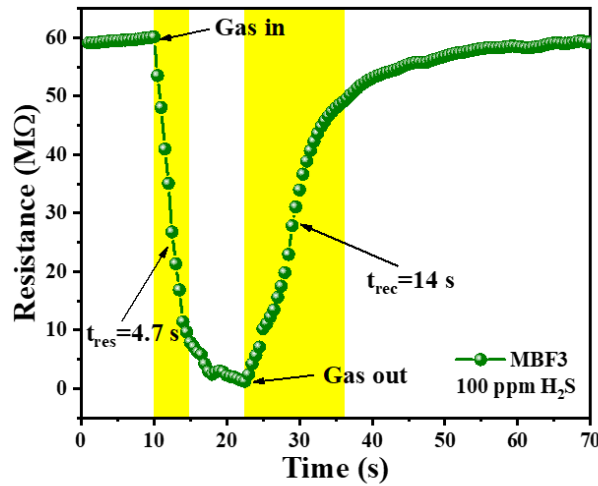
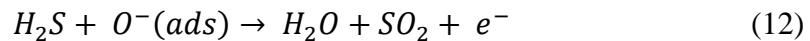


Fig. 5.16. Dynamic response and recovery transient of MBF3 based sensor to 100 ppm H₂S at 210 °C.

5.3.5. Mechanism of H₂S sensing

Gas sensing mechanism of metal oxide semiconductor (MOS)-based materials is mainly explained by adsorption of target gas on the active sites on the surface leading to band bending and change in resistance. The α -MoO₃/BiFeO₃ heterostructures-based sensors exhibited n-type sensing behaviour [11,37]. When an n-type MOS is exposed to air the oxygen molecules from the atmosphere are ionized by capturing electrons from the conduction band and get adsorbed on the sensing material's surface in the form of chemisorbed oxygen ions (O₂⁻, O⁻, O²⁻). These surface adsorbed oxygen species are controlled by the operating temperature of the sensor [36,38]. At operating temperature below 300 °C, the adsorbed oxygen species is O⁻. [39–41] Upon exposure to H₂S gas, these adsorbed oxygen ions react with the gas molecules and release electrons in the process that add up to the conduction band. Thus, depending on the concentration of the target gas, the resistance of the sensors decreases (eq. (11) and (12)),



H₂S sensing mechanism of α -MoO₃/BiFeO₃ heterostructures is schematically illustrated in Fig. 5.17(c-d). In addition to the above ionosorption model, the reasons behind the enhanced H₂S sensing behaviour of the α -MoO₃/BiFeO₃ heterostructures can be attributed to the following reasons.

The reason behind the enhanced H₂S sensing performance of the as-synthesised heterostructure has been explored together by invoking band structure of both the pristine materials as well as heterostructures. Firstly, as evident from the M-S plots (Fig. 5.13), all the α -MoO₃/BiFeO₃ heterostructures showed positive slope, which confirmed formation of n-n type heterojunction at the interface of n-type MoO₃ and n-type BiFeO₃, which plays advantageous role in sensing performance. Among the photoelectrochemical impedance spectra of α -MoO₃/BiFeO₃ heterostructure, MBF3, showed smallest arc radius, which indicates its best interface charge transfer efficiency. This observation corroborates with the PL spectra and photocurrent analysis, where MBF3 showed lowest PL intensity and highest photocurrent response [42,43].

The band positions and positions of fermi levels of two pristine semiconductors is schematically presented in Fig. 5.17a. Based on calculated band positions of CB and VB edges of BiFeO₃ and MBF0 from M-S plot, the possible charge transfer mechanism is schematically presented (Fig. 5.17b) when heterostructure is formed in presence of light. The CB edge of MBF0 is located in between the conduction band edge and the valence band edge of BiFeO₃. In general, electrons eject from VB only when irradiation of light energy equals or exceeds the band gap energy. As BiFeO₃ exhibits narrower band gap it can be activated using visible light. Accordingly, electrons from CB of BiFeO₃ transfers to CB of MBF0 and holes moves in the opposite path, i.e., from VB of MBF0 to VB of BiFeO₃, respectively, which suggests the formation of Type II heterojunction at the interface of two pristine semiconductors.[44,45] It facilitates charge separation of electron-hole pair and reduces the probability of charge recombination. In addition, Type II heterojunction of MBF0 and BiFeO₃ induces the formation of diffusion potential which is the reason for generation of electric field at the interface to induce further injection of electrons. As represented in the band diagram of the α -MoO₃/BiFeO₃ heterostructure, the electron transfer from CB of BiFeO₃ to CB of MoO₃ (as discussed in Fig. 5.17) promotes the gas sensing mechanism [11,46,47]. The conductivity of the heterostructures under influence of changing atmosphere can be represented in eq. (13) as follows [11],

$$G = G_0 \exp \left(\frac{-q\varphi_{eff}}{k_B T} \right) \quad (13)$$

where G_0 is a constant parameter, q is charge of an electron, k_B is Boltzmann's constant, and T is absolute temperature and φ_{eff} represents effective barrier height. When exposed to air, owing to upward bending of surface band of MoO₃ and BiFeO₃, the φ_{eff} value increases. When exposed to H₂S gas, the reaction in eq. (12) takes place and the electrons produced in

the process gets back to the CB of MoO_3 and BiFeO_3 , which causes decrease in φ_{eff} value at their interface. Therefore, change in barrier height and enhancement in charge separation directly effect H_2S sensing property of $\alpha\text{-MoO}_3/\text{BiFeO}_3$ heterostructures.

Secondly, it is reported that oxygen defect states can act as electron donors owing to introduction of a new donor level in between the CB and VB of the materials which acts as an electron trap state to suppress the photogenerated electron-hole recombination. [48,49] As donor density increases, charge transfer from MoO_3 to BiFeO_3 can be improved. Furthermore, the position of the Fermi level shifts towards the CB which significantly enhances the charge carrier separation at the semiconductor/electrolyte interfaces owing to the increased defect states.[50,51] Results of EPR analysis validated the direct evidence of oxygen vacancies in the heterostructures samples. As, MBF3 contained a highest number of oxygen deficiency states (confirmed from EPR analysis and core level XPS spectra of O 1s) compared to other heterostructures and pristine semiconductor, the higher number of photo redox electrons were generated. [52,53] Therefore, the improvement of charge separation and transfer is observed in MBF3. Which is the reason behind its highest H_2S sensing behaviour.

Lastly, oxygen vacancies are most common type of defects on a MOS. As observed from XPS analysis (ref. [Table 5.4](#)), higher percentage of defect oxygen (40.01%) was observed in MBF3 compared to MBF0 sample (17.05%). Higher concentration of O_D (oxygen vacancies) provides more active sites for gas adsorption. This indicates that loading of BiFeO_3 in the system resulted in surface sensitization of the samples. Moreover, MBF3 possessed larger pore size and 1.6 times higher BET surface area than bare MoO_3 , which also leads to enhanced sensing behaviour. All these factors indicate that, modification of band positions by formation of heterostructure between wide bandgap MoO_3 and with narrow bandgap BiFeO_3 to promote charge transfer and defect oxygen sites will enhance the material's applicability as H_2S gas sensor.

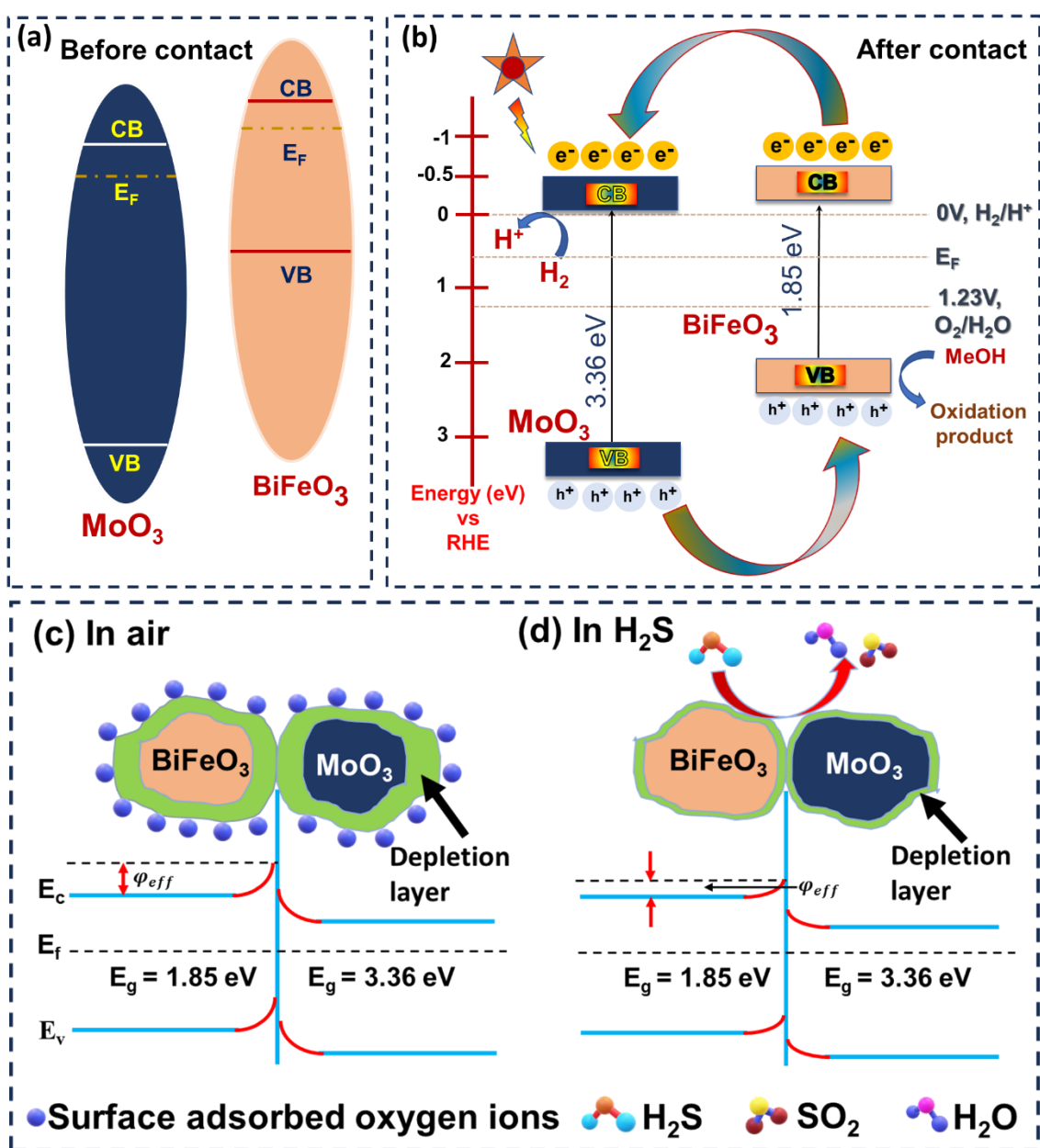


Fig 5.17. (a) Schematically presentation of the band diagram of semiconductors before contact. (b) After contact and light irradiation of Type II mechanism photocatalysis of MoO₃/BiFeO₃ heterostructure. (c-d) Schematic illustration of H₂S sensing mechanism of MoO₃/BiFeO₃ heterostructure.

5.4. Conclusion

In summary, we developed a Type-II heterostructure between n-type MoO_3 and n-type BiFeO_3 (with different loading of BiFeO_3) for H_2S gas sensing for environmental air quality monitoring. The photoelectrochemical measurement confirmed MBF3 exhibited the highest photocurrent density as well as low charge transfer resistance compared to all other heterostructures and pristine semiconductors. As a result, MBF3 exhibited enhanced sensing property with $\sim 98\%$ n-type sensing response to 100 ppm H_2S gas with rapid response/recovery time of 4.7s/14s. Owing to presence of higher oxygen defect in MBF3 compared to bare MoO_3 the localised states were generated within the bandgap of MBF3 which act as trapping centres for charge carriers (electrons and holes). Furthermore, these defect states serve as active sites for adsorption of gas molecules, facilitating the H_2S sensing activity. Thus, modification in the electronic structure of MBF3 and tuning of oxygen defect states influence the separation and migration of charge carriers, which is crucial for efficient H_2S sensing behaviour. Thus, prepared heterostructure could be promising material to sense H_2S for environmental air quality monitoring.

5.5. Reference

- [1] F. Gorini, E. Bustaffa, K. Chatzianagnostou, F. Bianchi, C. Vassalle, Hydrogen sulfide and cardiovascular disease: Doubts, clues, and interpretation difficulties from studies in geothermal areas, *Science of The Total Environment* 743 (2020) 140818.
- [2] C. Szabo, A timeline of hydrogen sulfide (H₂S) research: From environmental toxin to biological mediator, *Biochem Pharmacol* 149 (2018) 5–19.
- [3] F. Zhang, M. Zheng, X. Zhang, X. Cheng, M. Li, L. Huo, X. Zhou, Y. Xu, Rapid detection of H₂S gas driven by the catalysis of flower-like α -Bi₂Mo₃O₁₂ and its visual performance: A combined experimental and theoretical study, *J Hazard Mater* 424 (2022) 127734.
- [4] T. Xu, M. Zhang, F. Zhao, J. Zhao, W. Cong, C. Xie, Z. Yang, G. Wang, J. Li, Highly sensitive detection of H₂S gas at low temperature based on ZnCo₂O₄ microtube sensors, *J Hazard Mater* 440 (2022) 129753.
- [5] Y. Mo, Z. Tan, L. Sun, Y. Lu, X. Liu, Ethanol-sensing properties of α -MoO₃ nanobelts synthesized by hydrothermal method, *J Alloys Compd* 812 (2020) 152166.
- [6] D. Kwak, M. Wang, K.J. Koski, L. Zhang, H. Sokol, R. Maric, Y. Lei, Molybdenum Trioxide (α -MoO₃) Nanoribbons for Ultrasensitive Ammonia (NH₃) Gas Detection: Integrated Experimental and Density Functional Theory Simulation Studies, *ACS Appl Mater Interfaces* 11 (2019) 10697–10706.
- [7] F. Zhang, K. Liu, H. Li, S. Cui, D. Zhang, J. Zeng, Z. Yan, MoO₃Nanorods Decorated by PbMoO₄Nanoparticles for Enhanced Trimethylamine Sensing Performances at Low Working Temperature, *ACS Appl Mater Interfaces* 14 (2022) 24610–24619.
- [8] F. Rahman, A. Zavabeti, M.A. Rahman, A. Arash, A. Mazumder, S. Walia, S. Sriram, M. Bhaskaran, S. Balendhran, Dual Selective Gas Sensing Characteristics of 2D α -MoO₃- x via a Facile Transfer Process, *ACS Appl Mater Interfaces* 11 (2019) 40189–40195.
- [9] J. Bao, Z. Zhang, Y. Zheng, H₂S sensor based on two-dimensional MoO₃ nanoflakes: Transition between sulfidation and oxidation, *Sens Actuators B Chem* 345 (2021) 130408.
- [10] S.K. Shen, X.L. Cui, C.Y. Guo, X. Dong, X.F. Zhang, X.L. Cheng, L.H. Huo, Y.M. Xu, Sensing mechanism of Ag/ α -MoO₃ nanobelts for H₂S gas sensor, *Rare Metals* 40 (2021) 1545–1553.
- [11] X. Gao, Q. Ouyang, C. Zhu, X. Zhang, Y. Chen, Porous MoO₃/SnO₂ Nanoflakes with n-n Junctions for Sensing H₂S, *ACS Appl Nano Mater* 2 (2019) 2418–2425.
- [12] X. Gao, C. Li, Z. Yin, Y. Chen, Synthesis and H₂S sensing performance of MoO₃/Fe₂(MoO₄)₃ yolk/shell nanostructures, *RSC Adv* 5 (2015) 37703–37709.
- [13] T. Das, S. Mojumder, S. Chakraborty, D. Saha, M. Pal, Beneficial effect of Sn doping on bismuth ferrite nanoparticle-based sensor for enhanced and highly selective detection of trace formaldehyde, *Appl Surf Sci* 602 (2022) 154340.
- [14] S. Cao, C. Zhao, J. Xu, A facile synthesis and controlled growth of various MoO₃ nanostructures and their gas-sensing properties, *SN Appl Sci* 1 (2019) 1–6.
- [15] T. Xia, Q. Li, X. Liu, J. Meng, X. Cao, Morphology-controllable synthesis and characterization of single-crystal molybdenum trioxide, *Journal of Physical Chemistry B* 110 (2006) 2006–2012.
- [16] T. Das, S. Das, M. Karmakar, S. Chakraborty, D. Saha, M. Pal, Novel barium hexaferrite based highly selective and stable trace ammonia sensor for detection of renal disease by exhaled breath analysis, *Sens Actuators B Chem* 325 (2020) 128765.
- [17] Z. Guo, D. Wang, Z. Wang, Y. Gao, J. Liu, A Free-Standing α -MoO₃/MXene Composite Anode for High-Performance Lithium Storage, *Nanomaterials* 12 (2022).

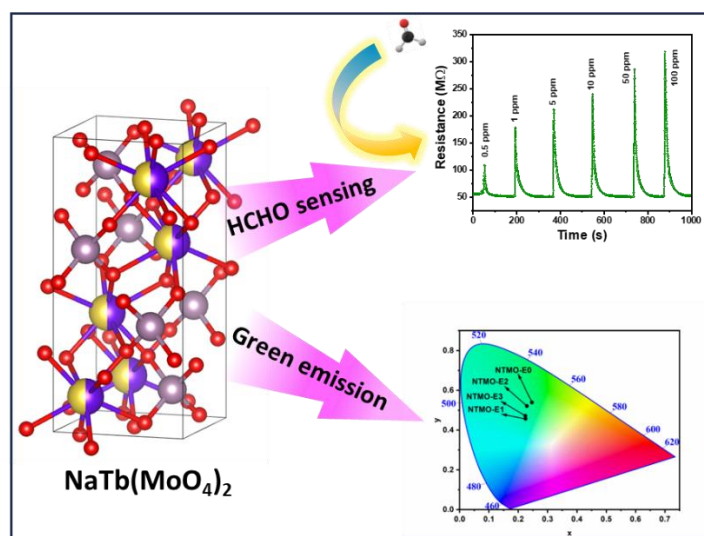
- [18] M.K. Patil, S.H. Gaikwad, S.P. Mukherjee, Phase- And Morphology-Controlled Synthesis of Tunable Plasmonic MoO_3 -xNanomaterials for Ultrasensitive Surface-Enhanced Raman Spectroscopy Detection, *Journal of Physical Chemistry C* 124 (2020) 21082–21093.
- [19] J. Wang, Y. Yang, H. Li, J. Gao, P. He, L. Bian, F. Dong, Y. He, Stable and tunable plasmon resonance of molybdenum oxide nanosheets from the ultraviolet to the near-infrared region for ultrasensitive surface-enhanced Raman analysis, *Chem Sci* 10 (2019) 6330–6335.
- [20] S. Bera, S. Ghosh, T. Maiyalagan, R.N. Basu, Band Edge Engineering of $\text{BiOX}/\text{CuFe}_2\text{O}_4$ Heterostructures for Efficient Water Splitting, *ACS Appl Energy Mater* 5 (2022) 3821–3833.
- [21] J. Yang, W. Han, J. Ma, C. Wang, K. Shimanoe, S. Zhang, Y. Sun, P. Cheng, Y. Wang, H. Zhang, G. Lu, Sn doping effect on NiO hollow nanofibers based gas sensors about the humidity dependence for triethylamine detection, *Sens Actuators B Chem* 340 (2021) 129971.
- [22] S. Xie, H. Zhang, G. Liu, X. Wu, J. Lin, Q. Zhang, Y. Wang, Tunable localized surface plasmon resonances in MoO_3 -x- TiO_2 nanocomposites with enhanced catalytic activity for CO_2 photoreduction under visible light, *Chinese Journal of Catalysis* 41 (2020) 1125–1131.
- [23] N. Illyaskutty, S. Sreedhar, G. Sanal Kumar, H. Kohler, M. Schwotzer, C. Natzeck, V.P.M. Pillai, Alteration of architecture of MoO_3 nanostructures on arbitrary substrates: Growth kinetics, spectroscopic and gas sensing properties, *Nanoscale* 6 (2014) 13882–13894.
- [24] J. Pan, P. Wang, P. Wang, Q. Yu, J. Wang, C. Song, Y. Zheng, C. Li, The photocatalytic overall water splitting hydrogen production of g- $\text{C}_3\text{N}_4/\text{CdS}$ hollow core-shell heterojunction via the HER/OER matching of Pt/MnO_x , *Chemical Engineering Journal* 405 (2021) 126622.
- [25] J. Wang, Q. Zhang, F. Deng, X. Luo, D.D. Dionysiou, Rapid toxicity elimination of organic pollutants by the photocatalysis of environment-friendly and magnetically recoverable step-scheme $\text{SnFe}_2\text{O}_4/\text{ZnFe}_2\text{O}_4$ nano-heterojunctions, *Chemical Engineering Journal* 379 (2020).
- [26] S. Bera, S. Ghosh, T. Maiyalagan, R. N. Basu, Band Edge Engineering of $\text{BiOX}/\text{CuFe}_2\text{O}_4$ Heterostructures for Efficient Water Splitting, *ACS Appl Energy Mater* 5 (2022) 3821–3833.
- [27] D. Klotz, D. A. Grave, H. Dotan, A. Rothschild, Empirical Analysis of the Photoelectrochemical Impedance Response of Hematite Photoanodes for Water Photo-oxidation, *J Phys Chem Lett* 9 (2018) 1466–1472.
- [28] S. Ghosh, S. Bera, S. Sardar, S. Pal, F. V. A. Camargo, C. D’Andrea, G. Cerullo, Role of Efficient Charge Transfer at the Interface between Mixed-Phase Copper-Cuprous Oxide and Conducting Polymer Nanostructures for Photocatalytic Water Splitting, *ACS Applied Materials & Interfaces* 15 (2023) 18867–18877.
- [29] S. Samajdar, S. Bera, P.S. Das, H. Finch, V.R. Dhanak, S. Chakraborty, T. Maiyalagan, K. Annapurna, S. Ghosh, Exploration of 1D-2D $\text{LaFeO}_3/\text{RGO}$ S-scheme heterojunction for photocatalytic water splitting, *Int J Hydrogen Energy* 48 (2023) 17838–17851.
- [30] S. Ghosh, S. Bera, A. Singh, S. Basu, R.N. Basu, Hierarchical $\text{Bi}_2\text{WO}_6/\text{BiFeWO}_6$ n-n heterojunction as an efficient photocatalyst for water splitting under visible light, *J Alloys Compd* 919 (2022) 165700.
- [31] J. Shang, X. Xu, K. Liu, Y. Bao, Yangyang, M. He, LSPR-driven upconversion enhancement and photocatalytic H_2 evolution for $\text{Er-Yb}:\text{TiO}_2/\text{MoO}_3$ -x nano-semiconductor heterostructure, *Ceram Int* 45 (2019) 16625–16630.
- [32] J. Shang, X. Xu, K. Liu, Y. Bao, M. He, LSPR-driven upconversion enhancement and photocatalytic H_2 evolution for $\text{Er-Yb}:\text{TiO}_2/\text{MoO}_3$ -x nano-semiconductor heterostructure, (2019).
- [33] Z. Wang, Z. Tian, D. Han, F. Gu, Highly Sensitive and Selective Ethanol Sensor Fabricated with In-Doped 3DOM ZnO , *ACS Appl Mater Interfaces* 8 (2016) 5466–5474.

- [34] Z. Wang, J. Xue, D. Han, F. Gu, Controllable defect redistribution of ZnO nanopyrramids with exposed {1011} facets for enhanced gas sensing performance, *ACS Appl Mater Interfaces* 7 (2015) 308–317.
- [35] S. Sardana, H. Kaur, B. Arora, D.K. Aswal, A. Mahajan, Self-Powered Monitoring of Ammonia Using an MXene/TiO₂/Cellulose Nanofiber Heterojunction-Based Sensor Driven by an Electrospun Triboelectric Nanogenerator, *ACS Sens* 7 (2022) 312–321.
- [36] X. Zhu, X. Chang, S. Tang, X. Chen, W. Gao, S. Niu, J. Li, Y. Jiang, S. Sun, Humidity-Tolerant Chemiresistive Gas Sensors Based on Hydrophobic CeO₂/SnO₂ Heterostructure Films, *ACS Appl Mater Interfaces* 14 (2022) 25680–25692.
- [37] A. Katoch, J.H. Kim, Y.J. Kwon, H.W. Kim, S.S. Kim, Bifunctional sensing mechanism of SnO₂-ZnO composite nanofibers for drastically enhancing the sensing behavior in H₂ gas, *ACS Appl Mater Interfaces* 7 (2015) 11351–11358.
- [38] B.Y. Song, X.F. Zhang, J. Huang, X.L. Cheng, Z.P. Deng, Y.M. Xu, L.H. Huo, S. Gao, Porous Cr₂O₃ Architecture Assembled by Nano-Sized Cylinders/Ellipsoids for Enhanced Sensing to Trace H₂S Gas, *ACS Appl Mater Interfaces* (2022).
- [39] W. Qin, Z. Yuan, Y. Shen, R. Zhang, F. Meng, Phosphorus-doped porous perovskite LaFe_{1-x}PxO_{3-δ} nanosheets with rich surface oxygen vacancies for ppb level acetone sensing at low temperature, *Chemical Engineering Journal* 431 (2022) 134280.
- [40] A. Shanmugasundaram, D.S. Kim, N.D. Chinh, J. Park, Y.J. Jeong, J.J. Piao, D. Kim, D.W. Lee, N-/S-dual doped C@ZnO: An excellent material for highly selective and responsive NO₂ sensing at ambient temperatures, *Chemical Engineering Journal* 421 (2021) 127740.
- [41] H. Song, S. Yan, Y. Yao, L. Xia, X. Jia, J. Xu, 3D α-Fe₂O₃ nanorods arrays@graphene oxide nanosheets as sensing materials for improved gas sensitivity, *Chemical Engineering Journal* 370 (2019) 1331–1340.
- [42] J. Wang, Q. Zhang, F. Deng, X. Luo, D.D. Dionysiou, Rapid toxicity elimination of organic pollutants by the photocatalysis of environment-friendly and magnetically recoverable step-scheme SnFe₂O₄/ZnFe₂O₄ nano-heterojunctions, *Chemical Engineering Journal* 379 (2020) 122264.
- [43] W. Guo, L. Huang, X. Liu, J. Wang, J. Zhang, Enhanced isoprene gas sensing performance based on p-CaFe₂O₄/n-ZnFe₂O₄ heterojunction composites, *Sens Actuators B Chem* 354 (2022) 131243.
- [44] K. Akbar, E. Moretti, A. Vomiero, Carbon Dots for Photocatalytic Degradation of Aqueous Pollutants: Recent Advancements, *Adv Opt Mater* 9 (2021) 2100532.
- [45] B. Palanivel, A. Mani, Conversion of a Type-II to a Z-Scheme Heterojunction by Intercalation of a 0D Electron Mediator between the Integrative NiFe₂O₄/g-C₃N₄ Composite Nanoparticles: Boosting the Radical Production for Photo-Fenton Degradation, *ACS Omega* 5 (2020) 19747–19759.
- [46] H. Shan, C. Liu, L. Liu, J. Zhang, H. Li, Z. Liu, X. Zhang, X. Bo, X. Chi, Excellent toluene sensing properties of SnO₂-Fe₂O₃ interconnected nanotubes, *ACS Appl Mater Interfaces* 5 (2013) 6376–6380.
- [47] J.H. Kim, S.S. Kim, Realization of ppb-Scale Toluene-Sensing Abilities with Pt-Functionalized SnO₂-ZnO Core-Shell Nanowires, *ACS Appl Mater Interfaces* 7 (2015) 17199–17208.
- [48] H. Tan, Z. Zhao, W. Bin Zhu, E.N. Coker, B. Li, M. Zheng, W. Yu, H. Fan, Z. Sun, Oxygen vacancy enhanced photocatalytic activity of perovskite SrTiO₃, *ACS Appl Mater Interfaces* 6 (2014) 19184–19190.
- [49] X. Wang, X. Wang, J. Huang, S. Li, A. Meng, Z. Li, Interfacial chemical bond and internal electric field modulated Z-scheme Sv-ZnIn₂S₄/MoSe₂ photocatalyst for efficient hydrogen evolution, *Nature Communications* 2021 12:1 12 (2021) 1–11.

- [50] S. Ghosh, D. Sarkar, S. Bastia, Y.S. Chaudhary, Band-structure tunability via the modulation of excitons in semiconductor nanostructures: manifestation in photocatalytic fuel generation, *Nanoscale* 15 (2023) 10939–10974.
- [51] J. He, L. Hu, C. Shao, S. Jiang, C. Sun, S. Song, Photocatalytic H₂O Overall Splitting into H₂Bubbles by Single Atomic Sulfur Vacancy CdS with Spin Polarization Electric Field, *ACS Nano* 15 (2021) 18006–18013.
- [52] A. Janotti, J.B. Varley, P. Rinke, N. Umezawa, G. Kresse, C.G. Van De Walle, Hybrid functional studies of the oxygen vacancy in TiO₂, *Phys Rev B Condens Matter Mater Phys* 81 (2010) 085212.
- [53] A. Naldoni, M. Allieta, S. Santangelo, M. Marelli, F. Fabbri, S. Cappelli, C.L. Bianchi, R. Psaro, V. Dal Santo, Effect of nature and location of defects on bandgap narrowing in black TiO₂ nanoparticles, *J Am Chem Soc* 134 (2012) 7600–7603.

CHAPTER 6

Structural disorder driven multifunctionality of $\text{NaTb}(\text{MoO}_4)_2$ nanoparticles toward green photoluminescence and detection of formaldehyde



This work is under communication

6.1. Introduction

Designing of multifunctional nanomaterials has been of high importance for various application fields such as light emitting diode,[1] gas sensing,[2] green energy generation,[3] catalysis[4,5] and energy storage and conversion.[6,7] This has spurred extensive research efforts to develop advanced functional nanomaterials that can combine multiple functions and seamlessly adapt to different application scenarios.[8] Therefore, exploration of advanced functional nanomaterials with improved performance and high efficiency has been going on for years. However, there has not been a clear understanding and established correlation between structural property of the material with its multifunctional applicability.

Defect engineering is recognized as one of the effective approaches for introducing multifunctionalities into materials, enabling the achievement of desired properties in various application areas like gas sensing, and optoelectronics. Oxygen vacancy (V_O) defects can have a substantial impact on material's properties. These defects can be purposefully controlled in order to customize the characteristics of the material for specific applications. There are several reports in literature on tailoring the structural defects in the system to induce oxygen vacancy driven photoluminescence spectra. Manju et al. reported that photoluminescence property of $SrZnO_2$ system has originated from disruption in the system caused by oxygen vacancies and supported their claim using first principle calculation.[9] Ji et al. demonstrated the role of oxygen vacancies on the colour change of $BaMgSiO_4:Eu^{2+}$ phosphor.[10] A report by Ding et al. showed near infrared luminescence property of solid-state reaction derived single-phase yttrium tungstate, in which the localised energy band position changed with oxygen vacancy concentration.[11] Choi et al. have investigated the temperature dependent strong photoluminescent property of one-dimensional SnO_2 nanowire originated due to migration of oxygen vacancies.[12] Wang et al. have suggested that increase of oxygen vacancy led to coexistence of Eu^{3+} and Eu^{2+} which influences photoluminescence property of $Ba_{1-x}Zn_{1-y}P_2O_7:xEu^{2+/3+}$ system.[13]

On the other hand, variation of electrical resistance of the chemiresistive gas is also greatly influenced by structural defects/ oxygen vacancies. Many reports have been found in literature that dealt with oxygen vacancy driven gas sensing activity, such as, Tong et al. have reported p-type ternary oxide $CuCrO_2$ with singly ionised oxygen vacancy plays active role in enhancement of VOC sensing property by promoting charge exchange between the sensing layer and the target gas molecule [14]. Du et al. reported oxygen vacancies enhance the gas-

sensing performance of In_2O_3 by providing donor level and supply more electrons in the conduction band [15]. Parayil et al. have demonstrated volatile organic compound (VOC) sensing property of photoluminescent $\text{Y}_2\text{Zr}_2\text{O}_7$ nanomaterial which is greatly influenced by oxygen vacancy in the system.[16]

Lanthanide double molybdates $\text{ALn}(\text{MoO}_4)_2$ (A= alkali metal ions, Ln= rare earth ions) of scheelite type structure with C_{4h} symmetry and space group $I4_1/a$ have gained significant research interest due to their chemical, thermal stability and emission in long wavelength range. Diverse application fields of these Scheelite-type molybdates include solid state lighting, display devices, fluorescent probes, thermographic phosphors, photocatalytic activity, gas sensor, anode for lithium-ion batteries and nano-electronic devices [17]. The key characteristics of the scheelite structure is its tetrahedral coordination and inherent symmetry which furnishes a stable host lattice for doping with lanthanide ions. Charge transfer from oxygen metal to molybdate phosphors leads to broad adsorption band in the rear-UV region [18]. Various reports can be found in literature where the luminescence properties have been studied for the scheelite type tetragonal double molybdate structures by varying synthesis technique, sintering temperature, morphology and dopant.[19–21] Morozov et al. have investigated the impact of various synthesis methods on the structural and PL properties of $\text{KTb}(\text{MoO}_4)_2$ single crystal.[22] Jia et al. demonstrated hydrothermal synthesis of Eu^{3+} doped $\text{NaTb}(\text{MoO}_4)_2$ which exhibited efficient energy transfer from MoO_4^{2-} to Tb^{3+} to Eu^{3+} .[23] Swaita et al. reported dual-functional activity of $\text{NaTb}(\text{MoO}_4)_2:\text{Dy}^{3+}$ @Phen nanoparticles synthesised via hydrothermal technique.[24] Wang et al. investigated photoluminescence property of solid-state reaction derived $\text{NaLa}_{1-x}\text{Tb}_x(\text{MoO}_4)_2$.[25] A work by Zhou et al. demonstrated multicolour luminescence property of Eu^{3+} activated $\text{NaTb}(\text{MoO}_4)_2$ microcrystals synthesised without surfactant.[26] As previous reports suggest, Tb^{3+} ion is a known for activator of green emission which originates from the transition from $^5\text{D}_4$ state to the $^7\text{F}_J$ ($J=6,5,4,3$) states. [27–29]

In the recent time, human health is at risk due to increase of toxic gas in environment. Formaldehyde (HCHO), a colourless toxic volatile organic compound, is one of most common indoor pollutant gas generally emitted from newly furnished furniture, paints and adhesives.[30] Exposure to high concentration of HCHO can damage to central nervous system and can even cause cancer.[31,32] According to World Health Organization (WHO) the threshold limit of exposure to HCHO has been restricted to 1-0.08 ppm.[33] Therefore, it is crucial to fabricate highly sensitive sensor system that can detect low concentration HCHO for environmental monitoring and health protection. Although there are techniques such as

mass chromatography (MS) techniques for gas detection, they are costly. Chemiresistive sensors offer several benefits such as, cost-effectiveness, simplistic, stable and fast sensing performance.

To the best of our knowledge no experimental study supported by theoretical DFT calculations have been performed on $\text{NaTb}(\text{MO}_4)_2$ system to understand multifunctionality of the system toward luminous property and gas sensing activity. In the present work, exploration of defect (V_O) engineering as a strategy to induce multifunctionality in scheelite type $\text{NaTb}(\text{MO}_4)_2$ toward photoluminescence and detection of toxic gas formaldehyde (HCHO) was studied for the first time by employing ab initio calculations based on density functional theory. The effect of oxygen vacancies on band structure of $\text{NaTb}(\text{MO}_4)_2$ nanoparticles has been studied and it revealed that by tuning of oxygen vacancy (V_O) and introducing disorder in the system induced green emission and gas sensing property of $\text{NaTb}(\text{MO}_4)_2$. Presence of V_O in $\text{NaTb}(\text{MO}_4)_2$ leads to formation of new energy states within the forbidden gap, induces disorder in the system and modifies the bond lengths. The oxygen vacancies are created in the system during controlled synthesis by using ethylenediaminetetraacetic acid (EDTA) which regulates the nucleation and growth of $\text{NaTb}(\text{MO}_4)_2$ nanomaterials and created deformation near Tb^{3+} ions. Analysis of XPS data indicates that the concentration of V_O has positive dependency on concentration of EDTA in the solution during the synthesis process. It slows down the reaction process and helps creating disorder in the samples resulting in the oxygen vacancy V_O . Moreover, positive correlation was found between the gas response and oxygen vacancy concentration. The trapped electrons in V_O serve as active sites for adsorption of atmospheric oxygen facilitating the gas sensing response of $\text{NaTb}(\text{MO}_4)_2$. DFT study was utilised to visualise the energy band structure of the nanomaterials and calculate the adsorption energy of formaldehyde gas molecule. Therefore, this study gives a new insight to the fabrication and engineering of nanomaterials which exhibits multifunctionality driven by oxygen vacancies.

6.2. Experimental section

6.2.1. Chemicals and materials

Terbium (III) nitrate hexahydrate [$\text{Tb}(\text{NO}_3)_3 \cdot 6\text{H}_2\text{O}$], sodium tungstate dihydrate ($\text{Na}_2\text{WO}_4 \cdot 2\text{H}_2\text{O}$), Ethylenediamine tetraacetic acid (EDTA), deionised water (DI), ethanol, isopropyl alcohol (IPA).

6.2.2. Synthesis of $\text{NaTb}(\text{MO}_4)_2$ nanoparticles

$\text{NaTb}(\text{MO}_4)_2$ nanoparticles were synthesised via EDTA assisted hydrothermal synthesis route. Firstly, 1.0 mmol terbium (III) nitrate hexahydrate $\text{Tb}(\text{NO}_3)_3 \cdot 6\text{H}_2\text{O}$ and Ethylenediamine tetraacetic acid (EDTA) 50 ml DI water and stirred for 20 mins using magnetic stirrer. 2.00 mmol sodium tungstate dihydrate ($\text{Na}_2\text{WO}_4 \cdot 2\text{H}_2\text{O}$) was dissolved in 20 ml water separately and dropwise added to the previous solution. The solution was stirred for 30 mins to achieve homogeneity. Then the solution was transferred to Teflon-lined stainless-steel autoclave of capacity 100 ml. The autoclave was put in a furnace 180 °C for 24 h for hydrothermal treatment. After the reaction, the yellowish-white powder was collected and centrifuged at 12000 rpm for 10 mins. Then the powder was retrieved and washed with DI water and ethanol and kept at oven at 70 °C for 24 h for drying. The dried powder was then calcined at 800 °C under nitrogen (N_2) atmosphere for 5 h to achieve final product. Similar procedure was followed with variation of EDTA concentration (viz, 0.0, 0.25, 0.50, 0.75 mmol) while other parameters were kept the same. The as-synthesised nanomaterials without EDTA, with 0.0, 0.25, 0.50, 0.75 mmol EDTA were named as NTMO-E0, NTMO-E1, NTMO-E2 and NTMO-E3, respectively. The schematic diagram of the synthesis procedure is illustrated in Fig. 6.1.

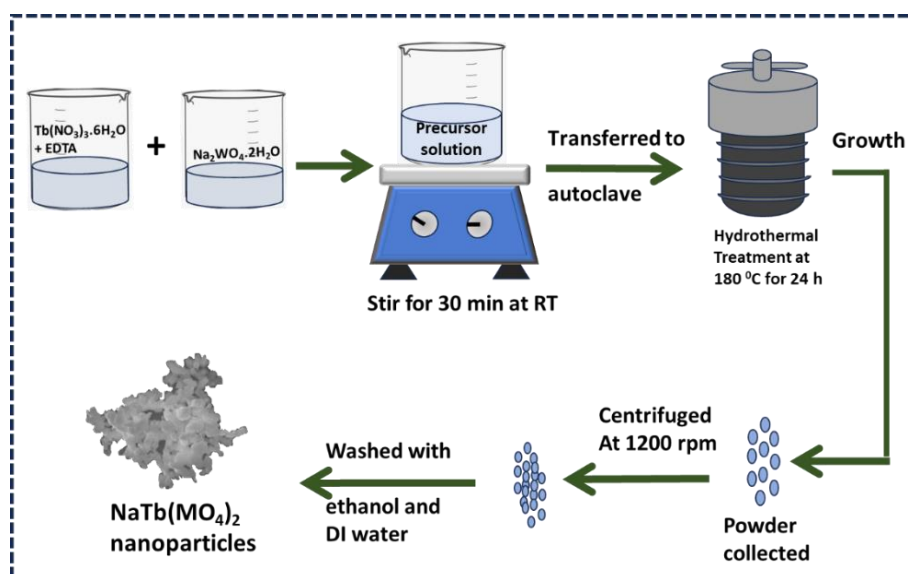


Fig. 6.1. Schematic diagram of the synthesis procedure of $\text{NaTb}(\text{MO}_4)_2$ nanoparticles.

6.2.3. Characterization techniques

X-ray diffraction (XRD) study of the as-synthesized nanomaterials patterns using X'pert Pro MPD XRD PANalytical diffractometer in the range $2\theta = 10^\circ$ - 80° with nickel filtered Cu-K_α radiation of wavelength, $\lambda = 0.15404$ nm. For elucidation of crystal structure and crystal

parameters of the nanomaterials, Rietveld refinement was conducted based on XRD data using FullProf suit software. The micrographs of morphological structure of the materials were captured by field-emission scanning electron microscopy (FESEM) (Carl Zeiss make Supra 35 VP microscope) of 10 kV accelerating voltage. Presence of different functional groups in the prepared nanomaterials was confirmed utilizing Fourier Transform Infrared (FTIR) spectrometer (Nicolet 380). Raman spectra and Photoluminescence (PL) spectra of the samples were recorded using a Jobin Yvon HR800 confocal Raman system (756 nm laser beam) and a fluorescence spectrophotometer (PL, F-7000, Japan). UV-Vis absorption spectra was recorded at room temperature using Shimadzu UV-Vis-NIR spectrometer (UV-3600). Gas sensing measurement was conducted using Agilent 34461A digital multimeter interfaced with Keysight Bengvue software. For the study of elemental composition of the as-synthesised materials, X-ray photoelectron spectroscopy (XPS) was employed (PHI 5000 Versa Probe II scanning XPS microprobe ULVAC-PHI, U.S) equipped with monochromatic $AlK\alpha$ ($h\nu=1486.6$ eV) source.

6.2.4. Fabrication of gas sensors using $NaTb(MO_4)_2$ nanomaterials

For the study of gas sensing property, chemiresistive type sensors were fabricated using of $NaTb(MO_4)_2$ nanomaterials. Taguchi type sensors were prepared using hollow cylindrical substrates of alumina of dimension, 3.5 mm (height) \times 1 mm (outer diameter) \times 0.5 mm (inner diameter). Pt electrodes were added to each end of the alumina substrate with conducting gold paste. To make the sensor film coating, 5mg quantity of the materials were grinded well with isopropyl alcohol to form a slurry paste. When the slurry achieved consistency of requirement, 6 μ L of the slurry was taken and drop coated on the outer surface of the alumina substrate. Then, the coated substrates are kept in oven of 120 $^{\circ}$ C for 6 h so that all the solvents evaporate. After this, the sensor substrates were welded on a six-pin module with double mesh on top (200 mesh each). Ni-Cr alloy wire was inserted inside the hollow of the alumina tube and welded with the two pins of the six-pin module. This Ni-Cr wire is required for heating up the sensor surface by applying voltage across it. These two pins of the socket is connected with a voltage source to regulate the temperature by changing the voltage. And other two pins were connected with a multimeter interfaced with a continuous data logging computer software to record the change in resistance of the sensors. Following the same manner all the sensors using the as-synthesised materials were prepared. For the gas sensing measurement study, the commercially available gas cylinders of 100 ppm concentration balanced in air were purchased from market. The required concentration for the sensing measurements were prepared by

mixing dry N₂ gas using a mass flow controller (MFC)[34]. The response was calculated using eq. (1),

$$S = \frac{R_{gas}}{R_{air}} \quad (1)$$

where R_{gas} is the resistance of the sensors in presence of target gas, and R_{air} is the resistance of the sensors in presence of air. The response and recovery times of the sensors were calculated by calculating the time taken by the sensor to reach 90% of the equilibrium-state resistance when the sensor is exposed to the target gas and when the target gas is removed, respectively.

6.2.5. Calculation using ab initio density functional theory (DFT)

First principle calculation based on density functional theory (DFT) was carried out to gain insight about optoelectronic property and band structure of NaTb(MoO₄)₂. Spin-polarised band structure, partial density of states (PDOS) and total density of states (TDOS) of all the NaTb(MoO₄)₂ samples were calculated using Vienna ab-initio Simulation Package (VASP) by implementing the plane wave pseudo-potential basis and Perdew-Burke-Ernzerhof (PBE) approximation exchange-correlation potential. To achieve convergence, the plane wave basis with cutoff energy 520 eV and a $5 \times 5 \times 2$ Monkhorst-Pack mesh was employed for sampling the Brillouin zone. For the calculations, the Hellmann–Feynman forces applied on each atom and the EDIFF parameter were set to 0.015 eV/Å and 10⁻⁶ eV, respectively.

For the understanding of gas sensing mechanism, the adsorption energy of formaldehyde (HCHO) on the slab surface was calculated. A vacuum region of 20 Å was considered for avoiding the interlayer interactions along z-axis. To attain convergence, 520 eV cut off energy, $3 \times 2 \times 1$ Monkhorst-Pack mesh and fixed 10⁻⁶ eV of EDIFF were employed. To gain insight on the adsorption mechanism, isolated HCHO molecule was modelled above the cleaved, most exposed (1 1 2) surface, with the molecule positioned at the centre of the unit cell in two configurations: vertical and horizontal. The adsorption energy of HCHO on the NaTb(MoO₄)₂ slab surface was calculated using eq. (2) as follows, to understand the influence of defect on HCHO sensing activity of NaTb(MoO₄)₂,[35]

$$E_{ads} = E_{slab + gas} - (E_{slab} + E_{gas}) \quad (2)$$

Here E_{slab} , E_{gas} , $E_{slab + gas}$, indicate the total energy of the slab, total energy of the slab with gas, energy of isolated HCHO gas molecule. According to the definition, negative binding energy indicates an exothermic reaction.

6.3. Results and discussion

6.3.1. Crystallographic structure and morphological analysis

XRD spectra analysis was utilised to determine the phase and structure of as-synthesized $\text{NaTb}(\text{MoO}_4)_2$ nanoparticles. Fig. 6.2 represents the XRD patterns of $\text{NaTb}(\text{MoO}_4)_2$ synthesized without EDTA (NTMO-E0) and with varying concentration of EDTA (NTMO-E1, NTMO-E2 and NTMO-E3). The patterns are analysed using X'pert HighScore Plus software and all of the patterns matched well with the ICDD card number 00-027-1422 and all of the patterns exhibit to tetragonal phase belonging to the space group 141/a (88). All the materials showed highly crystalline nature. No impurity peaks were observed in all the samples indicating phase purity of the as-synthesised $\text{NaTb}(\text{MoO}_4)_2$ nanoparticles. The average crystallite size of the samples was calculated using Debye-Scherrer formula as given in eq. (3) The strain (ϵ) was calculated using eq. (4),

$$D = \frac{K\lambda}{\beta \cos \theta} \quad (3)$$

$$\epsilon = \frac{\beta}{4 \tan (\theta)} \quad (4)$$

Where, D represents crystallites size, K is shape factor with a value of 0.89, λ is the wavelength of the X-ray source (here, 0.15406nm), β is full width at half maximum (FWHM) of the diffraction peak for the diffraction angle 2θ , and θ is the Bragg angle. The as-calculated of crystallite size are ~38 nm, 37 nm, 35 nm and 30 nm, for NTMO-E0, NTMO-E1, NTMO-E2 and NTMO-E3, respectively. The values of lattice strain (ϵ) for the samples were found out to be 0.0039, 0.0039, 0.0041, 0.0048 for NTMO-E0, NTMO-E1, NTMO-E2 and NTMO-E3, respectively. From the results it is clear that addition of EDTA during the synthesis process the crystallite size decreased gradually from NTMO-E0 to NTMO-E3. Additionally, the increase in the lattice strain value with increased EDTA concentration also indicates structural distortion in the system.

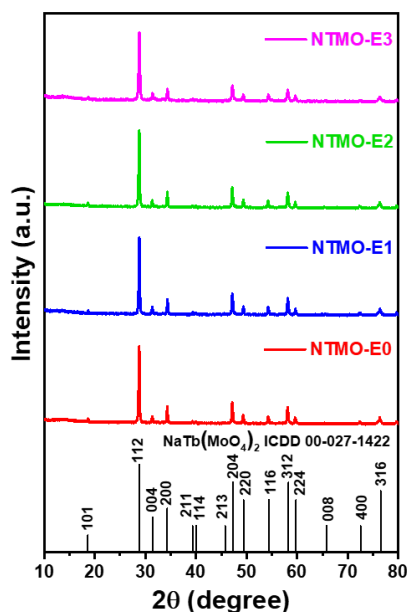


Fig. 6.2. XRD patterns of NTMO-E0, NTMO-E1, NTMO-E2, NTMO-E3 and NaTb(MoO₄)₂ ICDD pattern of card number 00-027-1422.

Rietveld refinement is a useful tool to obtain information about long range structural long range structural order-disorder of a system. Lattice parameters, unit cell volume, bond lengths and angles between (Mo-O)/(Na/Tb-O) were studied utilizing the refinement technique by analysing the XRD data of tetragonal phase of NaTb(MoO₄)₂. The refinement of the peak shape was done using the I4₁/a space group and Pseudo-Voigt profile function with asymmetry. The background data was refined using linear interpolation. During the refinement, the atomic positions of O were refined. The calculated data were in good agreement with the experimentally observed data indicating the credibility of the crystal structure, as can be seen from χ^2 value and R_p , R_{wp} . The observed and refined XRD pattern of NaTb(MO₄)₂ samples are displayed in Fig. 6.3(a-d). The refined structural parameters are summarised in Table 6.1. The unit cell of NaTb(MoO₄)₂ is visualized using the crystal parameters obtained from Rietveld refinement using VESTA software (as displayed in Fig. 6.3e). The crystal structure consists of randomly distributed Na⁺ and Tb³⁺ atoms at same 4b sites and coordinated to eight adjacent O atoms forming (Na/Ce)O₈ polyhedral that are connected to MoO₄ tetrahedra where Mo occupies 4a site. The lattice parameter a is observed to increase gradually from NTMO-E1 to NTMO-E3. Two bond different bond lengths of Na/Tb-O noted as $d_{1(\text{Na/Tb}-\text{O})}$ and $d_{2(\text{Na/Tb}-\text{O})}$ were formed which indicates the distortion in (Na/Tb)O₈ polyhedron. Two bond angles noted as $\alpha_{1(\text{O}-\text{Mo}-\text{O})}$ and $\alpha_{2(\text{O}-\text{Mo}-\text{O})}$ were formed. The bond length of Mo-O was found to increase

monotonously as 1.78813, 1.82054, 1.827 and 1.859, for NTMO-E0 to NTMO-E3, respectively. This suggests that the distortion in MoO_4 tetrahedra increases with increase amount of EDTA. This corroborates with the increasing trend in calculated strain (ϵ) value of lattice (as given in Table 6.1).

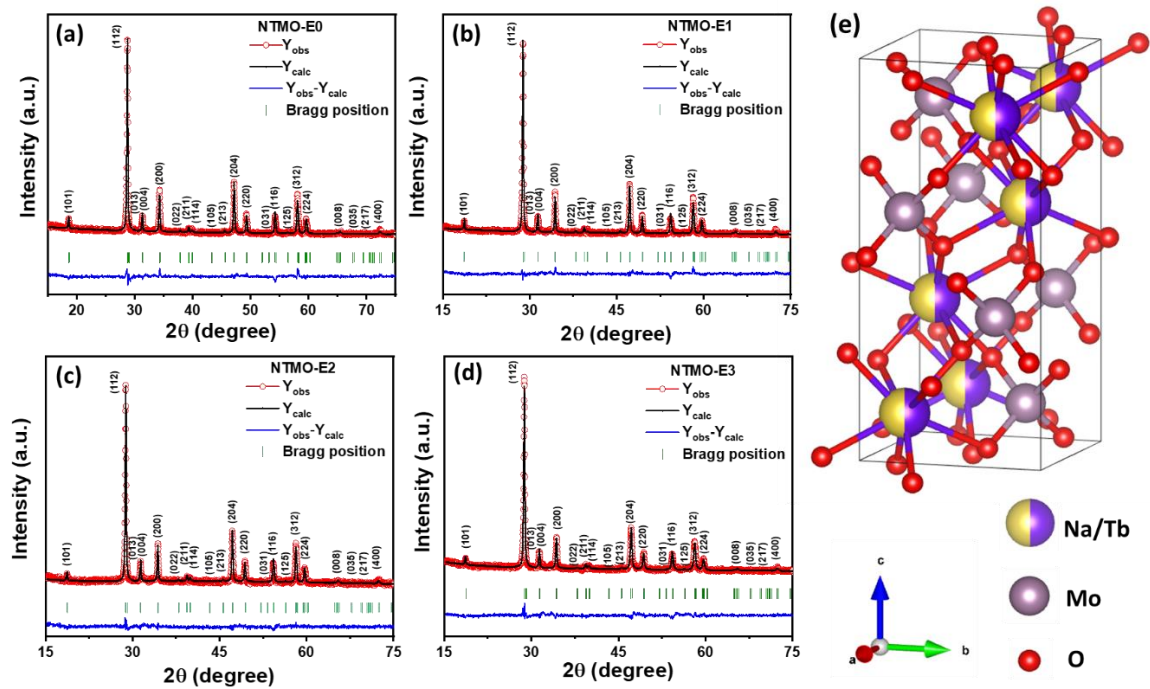


Fig. 6.3. The observed and refined XRD pattern of $\text{NaTb}(\text{MoO}_4)_2$ samples (a) NTMO-E0, (b) NTMO-E1, (c) NTMO-E2 and (d) NTMO-E3, (e) unit cell of $\text{NaTb}(\text{MoO}_4)_2$ tetragonal structure.

Table 6.1 Refined parameters of NTMO samples obtained from Rietveld refinement method using FullProf suite software.

Parameters		NTMO-E0	NTMO-E1	NTMO-E2	NTMO-E3
Lattice parameters	a = b (Å)	5.22570(13)	5.21890(12)	5.21929(13)	5.22173(15)
	c (Å)	11.4054(5)	11.3997(5)	11.4037(5)	11.3945(6)
Unit cell vol.	V (Å ³)	311.458(17)	310.494(16)	310.648(18)	310.69(2)
Bond length (Å)	d _{1(Na/Tb-O)}	2.33599(7)	2.29378(6)	2.346(11)	2.342(10)
	d _{2(Na/Tb-O)}	2.63101(6)	2.63597(6)	2.509(10)	2.477(9)
	Mo-O	1.78813(5)	1.82054(5)	1.827(11)	1.859(10)
Bond angle (°)	α _{1(O-Mo-O)}	113.2989(15)	113.9096(15)	110.5(7)	111.2(6)
	α _{2(O-Mo-O)}	102.061(3)	100.918(3)	109.0(4)	108.6(3)
R _p (%)		3.76	3.56	3.68	3.57
R _{wp} (%)		4.97	4.67	4.69	4.66
R _{exp} (%)		3.63	3.69	4.01	3.65
χ ²		1.87	1.60	1.37	1.63
Crystallite size (nm)		38	37	35	30
Lattice strain (ε)		0.0039	0.0039	0.0041	0.0048
Exp. band gap (E _g) (eV)		1.89	1.87	1.83	2.00
Theo. gap (E _g) (eV)		3.02	2.64	1.29	2.68

Morphological structure of the NaTb(MoO₄)₂ samples was investigated using the field effect transmission microscopy (FESEM). FESEM image of the as-synthesized samples, are shown in Fig. 6.4(a-d), reveal that agglomerated nanoparticles were formed. There is no clear visible boundary between these nanoparticles. With increase in EDTA amount, the agglomeration in the nanoparticles reduced visibly and particles became smaller in dimension. The energy dispersive X-ray (EDX) analysis confirmed the elemental presence of Na, Tb, Mo and O in the sample (Fig. 6.4e).

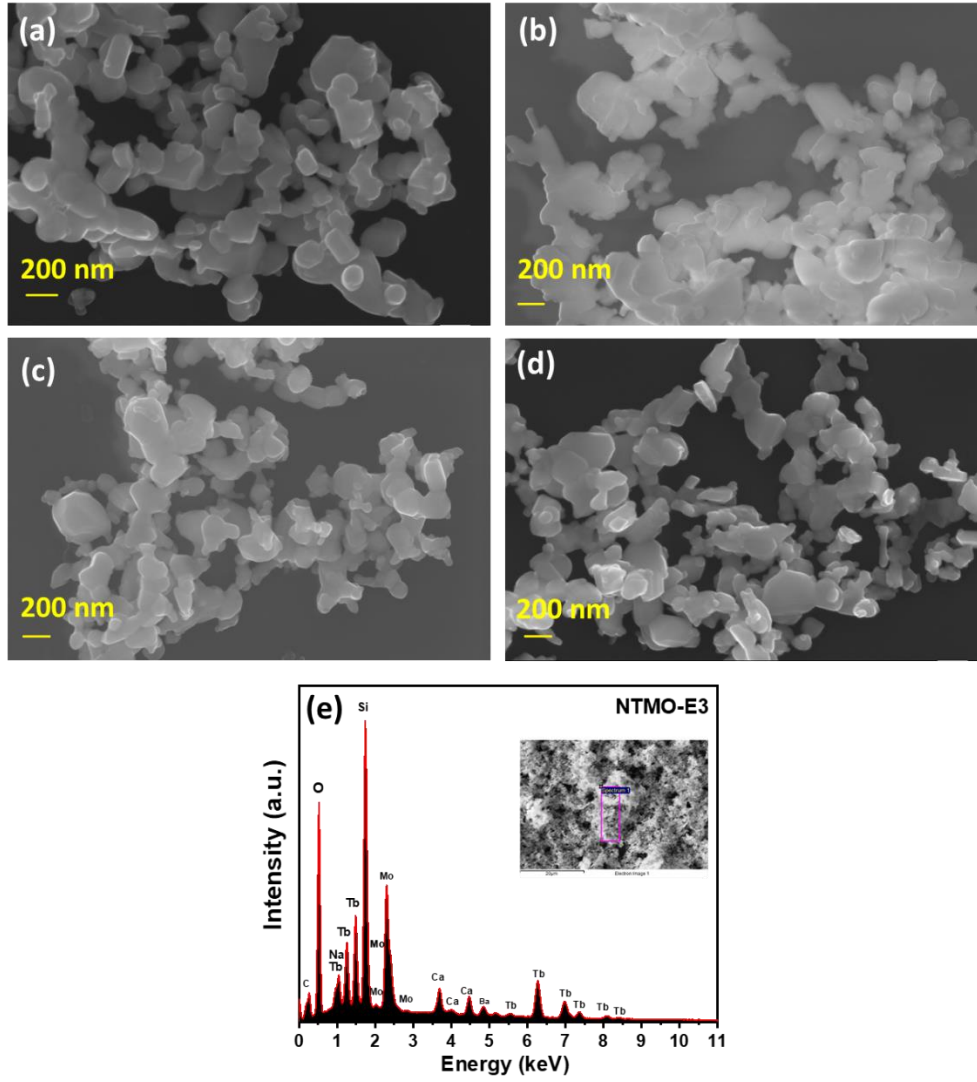


Fig. 6.4. FESEM micrograph of as-synthesised (a) NTMO-E0, (b) NTMO-E1, (c) NTMO-E2 and (d) NTMO-E3, respectively. (e) EDS spectra of NTMO-E3.

6.3.2. Spectroscopic analysis of defects and electronic property

Room temperature FTIR and Raman spectra of the samples were taken to obtain information about degree of structural order-disorder in the scheelite type $\text{NaTb}(\text{MoO}_4)_2$ samples of space group $I4_1/a$. According to the group theory, there are 26 vibrational modes present in the tetragonal double molybdate structure. The possible optically active modes in Raman (R) and infrared (IR) spectra are given in eq. (5),

$$\Gamma = 3A_g + 5B_g + 5E_g + 5A_u + 3B_u + 5E_u \quad (5)$$

where $A_u + E_u$ are acoustic modes, $2B_g + 2E_g + A_u + E_u$ are translator lattice modes, $A_g + E_g + B_u + E_u$ are rotatory lattice modes, and $2A_g + 3B_g + 2E_g + 3A_u + 2B_u + 2E_u$ are

internal vibrations of MoO_4^{2-} tetrahedra [36]. The odd vibrations, $4A_u$ and $4E_u$ are IR active and the even modes, $3A_g$, $5B_g$ and $5E_g$, are Raman active. The $3B_u$ modes are silent, whereas, $1A_u$ and $1E_u$ are acoustic modes. [37]

The FTIR absorbance spectra of the $\text{NaTb}(\text{MoO}_4)_2$ samples in the range $400\text{-}1000\text{ cm}^{-1}$ are presented in Fig. 6.5(a-d). As reported by Thongtem et al., $\nu_3(\text{F}_2)$ stretching and $\nu_4(\text{F}_2)$ bending modes are IR active modes.[38] All the tetragonal $\text{NaTb}(\text{MoO}_4)_2$ samples exhibited broad peaks of Mo-O bond in $650\text{-}950\text{ cm}^{-1}$ region. This broad characteristic absorption band is due to vibration coupling of long Mo-O bonds [39]. This broad peak was deconvoluted with Gaussian peaks centred at 906 , 854 , 804 and 708 cm^{-1} . The peak at 906 cm^{-1} is ascribed to symmetric stretching vibration of Mo-O bond in MoO_4 tetrahedra.[40] The absorption peaks situated at 854 cm^{-1} , 804 cm^{-1} and 708 cm^{-1} are corresponding to anti-symmetric stretching vibrations [$\nu_3(\text{F}_2)$ mode] of the MoO_4^{2-} tetrahedron.[40] A weak absorption peak centred at 440 cm^{-1} was observed in all the samples which is due to Mo-O asymmetric bending vibrations of $\nu_4(\text{F}_2)$ mode. These two bands are characteristics of scheelite-type double molybdates with tetragonal structure [41]. The peak positioned at 531 cm^{-1} is ascribed to interaction of Tb-O coordination.[42,43] The summary of deconvolution of FTIR spectra is listed in Table 6.2. It is known from bond length-stretching frequency correlation that the bond length decreases with vibrational frequency. Therefore, it can be concluded from the peak positions that, the lower wavenumber modes (440 , 854 , 804 and 708 cm^{-1}) correspond to distorted $\text{Mo}^{\text{D}}\text{O}_4$ tetrahedra and the modes with higher wavenumber (907 cm^{-1}) correspond to regular $\text{Mo}^{\text{R}}\text{O}_4$ tetrahedra. As calculated from the area under the curve, the area percentage of $\text{Mo}^{\text{D}}\text{O}_4$ is increasing as 87.16 , 87.22 and 87.61 from NTMO-E1 to NTMO-3, implying increasing distortion in MoO_4 tetrahedra from NTMO-E1 to NTMO-E3. This result corroborates with the XRD refinement parameters of the samples (as given in Table 6.1).

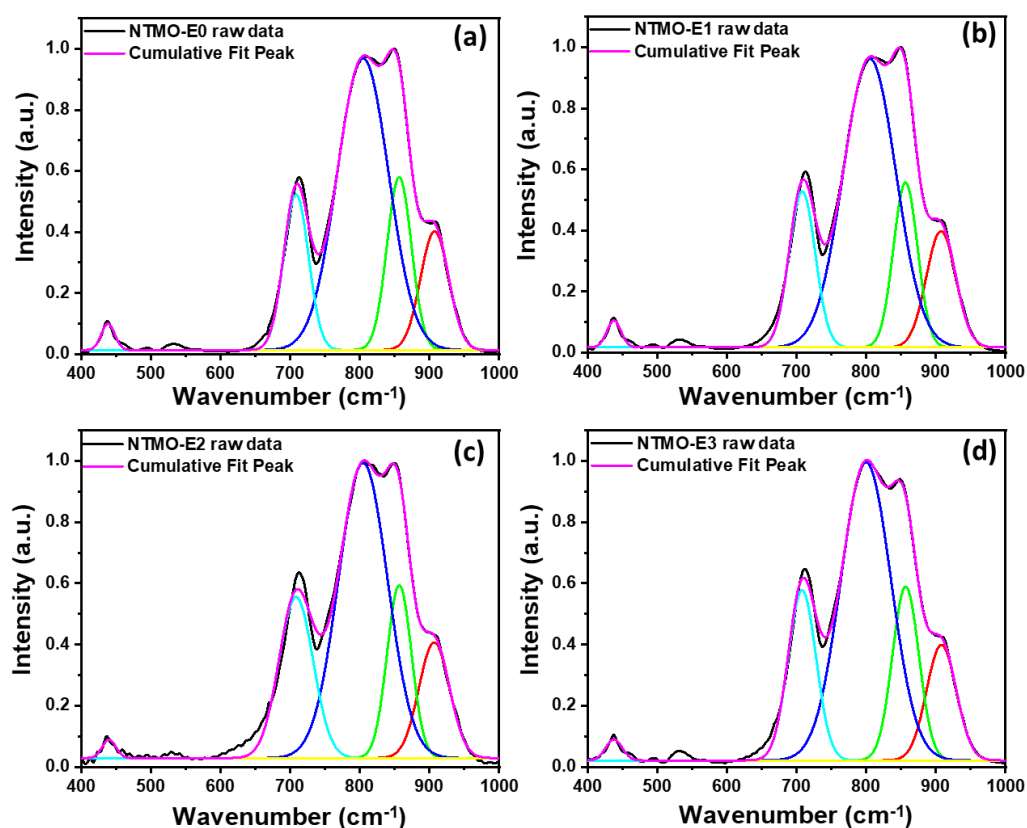


Fig. 6.5. Deconvoluted FTIR spectra of (a) NTMO-E0, (b) NTMO-E1, (c) NTMO-E2, (d) NTMO-E3, respectively, recorded at room temperature.

Table 6.2 Details of peaks obtained from deconvolution of FTIR spectra.

Sample name	Wavenumber (cm ⁻¹)	Area (cm ²)	Total area (A ₁ +A ₂ +A ₃ +A ₄)	Intensity (%)	Mo ^D O ₄ (%)
NTMO-E0	708.54	22.72	155.77	14.58	87.34
	804.38	88.39		56.74	
	854.44	24.94		16.01	
	907.19	19.72		12.65	
NTMO-E1	708.11	23.98	157.37	15.23	87.16
	804.78	89.81		57.06	
	856.32	23.38		14.85	
	907.28	20.20		12.83	
NTMO-E2	708.42	32.33	163.20	19.81	87.22
	804.53	85.19		52.19	
	856.57	24.83		15.21	
	906.67	20.85		12.77	
NTMO-E3	707.98	27.92	163.12	17.11	87.61
	799.52	87.96		53.92	
	856.61	27.04		16.57	
	907.86	20.20		12.38	

The 13 active Raman modes of Scheelite structures are given in eq. (6),

$$\Gamma_{Raman} = 3A_g + 5B_g + 5E_g \quad (6)$$

Among these thirteen modes, seven are internal vibrational modes and rest are external vibrational modes [44]. As shown in Fig. 6.6a the spectra it is evident all samples show similar characteristics of Raman spectra. The spectra of all the samples consist of three bands of Raman mode regions: 50-240 cm^{-1} , 250-500 cm^{-1} , and 660-1000 cm^{-1} , where peaks in lower wavenumber range of 50-250 cm^{-1} are associated with external vibration modes and peaks in the range of 250-1000 cm^{-1} are related to internal vibration modes [45]. The wide gap in the range 450-750 is similar to CaMoO_4 [46]. The peaks in the range 700-900 cm^{-1} are correlated to Mo-O symmetric and asymmetric stretching vibration (ν_1 and ν_3) of MoO_4^{2-} tetrahedra [47]. With the increment of EDTA amount the intensity of the corresponding Raman peaks centred at 834 cm^{-1} was observed to increase monotonously from NTMO-E1 to NTMO-E3, which is directly correlated to distortion of MoO_4^{2-} tetrahedra and corroborates with the XRD refinement and FTIR spectra analysis. The peaks centred at 320 and 394 cm^{-1} correspond to O–Mo–O symmetric (ν_2) and asymmetric bending (ν_4) modes of the tetrahedron. The peaks around 88-100 cm^{-1} are correlated to translations and liberations (ν_{ext}) of MoO_4^{2-} and Na-O/Tb-O bond stretching [48]. Similar observation in Raman spectra was reported in $\text{NaY}(\text{MoO}_4)_2$ [47] and $\text{NaCe}(\text{MoO}_4)_2$ [48]. The vibrational mode of Raman spectra of $\text{NaTb}(\text{MoO}_4)_2$ samples with highest relative intensity was observed at around 886 cm^{-1} which belongs to the symmetric stretching (ν_1) of MoO_4^{2-} which is in correlation with simple scheelite as reported in literature SrMoO_4 [49] and PbMoO_4 [50]. The Raman spectra of NTMO-E3 is fitted with fifteen Gaussian sub-peaks for clear understanding of the modes Fig. 6.6b.

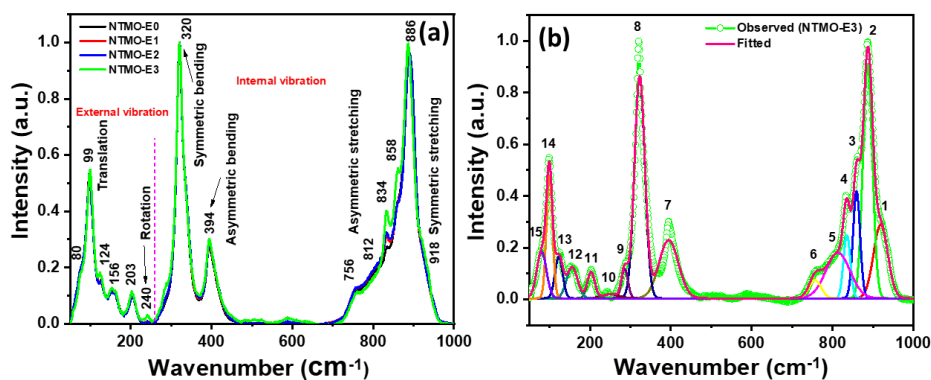


Fig. 6.6. (a) Raman spectra of all samples. (b) Deconvoluted Raman spectra of NTMO-E3 with all peaks identified with numbers from 1 to 15.

Local electronic environment and valence band structure are affected by disorder induced by the presence of V_O in the system. Therefore, to gain information about V_O -induced surface electronic structure of the system and valence states of the constituent elements Na, Tb, Mo and O, XPS have been employed. All the recorded binding energy data have been corrected with respect to adventitious carbon peak C 1s with binding energy at 284.6 eV arising from environmental carbon. XPS survey scan spectra of all samples are given in Fig. 6.7a. In which peaks of Na, Tb, Mo, C and O were detected. The narrow scan spectra of Mo 3d consists of two peaks at ~232.3 eV and ~235.5 eV correspond to orbital electrons of Mo 3d_{5/2} and Mo 3d_{3/2} of Mo⁶⁺, respectively, as displayed in Fig. 6.7b. The peaks were deconvoluted in four sub-peaks M_a (231.8 eV), M_b (232.4 eV), M_c (234.8 eV), M_d (235.5 eV), correspondingly. Here, the peaks M_a and M_c are correlated to disordered tetrahedra Mo^DO₄ and the peaks M_b and M_d are correlated to regular tetrahedra, Mo^RO₄. The energy difference between 3d_{5/2} and 3d_{3/2} of Mo^DO₄ (~2.7 eV) is observed to be lesser than that of Mo^RO₄ (~3.1 eV), which suggests the influence of local field that is generated from V_O upon coupling of spin-orbit. As calculated, the weighted percentage of Mo^DO₄ has increased monotonously as 22.5%, 28.46%, 36.1% for NTMO-E1, NTMO-E2 and NTMO-E3, respectively, which corroborates well with the findings of XRD, Raman and FTIR analysis results. The narrow scan of Tb 3d were deconvoluted into two doublet peaks located at ~1241.5 eV and ~1275.9 eV which correspond to spin orbit splitting Tb 3d_{5/2} and Tb 3d_{3/2} of Tb³⁺, respectively (shown in Fig. 6.7c). Tb 3d_{5/2} peak was deconvoluted into two subpeaks namely, Tb_a (1239.3 eV) and Tb_b (1242.0 eV), similarly, Tb 3d_{3/2} was deconvoluted into Tb_c (1274.6 eV) and Tb_d (1276.4 eV). Tb_a and Tb_c can be ascribed to regular and Tb_b and Tb_d can be ascribed to distorted TbO₈ polyhedron. The ratio of distortion was calculated from the area under the peaks. The calculated values are 0.79, 1.12, 1.03, 1.44, indicating distortion in the system. [51] The narrow scan XPS spectra of O 1s of all the samples exhibited asymmetric nature (shown in Fig. 6.7d). The peaks were deconvoluted into two components indicating that there are two species of oxygen present in the samples at ~530.0 eV and ~531.8 eV, which correspond to lattice oxygen (namely, O_L) and adsorbed surface hydroxyls associated with O₂(ads) on the surface (namely, chemisorbed oxygen O_C). The O_C is positively correlated with presence of defect in the system. The as calculated concentration ratio of O_C/ O_L is observed to gradually increase as 0.20, 0.27, 0.30 and 0.32 for NTMO-E0, NTMO-E1, NTMO-E2 and NTMO-E3, respectively, indicating increase in defect oxygen content in the samples. The summary of XPS analysis is given in Table 6.3.

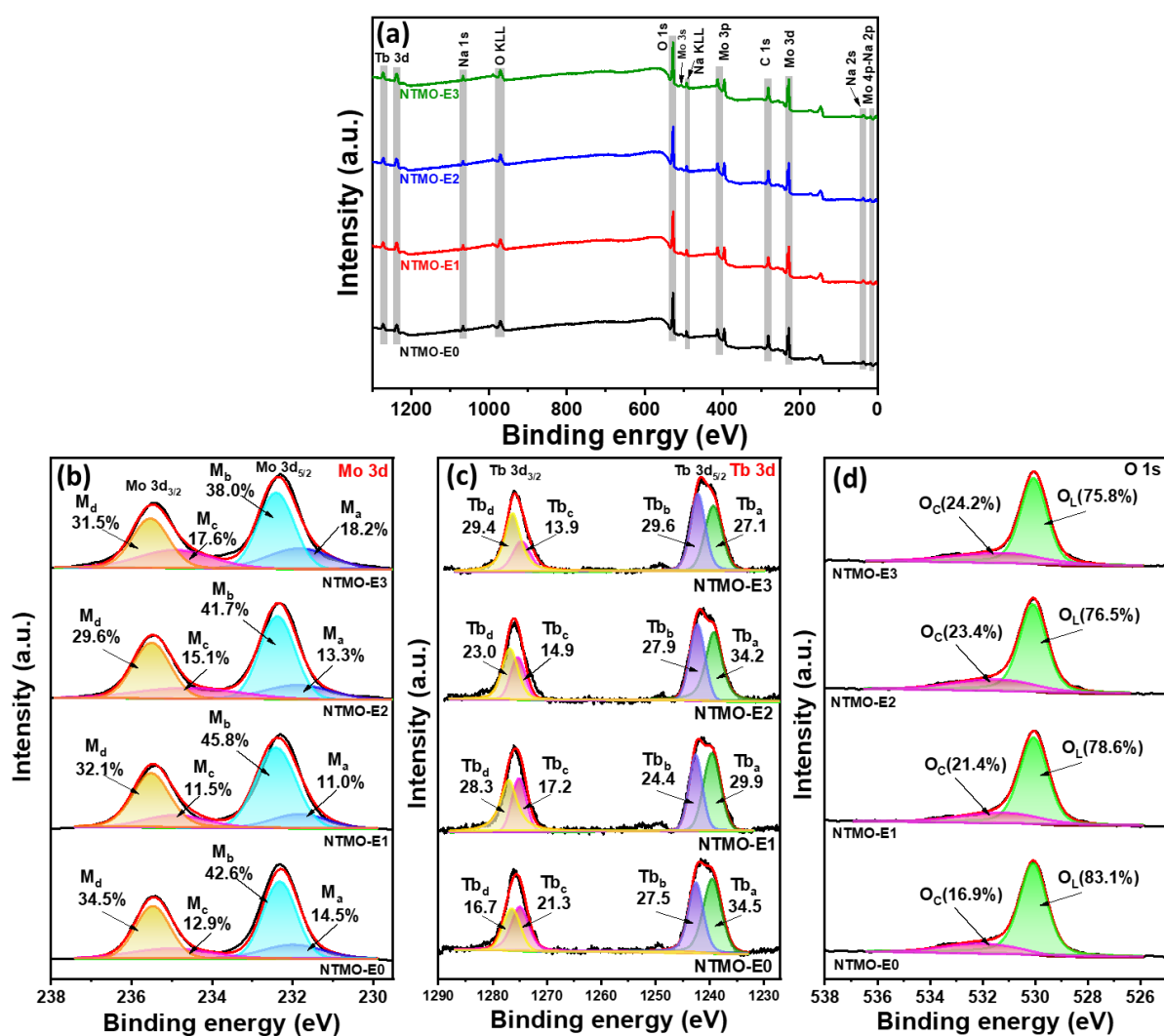


Fig. 6.7. (a) XPS survey scan spectra of all samples. XPS narrow scan spectra of NTMO-E0, NTMO-E1, NTMO-E2, NTMO-E3 nanomaterials for (a) Mo 3d, (b) Tb 3d, (c) O 1s region, respectively.

Table 6.3 Details of peaks obtained from deconvolution of Mo 3d and O 1s XPS spectra.

Samples	Element		Binding energy (eV)	Area percentage	Ratio
NTMO-E0	Mo	Mo 3d _{5/2}	232.0 (M _a)	14.5 (Mo ^D O ₄)	Mo ^D O ₄ / Mo ^R O ₄ =0.35
			232.3 (M _b)	42.6 (Mo ^R O ₄)	
		Mo 3d _{3/2}	235.0 (M _c)	12.9 (Mo ^D O ₄)	
			235.5 (M _d)	34.5 (Mo ^R O ₄)	
	O	O _L	530.1	83.1	O _C /O _L =0.20
		O _C	532.1	16.9	
NTMO-E1	Mo	Mo 3d _{5/2}	231.8 (M _a)	11.0 (Mo ^D O ₄)	Mo ^D O ₄ / Mo ^R O ₄ =0.28
			232.4 (M _b)	45.8 (Mo ^R O ₄)	
		Mo 3d _{3/2}	234.9 (M _c)	11.5 (Mo ^D O ₄)	
			235.5 (M _d)	32.1 (Mo ^R O ₄)	
	O	O _L	530.0	78.6	O _C /O _L =0.27
		O _C	531.3	21.4	
NTMO-E2	Mo	Mo 3d _{5/2}	231.9 (M _a)	13.3 (Mo ^D O ₄)	Mo ^D O ₄ / Mo ^R O ₄ =0.39
			232.4 (M _b)	41.7 (Mo ^R O ₄)	
		Mo 3d _{3/2}	234.6 (M _c)	15.1 (Mo ^D O ₄)	
			235.5 (M _d)	29.6 (Mo ^R O ₄)	
	O	O _L	530.1	76.5	O _C /O _L =0.30
		O _C	531.6	23.4	
NTMO-E3	Mo	Mo 3d _{5/2}	231.8 (M _a)	18.2 (Mo ^D O ₄)	Mo ^D O ₄ / Mo ^R O ₄ =0.52
			232.4 (M _b)	38.0 (Mo ^R O ₄)	
		Mo 3d _{3/2}	234.9 (M _c)	17.6 (Mo ^D O ₄)	
			235.5 (M _d)	31.5 (Mo ^R O ₄)	
	O	O _L	530.0	75.8	O _C /O _L =0.32
		O _C	531.3	24.2	

6.3.3. Analysis of optical properties

UV-Vis absorbance spectra of the NaTb(MoO₄)₂ samples were captured at room temperature, displayed in Fig. 6.8a. All samples exhibited good optical absorption in the visible wavelength region with absorption edge $\lambda > 400$ nm. The optical bandgap (E_{gap}) of the samples were estimated using the Kubelka-Munk equation given as following eq. (7),

$$\alpha h\nu = C_1(h\nu - E_{\text{gap}})^n \quad (7)$$

Where α is linear absorption coefficient, $h\nu$ is photon energy, C_1 is absorption constant and n is a constant associated with the type of electronic transition of the semiconductor $n =$

$\frac{1}{2}$, 2 , $\frac{3}{2}$ and 3 for direct allowed, indirect allowed, direct forbidden and indirect forbidden transitions, respectively. [52] All the $\text{NaTb}(\text{MoO}_4)_2$ samples exhibited direct allowed electronic transition, which is consistent with the reports in literature. [53] The direct bandgap values, as calculated using $n = \frac{1}{2}$, are 1.89 eV, 1.87 eV, 1.83 eV and 2.00 eV of NTMO-E0, NTMO-E1, NTMO-E2 and NTMO-E3, respectively. As observed, the bandgap energy values shifted gradually to visible region from NTMO-E0 to NTMO-E3. The decrease in the band gap values in the samples with increasing EDTA amount is ascribed to formation of localised states within the bandgap originating from structural defects in the system.[54]

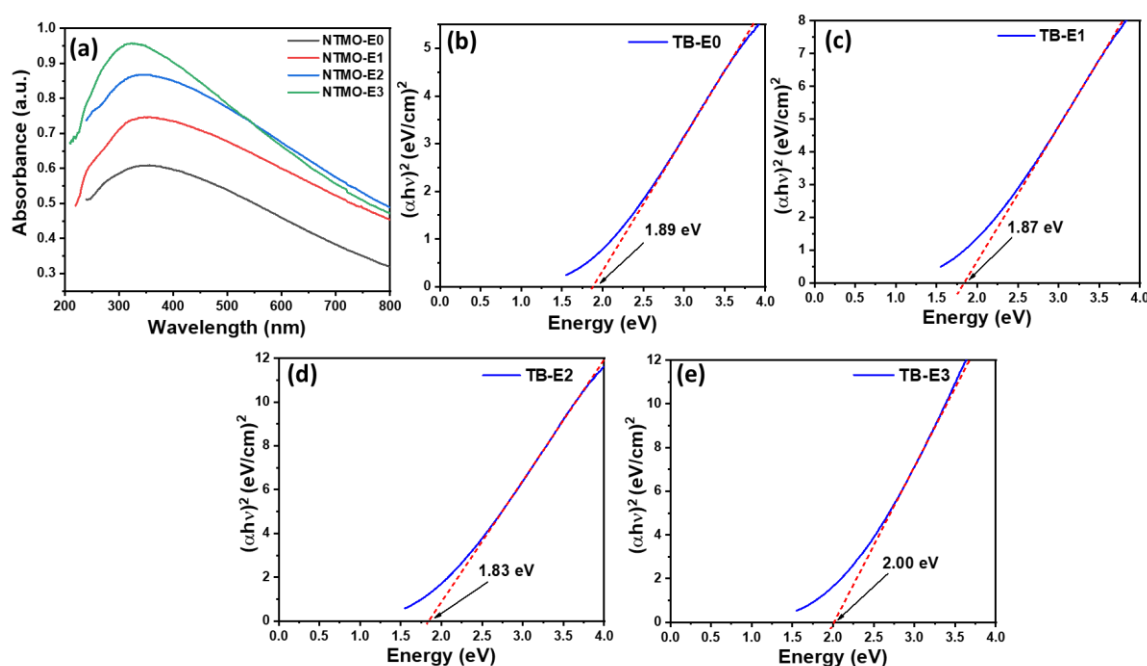


Fig. 6.8. (a) UV-Vis absorbance spectra of all samples taken at room temperature. The Kubelka–Munk plot of (b) NTMO-E0, (c) NTMO-E1, (d) NTMO-E2, (e) NTMO-E3, respectively.

The photoluminescence excitation spectra (PLE) of all samples were recorded at emission wavelength $\lambda_{\text{em}} = 545$ nm at room temperature (as presented in Fig. 6.9). The excitation spectra of all samples showed broad asymmetric spectra with very high intensity in the range 260-290 nm that corresponds to charge transfer (CT) due to $\text{O}^{2-} \rightarrow \text{Mo}^{6+}/\text{Tb}^{3+}$ transition. The high intensity of CT band in the excitation spectra indicates effective energy transfer from MoO_4^{2-} to Tb^{3+} ion.[26] The charge transfer band (CTB) of the samples are displayed in Fig. 6.9(a-d). For better understanding of the charge transfer mechanism the broad CTB bands of the samples were deconvoluted into two peaks centred at 270.03 nm and 273.56

nm correspond to the charge transfer from $O^{2-} \rightarrow Tb^{3+}$ and $O^{2-} \rightarrow Mo^{6+}$, respectively. As calculated from the area under the deconvoluted peaks, the areal ratio of two peaks ($\frac{A_{O \rightarrow Mo}}{A_{O \rightarrow Tb}}$) are 0.56, 1.02, 1.32 and 5.47 for NTMO-E0, NTMO-E1, NTMO-E2 and NTMO-E3, respectively. This implies, in the sample NTMO-E0 the energy transfer is dominated by $O^{2-} \rightarrow Tb^{3+}$, with increase in EDTA in the system, as the disorder increased, the $O^{2-} \rightarrow Mo^{6+}$ charge transfer process started to dominate. In the maximum disordered (MoO_4 tetrahedra) system, the energy was firstly adsorbed by MoO_4^{2-} then it is transferred to Tb^{3+} non-radiatively, after that the energy is emitted by Tb^{3+} . [55] Fig. 6.9(e-h) shows magnified PLE spectra in the range 300-370 nm. As observed, all samples exhibited broad peak at wavelength region 300-370 nm. Careful deconvolution of the peaks revealed that it consists of three sub-peaks which corresponds to the intra-configurational partially forbidden f-f transitions within Tb^{3+} having $4f^8$ electron configuration. The peaks positioned at ~320 nm, 336 nm and 351 nm are attributed to transition from ground state (7F_6) to different higher energy states of Tb^{3+} : 5D_0 (319 nm), 5G_2 (340 nm), 5D_2 (352 nm), respectively. [56–58] The most intense PLE peak observed at approximately 330 nm was utilized as the excitation wavelength for recording the photoluminescence (PL) spectra. The weak peak recorded ~400 nm is ascribed to $^7F_6 \rightarrow ^5D_3$. [59] The peaks of weak intensity in the range 420-500 nm are ascribed to $^7F_6 \rightarrow ^5D_4$ transition of Tb^{3+} . [58] From the literature survey it can be concluded that the measured PLE spectra of NTMO samples are not sharp because of distorted structure of the systems. [60]

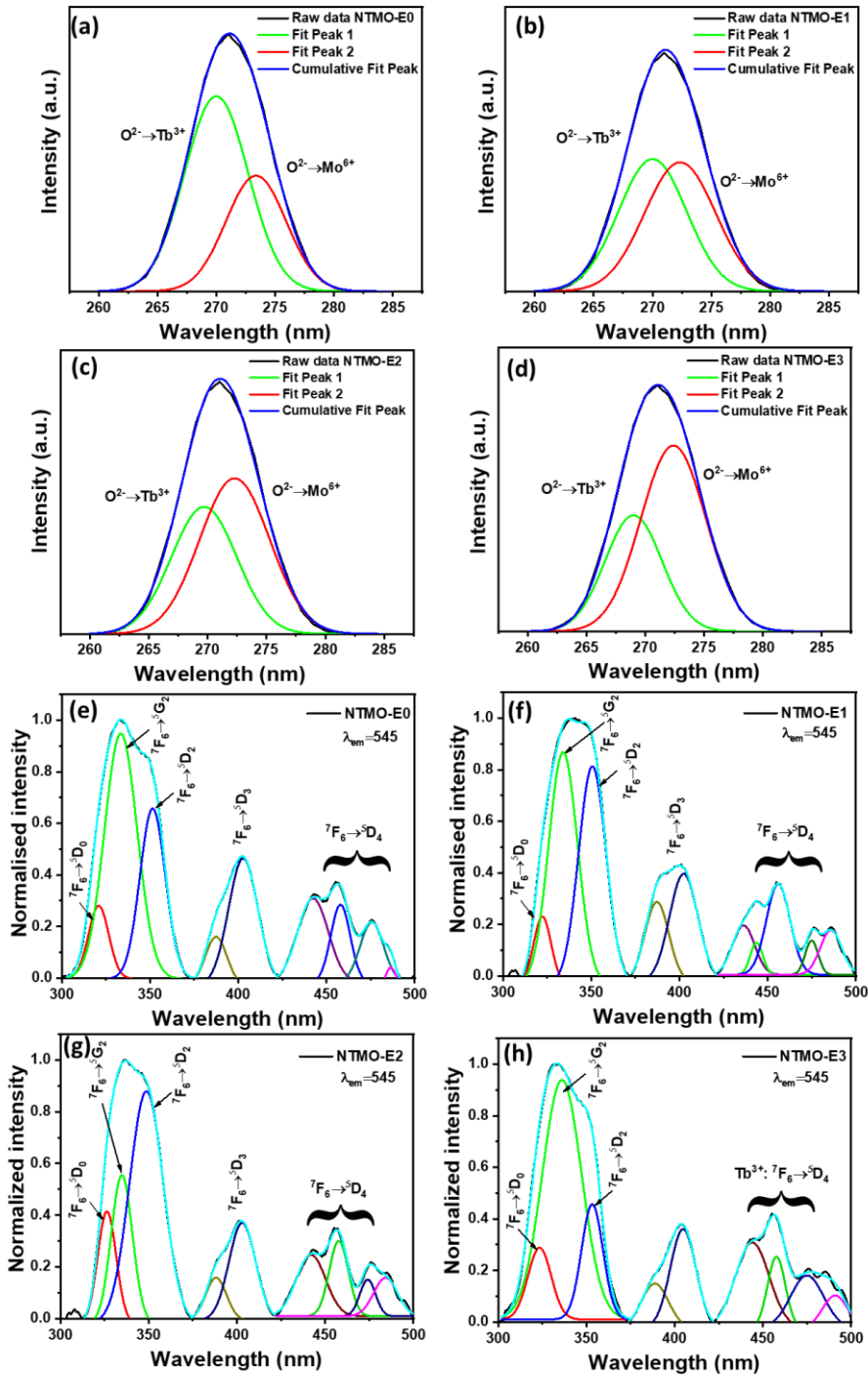


Fig. 6.9. (a-d) Charge transfer band and (e-h) Room temperature PL excitation spectra of all samples recorded at $\lambda_{em} = 545$ nm.

Room temperature PL emission spectra of $\text{NaTb}(\text{MoO}_4)_2$ samples were recorded at excitation wavelength $\lambda_{ex} = 330$ nm, and the normalised PL intensities are shown in Fig. 6.10(a-d). The PL spectrum of all samples exhibited group of spectral lines in the spectral region of 400-600 nm. The low intensity peaks observed at ~ 407 nm and 435 nm correspond to $^5D_3 \rightarrow ^7F_5$

transitions. The weak emission peaks located in blue region at 470 nm and 490 nm are assigned to $^5D_4 \rightarrow ^7F_6$ transition. The most prominent emission peak was observed in the green region 547 nm which corresponds to characteristic $^5D_4 \rightarrow ^7F_5$ magnetic dipole allowed transition ($\Delta J=1$) of Tb^{3+} . Fig. 6.11(a-d) represents the normalised intensity of peaks in the range 510 nm-565 nm. Interestingly, the luminescence intensity of peaks corresponding 547 nm was Stark split in to two peaks.[61] The deconvolution of the peaks revealed two peaks with centre: at 530 nm with full width at half maximum (FWHM) of 8.6 nm, 8.4 nm, 10.2 nm, 9.1 nm and at 547 nm with that of 10.8 nm, 11.6 nm, 12.6 nm, 9.8 nm. The systematic change in the peak intensity at 530 nm with respect to the peak 547 nm was observed. This split in the PL band can be attributed to distorting effect of the disorder in the system[61]. The luminescence intensity ratio was calculated using the following eq. (8),

$$LIR = \frac{I(5D_4 - 7F_5)_{530}}{I(5D_4 - 7F_5)_{547}} \quad (8)$$

Where $I(5D_4 - 7F_5)_{530}$ and $I(5D_4 - 7F_5)_{547}$ are the intensity of the peaks at 530 nm and 547 nm, respectively. The calculated LIR values are 0.944, 0.532, 0.786, 1.164 for NTMO-E0, NTMO-E1, NTMO-E2 and NTMO-E3, respectively. The gradual increase in LIR indicates that the disorder in the NTMO-E3 system is maximum. The weak emission band recorded at 571 and 590 nm are due to $^5D_4 \rightarrow ^7F_4$ transitions of Tb^{3+} . These observations are in accordance with the literature. [56,58,62–64] Bar diagram of normalized PL intensity of all samples are displayed in Fig. 6.11e.

The calculated values of Commission International de l'Eclairage (CIE) chromaticity coordinates of $NaTb(MoO_4)_2$ samples are given in Table 6.4, which indicates the green region as shown in Fig. 6.11f. As seen from the Table 6.4, all the coordinates are located on the green region which correspond to the emission peak at 547 nm. The colour purity (CP) of the samples were calculated using the eq. (9) given as follows [65],

$$CP = \frac{\sqrt{(x - x_i)^2 + (y - y_i)^2}}{\sqrt{(x_d - x_i)^2 + (y_d - y_i)^2}} \times 100 \% \quad (9)$$

Where, (x,y) indicates the CIE coordinate of the samples, (x_i, y_i) indicates the illuminate point of the CIE standard score with colour coordinates (0.3101, 0.3162), (x_d, y_d) indicates the colour coordinate of the dominant wavelength. The correlated colour temperatures (CCTs) of the $NaTb(MoO_4)_2$ samples are calculated using the McCamy relation as given in eq. (10) [66],

$$CCT = 449n^3 + 3525n^2 + 6823.3n + 5520.3 \quad (10)$$

Where, $n = \frac{(x - 0.3320)}{(y - 0.1858)}$; (x, y) represents as chromaticity coordinate. The calculated CP and CCT values are listed in Table 6.4. The results of the calculation indicate that NaTb(MoO₄)₂ samples can be potential candidate for solid state lighting.

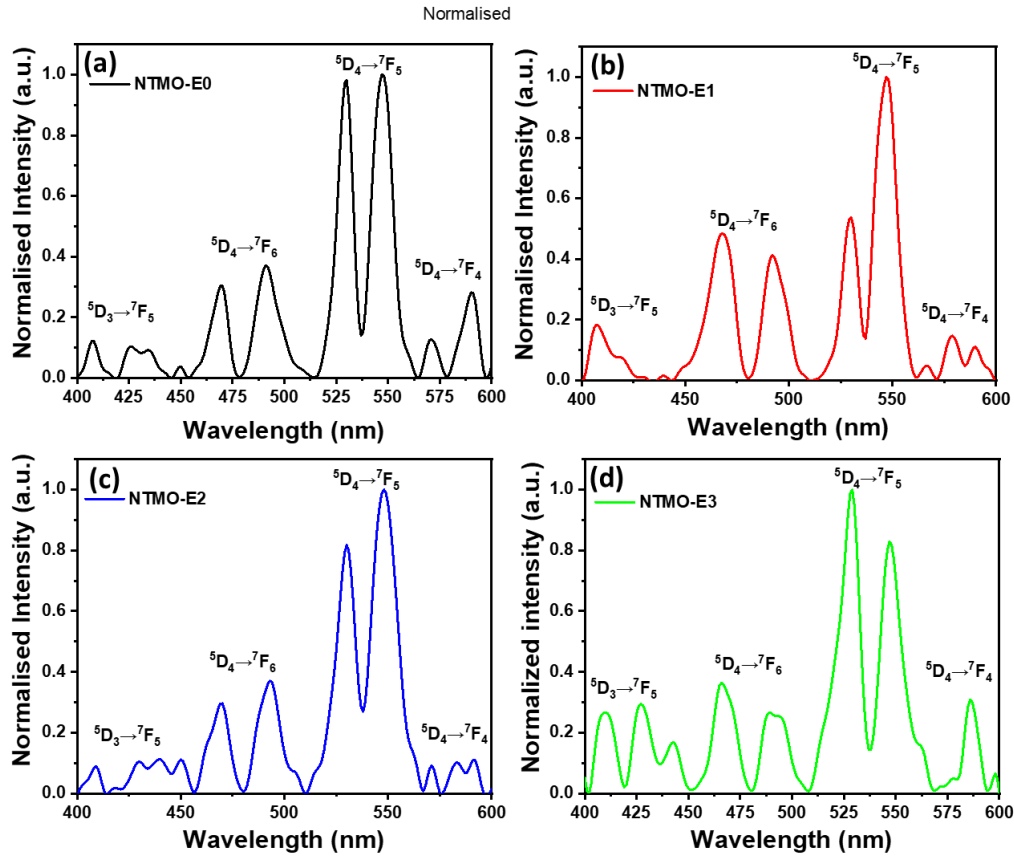


Fig. 6.10. Room temperature PL emission spectra of (a) NTMO-E0, (b) NTMO-E1, (c) NTMO-E2 and (d) NTMO-E3 recorded at 330 nm.

Table 6.4 List of CIE co-ordinates of NaTb(MoO₄)₂ samples in this work.

Materials name	CIE coordinate		CP (%)	CCT (K)
	x	y		
NTMO-E0	0.247	0.539	54	7373
NTMO-E1	0.225	0.456	39	8303
NTMO-E2	0.229	0.521	53	7963
NTMO-E3	0.224	0.471	41	8634

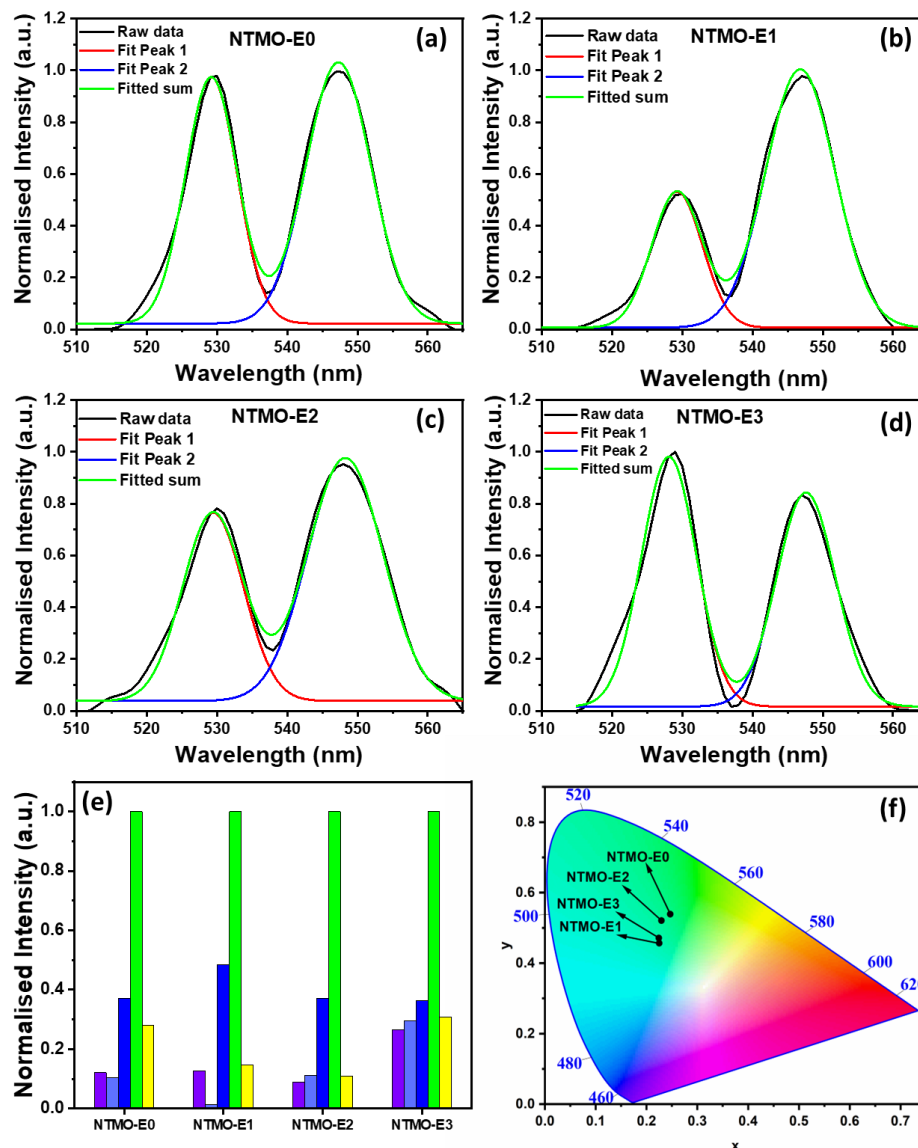
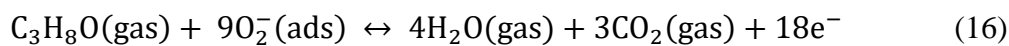
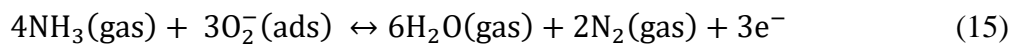
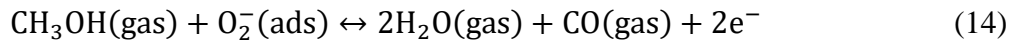
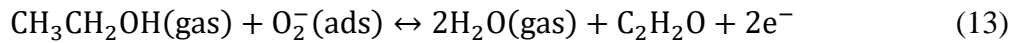
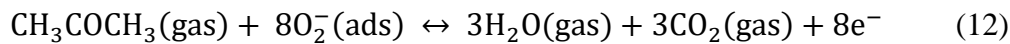
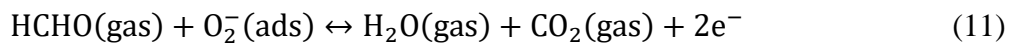


Fig. 6.11. (a-d) Normalised PL peaks showing stark split at 547 nm. (e) Bar diagram of normalized PL intensity of all samples and (f) CIE diagram of NTMO-E0, NTMO-E1, NTMO-E2 and NTMO-E3 samples.

6.3.4. Gas sensing properties of $\text{NaTb}(\text{MoO}_4)_2$ nanoparticles

Gas sensing phenomena of semiconductor metal oxides relies on the gas-solid interaction between the sensing material and the target analyte molecules at the sensor surface. This surface phenomena relies on the presence of defects such as, V_O on the surface. V_O act as active sites for gas adsorption as they can trap free electrons (e') and can create donor level within the bandgap E_g . [67] Moreover, at high temperature, V_O enable ionic conductivity which is beneficial for chemiresistive type sensor operation. [68] Thus, having abundant V_O on the

surface of sensing material increases the availability of electrons that take part in the chemical reactions involving the target gas molecules. V_O also contributes in enhancing adsorption of atmospheric oxygen molecules on the sensor surface generating oxygen-ion species, O^{2-} , described by following equation, $O_2(gas) + e^- \leftrightarrow O_2^-(ads)$. [69] From structural analysis we have found the presence of V_O in $NaTb(MoO_4)_2$ samples. Moreover, from the analysis of XPS spectra of the prepared $NaTb(MoO_4)_2$ nanoparticles, the presence of chemisorbed oxygen species (O_c) in the samples were detected, which is beneficial for the adsorption of target gas molecules. Therefore, to validate the influence of V_O on sensing performance of $NaTb(MoO_4)_2$ based sensors (namely, NTMO-E0, NTMO-E1, NTMO-E2 and NTMO-E3), detailed gas sensing measurements have been carried out. As reported in literature, the surface redox reaction between semiconductor metal oxide-based sensing material and the target analytes such as formaldehyde (HCHO), acetone (CH_3COCH_3), ethanol (C_2H_5OH), methanol (CH_3OH), ammonia (NH_3) and isopropyl alcohol (C_3H_8O) facilitated by surface ionised oxygen species $O_2^-(ads)$ can be presented by following eq. (11-16),[34] [70] [71]



To validate the gas sensing ability of $NaTb(MoO_4)_2$ nanoparticles, at first, the optimum temperature for the maximum gas sensing performance was determined. As, $NaTb(MoO_4)_2$ nanoparticles are semiconductors in nature, they need elevated temperature to gain more majority charge carriers in the conduction band. Therefore, the sensors were tested for their sensing performance in presence of 100 ppm of different target analytes (Acetone, ethanol, formalin, ammonia, methanol, isopropyl alcohol). The sensors exhibited p-type formaldehyde sensing activity. The optimization of operating temperature for formalin sensing was determined by recording the formalin sensing response in the operating temperature 150-300 °C, as shown in Fig. 6.12a. The NTMO-E0 sensor showed no sensing activity in 150-300 °C operating temperature range and it showed very high resistance value in presence of air. Whereas, NTMO-E1, NTMO-E2, NTMO-E3 sensors showed gas sensing activity.

The temperature calibration curve (Fig. 6.12a) of NTMO-E1, NTMO-E2 and NTMO-E3 showed increase-maximum-decrease trend and maximum formalin sensing activity was observed at 180 °C operating temperature for all three sensors. This is because, gas sensing activity is influenced by adsorption and desorption kinetics of the target gas. Below this temperature, due to lack of energy the gas adsorption process is not initiated, therefore resulting in lower response value. While at optimum temperature, the adsorption rate of target analyte is greater than desorption rate. Above optimum temperature, the desorption process dominates, therefore, sensing value decreases. Fig. 6.12(b-d) shows dynamic response curve of NTMO-E1, NTMO-E2 and NTMO-E3 for different concentration of HCHO at 180 °C. The response value of the sensors gradually increased with increasing gas concentration. The response performance of the sensors also increased monotonously from NTMO-E1 to NTMO-E3, while NTMO-E3 showed highest sensitivity ($S = \frac{R_{gas}}{R_{air}}$) ~1.9, 3.5, 4.2, 4.7, 5.6 and 6.3 to 0.5, 1, 10, 50, 100 ppm HCHO measured at operating temperature 180 °C. NTMO-E1 and NTMO-E2 sensors could not detect HCHO concentration below 5 ppm whereas, NTMO-E3 detected HCHO down to 0.5 ppm with response value 1.9. This observation shows that increase in V_O and $2V_O$ defects in the system may have contributed in the improved sensing performance of NTMO-E3. To have more insight on the role of V_O on gas adsorption/desorption kinetics, double logarithmic treatment was used for the response data to fit the Freundlich gas adsorption model of the semiconductors. The empirical equation for the metal oxide semiconductor-based gas sensors can be presented as follows,

$$S_g = \alpha C_g^\beta \quad (17)$$

$$\text{Or, } \log(S) = \log(\alpha) + \beta \log(C) \quad (18)$$

Where S_g and C_g are the response value and concentration of the target gas, α and β are constants that is determined by the electrical charge of surface oxygen species and stoichiometry of the surface reactions. [72] Fig. 6.12e displays Freundlich isotherm fitting of the response data with linear regression of all sensors. The R^2 value for the fittings were 0.7915, 0.8264, 0.9059 and for the NTMO-E1, NTMO-E2 and NTMO-E3, respectively. This implies the correlation between the response value and the gas concentration is best for NTMO-E3 sensor. It is reported that from the value of ' β ' the chemisorbed oxygen species on the surface can be deducted. If the value is ~0.5, the O^{2-} species is adsorbed and when it is ~1, the adsorbed species is O^- . [73,74] For NTMO sensors, the calculated ' β ' values are ~0.123, 0.158, 0.188 for NTMO-E1, NTMO-E2 and NTMO-E3, respectively, suggesting V_O facilitates generation

of O^{2-} species which is comparatively more unstable and energetic than other oxygen ion species. Presence of large number of O^{2-} species in the samples account for high HCHO response. Repeatability in gas sensing data was investigated for NTMO-E3 at 180 °C toward 1 ppm formalin (as shown in Fig. 6.12f). The sensor showed similar data for five consecutive cycles of gas on and off proving its excellent short time stability. Selectivity is a crucial aspect in gas sensing evaluation. Therefore, the selectivity measurement was done by comparing the response to 100 ppm formalin to that of other interfering volatile organic compounds (viz. acetone, ethanol, methanol, ammonia, isopropyl alcohol). As shown in Fig. 6.12g, all NTMO sensors exhibited HCHO selectivity. Particularly, the NTMO-E3 sensor showed highest selectivity toward HCHO with insignificant variation in resistance when exposed to 100 ppm other target gases with response ($S = \frac{R_{gas}}{R_{air}}$) values 1.5, 1.4, 1.3, 1.6 and 1.2 for CH_3COCH_3 , C_2H_5OH , CH_3OH , NH_3 and C_3H_8O , respectively. The influencing factor behind the selective sensitivity toward HCHO is bond dissociation energy (BDE) of the target gases. When the BDE of the functional groups present in the target gas is low, the gas molecule will be easier to break at low operating temperature. As per literature, HCHO has comparatively lower BDE 364 kJ/mol in comparison with acetone (393 kJ/mol), ethanol (458 kJ/mol), methanol (439 kJ/mol), ammonia (435 kJ/mol), IPA (440 kJ/mol) [70,75,76]. Therefore, molecules at 180 °C operating temperature reaction with the sensor surface and the HCHO gas will be easier. Fig. 6.12h displays response/recovery time of NTMO sensors for different concentration of HCHO. As observed, NTMO-E3 exhibited ultrafast response and recovery time ~ 4.8s/ 32.2s to 100 ppm HCHO, this proves its suitability in practical application. Long term stability of the sensors (NTMO-E1, E2, E3) were checked for 90 days, as shown in Fig. 6.12i the sensors showed very stable data with negligible deterioration which proves the credibility of $NaTb(MO_4)_2$ based HCHO sensor as real-time indoor air quality monitoring application.

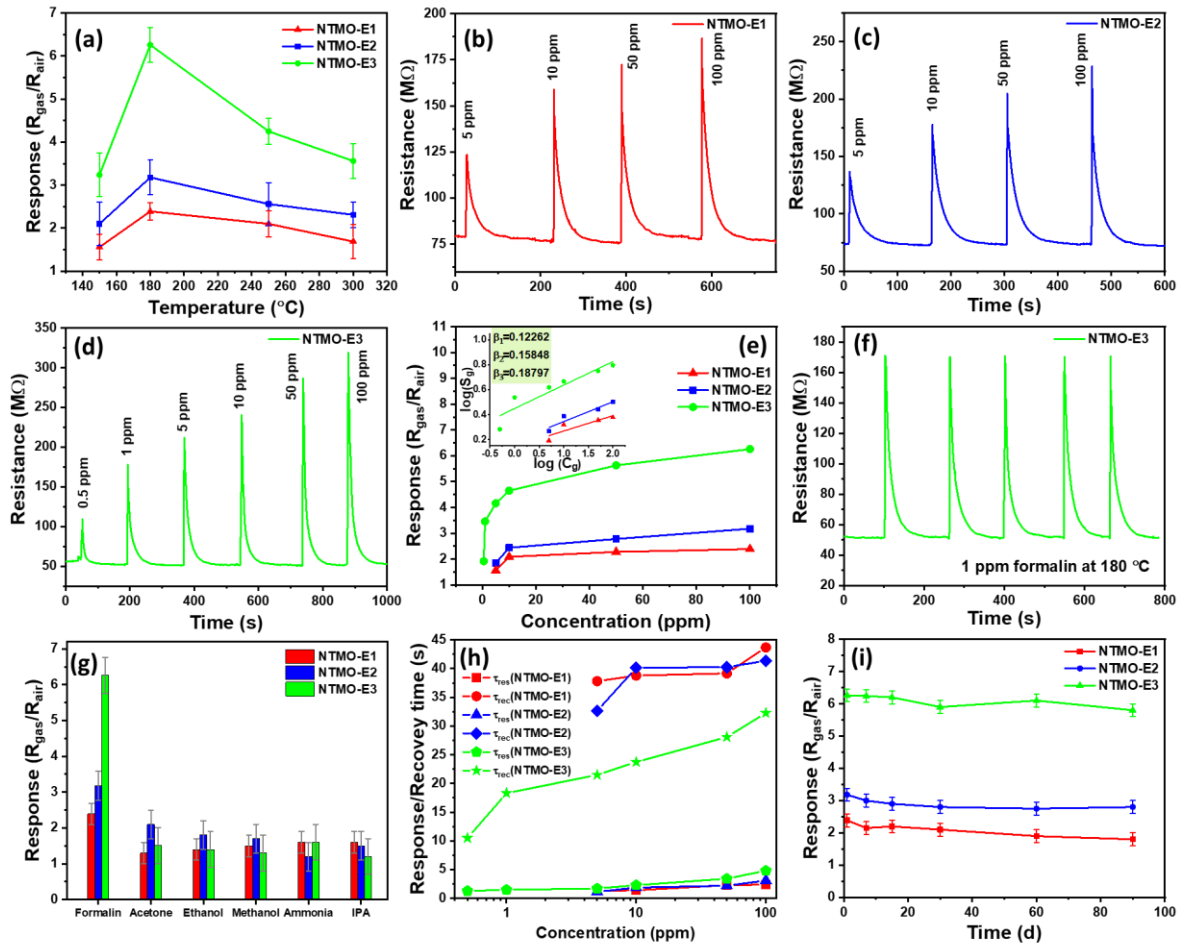


Fig. 6.12. (a) Temperature calibration curves NTMO-E1, NTMO-E2 and NTMO-E3 sensors. Dynamic response curve of (b) NTMO-E1, (c) NTMO-E2, (d) NTMO-E3 sensor to formalin concentrations at 180 °C. (e) Response values of sensors as a function of formalin concentration (Inset: Isotherm fitting curve of all sensors with linear regression). (f) Short-time stability and repeatability of NTMO-E2 sensor for 1 ppm formalin at 180 °C. (g) Selectivity toward 100 ppm formalin against 100 ppm concentration of other gases at temperature 180 °C. (h) Response and recovery times of NTMO-E1, NTMO-E2 and NTMO-E3 sensors for different concentrations of formalin at 180 °C. (i) Long-term stability of response data of all sensors for 100 ppm formalin at 180 °C.

6.3.5. Band structure and adsorption energy calculations using density functional theory (DFT)

Ab initio calculation of the electronic structure of $\text{NaTb}(\text{MoO}_4)_2$ samples were carried out using density functional theory to gain information about effect of disorder in the system on its optical and gas sensing characteristics. Before going into the analysis of disorder effect, at first, band

structure of the materials, PDOS of the elements present in the materials and total density of states (TDOS) were calculated accordingly. Prior to the band structure calculation, the atomic position was optimized, keeping the lattice parameters and symmetry same as the experimental results of the refined unit cell of the materials obtained from the Rietveld refinement. The band structure was calculated along high symmetry k-point within the Brillouin zone. Theoretically calculated band gap values followed the trend as experimentally calculated band gap which indicates good choice of exchange pseudopotential function. The valence band maximum (VBM) was set to zero. The electronic band structure of NTMO-E0 is displayed in Fig. 6.13a, which shows that the sample exhibits band gap value, $E_g \sim 3.02$ eV. As can be seen from the Fig. 6.13a, valence band maxima (VBM) and conduction band minima (CBM) are situated at Γ -point, indicating direct band gap of the sample. The calculated partial density of states (PDOS) of Na, Tb, Mo, O and total density of states (TDOS) of NTMO-E0 sample is shown in Fig. 6.13(b-f), respectively. As observed, the upper part of VBM mainly consists of O 2p orbitals, middle part of VBM consists with mixture of O 2p and Tb 4f – 4d orbitals and lower part consisted with admixture of O 2p, Tb 4f and Mo 4d orbitals. While, the lower part of CBM majorly contributed by Tb 4f orbitals and upper part of CBM O 2p and Mo 4f orbitals. From here we can say that the electronic transition VB to CB is directly associated with MoO_4 tetrahedron to TbO_8 polyhedron. Similarly, the band gap of NTMO-E1, NTMO-E2, NTMO-E3 samples, $E_g \sim 2.64, 1.29$ and 2.68 eV along with band structure, PDOS and TDOS are calculated and shown in Fig. 6.14-16, respectively. The VBM and CBM both the points are pointed at Γ -point for the three samples (NTMO-E1, NTMO-E2, NTMO-E3). As lower part of CBM majorly contributed by the Tb 4f orbitals, this correlates with the experimental data obtained from PL. During PL excitation, initial electronic transition mainly occurs from O 2p orbitals in VB to Tb 4f orbitals in CB for NTMO-E0 material. From the Fig. 13(c)-15(c), it was observed that with the enhancement of EDTA concentration, the contribution of Tb 4f orbitals decreased and the contribution of Mo increased in a systematic way. The above analysis directly corroborated with our observed charge transfer band in PLE spectra.

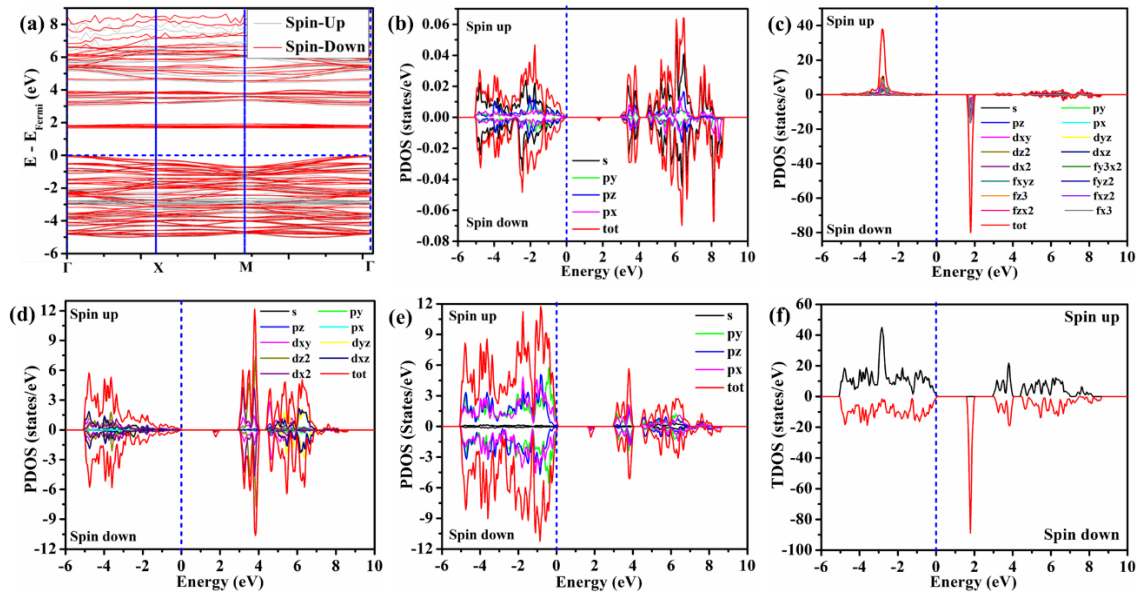


Fig. 6.13. NTMO-E0: (a) Band structure, (b) PDOS of Na, (c) PDOS of Tb, (d) PDOS of Mo, (e) PDOS of O, (f) TDOS.

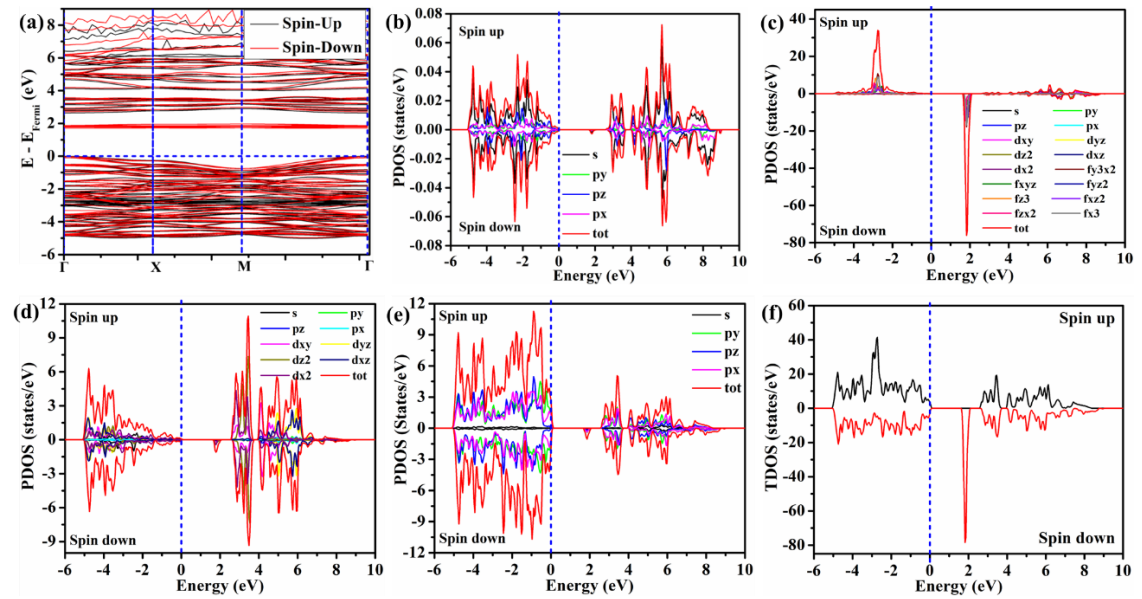


Fig. 6.14. NTMO-E1: (a) Band structure, (b) PDOS of Na, (c) PDOS of Tb, (d) PDOS of Mo, (e) PDOS of O, (f) TDOS.

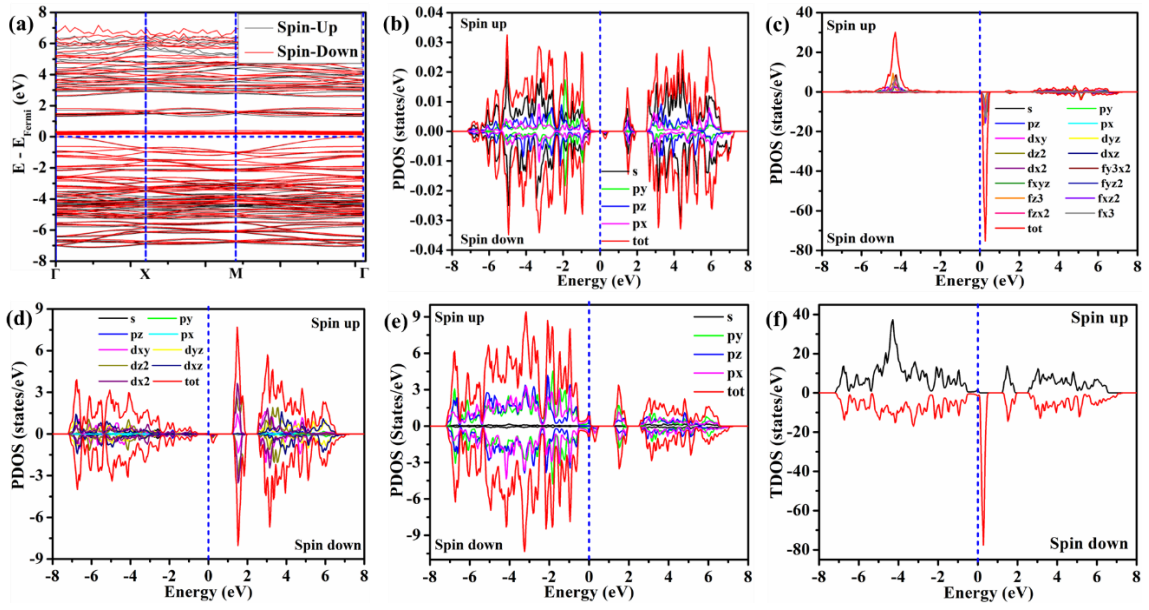


Fig. 6.15. NTMO-E2: (a) Band structure, (b) PDOS of Na, (c) PDOS of Tb, (d) PDOS of Mo, (e) PDOS of O, (f) TDOS.

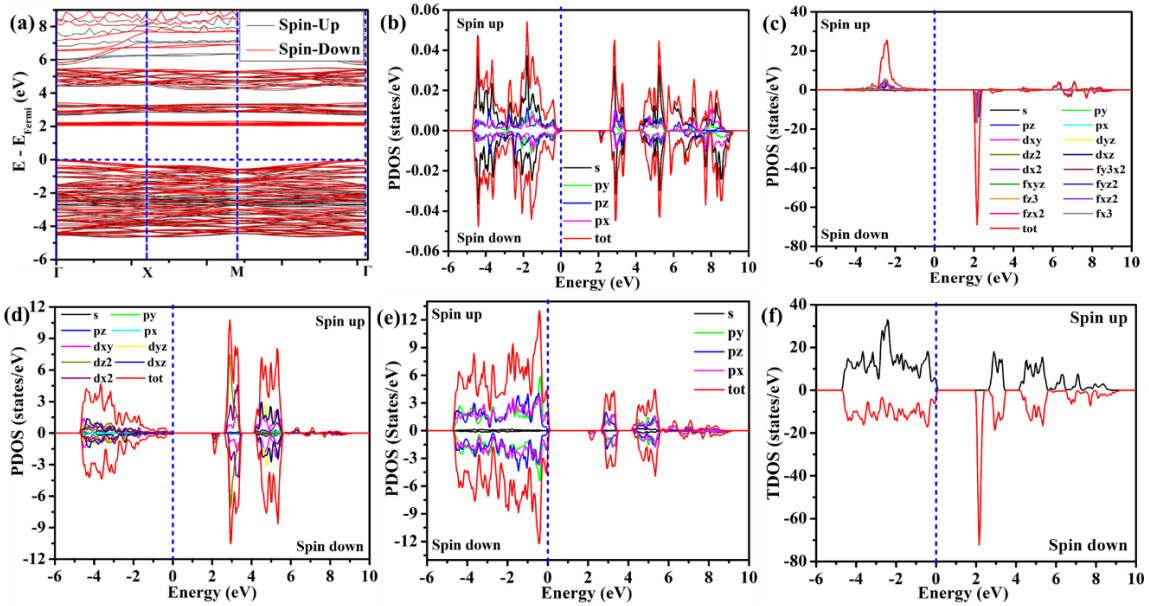


Fig. 6.16. NTMO-E3: (a) Band structure, (b) PDOS of Na, (c) PDOS of Tb, (d) PDOS of Mo, (e) PDOS of O, (f) TDOS.

Moreover, density functional theory has been employed to investigate the interaction of HCHO with the (1 1 6) plane surface of NTMO-E0 and NTMO-E3 samples. Two possible layouts such as the vertical and horizontal position of HCHO on (1 1 6) surface plane have been used to understand the interaction, shown in Fig. 6.17. The corresponding adsorption energy of NTMO-E0 and NTMO-E3 sensor materials with different orientations of HCHO molecule is listed in Table 6.5. As observed, NTMO-T3 materials, the adsorption energy tends to zero

(minimum) for horizontal position indicating this position to be most stable for HCHO molecule for adsorption on the surface of (1 1 6) plane. The calculated value of optimised distance between adsorbed HCHO molecule and sensing material surface is found to be ~ 1.8 - 2.5 Å. This indicates, there is no intermediate compound formed between HCHO and the sensing material making the gas adsorption process a reversible one. Also, it was observed that, the adsorption energy of HCHO on NTMO-E3 surface (+0.09 eV) in horizontal orientation is less in comparison with that of NTMO-E0 (+0.71 eV), suggesting NTMO-E3 will adsorb HCHO more easily while it is less likely for NTMO-E0 to interact with HCHO molecules. This explains the gas sensing inability of NTMO-E0 and also corroborates with our gas sensing experiment data.

Table 6.5 Adsorption energy of formaldehyde gas on (1 1 2) plane surface of targeted sensor nanomaterials.

Parameters	NTMO-E0		NTMO-E3	
	VOC (Vertical)	VOC (Horizontal)	VOC (Vertical)	VOC (Horizontal)
Formaldehyde (VOC) (eV)	-22.11	-22.14	-22.11	-22.14
Slab (12) (eV)	-693.04	-692.98	-674.38	-674.38
Slab (112) + VOC (eV)	-712.51	-714.41	-690.94	-696.43
Ads. Energy (eV)	+2.64	+0.71	+5.55	+0.09

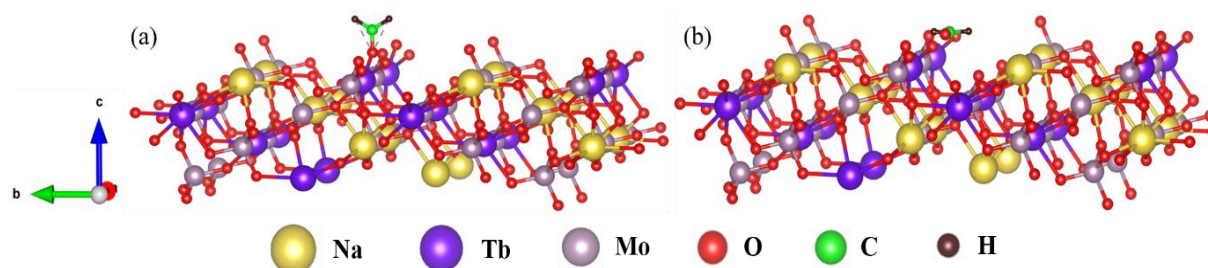


Fig. 6.17. Two possible layouts of HCHO molecule and (1 1 6) plane surface of NTMO-E3 material: (a) vertical position and (b) horizontal position.

6.4. Conclusion

In summary, structural disorder induced photoluminescence and gas sensing property of $\text{NaTb}(\text{MoO}_4)_2$ has been delineated in this work. The disorder in MoO_4 tetrahedra was controlled by varying the EDTA concentration during synthesis via hydrothermal method. NTMO samples exhibited luminescence property which lies in the green spectral range at 330 nm excitation. The main luminescence peak corresponding to the $^5\text{D}_4 \rightarrow ^7\text{F}_5$ magnetic dipole allowed transition of ($\Delta J=1$) of Tb^{3+} at 547 nm was Stark split into two separate peaks, which is caused by the decrease in PDOS of Tb in the samples with increasing disorder in the system. The gradual increase in the splitting peak intensity at 530 nm corroborates with the increasing disorder in the MoO_4 tetrahedra as validated by both experimental and theoretical calculations. The increase in PDOS of Mo in the disordered systems suggest the transfer of electrons from O^{2-} to Mo^{6+} then to Tb^{3+} . Disordered $\text{NaTb}(\text{MoO}_4)_2$ exhibited HCHO sensing activity with p-type response value of 3.5-fold to 1 ppm gas concentration and rapid response/recovery time (1.5s/18.3s) with high selectivity. DFT calculations revealed minimum adsorption energy of HCHO on NTMO-E3 material surface. Therefore, structural disorder induced multifunctional $\text{NaTb}(\text{MoO}_4)_2$ nanomaterial is a potential candidate for applications in lighting equipment and its HCHO sensing performance makes it a good formaldehyde sensing material applicable for indoor air-quality monitoring.

6.5. References

- [1] C. Bao, Z. Yuan, W. Niu, J. Yang, Z. Wang, T. Yu, J. Wang, F. Gao, A multifunctional display based on photo-responsive perovskite light-emitting diodes, *Nature Electronics* 2024 7:5 7 (2024) 375–382.
- [2] R. Jana, S. Hajra, P.M. Rajaittha, K. Mistewicz, H.J. Kim, Recent advances in multifunctional materials for gas sensing applications, *J Environ Chem Eng* 10 (2022) 108543.
- [3] J. Yang, J.K. Cooper, F.M. Toma, K.A. Walczak, M. Favaro, J.W. Beeman, L.H. Hess, C. Wang, C. Zhu, S. Gul, J. Yano, C. Kisielowski, A. Schwartzberg, I.D. Sharp, A multifunctional biphasic water splitting catalyst tailored for integration with high-performance semiconductor photoanodes, *Nature Materials* 2016 16:3 16 (2016) 335–341.
- [4] A. Dokania, A. Ramirez, A. Bavykina, J. Gascon, Heterogeneous Catalysis for the Valorization of CO₂: Role of Bifunctional Processes in the Production of Chemicals, *ACS Energy Lett* 4 (2019) 167–176.
- [5] A. Ramirez, P. Ticali, D. Salusso, T. Cordero-Lanzac, S. Ould-Chikh, C. Ahoba-Sam, A.L. Bugaev, E. Borfecchia, S. Morandi, M. Signorile, S. Bordiga, J. Gascon, U. Olsbye, Multifunctional Catalyst Combination for the Direct Conversion of CO₂ to Propane, *JACS Au* 1 (2021) 1719–1732.
- [6] P. Ladpli, R. Nardari, F. Kopsaftopoulos, F.K. Chang, Multifunctional energy storage composite structures with embedded lithium-ion batteries, *J Power Sources* 414 (2019) 517–529.
- [7] L.A. Wehner, N. Mittal, T. Liu, M. Niederberger, Multifunctional batteries: Flexible, transient, and transparent, *ACS Cent Sci* 7 (2021) 231–244.
- [8] Q. Zhang, G. Xie, M. Duan, Y. Liu, Y. Cai, M. Xu, K. Zhao, H. Tai, Y. Jiang, Y. Su, Zinc Oxide Nanorods for Light-Activated Gas Sensing and Photocatalytic Applications, *ACS Appl Nano Mater* 6 (2023) 17445–17456.
- [9] Manju, M. Jain, S. Madas, P. Vashishtha, P. Rajput, G. Gupta, M.U. Kahaly, K. Özdoğan, A. Vij, A. Thakur, Oxygen vacancies induced photoluminescence in SrZnO_2 nanophosphors probed by theoretical and experimental analysis, *Scientific Reports* 2020 10:1 10 (2020) 1–10.
- [10] W. Ji, M.H. Lee, L. Hao, X. Xu, S. Agathopoulos, D. Zheng, C. Fang, Role of oxygen vacancy on the photoluminescence of BaMgSiO₄:Eu phosphors: Experimental and theoretical analysis, *Inorg Chem* 54 (2015) 1556–1562.
- [11] B. Ding, H. Qian, C. Han, J. Zhang, S.E. Lindquist, B. Wei, Z. Tang, Oxygen vacancy effect on photoluminescence properties of self-activated yttrium tungstate, *Journal of Physical Chemistry C* 118 (2014) 25633–25642.
- [12] E. Choi, D. Lee, H.J. Shin, N. Kim, L. De Los Santos Valladares, J. Seo, Role of Oxygen Vacancy Sites on the Temperature-Dependent Photoluminescence of SnO₂ Nanowires, *Journal of Physical Chemistry C* 125 (2021) 14974–14978.
- [13] H. Wang, K. Su, L. Mei, Q. Guo, L. Liao, Vacancy-Enhanced Self-Reduction of Eu in Pyrophosphate Phosphor, *Inorg Chem* 62 (2023) 12468–12479.
- [14] B. Tong, Z. Deng, B. Xu, G. Meng, J. Shao, H. Liu, T. Dai, X. Shan, W. Dong, S. Wang, S. Zhou, R. Tao, X. Fang, Oxygen Vacancy Defects Boosted High Performance p-Type Delafossite CuCrO₂ Gas Sensors, *ACS Appl Mater Interfaces* 10 (2018) 34727–34734.
- [15] W. Du, W. Si, F. Wang, L. Lv, L. Wu, Z. Wang, J. Liu, W. Liu, Creating oxygen vacancies on porous indium oxide nanospheres via metallic aluminum reduction for enhanced nitrogen dioxide detection at low temperature, *Sens Actuators B Chem* 303 (2020) 127221.

- [16] R.T. Parayil, S.K. Gupta, R. Rohilla, J. Prakash, K. Sudarshan, M. Mohapatra, Luminescent Y₂Zr₂O₇ for Ultrasensitive Detection of Volatile Organic Compounds Driven by Oxygen Vacancies, *ACS Appl Electron Mater* 5 (2023) 5151–5163.
- [17] J.V.B. Moura, C. Luz-Lima, G.S. Pinheiro, P.T.C. Freire, Temperature-induced isostructural phase transition on NaCe(MoO₄)₂ system: A Raman scattering study, *Spectrochim Acta A Mol Biomol Spectrosc* 208 (2019) 229–235.
- [18] V.A. Morozov, A. V. Arakcheeva, P. Pattison, K.W. Meert, P.F. Smet, D. Poelman, N. Gauquelin, J. Verbeeck, A.M. Abakumov, J. Hadermann, KEu(MoO₄)₂: Polymorphism, Structures, and Luminescent Properties, *Chemistry of Materials* 27 (2015) 5519–5530.
- [19] V.A. Morozov, S.M. Posokhova, D. V. Deyneko, A.A. Savina, A. V. Morozov, O.A. Tyablikov, B.S. Redkin, D.A. Spassky, J. Hadermann, B.I. Lazoryak, Influence of annealing conditions on the structure and luminescence properties of KGd_{1-x}Eux(MoO₄)₂ (0 ≤ x ≤ 1), *CrystEngComm* 21 (2019) 6460–6471.
- [20] V.A. Morozov, A. V. Arakcheeva, P. Pattison, K.W. Meert, P.F. Smet, D. Poelman, N. Gauquelin, J. Verbeeck, A.M. Abakumov, J. Hadermann, KEu(MoO₄)₂: Polymorphism, Structures, and Luminescent Properties, *Chemistry of Materials* 27 (2015) 5519–5530.
- [21] Y. Gan, W. Liu, W. Zhang, W. Li, Y. Huang, K. Qiu, Effects of Gd³⁺ codoping on the enhancement of the luminescent properties of a NaBi(MoO₄)₂:Eu³⁺ red-emitting phosphors, *J Alloys Compd* 784 (2019) 1003–1010.
- [22] V.A. Morozov, S.M. Posokhova, S.Y. Istomin, D. V. Deyneko, A.A. Savina, B.S. Redkin, N. V. Lyskov, D.A. Spassky, A.A. Belik, B.I. Lazoryak, KTb(MoO₄)₂:Green Phosphor with K⁺-Ion Conductivity: Derived from Different Synthesis Routes, *Inorg Chem* 60 (2021) 9471–9483.
- [23] G. Jia, J. Tian, P. Lin, S. Liu, Y. Sun, L. Chen, M. Zhang, R. Yao, Y. Zheng, C. Zhang, Hydrothermal synthesis of NaTb(MoO₄)₂ hierarchical architectures with novel morphology and luminescence properties, *Ceram Int* 42 (2016) 17936–17940.
- [24] S. Devi, C. Sen, R. Singhaal, H.N. Sheikh, Fabrication of multifunctional 3D-flower-shaped NaTb(MoO₄)₂:Dy³⁺@Phen and NaTb(WO₄)₂:Dy³⁺@Phen nanoparticle materials for efficacious luminescence sensing of Fe²⁺ ions and photocatalytic degradation of rhodamine B in an aqueous medium, *New Journal of Chemistry* 47 (2023) 22192–22204.
- [25] Z. Wang, H. Liang, Q. Wang, L. Luo, M. Gong, Luminescent properties of Tb³⁺ activated double molybdates and tungstates, *Materials Science and Engineering: B* 164 (2009) 120–123.
- [26] L. Zhou, S. Hu, X. Zhou, J. Tang, J. Yang, One-step surfactant-free synthesis of Eu³⁺-activated NaTb(MoO₄)₂ microcrystals with controllable shape and their multicolor luminescence properties, *CrystEngComm* 18 (2016) 7590–7600.
- [27] Y. Wang, P. Darapaneni, O. Kizilkaya, J.A. Dorman, Role of Ce in Manipulating the Photoluminescence of Tb Doped Y₂Zr₂O₇, *Inorg Chem* 59 (2020) 2358–2366.
- [28] Z. Xia, R.S. Liu, Tunable blue-green color emission and energy transfer of Ca₂Al₃O₆F:Ce³⁺, Tb³⁺ phosphors for near-UV white LEDs, *Journal of Physical Chemistry C* 116 (2012) 15604–15609.
- [29] S.K.K. Shaat, H.C. Swart, O.M. Ntwaeaborwa, Tunable and white photoluminescence from Tb³⁺–Eu³⁺ activated Ca_{0.3}Sr_{0.7}Al₂O₄ phosphors and analysis of chemical states by X-ray photoelectron spectroscopy, *J Alloys Compd* 587 (2014) 600–605.
- [30] T. Das, S. Mojumder, S. Chakraborty, D. Saha, M. Pal, Beneficial effect of Sn doping on bismuth ferrite nanoparticle-based sensor for enhanced and highly selective detection of trace formaldehyde, *Appl Surf Sci* 602 (2022) 154340.

- [31] K.H. Luo, I.P. Liu, C.C. Chiu, K.W. Lin, W.C. Hsu, W.C. Liu, Comprehensive study of formaldehyde gas sensing performance of a GTO thin film incorporated with gold nanoparticles, *Sens Actuators B Chem* 398 (2024) 134770.
- [32] D. Zhang, Y. Cao, Z. Yang, J. Wu, Nanoheterostructure Construction and DFT Study of Ni-Doped In₂O₃ Nanocubes/WS₂ Hexagon Nanosheets for Formaldehyde Sensing at Room Temperature, *ACS Appl Mater Interfaces* 12 (2020) 11979–11989.
- [33] K. Wan, D. Wang, F. Wang, H. Li, J. Xu, X. Wang, J. Yang, Hierarchical In₂O₃@SnO₂ Core-Shell Nanofiber for High Efficiency Formaldehyde Detection, *ACS Appl Mater Interfaces* 11 (2019) 45214–45225.
- [34] T. Das, S. Mojumder, D. Saha, M. Pal, Enhanced ammonia sensing performance of barium hexaferrite enabled through Zn doping: Mechanistic study considering modulation of Fe²⁺/Fe³⁺ ratio and oxygen vacancy, *Sens Actuators B Chem* 406 (2024) 135358.
- [35] C. Li, H. Zhou, S. Yang, L. Wei, Z. Han, Y. Zhang, H. Pan, Preadsorption of O₂ on the Exposed (001) Facets of ZnO Nanostructures for Enhanced Sensing of Gaseous Acetone, *ACS Appl Nano Mater* 2 (2019) 6144–6151.
- [36] Pushpendra, R.K. Kunchala, S.N. Achary, A.K. Tyagi, B.S. Naidu, Rapid, Room Temperature Synthesis of Eu³⁺ Doped NaBi(MoO₄)₂ Nanomaterials: Structural, Optical, and Photoluminescence Properties, *Cryst Growth Des* 19 (2019) 3379–3388.
- [37] Maheshwary, B.P. Singh, R.A. Singh, Color tuning in thermally stable Sm³⁺-activated CaWO₄ nanophosphors, *New Journal of Chemistry* 39 (2015) 4494–4507.
- [38] T. Thongtem, A. Phuruangrat, S. Thongtem, Characterization of MeWO₄ (Me = Ba, Sr and Ca) nanocrystallines prepared by sonochemical method, *Appl Surf Sci* 254 (2008) 7581–7585.
- [39] Z. Xu, P. Du, Q. Zhu, X. Li, X. Sun, J.G. Li, KLn(MoO₄)₂ micro/nanocrystals (Ln = La–Lu, Y): systematic hydrothermal crystallization, structure, and the performance of doped Eu³⁺ for optical thermometry, *Dalton Transactions* 50 (2021) 17703–17715.
- [40] K. Thomas, D. Alexander, S. Sisira, P.R. Biju, N. V. Unnikrishnan, M.A. Ittyachen, C. Joseph, NUV/blue LED excitable intense green emitting terbium doped lanthanum molybdate nanophosphors for white LED applications, *Journal of Materials Science: Materials in Electronics* 28 (2017) 17702–17709.
- [41] J.C. Sczancoski, L.S. Cavalcante, N.L. Marana, R.O. da Silva, R.L. Tranquilin, M.R. Joya, P.S. Pizani, J.A. Varela, J.R. Sambrano, M. Siu Li, E. Longo, J. Andrés, Electronic structure and optical properties of BaMoO₄ powders, *Current Applied Physics* 10 (2010) 614–624.
- [42] Z. Yu, L. Shen, D. Li, E.Y.B. Pun, X. Zhao, H. Lin, Fluctuation of photon-releasing with ligand coordination in polyacrylonitrile-based electrospun nanofibers, *Scientific Reports* 2020 10:1 10 (2020) 1–13.
- [43] M.G. RJ, S. Gopi, S.M. Simon, A.C. Saritha, P.R. Biju, C. Joseph, N. V. Unnikrishnan, Tunable luminescence of Tb³⁺ doped SiO₂-TiO₂-PDMS hybrid ORMOSILs, *J Lumin* 241 (2022) 118520.
- [44] N. Dirany, E. McRae, M. Arab, Morphological and structural investigation of SrWO₄ microcrystals in relationship with the electrical impedance properties, *CrystEngComm* 19 (2017) 5008–5021. <https://doi.org/10.1039/C7CE00802C>.
- [45] J. Victor Barbosa Moura, A. Amison Gomes de Souza, P. de Tarso Cavalcante Freire, C. da Luz Lima, T. Mielle Brito Ferreira Oliveira, Blue-light-excited NaCe(MoO₄)₂ microcrystals for photoelectrochemical water splitting, *Int J Appl Ceram Technol* 18 (2021) 615–621.
- [46] J. Bao, H. Li, X. Xu, W. Guo, Y. Chen, Y. Zhang, J. Du, H. Wu, G. Duan, Z. Yue, Crystal structure, Raman spectrum, bond characteristics, and terahertz time-domain spectrum of novel Na₅Tm(MoO₄)₄

microwave dielectric ceramic with ultra-low sintering temperature and high quality factor, *J Alloys Compd* 939 (2023) 168652.

- [47] J. Zheng, H. Shen, Y. Li, H. Li, Z. Yue, Structural and down-conversion luminescence of Ce³⁺ and Yb³⁺ doped NaY(MoO₄)₂ phosphor, *Journal of Materials Science: Materials in Electronics* 2024 35:18 35 (2024) 1–13.
- [48] J.V.B. Moura, C. Luz-Lima, G.S. Pinheiro, P.T.C. Freire, Temperature-induced isostructural phase transition on NaCe(MoO₄)₂ system: A Raman scattering study, *Spectrochim Acta A Mol Biomol Spectrosc* 208 (2019) 229–235.
- [49] D. Errandonea, L. Gracia, R. Lacomba-Perales, A. Polian, J.C. Chervin, Compression of scheelite-type SrMoO₄ under quasi-hydrostatic conditions: Redefining the high-pressure structural sequence, *J Appl Phys* 113 (2013).
- [50] R. Vilaplana, O. Gomis, F.J. Manjón, P. Rodríguez-Hernández, A. Muñoz, D. Errandonea, S.N. Achary, A.K. Tyagi, Raman scattering study of bulk and nanocrystalline PbMoO₄ at high pressures, *J Appl Phys* 112 (2012).
- [51] M.T. Colomer, E. Rodríguez, M. Morán-Pedroso, F. Vattier, A. de Andrés, Impact of Tb⁴⁺ and morphology on the thermal evolution of Tb-doped TiO₂ nanostructured hollow spheres and nanoparticles, *J Alloys Compd* 853 (2021) 156973.
- [52] J.V.B. Moura, G.S. Pinheiro, J. V. Silveira, P.T.C. Freire, B.C. Viana, C. Luz-Lima, NaCe(MoO₄)₂ microcrystals: Hydrothermal synthesis, characterization and photocatalytic performance, *Journal of Physics and Chemistry of Solids* 111 (2017) 258–265.
- [53] R. Lacomba-Perales, J. Ruiz-Fuertes, D. Errandonea, D. Martínez-García, A. Segura, Optical absorption of divalent metal tungstates: Correlation between the band-gap energy and the cation ionic radius, *Europhys Lett* 83 (2008) 37002.
- [54] M. Anicete-Santos, F.C. Picon, C.N. Alves, P.S. Pizani, J.A. Varela, E. Longo, The role of short-range disorder in BaWO₄ crystals in the intense green photoluminescence, *Journal of Physical Chemistry C* 115 (2011) 12180–12186.
- [55] L. Zhou, S. Hu, X. Zhou, J. Tang, J. Yang, One-step surfactant-free synthesis of Eu³⁺-activated NaTb(MoO₄)₂ microcrystals with controllable shape and their multicolor luminescence properties, *CrystEngComm* 18 (2016) 7590–7600.
- [56] J. Zhan, S. Peng, Y. Zhu, Z. Zhu, J. Liu, H. Peng, X. Meng, L. Yang, Phase transitions and optical properties of Tb³⁺ activated NaY(WO₄)₂ phosphors, *Ceram Int* 50 (2024) 4896–4906.
- [57] J. Liao, B. Qiu, H. Wen, W. You, Y. Xiao, Synthesis and optimum luminescence of monodispersed spheres for BaWO₄-based green phosphors with doping of Tb³⁺, *J Lumin* 130 (2010) 762–766.
- [58] J. Liao, S. Zhang, H. You, H.R. Wen, J.L. Chen, W. You, Energy transfer and luminescence properties of Eu³⁺-doped NaTb(WO₄)₂ phosphor prepared by a facile hydrothermal method, *Opt Mater (Amst)* 33 (2011) 953–957.
- [59] A.K. Munirathnappa, S.K. Maurya, K. Kumar, K.K. Navada, A. Kulal, N.G. Sundaram, Scheelite like NaTb(WO₄)₂ nanoparticles: Green fluorescence and in vitro cell imaging applications, *Materials Science and Engineering: C* 106 (2020) 110182.
- [60] S.K. Gupta, P.S. Ghosh, A.K. Yadav, N. Pathak, A. Arya, S.N. Jha, D. Bhattacharyya, R.M. Kadam, Luminescence Properties of SrZrO₃/Tb³⁺ Perovskite: Host-Dopant Energy-Transfer Dynamics and Local Structure of Tb³⁺, *Inorg Chem* 55 (2016) 1728–1740.
- [61] G. Gao, A. Winterstein-Beckmann, O. Surzhenko, C. Dubs, J. Dellith, M.A. Schmidt, L. Wondraczek, Faraday rotation and photoluminescence in heavily Tb³⁺-doped GeO₂-B₂O₃-Al₂O₃-Ga₂O₃ glasses for fiber-integrated magneto-optics, *Scientific Reports* 2015 5:1 5 (2015) 1–6.

- [62] M. Xia, X. Wu, Y. Zhong, H.T. Bert Hintzen, Z. Zhou, J. Wang, Photoluminescence properties and energy transfer in a novel $\text{Sr}_8\text{ZnY}(\text{PO}_4)_7:\text{Tb}^{3+},\text{Eu}^{3+}$ phosphor with high thermal stability and its great potential for application in warm white light emitting diodes, *J Mater Chem C Mater* 7 (2019) 2927–2935.
- [63] V.A. Morozov, S.M. Posokhova, S.Y. Istomin, D. V. Deyneko, A.A. Savina, B.S. Redkin, N. V. Lyskov, D.A. Spassky, A.A. Belik, B.I. Lazoryak, $\text{KTb}(\text{MoO}_4)_2$ Green Phosphor with K^{+} -Ion Conductivity: Derived from Different Synthesis Routes, *Inorg Chem* 60 (2021) 9471–9483.
- [64] G. Jia, J. Tian, P. Lin, S. Liu, Y. Sun, L. Chen, M. Zhang, R. Yao, Y. Zheng, C. Zhang, Hydrothermal synthesis of $\text{NaTb}(\text{MoO}_4)_2$ hierarchical architectures with novel morphology and luminescence properties, *Ceram Int* 42 (2016) 17936–17940.
- [65] X. Wang, Z. Zhao, Q. Wu, C. Wang, Q. Wang, L. Yanyan, Y. Wang, Structure, photoluminescence and abnormal thermal quenching behavior of Eu^{2+} -doped $\text{Na}_3\text{Sc}_2(\text{PO}_4)_3$: a novel blue-emitting phosphor for n-UV LEDs, *J Mater Chem C Mater* 4 (2016) 8795–8801.
- [66] M. Rai, G. Kaur, S.K. Singh, S.B. Rai, Probing a new approach for warm white light generation in lanthanide doped nanophosphors, *Dalton Transactions* 44 (2015) 6184–6192.
- [67] Y. Xu, L. Zheng, C. Yang, W. Zheng, X. Liu, J. Zhang, Oxygen Vacancies Enabled Porous SnO_2 Thin Films for Highly Sensitive Detection of Triethylamine at Room Temperature, *ACS Appl Mater Interfaces* 12 (2020) 20704–20713.
- [68] U. Aschauer, R. Pfenninger, S.M. Selbach, T. Grande, N.A. Spaldin, Strain-controlled oxygen vacancy formation and ordering in CaMnO_3 , *Phys Rev B Condens Matter Mater Phys* 88 (2013) 054111.
- [69] H. Fang, S. Li, W. Jiang, H. Zhao, C. Han, J. Li, G. Wang, Y. Zhang, S. Wang, J. Deng, B. Feng, D. Wang, Ppb-level H_2S gas sensor based on CuNi -MOFs derivatives for meat freshness detection at low temperature environment, *Sens Actuators B Chem* 368 (2022) 132225.
- [70] T. Das, S. Mojumder, S. Chakraborty, D. Saha, M. Pal, Beneficial effect of Sn doping on bismuth ferrite nanoparticle-based sensor for enhanced and highly selective detection of trace formaldehyde, *Appl Surf Sci* 602 (2022) 154340.
- [71] T. Das, S. Das, M. Karmakar, S. Chakraborty, D. Saha, M. Pal, Novel barium hexaferrite based highly selective and stable trace ammonia sensor for detection of renal disease by exhaled breath analysis, *Sens Actuators B Chem* 325 (2020) 128765.
- [72] Z. Wang, J. Xue, D. Han, F. Gu, Controllable defect redistribution of ZnO nanopyramids with exposed {1011} facets for enhanced gas sensing performance, *ACS Appl Mater Interfaces* 7 (2015) 308–317.
- [73] M.R. Alenezi, A.S. Alshammari, K.D.G.I. Jayawardena, M.J. Beliatas, S.J. Henley, S.R.P. Silva, Role of the exposed polar facets in the performance of thermally and UV activated ZnO nanostructured gas sensors, *Journal of Physical Chemistry C* 117 (2013) 17850–17858.
- [74] Y. Shi, M. Wang, C. Hong, Z. Yang, J. Deng, X. Song, L. Wang, J. Shao, H. Liu, Y. Ding, Multi-junction joints network self-assembled with converging ZnO nanowires as multi-barrier gas sensor, *Sens Actuators B Chem* 177 (2013) 1027–1034.
- [75] C. Zhang, J. Wang, R. Hu, Q. Qiao, X. Li, Synthesis and gas sensing properties of porous hierarchical SnO_2 by grapefruit exocarp biotemplate, *Sens Actuators B Chem* 222 (2016) 1134–1143.
- [76] Y. Li, N. Chen, D. Deng, X. Xing, X. Xiao, Y. Wang, Formaldehyde detection: SnO_2 microspheres for formaldehyde gas sensor with high sensitivity, fast response/recovery and good selectivity, *Sens Actuators B Chem* 238 (2017) 264–273.

CHAPTER 7

Overall conclusion and future prospects

7.1. Conclusion

The present thesis work delineates exploration of gas sensing property of novel metal oxide semiconductor nanomaterials and the study of effect of different strategies such as doping, bandgap engineering, formation of heterostructure, modulation of defects in the system on the gas sensing mechanism of the nanomaterials. The nanomaterials and its composites were synthesised via facile route. Sensors were fabricated based on the nanomaterials for the purpose of cost-effective, real-time monitoring of exhaled breath, which helps in non-invasive monitoring and pre-diagnosis of disease and also for the detection of toxic gases in the environment. The fabricated sensors were tested for their practical applicability by simulated breath study, in which the sensors showed excellent performance proving the sensor materials' potentiality for device application. It can be concluded from the study that, gas sensing and optical property of nanomaterials are both driven by structural property of nanomaterials (such as band gap, defect states, separation of electron-holes, charge transfer mechanism, surface active sites). Therefore, by strategic controlling of these parameters, the characteristics of the nanomaterials can be modulated as per need. Hence, multifunctional property (toward gas sensing and photoluminescence) in a single system have been achieved in a single system by systematic modulation of these influencing parameters.

The detailed study of chemiresistive gas sensors and their application areas has been conducted along with their ease of use, cost-effectiveness, synthesis procedure has been highlighted keeping in mind the objectives of the work. Emphasis has been given on the study of the general working principle and the influencing parameters of gas sensing kinetics of basic chemiresistive sensors based on binary metal oxide semiconductors. The synthesis procedures and characterization techniques for nanomaterials have been examined in alignment with the objectives of this thesis.

Trace ammonia sensing capability with high sensitivity and selectivity using barium hexaferrite nanoparticles ($\text{BaFe}_{12}\text{O}_{19}$) has been successfully synthesized by facile solid-state route. The developed sensor exhibited p-type sensing nature and showed high sensitivity to different trace concentrations of ammonia vapor, viz. ~ 2.34 folds to 1ppm ammonia vapor, and ~ 1.46 folds to 0.2ppm ammonia. It also exhibited fast response (2.88s) and recovery times (39.4s) along with negligible cross-sensitivities towards other major interfering breath volatiles, viz. acetone, ethanol, and saturated moisture vapor. Such excellent sensing properties were attributed to high specific surface area, optimized operating temperature, and small size of ammonia molecule. In totality the superior sensing properties of the prepared sensor towards

trace ammonia makes BaFe₁₂O₁₉ nanoparticles a promising candidate for the detection of renal diseases by exhaled breath analysis.

In the next exploration, trace ammonia sensing performance of BaFe₁₂O₁₉ nanoparticles has been improved significantly by doping with Zn. 3% Zn-doped BaFe₁₂O₁₉-based sensor exhibited greater selectivity toward ammonia with negligible effect of humidity, enhanced response ($R_{\text{gas}}/R_{\text{air}}=7.36$) towards 1 ppm NH₃ at 250 °C, lower detection limit of 150 ppb, fast response/recovery times 2.66s/35.25s. It has been concluded that, Enhanced response is attributed to the modulation of the surface oxygen defect and active gas-adsorption sites by introducing Zn²⁺ in the system in place of Fe³⁺ and the results has been validated utilising XPS analysis. Wide range of ammonia concentration sensing capability of Zn-doped BaFe₁₂O₁₉-based sensor proves its superiority over other sensing materials. Additionally, simulated breath test of the sensor has showed excellent result. Therefore, this work is important for developing an ammonia sensor with versatile applications, including health monitoring through the detection of ammonia in exhaled breath and environmental air-quality surveillance for monitoring ammonia exposure.

Pure and Sn-doped BiFeO₃ nanoparticles have been synthesized using sol-gel route and their formaldehyde gas sensing performances have been investigated. It has been observed that both pristine and Sn-doped BiFeO₃ nanoparticles delineates p-type sensing characteristics and sensitivity enhances more than 2.4 times towards formaldehyde gas when doped with Sn. As synthesised 1.5% Sn doped BiFeO₃ nanoparticles-based sensor showed response ~3.01 towards 1ppm formaldehyde gas at 280 °C operating temperature, with a fast response/recovery time of 2.71s/25.22s, good selectivity, resolution, detection limit down to 100 ppb and exceptional 600 days stability. Experimental results suggest that creation of oxygen defects due to Sn doping is responsible for enhanced sensing activity. It has been observed that, Sn-doped BiFeO₃ nanoparticles-based sensor is a promising candidate for development of high-performance formaldehyde sensing device for the monitoring of indoor air quality.

The drawbacks of H₂S sensing activity of large band gap MoO₃ has been overcome through heterojunction formation with BiFeO₃ nanoparticles. A Type-II heterostructure has been formed between n-type MoO₃ nanorods and n-type BiFeO₃ nanoparticles for H₂S gas sensing for environmental air quality monitoring. The photoelectrochemical measurement confirmed that the optimised α -MoO₃/BiFeO₃ heterostructure exhibited the highest photocurrent density as well as low charge transfer resistance. As a result, it exhibited enhanced

sensing property with $\sim 98\%$ n-type sensing response to 100 ppm H_2S gas with rapid response/recovery time of 4.7s/14s. Owing to presence of higher oxygen defect in optimised $\alpha\text{-MoO}_3/\text{BiFeO}_3$ compared to bare MoO_3 the localised states were generated within the bandgap of the heterostructure which act as trapping centres for charge carriers (electrons and holes). Furthermore, these defect states serve as active sites for adsorption of gas molecules, facilitating the H_2S sensing activity. Thus, modification in the electronic structure of $\alpha\text{-MoO}_3/\text{BiFeO}_3$ and tuning of oxygen defect states influence the separation and migration of charge carriers, which is crucial for efficient H_2S sensing behaviour. Thus, prepared $\alpha\text{-MoO}_3/\text{BiFeO}_3$ heterostructure could be promising material to sense H_2S for environmental air quality monitoring.

During the investigation of MoO_3 -based systems for gas sensing activity (as discussed in chapter 5) it has been found out that MoO_3 exhibits excellent optical property driven by structural defects. In relation to that, it has also been found out that scheelite type molybdate structure, $\text{ALn}(\text{MoO}_4)_2$ (A= alkali metal ions, Ln= rare earth ions), exhibit photoluminescence property which can be readily tuned by doping with rare earth metals. In the final work, structural disorder induced multifunctional property of $\text{NaTb}(\text{MoO}_4)_2$ for gas sensing and photoluminescence application has been delineated. The disorder in MoO_4 tetrahedra was controlled during synthesis via hydrothermal method. $\text{NaTb}(\text{MoO}_4)_2$ nanoparticles exhibited green luminescence property at 330 nm excitation. The main luminescence peak corresponding to the $^5\text{D}_4 \rightarrow ^7\text{F}_5$ magnetic dipole allowed transition of ($\Delta J=1$) of Tb^{3+} at 547 nm was Stark split into two separate peaks. Theoretical calculation-based density functional theory (DFT) revealed that the splitting of most prominent PL peak is caused by the decrease in partial density of states (PDOS) of Tb in the samples with increasing disorder in the system. Moreover, the gradual decrease of main PL peak (at 574 nm) and simultaneous increase in the peak intensity at 530 nm corroborates with the increasing disorder in the MoO_4 tetrahedra as validated by both experimental and theoretical calculations. The increase in PDOS of Mo in the disordered systems suggest the transfer of electrons from O^{2-} to Mo^{6+} then to Tb^{3+} . The CIE coordinates, colour temperature of $\text{NaTb}(\text{MoO}_4)_2$ proves its potential applicability in commercial light display systems. Additionally, disordered $\text{NaTb}(\text{MoO}_4)_2$ exhibited formaldehyde (HCHO) sensing activity with p-type response value of 3.5-fold to 1 ppm gas concentration and rapid response/recovery time (1.5s/18.3s) with high selectivity. DFT calculations revealed minimum adsorption energy of HCHO on disordered $\text{NaTb}(\text{MoO}_4)_2$ material surface. Therefore this can be concluded that, structural disorder induced multifunctional $\text{NaTb}(\text{MoO}_4)_2$ nanomaterial is a

potential candidate for applications in lighting equipment and its HCHO sensing performance makes it a good HCHO sensing material applicable for indoor air-quality monitoring.

Throughout this thesis work, various novel materials for gas sensing applications have been synthesised and the characteristics have been studied thoroughly. The fabricated novel sensors based on these materials exhibited superior sensing property compared to the existing gas sensing materials reported in literature. Toxic volatile organic compounds and gas molecule detection has been delineated based on the fabricated sensors. Along with, the mechanism of photoluminescence and the parameters influencing the activity has been studied. It can be concluded that, this thesis has fulfilled all the objectives of the research and it paves the way of fabrication of nanomaterials and its composites-based stable sensors for potential device application for real-time gas detection. The final work provides unprecedented insights into the strategic designing and realization of multifunctionality in a single nanomaterial/or its composite systems potentially paving the way for the development of multifunctional electronic application platforms.

7.2. Future prospects

This thesis elaborates the fabrication of emerging sensing nanomaterials-based gas sensors and their advancement by tailoring structural and electronic properties, which leads the research work to the direction of innovation of further novel gas sensors. Further, analysis and study of the nanomaterials can be conducted in depth by the support of theoretical calculations based on density functional theory (DFT), which can be helpful in material designing and optimization by provide more insight knowledge on electronic band structure, molecular adsorption mechanism of the nanomaterials. Utilizing DFT calculations, the selectivity of the sensors can be predicted which makes it a useful tool for material designing.

- 1) Emerging sensing materials for device application:** Metal organic frameworks are emerging class of materials due to their ultrahigh surface area, porosity, large accessible surface-active sites. These materials can be tuned and functionalised easily with other compounds to form high-performance sensor systems.
- 2) Portable/handheld gas sensor devices for health monitoring:** Most of the currently available gas sensing devices are designed to detect higher gas concentrations, making them suitable for industrial applications. There are no commercially available sensing devices that is capable of non-invasive detection of trace-level biomarkers in exhaled breath, which would be crucial for breath analysis in monitoring diseases such as renal disease, diabetes,

cardiovascular disorder, lung cancer etc. Therefore, handheld/portable gas sensing devices can be developed utilizing Arduino-based electronic systems consisting of tailored nanomaterials for precise and real-time breath analysis.

- 3) **Flexible and wearable smart gas sensors:** Flexible/wearable sensing device can be developed on various substrates such as textiles, papers utilising cutting edge technology and emerging materials (MOF, 2D/1D nanomaterials) for health monitoring, toxic gas exposure monitoring.
- 4) **Self-powering sensor systems:** In this era of high energy demand, it is of high significant to develop self-powering systems for conservation of energy. Utilizing energy harvesting materials and integrating it into sensor devices, self-sustained sensor systems can be designed which will help in sustainable development of modern technology.
- 5) **Designing of multifunctional nanomaterials for various applications:** Utilizing the knowledge on designing and fabrication of nanomaterials, multifunctional materials can be developed by tailoring their surface catalytic activity and charge transport mechanism to address the need for renewable energy and environmental remedy.

Appendix I

List of publications

- 1) **T. Das**, S. Das, M. Karmakar, S. Chakraborty, D. Saha, M. Pal, Novel barium hexaferrite based highly selective and stable trace ammonia sensor for detection of renal disease by exhaled breath analysis, *Sens Actuators B Chem* 325 (2020) 128765. <https://doi.org/10.1016/J.SNB.2020.128765>.
- 2) **T. Das**, S. Mojumder, S. Chakraborty, D. Saha, M. Pal, Beneficial effect of Sn doping on bismuth ferrite nanoparticle-based sensor for enhanced and highly selective detection of trace formaldehyde, *Appl Surf Sci* 602 (2022) 154340. <https://doi.org/10.1016/J.APSUSC.2022.154340>.
- 3) **T. Das**, S. Mojumder, D. Saha, M. Pal, Enhanced ammonia sensing performance of barium hexaferrite enabled through Zn doping: Mechanistic study considering modulation of Fe²⁺/Fe³⁺ ratio and oxygen vacancy, *Sens Actuators B Chem* 406 (2024) 135358. <https://doi.org/10.1016/J.SNB.2024.135358>.
- 4) **T. Das**, S. Mojumder, D. Sarkar, S. Ghosh, M. Pal, Multifunctional n-n Type α MoO₃/BiFeO₃ Heterostructures for Enhanced Charge Transfer Induced Photocatalytic Water Splitting and H₂S Gas Sensing. [Manuscript- Under Review]
- 5) **T. Das**, K. R. Sahoo, M. Pal, C. K. Ghosh, Structural disorder driven multifunctionality of NaTb(MoO₄)₂ nanoparticles toward green photoluminescence and detection of HCHO [Manuscript- Under Review]
- 6) S. Mojumder, **T. Das**, T. Mondal, S. Ghosh, D. Saha, C.K. Ghosh, M. Pal, Improved ammonia sensing performance achieved through defect modulation by Li doping in cauliflower-like ZnO for exhaled breath analysis towards renal diseases detection: An experimental venture supported by DFT calculation, *TrAC Trends in Analytical Chemistry* 180 (2024) 117896. <https://doi.org/10.1016/J.TRAC.2024.117896>.
- 7) N. Halder, T. Mondal, **T. Das**, D. Sarkar, M. Pal, A.H. Seikh, C.K. Ghosh, A truncated octahedron NaCe(MoO₄)₂ nanostructure: a potential material for blue emission and acetone sensing, *Mater Adv* 5 (2024) 4480–4490. <https://doi.org/10.1039/D4MA00306C>.
- 8) S. Mojumder, **T. Das**, D. Saha, M. Pal, Highly sensitive and selective chemiresistive temperature-dependent trace formalin sensor using hydrothermally grown hexagonal yttrium ferrite, *Mater Chem Phys* 319 (2024). <https://doi.org/10.1016/J.MATCHEMPHYS.2024.129329>.
- 9) S. Mojumder, **T. Das**, M. Mukherjee, D. Saha, A. Datta, M. Pal, Development of highly sensitive and selective trace acetone sensor using perovskite yttrium ferrite: Mechanism,

- kinetics and phase dependence study, Chemical Engineering Journal 477 (2023) 146855. <https://doi.org/10.1016/J.CEJ.2023.146855>.
- 10) N. Haldar, T. Mondal, **T. Das**, D. Sarkar, M. Pal, C.K. Ghosh, Hydrothermal synthesis of defect-induced pristine α -NaCe(WO₄)₂: a novel material for solid state lighting and gas sensing, CrystEngComm 25 (2023) 3514–3527. <https://doi.org/10.1039/D3CE00312D>.
 - 11) S. Mojumder, **T. Das**, S. Das, N. Chakraborty, D. Saha, M. Pal, Y and Al co-doped ZnO-nanopowder based ultrasensitive trace ethanol sensor: A potential breath analyzer for fatty liver disease and drunken driving detection, Sens Actuators B Chem 372 (2022). <https://doi.org/10.1016/J.SNB.2022.132611>.
 - 12) S. Das, P.L. Mahapatra, P.P. Mondal, **T. Das**, M. Pal, D. Saha, A highly sensitive cobalt chromite thick film based trace acetone sensor with fast response and recovery times for the detection of diabetes from exhaled breath, Mater Chem Phys 262 (2021). <https://doi.org/10.1016/J.MATCHEMPHYS.2021.124291>.
 - 13) P.L. Mahapatra, S. Das, P.P. Mondal, **T. Das**, D. Saha, M. Pal, Microporous copper chromite thick film based novel and ultrasensitive capacitive humidity sensor, J Alloys Compd 859 (2021). <https://doi.org/10.1016/J.JALLCOM.2020.157778>.
 - 14) S. Sau, S. Chakraborty, **T. Das**, M. Pal, Ethanol Sensing Properties of Nanocrystalline α -MoO₃, Front Mater 6 (2019) 482190. <https://doi.org/10.3389/FMATS.2019.00285/BIBTEX>.
 - 15) K. R. Sahoo, **T. Das**, M. Pal, R. Karim, A. Seikh, C. K. Ghosh, Multifunctional NaEu(WO₄)₂: defect-tuned red emission and acetone sensing at room temperature. [Manuscript- Accepted in RSC Mater Adv (2024)]
[DOI: 10.1039/D4MA00617H](https://doi.org/10.1039/D4MA00617H)
 - 16) S. Mojumder, **T. Das**, S. Monga, D. Sarkar, S. Bhattacharya, S. Ghosh, M. Pal, Tuning of important parameters for enhanced CO sensing of Zinc Oxide-Zinc Ferrite based n-n type heterostructure: An experimental study supported by theoretical calculation. [Manuscript- Under Review]
 - 17) S. Dash, S. Mojumder, **T. Das**, D. Saha, M. Pal, Highly sensitive and selective rGO LaFeO₃ nanocomposite based formaldehyde sensors towards air quality monitoring. [Manuscript- Under Review]

Appendix II

Awards

- 1) **“MRSI Young Scientist Award 2022”** for **best oral presentation** at “Young Scientists’ Colloquium 2022” organized by Materials Research Society of India (MRSI), Kolkata Chapter at CSIR-Central Glass and Ceramic Research Institute, Kolkata, on December 16, 2022.
- 2) **Best oral presentation** award at 3rd One Day Symposium on “Sensors for Society, organised by ECS-Jawaharlal Nehru University Student Chapter, JNU, New Delhi, INDIA, on 12th January 2023.
- 3) **Best poster presentation** award at International Conference on Thin Films & Nanotechnology: Knowledge, Leadership, & Commercialization, organised by Department of Physics of Indian Institute of Technology Madras, IIT Madras, July 6-8, 2023.

Appendix III

List of conference attended

- 1) 2nd Indian Materials Conclave and 31st AGM of MRSI, February 2020, MRSI Kolkata chapter, India.
Mode of presentation: **Poster presentation**
Topic of poster presentation: Barium hexaferrite nanocomposites-based trace level ammonia sensor for advanced medical application.
- 2) International Symposium on Materials of the Millennium: Emerging Trends and Future Prospects (MMETFP-2021), November 2021, Gandhinagar, Gujarat, India.
Mode of presentation: **Oral presentation**
Topic of presentation: ZnO nanostructured based trace ammonia sensor for medical application.
- 3) 2nd International Conference on Multifunctional Materials (2nd ICMM-2022), Geethanjali College of Engineering and Technology (GCET), Keesara, Hyderabad, December 22-24, 2022.
Mode of presentation: **Oral presentation**
Topic of presentation: PVA Assisted Synthesis of ZnO Nanostructure as Ammonia Sensor Towards Non-invasive Monitoring of Renal Disease.
- 4) Young Scientists' Colloquium 2022, Materials Research Society of India (Kolkata Chapter), December 16, 2022.
Mode of presentation: **Oral presentation**
Topic of oral presentation: Trace formaldehyde sensor based on Sn doped on bismuth ferrite nanoparticles for indoor air quality monitoring
- 5) 3rd One Day Symposium on "Sensors for Society, organised by ECS-Jawaharlal Nehru University Student Chapter, JNU, New Delhi, INDIA, on 12th January 2023.
Mode of presentation: **Oral presentation**
Topic of oral presentation: Sndoped on bismuth ferrite nanoparticles-based sensor towards enhanced and highly selective detection of trace formaldehyde for indoor air quality monitoring
- 6) International Conference on Thin Films & Nanotechnology: Knowledge, Leadership, & Commercialization, organised by Department of Physics of Indian Institute of Technology Madras, IIT Madras, Chennai-600036, from July 6-8, 2023

Mode of presentation: **Poster presentation**

Topic of poster presentation: Enhanced Ammonia Sensing Performance of Zn Doped BaFe₁₂O₁₉ Nanoparticles-Based Sensor for Noninvasive Detection of Ammonia in Exhaled Breath of Patients with Renal Diseases

- 7) Young Scientists Colloquium YSC-2023 Organised by Materials Research Society of India (Kolkata Chapter) In association with School of Materials Science & Nanotechnology Jadavpur University In collaboration with Indian Institute of Engineering Science & Technology, Shibpur, Friday, December 01, 2023

Mode of presentation: **Poster presentation**

Topic of poster presentation: Electron Compensation Mechanism to Promote Oxygen Vacancies in Favour of Enhanced CO Sensing Performance of Sn-doped BaFe₁₂O₁₉

- 8) 34th Annual General Meeting of MRSI And 5th Indian Materials Conclave organized by the School of Materials Science and Technology Indian Institute of Technology (BHU) Varanasi, from December 12-15, 2023

Mode of presentation: **Poster presentation**

Topic of poster presentation: Enhanced ammonia sensing of Zn Doped BaFe₁₂O₁₉ Nanoparticles-Based Sensor for the detection of renal diseases by breath analysing

- 9) 4th Global Ceramic Leadership Roundtable on Ceramics for Frontier Sectors: Emerging Advances and Prospects (CerAP2024) organized by Center for Space Science and Technology IIT Roorkee in association with The American Ceramic Society (Northeast India Chapter) on March 11-12, 2024

Mode of presentation: **Poster presentation**

Topic of poster presentation: Electron Compensation Mechanism to Promote Oxygen Vacancies in Favour of Enhanced CO Sensing Performance of Sn-Doped BaFe₁₂O₁₉ Ceramic for Environmental Air Quality Monitoring

- 10) International Conference on Fundamental and Advanced Research in Chemistry 2024 (FARC-2024), Indian Institute of Technology Mandi, on 8-10 June, 2024.

Mode of presentation: **Poster presentation**

Topic of poster presentation: α -MoO₃/BiFeO₃ Heterostructure for Enhanced Charge Transfer Induced Multifunctional Application in Photocatalytic H₂ Generation from Water and H₂S sensing